Brain institute bets big on open science *p. 329*

Regulating genome editing *p. 337*

Consoling prairie voles *p. 375*

Science

$15
22 JANUARY 2016
sciencemag.org

AAAS

Molecular weaving

A route to flexible framework materials

pp. 336 & 365

CONTENTS

22 JANUARY 2016 • VOLUME 351 • ISSUE 6271

330
The solar system gains a planet

NEWS

IN BRIEF

320 News at a glance

IN DEPTH

323 **SHELL TRADE PUSHES GIANT CLAMS TO THE BRINK**
With elephant tusks harder to obtain, the "jade of the sea" is the new ivory in China *By C. Larson*

324 **DEBATE SHARPENS OVER U.K. THREAT TO LEAVE EUROPE**
Many researchers worry about a loss of funds and influence, but some say the fears are overblown *By E. Stokstad and T. Rabesandratana*

325 **BIDEN SEEKS CLEAR COURSE FOR HIS CANCER MOONSHOT**
Researchers have plenty of ideas for the vice president's bid to boost collaboration and improve treatments *By J. Kaiser and J. Couzin-Frankel*

326 **STANDOFF IMPERILS OREGON REFUGE**
Takeover disrupts what observers call a model public-private restoration effort *By R. F. Service*

328 **DATA CHECK: TRACKING FIRST JOBS TO MEASURE THE IMPACT OF RESEARCH FUNDING**
Study of recent Ph.D.s at eight Midwestern universities demonstrates value of the new science of science policy *By J. Mervis*

329 **MONTREAL INSTITUTE GOING 'OPEN' TO ACCELERATE SCIENCE**
Experiment aims to show whether forgoing patents and freeing up data can boost neuroscience research *By B. Owens*

FEATURE

330 **NUMBER 9**
A new giant planet, still unseen, appears to be shaping the orbits of objects beyond Neptune *By E. Hand*
▸ PODCAST

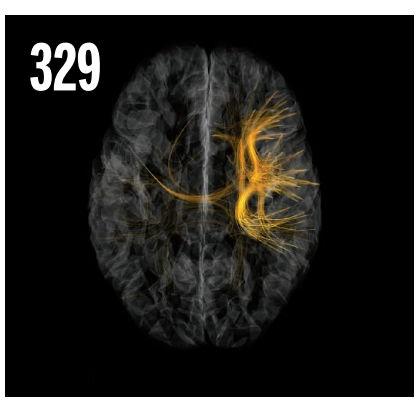

INSIGHTS

PERSPECTIVES

334 **PLASMONICS—TURNING LOSS INTO GAIN**
The optical losses usually associated with plasmonic materials could be used in applications *By J. C. Ndukaife* et al.

336 **INTERLACING MOLECULAR THREADS**
Materials with a fabric-like microstructure are highly elastic *By E. Gutierrez-Puebla*
▸ REPORT P. 365

337 **EDITING POLICY TO FIT THE GENOME?**
Framing genome editing policy requires setting thresholds of acceptability *By R. Isasi* et al.

340 **HOW CHERENKOV RADIATIVE LOSSES CAN IMPROVE OPTICAL FREQUENCY COMBS**
Broader optical frequency combs on a photonic chip can help refine time standards *By N. Akhmediev and N. Devine*
▸ REPORT P. 357

341 **OLIGODENDROCYTES FOLLOW BLOOD VESSEL TRAILS IN THE BRAIN**
Brain microvasculature is a scaffold for neuroglial migration *By E. Dejana and C. Betsholtz*
▸ REPORT P. 379

342 **THE DO-IT-ALL NITRIFIER**
The discovery of bacteria that can oxidize both ammonia and nitrite upends a long-held dogma *By A. E. Santoro*

344 **KNOWLEDGE CAPITAL, GROWTH, AND THE EAST ASIAN MIRACLE**
Access to schools achieves only so much if quality is poor *By E. A. Hanushek and L. Woessmann*

BOOKS *ET AL.*

346 **THE CABARET OF PLANTS**
By R. Mabey, reviewed by H. A. Curry

347 **TRAUMA**
Reviewed by G. Frazzetto

LETTERS

348 **EDITORIAL EXPRESSION OF CONCERN**
By M. McNutt

348 **ERADICATING POLIO: A BALANCING ACT**
By V. Agol et al.

348 **PRACTICALITIES OF POLITICAL AGENCY**
By I. Kelman

349 **RESPONSE**
By K. O'Brien

Published by AAAS

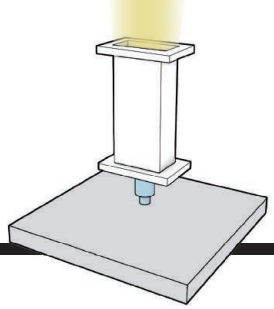

334
Plasmonics applications heat up

341 & 379
Neuroglia follow vascular paths

RESEARCH

IN BRIEF

350 From *Science* and other journals

REVIEW

353 **SOLAR ENERGY**
Research opportunities to advance solar energy utilization *N. S. Lewis*
REVIEW SUMMARY; FOR FULL TEXT:
dx.doi.org/10.1126/science.aad1920

REPORTS

354 **RADIO ASTRONOMY**
Real-time detection of an extreme scattering event: Constraints on Galactic plasma lenses
K. W. Bannister et al.

357 **APPLIED OPTICS**
Photonic chip–based optical frequency comb using soliton Cherenkov radiation
V. Brasch et al.
▸ PERSPECTIVE P. 340

361 **ELECTROCHEMISTRY**
Active sites of nitrogen-doped carbon materials for oxygen reduction reaction clarified using model catalysts
D. Guo et al.

365 **MOLECULAR FRAMEWORKS**
Weaving of organic threads into a crystalline covalent organic framework
Y. Liu et al.
▸ PERSPECTIVE P. 336

369 **PHOTOPHYSICS**
Direct observation of triplet energy transfer from semiconductor nanocrystals
C. Mongin et al.

372 **GEOCHEMISTRY**
Archean upper crust transition from mafic to felsic marks the onset of plate tectonics *M. Tang* et al.

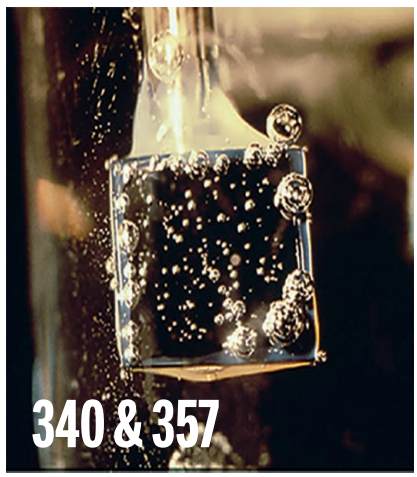

375 **COMPARATIVE BEHAVIOR**
Oxytocin-dependent consolation behavior in rodents
J. P. Burkett et al.

379 **NEURODEVELOPMENT**
Oligodendrocyte precursors migrate along vasculature in the developing nervous system *H.-H. Tsai* et al.
▸ PERSPECTIVE P. 341

384 **PLANT DEVELOPMENT**
Cyclic programmed cell death stimulates hormone signaling and root development in *Arabidopsis*
W. Xuan et al.

387 **POLLINATOR DIVERSITY**
Mutually beneficial pollinator diversity and crop yield outcomes in small and large farms
L. A. Garibaldi et al.

SMALL RNAS

391 Biogenesis and function of tRNA fragments during sperm maturation and fertilization in mammals
U. Sharma et al.

397 Sperm tsRNAs contribute to intergenerational inheritance of an acquired metabolic disorder
Q. Chen et al.

GENE EDITING

400 Postnatal genome editing partially restores dystrophin expression in a mouse model of muscular dystrophy *C. Long* et al.

403 In vivo genome editing improves muscle function in a mouse model of Duchenne muscular dystrophy
C. E. Nelson et al.

407 In vivo gene editing in dystrophic mouse muscle and muscle stem cells
M. Tabebordbar et al.

DEPARTMENTS

319 **EDITORIAL**
Future Earth
By Johan Rockström

418 **WORKING LIFE**
Disability is not a disqualification
By Jesse Shanahan

ON THE COVER

Illustration of woven molecular fabric. Interlacing threads to create woven patterns is among the oldest methods of making fabric, but until now, this technique has not been duplicated in complex chemical structures. Liu *et al.* used threads made from organic molecules linked together by strong covalent bonds to weave a three-dimensional covalent organic framework with unusual dynamical and mechanical properties. This molecular weaving method will enable the production of materials with increased precision and functionality. See pages 336 and 365. *Illustration: C. Bickel*/Science

Science Staff 318
New Products 412
Science Careers 414

SCIENCE (ISSN 0036-8075) is published weekly on Friday, except the last week in December, by the American Association for the Advancement of Science, 1200 New York Avenue, NW, Washington, DC 20005. Periodicals mail postage (publication No. 484460) paid at Washington, DC, and additional mailing offices. Copyright © 2016 by the American Association for the Advancement of Science. The title SCIENCE is a registered trademark of the AAAS. Domestic individual membership and subscription (51 issues): $165 ($74 allocated to subscription). Domestic institutional subscription (51 issues): $1522; Foreign postage extra: Mexico, Caribbean (surface mail) $55; other countries (air assist delivery) $89. First class, airmail, student, and emeritus rates on request. Canadian rates with GST available upon request, GST #1254 88122. Publications Mail Agreement Number 1069624. **Printed in the U.S.A.**
Change of address: Allow 4 weeks, giving old and new addresses and 8-digit account number. **Postmaster:** Send change of address to AAAS, P.O. Box 96178, Washington, DC 20090–6178. **Single-copy sales:** $15.00 current issue, $20.00 back issue prepaid includes surface postage; bulk rates on request. **Authorization to photocopy** material for internal or personal use under circumstances not falling within the fair use provisions of the Copyright Act is granted by AAAS to libraries and other users registered with the Copyright Clearance Center (CCC) Transactional Reporting Service, provided that $35.00 per article is paid directly to CCC, 222 Rosewood Drive, Danvers, MA 01923. The identification code for *Science* is 0036-8075. *Science* is indexed in the *Reader's Guide to Periodical Literature* and in several specialized indexes.

Published by AAAS

Science
AAAS
1200 New York Avenue, NW, Washington, DC 20005
Bateman House, 82-88 Hills Road, Cambridge, UK CB2 1LQ

Editor-in-Chief Marcia McNutt
Executive Editor Monica M. Bradford **News Editor** Tim Appenzeller
Managing Editor, Research Journals Katrina L. Kelner
Deputy Editors Barbara R. Jasny, Andrew M. Sugden(UK), Valda J. Vinson, Jake S. Yeston

Research and Insights

SR. EDITORS Caroline Ash(UK), Gilbert J. Chin, Lisa D. Chong, Julia Fahrenkamp-Uppenbrink(UK), Pamela J. Hines, Stella M. Hurtley(UK), Paula A. Kiberstis, Marc S. Lavine(Canada), Kristen L. Mueller, Ian S. Osborne(UK), Beverly A. Purnell, L. Bryan Ray, Guy Riddihough, H. Jesse Smith, Jelena Stajic, Peter Stern(UK), Phillip D. Szuromi, Sacha Vignieri, Brad Wible, Nicholas S. Wigginton, Laura M. Zahn **ASSOCIATE EDITORS** Brent Grocholski, Keith T. Smith **ASSOCIATE BOOK REVIEW EDITOR** Valerie B. Thompson **ASSOCIATE LETTERS EDITOR** Jennifer Sills **CHIEF CONTENT PRODUCTION EDITOR** Cara Tate **SR. CONTENT PRODUCTION EDITORS** Harry Jach, Lauren Kmec **CONTENT PRODUCTION EDITORS** Jeffrey E. Cook, Chris Filiatreau, Cynthia Howe, Barbara P. Ordway, Catherine Wolner **SR. EDITORIAL COORDINATORS** Carolyn Kyle, Beverly Shields **EDITORIAL COORDINATORS** Joi S. Granger, Lisa Johnson, Anita Wynn **PUBLICATIONS ASSISTANTS** Aneera Dobbins, Jeffrey Hearn, Dona Mathieu, Le-Toya Mayne Flood, Shannon McMahon, Scott Miller, Caitlyn Phillips, Jerry Richardson, Rachel Roberts(UK), Alice Whaley(UK), Brian White **EXECUTIVE ASSISTANT** Anna Bashkirova **ADMINISTRATIVE SUPPORT** Janet Clements(UK), Lizanne Newton(UK), Maryrose Madrid, John Wood(UK)

News

NEWS MANAGING EDITOR John Travis **INTERNATIONAL EDITOR** Richard Stone **DEPUTY NEWS EDITORS** Daniel Clery(UK), Robert Coontz, Elizabeth Culotta, David Grimm, David Malakoff, Leslie Roberts **CONTRIBUING EDITOR** Martin Enserink(Europe) **SR. CORRESPONDENTS** Jeffrey Mervis, Elizabeth Pennisi **NEWS WRITERS** Adrian Cho, Jon Cohen, Jennifer Couzin-Frankel, Carolyn Gramling, Eric Hand, Jocelyn Kaiser, Catherine Matacic, Kelly Servick, Robert F. Service, Erik Stokstad(Cambridge, UK), Emily Underwood **INTERNS** Hanae Armitage, Nala Rogers **CONTRIBUTING CORRESPONDENTS** Michael Balter(Paris), John Bohannon, Ann Gibbons, Mara Hvistendahl, Sam Kean, Eli Kintisch, Kai Kupferschmidt(Berlin), Andrew Lawler, Christina Larson(Beijing), Mitch Leslie, Charles C. Mann, Eliot Marshall, Virginia Morell, Dennis Normile(Shanghai), Heather Pringle, Tania Rabesandratana(London), Gretchen Vogel(Berlin), Lizzie Wade(Mexico City) **CAREERS** Donisha Adams, Rachel Bernstein(Editor) **COPY EDITORS** Julia Cole, Dorie Chevlen, Jennifer Levin (Chief) **ADMINISTRATIVE SUPPORT** Jessica Williams

Executive Publisher Rush D. Holt
Acting Publisher Bill Moran **Chief Digital Media Officer** Rob Covey

BUSINESS OPERATIONS AND PORTFOLIO MANAGEMENT DIRECTOR Sarah Whalen **BUSINESS SYSTEMS AND FINANCIAL ANALYSIS DIRECTOR** Randy Yi **MANAGER OF FULFILLMENT SYSTEMS** Neal Hawkins **SYSTEMS ANALYST** Nicole Mehmedovich **ASSISTANT DIRECTOR, BUSINESS OPERATIONS** Eric Knott **MANAGER, BUSINESS OPERATIONS** Jessica Tierney **BUSINESS ANALYSTS** Cory Lipman **FINANCIAL ANALYST** Robert Clark **RIGHTS AND PERMISSIONS ASSISTANT DIRECTOR** Emilie David **PERMISSIONS ASSOCIATE** Elizabeth Sandler **RIGHTS, CONTRACTS, AND LICENSING ASSOCIATE** Lili Kiser

MARKETING DIRECTOR Elise Swinehart **ASSOCIATE DIRECTOR OF ACQUISITION AND RETENTION** Julianne Wielga **MARKETING ASSOCIATE** Elizabeth Sattler **SR. MARKETING EXECUTIVE** Jennifer Reeves **ASSOCIATE DIRECTOR, CREATIVE SERVICES** Tzeitel Sorrosa **ART ASSOCIATE** Seil Lee **JR. ART ASSOCIATE** Kim Huynh **ASSISTANT COMMERCIAL EDITOR** Selby Frame **MARKETING PROJECT MANAGER** Angelissa McArthur **PROGRAM DIRECTOR, AAAS MEMBER CENTRAL** Peggy Mihelich **FULFILLMENT SYSTEMS AND OPERATIONS** membership@aaas.org **MANAGER, MEMBER SERVICES** Pat Butler **SPECIALISTS** Terrance Morrison, Latasha Russell **MANAGER, DATA ENTRY** Mickie Napoleoni **DATA ENTRY SPECIALISTS** Brenden Aquilino, Fiona Giblin

DIRECTOR, SITE LICENSING Tom Ryan **DIRECTOR, CORPORATE RELATIONS** Eileen Bernadette Moran **SR. PUBLISHER RELATIONS SPECIALIST** Kiki Forsythe **PUBLISHER RELATIONS MANAGER** Catherine Holland **PUBLISHER RELATIONS, EASTERN REGION** Keith Layson **PUBLISHER RELATIONS, WESTERN REGION** Ryan Rexroth **SALES RESEARCH COORDINATOR** Aiesha Marshall **MANAGER, SITE LICENSE OPERATIONS** Iquo Edim **SENIOR PRODUCTION SPECIALIST** Robert Koepke **SENIOR OPERATIONS ANALYST** Lana Guz **FULFILLMENT ANALYST** Judy Lillibridge **ASSOCIATE DIRECTOR, MARKETING** Christina Schlecht **MARKETING ASSOCIATES** Thomas Landreth, Isa Sesay-Bah

WEB TECHNOLOGIES SR. DEVELOPER Chris Coleman **DEVELOPERS** Dan Berger, Jimmy Marks, Ryan Jensen **SR. PROJECT MANAGER** Trista Smith **PROJECT MANAGER** Nick Fletcher

MULTIMEDIA DIRECTOR OF ANALYTICS Enrique Gonzales **SR. WEB PRODUCER** Sarah Crespi **WEB PRODUCER** Alison Crawford **VIDEO PRODUCER** Nguyen Nguyen **SOCIAL MEDIA PRODUCER** Brice Russ

DIRECTOR OF OPERATIONS PRINT AND ONLINE Lizabeth Harman **DIGITAL/PRINT STRATEGY MANAGER** Jason Hillman **QUALITY TECHNICAL MANAGER** Marcus Spiegler **PROJECT ACCOUNT MANAGER** Tara Kelly **DIGITAL PRODUCTION MANAGER** Lisa Stanford **ASSISTANT MANAGER DIGITAL/PRINT** Rebecca Doshi **SENIOR CONTENT SPECIALISTS** Steve Forrester, Antoinette Hodal, Lori Murphy, Anthony Rosen **CONTENT SPECIALISTS** Jacob Hedrick, Kimberley Oster

DESIGN DIRECTOR Beth Rakouskas **DESIGN EDITOR** Marcy Atarod **SENIOR DESIGNER** Garvin Grullón **DESIGNER** Chrystal Smith **GRAPHICS MANAGING EDITOR** Alberto Cuadra **SENIOR SCIENTIFIC ILLUSTRATORS** Chris Bickel, Katharine Sutliff **SCIENTIFIC ILLUSTRATOR** Valerie Altounian **SENIOR ART ASSOCIATES** Holly Bishop, Nathalie Cary, Preston Huey **SENIOR PHOTO EDITOR** William Douthitt **PHOTO EDITORS** Leslie Blizard, Christy Steele

DIRECTOR, GLOBAL COLLABORATION, CUSTOM PUBLICATIONS, ADVERTISING Bill Moran **EDITOR, CUSTOM PUBLISHING** Sean Sanders: 202-326-6430 **ASSISTANT EDITOR, CUSTOM PUBLISHING** Tianna Hicklin: 202-326-6463 **ADVERTISING MARKETING MANAGER** Justin Sawyers: 202-326-7061 science_advertising@aaas.org **ADVERTISING MARKETING ASSOCIATE** Javia Flemmings **ADVERTISING SUPPORT MANAGER** Karen Foote: 202-326-6740 **ADVERTISING PRODUCTION OPERATIONS MANAGER** Deborah Tompkins **SR. PRODUCTION SPECIALIST/GRAPHIC DESIGNER** Amy Hardcastle **SR. TRAFFIC ASSOCIATE** Christine Hall **SALES COORDINATOR** Shirley Young **ASSOCIATE DIRECTOR, COLLABORATION, CUSTOM PUBLICATIONS/CHINA/TAIWAN/KOREA/SINGAPORE** Ruolei Wu: +86-186 0082 9345, rwu@aaas.org **COLLABORATION/CUSTOM PUBLICATIONS/JAPAN** Adarsh Sandhu + 81532-81-5142 asandhu@aaas.org **EAST COAST/E. CANADA** Laurie Faraday: 508-747-9395, FAX 617-507-8189 **WEST COAST/W. CANADA** Lynne Stickrod: 415-931-9782, FAX 415-520-6940 **MIDWEST** Jeffrey Dembksi: 847-498-4520 x3005, Steven Loerch: 847-498-4520 x3006 **UK EUROPE/ASIA** Roger Goncalves: TEL/FAX +41 43 243 1358 **JAPAN** Katsuyoshi Fukamizu(Tokyo): +81-3-3219-5777 kfukamizu@aaas.org **CHINA/TAIWAN** Ruolei Wu: +86-186 0082 9345, rwu@aaas.org

WORLDWIDE ASSOCIATE DIRECTOR OF SCIENCE CAREERS Tracy Holmes: +44 (0) 1223 326525, FAX +44 (0) 1223 326532 tholmes@science-int.co.uk **CLASSIFIED** advertise@sciencecareers.org **U.S. SALES** Tina Burks: 202-326-6577, Nancy Toema: 202-326-6578 **EUROPE/ROW SALES** Sarah Lelarge **SALES ASSISTANT** Kelly Grace **JAPAN** Hiroyuki Mashiki(Kyoto): +81-75-823-1109 hmashiki@aaas.org **CHINA/TAIWAN** Ruolei Wu: +86-186 0082 9345 rwu@aaas.org **MARKETING MANAGER** Allison Pritchard **MARKETING ASSOCIATE** Aimee Aponte

AAAS BOARD OF DIRECTORS RETIRING PRESIDENT, CHAIR Gerald R. Fink **PRESIDENT** Geraldine (Geri) Richmond **PRESIDENT-ELECT** Barbara A. Schaal **TREASURER** David Evans Shaw **CHIEF EXECUTIVE OFFICER** Rush D. Holt **BOARD** Bonnie L. Bassler, May R. Berenbaum, Carlos J. Bustamante, Stephen P.A. Fodor, Claire M. Fraser, Michael S. Gazzaniga, Laura H. Greene, Elizabeth Loftus, Mercedes Pascual

SUBSCRIPTION SERVICES For change of address, missing issues, new orders and renewals, and payment questions: 866-434-AAAS (2227) or 202-326-6417, FAX 202-842-1065. Mailing addresses: AAAS, P.O. Box 96178, Washington, DC 20090-6178 or AAAS Member Services, 1200 New York Avenue, NW, Washington, DC 20005

INSTITUTIONAL SITE LICENSES 202-326-6730 **REPRINTS:** Author Inquiries 800-635-7181 **COMMERCIAL INQUIRIES** 803-359-4578 **PERMISSIONS** 202-326-6765, permissions@aaas.org **AAAS Member Services** 202-326-6417 or http://membercentral.aaas.org/discounts

Science serves as a forum for discussion of important issues related to the advancement of science by publishing material on which a consensus has been reached as well as including the presentation of minority of conflicting points of view. Accordingly, all articles published in *Science*—including editorials, news and comment, and books reviews—are signed and reflect the individual views of the authors and not official points of view adopted by AAAS or the institutions with which the authors are affiliated.

INFORMATION FOR AUTHORS See pages 678 and 679 of the 6 February 2015 issue or access www.sciencemag.org/about/authors

SENIOR EDITORIAL BOARD

Robert H. Grubbs, *California Institute of Technology,* **Gary King,** *Harvard University*
Susan M. Rosenberg, *Baylor College of Medicine,* **Ali Shilatifard,** *Northwestern University Feinberg School of Medicine,* **Michael S. Turner,** *U. of Chicago*

BOARD OF REVIEWING EDITORS (Statistics board members indicated with **(S)**)

Adriano Aguzzi, *U. Hospital Zürich*
Takuzo Aida, *U. of Tokyo*
Leslie Aiello, *Wenner-Gren Foundation*
Judith Allen, *U. of Edinburgh*
Sonia Altizer, *U. of Georgia*
Sebastian Amigorena, *Institut Curie*
Kathryn Anderson, *Memorial Sloan-Kettering Cancer Center*
Meinrat O. Andreae, *Max-Planck Inst. Mainz*
Paola Arlotta, *Harvard U.*
Johan Auwerx, *EPFL*
David Awschalom, *U. of Chicago*
Clare Baker, *University of Cambridge*
Jordi Bascompte, *University of Zurich*
Facundo Batista, *London Research Inst.*
Ray H. Baughman, *U. of Texas, Dallas*
David Baum, *U. of Wisconsin*
Carlo Beenakker, *Leiden U.*
Kamran Behnia, *ESPCI-ParisTech*
Yasmine Belkaid, *NIAID, NIH*
Philip Benfey, *Duke U.*
May Berenbaum, *U. of Illinois*
Gabriele Bergers, *U. of California, San Francisco*
Bradley Bernstein, *Massachusettes General Hospital*
Peer Bork, *EMBL*
Bernard Bourdon, *Ecole Normale Supérieure de Lyon*
Chris Bowler, *École Normale Supérieure*
Ian Boyd, *U. of St. Andrews*
Emily Brodsky, *U. of California, Santa Cruz*
Ron Brookmeyer, *U. of California Los Angeles* **(S)**
Christian Büchel, *U. Hamburg-Eppendorf*
Joseph A. Burns, *Cornell U.*
Carter Tribley Butts, *U. of California, Irvine*
Gyorgy Buzsaki, *New York U. School of Medicine*
Blanche Capel, *Duke U.*
Mats Carlsson, *U. of Oslo*
Ib Chorkendorff, *U. of Denmark*
David Clapham, *Children's Hospital Boston*
Joel Cohen, *Rockefeller U., Columbia U.*
James J. Collins, *MIT*
Robert Cook-Deegan, *Duke U.*
Lisa Coussens, *Oregon Health & Science U.*
Alan Cowman, *Walter & Eliza Hall Inst.*
Robert H. Crabtree, *Yale U.*
Roberta Croce, *Vrije Universiteit*
Janet Currie, *Princeton U.*
Jeff L. Dangl, *U. of North Carolina*
Tom Daniel, *U. of Washington*
Frans de Waal, *Emory U.*
Stanislas Dehaene, *Collège de France*
Robert Desimone, *MIT*
Claude Desplan, *New York U.*
Dennis Discher, *U. of Pennsylvania*
Gerald W. Dorn II, *Washington U. School of Medicine*
Jennifer A. Doudna, *U. of California, Berkeley*
Bruce Dunn, *U. of California, Los Angeles*
William Dunphy, *Caltech*
Christopher Dye, *WHO*
Todd Ehlers, *U. of Tuebingen*
David Ehrhardt, *Carnegie Inst. of Washington*
Tim Elston, *U. of North Carolina at Chapel Hill*
Gerhard Ertl, *Fritz-Haber-Institut, Berlin*
Barry Everitt, *U. of Cambridge*
Ernst Fehr, *U. of Zurich*
Anne C. Ferguson-Smith, *U. of Cambridge*
Michael Feuer, *The George Washington U.*
Toren Finkel, *NHLBI, NIH*
Kate Fitzgerald, *U. of Massachusetts*
Peter Fratzl, *Max-Planck Inst.*
Elaine Fuchs, *Rockefeller U.*
Daniel Geschwind, *UCLA*
Karl-Heinz Glassmeier, *TU Braunschweig*
Ramon Gonzalez, *Rice U.*
Julia R. Greer, *Caltech*
Elizabeth Grove, *U. of Chicago*
Nicolas Gruber, *ETH Zurich*
Kip Guy, *St. Jude's Children's Research Hospital*
Taekjip Ha, *U. of Illinois at Urbana-Champaign*
Christian Haass, *Ludwig Maximilians U.*
Michael Hasselmo, *Boston U.*
Martin Heimann, *Max-Planck Inst. Jena*
Yka Helariutta, *U. of Cambridge*
James A. Hendler, *Rensselaer Polytechnic Inst.*
Janet G. Hering, *Swiss Fed. Inst. of Aquatic Science & Technology*
Kai-Uwe Hinrichs, *U. of Bremen*
David Hodell, *U. of Cambridge*
David Holden, *Imperial College*
Lora Hooper, *UT Southwestern Medical Ctr. at Dallas*
Tamas Horvath, *Yale University*
Raymond Huey, *U. of Washington*
Auke Ijspeert, *EPFL Lausanne*
Steven Jacobsen, *U. of California, Los Angeles*
Stephen Jackson, *U. of Arizona*
Kai Johnsson, *EPFL Lausanne*
Peter Jonas, *Inst. of Science & Technology (IST) Austria*
Matt Kaeberlein, *U. of Washington*
William Kaelin Jr., *Dana-Farber Cancer Inst.*
Daniel Kahne, *Harvard U.*
Daniel Kammen, *U. of California, Berkeley*
Masashi Kawasaki, *U. of Tokyo*
V. Narry Kim, *Seoul National U.*
Joel Kingsolver, *U. of North Carolina at Chapel Hill*
Robert Kingston, *Harvard Medical School*
Etienne Koechlin, *Ecole Normale Supérieure*
Alexander Kolodkin, *Johns Hopkins U.*
Thomas Langer, *U. of Cologne*
Mitchell A. Lazar, *U. of Pennsylvania*
David Lazer, *Harvard U.*
Thomas Lecuit, *IBDM*
Virginia Lee, *U. of Pennsylvania*
Stanley Lemon, *U. of North Carolina at Chapel Hill*
Ottoline Leyser, *Cambridge U.*
Wendell Lim, *U.C. San Francisco*
Marcia C. Linn, *U. of California, Berkeley*
Jianguo Liu, *Michigan State U.*
Luis Liz-Marzan, *CIC biomaGUNE*
Jonathan Losos, *Harvard U.*
Ke Lu, *Chinese Acad. of Sciences*
Christian Lüscher, *U. of Geneva*
Laura Machesky, *CRUK Beatson Inst. for Cancer Research*
Anne Magurran, *U. of St. Andrews*
Oscar Marin, *CSIC & U. Miguel Hernández*
Charles Marshall, *U. of California, Berkeley*
C. Robertson McClung, *Dartmouth College*
Graham Medley, *U. of Warwick*
Tom Misteli, *NCI*
Yasushi Miyashita, *U. of Tokyo*
Mary Ann Moran, *U. of Georgia*
Richard Morris, *U. of Edinburgh*
Alison Motsinger-Reif, *NC State U.* **(S)**
Thomas Murray, *The Hastings Center*
Daniel Neumark, *U. of California, Berkeley*
Kitty Nijmeijer, *U. of Twente*
Pär Nordlund, *Karolinska Inst.*
Helga Nowotny, *European Research Advisory Board*
Ben Olken, *MIT*
Joe Orenstein, *U. of California Berkeley & Lawrence Berkeley National Lab*
Harry Orr, *U. of Minnesota*
Andrew Oswald, *U. of Warwick*
Steve Palumbi, *Stanford U.*
Jane Parker, *Max-Planck Inst. of Plant Breeding Research*
Giovanni Parmigiani, *Dana-Farber Cancer Inst.* **(S)**
John H. J. Petrini, *Memorial Sloan-Kettering Cancer Center*
Samuel Pfaff, *Salk Institute for Biological Studies*
Joshua Plotkin, *U. of Pennsylvania*
Albert Polman, *FOM Institute AMOLF*
Philippe Poulin, *CNRS*
Jonathan Pritchard, *Stanford U.*
David Randall, *Colorado State U.*
Felix Rey, *Institut Pasteur*
Trevor Robbins, *U. of Cambridge*
Jim Roberts, *Fred Hutchinson Cancer Research Ctr.*
Barbara A. Romanowicz, *U. of California,Berkeley*
Amy Rosenzweig, *Northwestern University*
Mike Ryan, *U. of Texas, Austin*
Mitinori Saitou, *Kyoto U.*
Shimon Sakaguchi, *Kyoto U.*
Miquel Salmeron, *Lawrence Berkeley National Lab*
Jürgen Sandkühler, *Medical U. of Vienna*
Alexander Schier, *Harvard U.*
Vladimir Shalaev, *Purdue U.*
Robert Siliciano, *Johns Hopkins School of Medicine*
Denis Simon, *Arizona State U.*
Uri Simonsohn, *U. of Pennsylvania*
Alison Smith, *John Innes Centre*
Richard Smith, *U. of North Carolina* **(S)**
John Speakman, *U. of Aberdeen*
Allan C. Spradling, *Carnegie Institution of Washington*
Jonathan Sprent, *Garvan Inst. of Medical Research*
Eric Steig, *U. of Washington*
Paula Stephan, *Georgia State U. and National Bureau of Economic Research*
Molly Stevens, *Imperial College London*
V. S. Subrahmanian, *U. of Maryland*
Ira Tabas, *Columbia U.*
Sarah Teichmann, *Cambridge U.*
John Thomas, *North Carolina State U.*
Shubha Tole, *Tata Institute of Fundamental Research*
Christopher Tyler-Smith, *The Wellcome Trust Sanger Inst.*
Herbert Virgin, *Washington U.*
Bert Vogelstein, *Johns Hopkins U.*
Cynthia Volkert, *U. of Göttingen*
Douglas Wallace, *Dalhousie U.*
David Wallach, *Weizmann Inst. of Science*
Ian Walmsley, *U. of Oxford*
Jane-Ling Wang, *U. of California, Davis* **(S)**
David A. Wardle, *Swedish U. of Agric. Sciences*
David Waxman, *Fudan U.*
Jonathan Weissman, *U. of California, San Francisco*
Chris Wikle, *U. of Missouri* **(S)**
Ian A. Wilson, *The Scripps Res. Inst.* **(S)**
Timothy D. Wilson, *U. of Virginia*
Rosemary Wyse, *Johns Hopkins U.*
Jan Zaanen, *Leiden U.*
Kenneth Zaret, *U. of Pennsylvania School of Medicine*
Jonathan Zehr, *U. of California, Santa Cruz*
Len Zon, *Children's Hospital Boston*
Maria Zuber, *MIT*

BOOK REVIEW BOARD

David Bloom, *Harvard U.,* **Samuel Bowring,** *MIT,* **Angela Creager,** *Princeton U.,* **Richard Shweder,** *U. of Chicago,* **Ed Wasserman,** *DuPont*

EDITORIAL

Future Earth

Johan Rockström is Professor in Global Sustainability at Stockholm University, Stockholm, Sweden, and chair of the Earth League. E-mail: johan.rockstrom@su.se

The new year ushers in important international agendas secured at the end of 2015: the Paris climate agreement to limit global warming to a 1.5° to 2°C increase and adoption of the United Nations Sustainable Development Goals. Both actions reflect the world's recognition that development in all nations hinges on a stable and resilient Earth system. This is a political paradigm shift, fortified by three decades of remarkable advancements in Earth system science. The International Geosphere-Biosphere Programme (IGBP), which ended in December 2015, can take considerable credit for coordinating and catalyzing much of this fundamental research. The recently launched Future Earth research program builds on this legacy and is the right response to the new scientific challenges.

"Future Earth...is the right response to the new scientific challenges."

Formed in 1986, IGBP became the first major international program to conceptualize Earth as a whole system. Its objective was "to describe and understand the interactive physical, chemical and biological processes that regulate the total Earth system...and the manner in which they are influenced by human activities." Its visionary research agenda attracted leading scientists from advanced and developing countries, and brought together thousands of researchers through interlinked research initiatives such as the Global Carbon Project (GCP) and the Past Global Changes (PAGES) project, all of which continue to generate key scientific insights. In December 2015, GCP published its 10th annual carbon budget during the Paris climate summit, indicating a decline of 0.6% in the growth rate of carbon dioxide emissions in 2015, potentially the first decrease during a time of world economic growth. Earlier last year, PAGES researchers concluded that sea levels could stabilize at around 6 meters higher than preindustrial levels if global temperature were to increase 1° to 2°C.

The integrated systems perspective is what made IGBP so important, particularly its focus on the dynamics and feedbacks between the climate system and the biosphere. From its freewheeling intellectual spirit, unbounded by political mandates, emerged profound scientific insights, such as the concept of the "Great Acceleration" in human activity since the 1950s, and quantification of this impact on Earth. IGBP will forever be associated with the concept of the Anthropocene—the scientific conclusion that Earth has entered a new geological epoch dominated by human interference—which was first discussed at an IGBP meeting in 2000, was published in the IGBP newsletter that same year, and was central to IGBP's first synthesis report, *Global Change and the Earth System: A Planet Under Pressure*. IGBP was a foundation for the now-established field of Earth system science and influenced the research trajectory of many institutes.

This new knowledge, and the sheer scale of responsibility that the Anthropocene represents, necessitate an evolution to global sustainability science. Future Earth is the next logical step and brings together natural and social sciences to work toward more integrative global change science and solutions-oriented research that engages governments, civil society, research funders, and the private sector. The new initiative has the support of an influential coalition of international bodies, including the International Council for Science, the United Nations, and the major national research funders. Future Earth international offices have now been established in Canada, France, Japan, Sweden, and the United States, and national and regional networks and offices are growing rapidly. But Future Earth's success will lie in its ability to stay true to IGBP's legacy. As IGBP projects transfer to Future Earth, the new program must continue to attract the best scientists and institutions.

Earth system resilience and stabilization are necessarily rising to the top of political and scientific research agendas. With humanity at a critical juncture, Future Earth has the potential to become the largest, most ambitious international research program ever undertaken.

– Johan Rockström

10.1126/science.aaf2138

PHOTOS: (RIGHT) M. AXELSSON/AZOTE; (INSET) STOCKFINLAND/ISTOCKPHOTO.COM

Published by AAAS

NEWS

0.88 Degrees, in Celsius, by which global temperatures in 2015 exceeded the 20th century average, NASA and the National Oceanic and Atmospheric Administration announced this week. That makes 2015 the hottest year on record—and shatters the record set in 2014 by a full 0.1°C.

IN BRIEF

An unfolding clinical trial disaster

French health minister Marisol Touraine speaks to reporters 15 January about the disastrous clinical trial.

One person died and five more were hospitalized after a phase I clinical trial in France went horribly wrong. At least three of the patients—all men aged between 28 and 49 years old—may suffer irreversible brain damage if they survive, a doctor treating them said last week; one suffered no symptoms but was hospitalized for observation. The patients were previously healthy volunteers who participated in a study conducted by Rennes-based Biotrial to test the tolerability of a candidate drug produced by Bial, a Portuguese pharmaceutical company. The drug was an inhibitor of fatty acid amide hydrolase (FAAH), an enzyme that breaks down endocannabinoids in the brain. FAAH inhibitors have been proposed as a treatment against chronic pain. The drug had been tested on animals, said French health minister Marisol Touraine at a press conference on 15 January, and France's National Agency for Medicine and Health Products Safety (ANSM) approved the trial last June. Bial says 108 people had received the drug earlier without any serious side effects. The six volunteers, all part of the same trial group, received multiple daily doses of the drug, beginning on 7 January. The first symptoms appeared on 10 January, and the trial was halted the next day. Prosecutors in Rennes have opened an investigation; so have ANSM and another government agency. http://scim.ag/Frenchclintrial

AROUND THE WORLD

Ebola is back ... or never left

FREETOWN | It was a short-lived celebration. Just hours after the World Health Organization (WHO) declared the Ebola outbreak in West Africa over on 14 January, Sierra Leone reported a new case of the disease to WHO. A 22-year-old woman, who died earlier in the week, tested positive for the virus; WHO confirmed the case on 15 January. At least 27 people who came into contact with the woman are at high risk of having been infected with Ebola virus, says Christopher Dye of WHO in Geneva, Switzerland. Those contacts may be given a vaccine produced by Merck that protected people from the deadly virus in a trial in Guinea last year. Even as WHO officials declared the outbreak over last week, they had warned of the risk of flare-ups: Because Ebola virus can persist in some tissues and bodily fluids of survivors for months, there is a danger that they can pass the virus on to others, for instance through unprotected sex. http://scim.ag/Ebolaback

Seabird die-off in Alaska

WHITTIER, ALASKA | Thousands of dead common murres, an abundant Arctic cliff-dwelling bird, have washed up on

Common murres washed up on an Alaskan beach.

PHOTOS: (LEFT TO RIGHT) MATHIEU PATTIER/SIPA/NEWSCOM; AP PHOTO/MARK THIESSEN

Published by AAAS

the beaches of Prince William Sound this month. The birds appear emaciated, according to U.S. Fish and Wildlife Service scientists, but the exact cause of their starvation is unclear. Warmer surface waters in the North Pacific—perhaps as a result of a combination of global warming and this year's intense El Niño weather pattern—may have reduced stocks of the birds' forage fish or possibly driven them deeper to where the birds can't access them. Strong storms in the North Pacific this winter may have also prevented already weakened birds from foraging. Murres, which weigh about 1 kilogram, must eat about half their body weight each day. Last August and September, and again in late December, large numbers of malnourished common murres also turned up on northern California beaches.

Zika virus prompts travel alert

ATLANTA | The U.S. Centers for Disease Control and Prevention has warned pregnant women to avoid travel to countries in which Zika virus is circulating. That list is growing, with local transmission reported in 18 countries in Latin America and the Caribbean by 18 January. Zika virus, which in adults usually causes only mild symptoms, has infected as many as 1.5 million people in Brazil in the last year. It is strongly suspected of causing a surge in birth defects in the country; more than 3500 babies born in the last 6 months have been diagnosed with microcephaly, a disorder in which the brain fails to develop properly. On 15 January, health officials in Hawaii announced that a baby born in an Oahu hospital had been diagnosed with the disorder. The baby's mother was living in Brazil during the early part of her pregnancy and was likely infected there.

U.S. genome centers' next phase

BETHESDA, MARYLAND | The U.S. National Human Genome Research Institute (NHGRI) plans to sequence up to 200,000 human genomes in search of genes that influence a person's risk of common diseases such as heart disease, autism, and diabetes. On 14 January, NHGRI announced the latest phase of its genome sequencing program, which will award $240 million over 4 years to three long-running sequencing centers—the Broad Institute in Cambridge, Massachusetts; Washington University in St. Louis in Missouri; and Baylor College of Medicine in Houston, Texas—and a newcomer, the New York Genome Center in New York City. The institute is also renewing its $40 million, 4-year Centers for Mendelian Genomics program, in which five institutions will seek genes underlying rare inherited disorders.

Some pikas may be too good at keeping warm.

PHOTO: KATHERINE SOLARI

Pikas' cold adaptation a liability with climate change

Pikas are champs when it comes to keeping warm in cold weather. But this adaptation comes at a cost—they may struggle to cope with climate change. Different species of pikas live at different elevations—anywhere from sea level to 6400 meters high—but all species are sensitive to heat. That has made them a poster child for climate change: Scientists worry whether low-living species can shift upslope rapidly enough and far enough to beat the heat. But these low-altitude pikas—some living at sea level—have another problem, reported graduate student Katherine Solari of Stanford University in Palo Alto, California, last week at the American Society of Naturalists meeting in Pacific Grove, California. Higher altitude pikas have a very efficient protein for harnessing oxygen for energy production. The low-altitude species, however, have a modified version of the protein that likely produces more heat and less energy—which works fine for keeping warm at lower altitudes, but could make it much harder for them to survive as they are forced by global warming to ascend to greater heights.

No more whaling reviews

CAMBRIDGE, U.K. | Thirty-two scientists are calling for an end to the International Whaling Commission's (IWC's) current program for reviewing "scientific whaling" proposals. In a letter to the editor in this week's issue of *Nature*, the researchers, who are members of IWC's scientific committee, argue that Japan has ignored the committee's latest recommendations to employ nonlethal methods to collect whale tissue, and instead "is proceeding to kill whales under a self-determined quota." Continuing to review Japan's whaling program, the scientists say, "is a waste of time," and IWC should develop a new method that scientists respect and member countries will abide by. Japanese whalers are now in the Southern Ocean and targeting 333 minke whales.
http://scim.ag/Whalingreviews

Jason-3 rises into orbit

VANDENBERG AIR FORCE BASE, CALIFORNIA | On 17 January, the Jason-3 radar altimetry satellite blasted into orbit atop a SpaceX rocket. Jason-3 will measure changes in the height of the ocean surface to aid in studies of ocean currents,

Published by AAAS

wind speeds, and climate change. It is the fourth in a series of missions that, since 1992, have seen a 7-centimeter rise in global sea level, at a rate of 3 millimeters per year. The $364 million mission is headed by the National Oceanic and Atmospheric Administration (NOAA), but has been built and managed by NASA. Significant contributions were made to the mission by the French space agency CNES and NOAA's European counterpart, EUMETSAT.

NEWSMAKERS

SARS hero to be new Taiwan VP

Epidemiologist **Chen Chien-Jen**, who helped end Taiwan's SARS outbreak in 2003 after taking over as head of the Department of Health in the middle of the crisis, is now set to become the country's next vice president. Chen, 64, was on the winning Democratic Progressive Party (DPP) ticket in elections on 16 January. Educated at National Taiwan University in Taipei and Johns Hopkins University in Baltimore, Maryland, Chen first garnered scientific attention for work on arsenic that led to the revision of international health standards for exposure. Last fall, he resigned as vice president of Academia Sinica, the island's national research labs, to enter politics. Chen and his presidential running mate, Tsai Ing-Wen, take office in May. One challenge for the new team will be continuing to expand scientific ties with the mainland despite DPP's advocacy of independence for the island, which China considers a breakaway province.

FINDINGS

Tracing Anglo-Saxon heritage

Waves of Anglo-Saxons, Germanic tribes from Europe's North Sea coast, arrived in the eastern United Kingdom between 400 C.E. and 650 C.E. There, they met an already diverse population, including indigenous British people and migrants from the far-flung reaches of the Roman Empire. Modern British genomes are mostly a mix of these populations, but researchers have puzzled over just how much the Anglo-Saxons contributed because of the small genetic differences between European groups. Now, researchers have sequenced the whole genomes of 10 skeletons buried near Cambridge, U.K., between about 100 B.C.E. and 800 C.E. Three of these people lived before the Anglo-Saxons arrived, whereas the other seven were Anglo-Saxons, as reported in *Nature Communications*. By comparing rare genetic variants in both groups and in modern day British people, researchers conclude that, on average, about 38% of British ancestry comes from Anglo-Saxons, and that Anglo-Saxons themselves were genetically similar to modern Danish and Dutch people.

U.K. archaeologists sift through the remains of 3000-year-old stilt houses.

PHOTO: CHRIS RADBURN/PA WIRE/AP IMAGES

Remains of stilt houses paint rich picture of Bronze Age life

Almost 3000 years ago, two stilt-supported houses caught fire and plunged into a marsh in what is now Peterborough, U.K. The mud first quenched the flames, then preserved the remains of the homes for centuries. Archaeologists now studying the site say it offers the most complete glimpse yet of the life of people living in the United Kingdom during the Bronze Age. The artifacts they left behind as they fled the fire paint a picture of wealth: jewelry, spears, daggers, food storage jars, glass beads, and textiles; domestic animal bones, including those of sheep, pigs, and cattle, suggest a diet of meat rather than fish, and further support that picture of abundance. First discovered in 2006, the site's exceptional preservation—along with evidence of a rapid evacuation—has drawn comparisons to the famous archaeological site at Pompeii, Italy.

BY THE NUMBERS

From *Science & Engineering Indicators 2016*, released this week by the National Science Foundation. This is the 22nd edition of the biennial report, which covers global trends in science and engineering, and the first to be entirely digital.

47%

The combined share of global R&D spending in 2013 by the United States (27%) and China (20%); Japan (10%) and Germany (6%) rank a distant third and fourth. Overall spending has doubled since 2003, to $1.67 trillion, with China accounting for one-third of that growth.

49%

Fraction of first university degrees awarded in science and engineering (S&E) in China in 2012—down from 73% in 2000, reflecting the increasing popularity of the humanities. The proportion of S&E degrees in the United States has stayed at roughly one-third.

Published by AAAS

Intensely harvested for their translucent shells, giant clams, like this one at Tecas Reef in the Philippines, are growing scarce.

MARINE CONSERVATION

Shell trade pushes giant clams to the brink

With elephant tusks harder to obtain, the "jade of the sea" is the new ivory in China

By **Christina Larson**, *in Tanmen, China*

At the Xiaobao Craft Store in Tanmen on Hainan Island, in southern China, co-owner Mo Xiaobao gestures to glass cabinets filled with white and yellow bead necklaces, translucent bracelets, and pendants strung with dragons or Buddhas. "All this is carved from giant clams," he says, proudly. Behind him, wooden shelves hold ornate statues up to a meter tall: leaping fish, eagles with spread wings, grapevines intertwined with fruit. Prices approach $3000. Mo is eager to make a sale, but don't try to leave China with one of these curios, he warns: "You might have trouble with foreign customs."

As countries crack down on the trade of elephant tusks, constricting illegal ivory exports to China, shells of giant clams—the "jade of the sea"—have become the new rage in scrimshaw. In China, "there's huge demand, which has pushed up giant clam prices," says Zhang Hongzhou, an expert on the trade at Nanyang Technological University in Singapore. And that is taking a heavy toll on the mollusks, which can span a meter and play a key role in reef ecosystems. The main giant clam species targeted—*Tridacna gigas*—is considered vulnerable to extinction based on survey data from 20 years ago. Its status has since eroded considerably, says Mei Lin Neo, a marine biologist at the National University of Singapore. "There is a wide-scale consensus among numerous nations that clam numbers have declined over the past 10 years," she says.

For centuries, Hainan fishers harvested giant clams for meat, which is considered an aphrodisiac in China and a delicacy in France, Japan, and elsewhere. Found throughout the tropical Indo-Pacific, the mollusks thrive in the South China Sea, which is an "especially important" part of their habitat, Neo says. Trade in the shells—translucent white, sometimes streaked with yellow or red, and weighing up to 200 kilograms—began about 20 years ago, Zhang says, when a Taiwanese entrepreneur showed locals how to carve intricate designs.

But only in the past few years has the handicraft industry taken off. Fueling the boom, Zhang says, are improved carving techniques, Hainan's popularity with tourists, the growth in e-commerce and the domestic wholesale market, and rising demand as ivory sources dry up. Tanmen, once a sleepy fishing village, is the epicenter of the trade: According to Zhang, it now has at least 460 shops and 100 workshops, and the industry supports nearly 100,000 people on Hainan. Prices paid to fishers for large raw giant clam shells have leaped 40-fold in 5 years, from a few thousand yuan a few years ago to 80,000 yuan ($12,100) today, he says. A Hainan government report states that especially fine and large carvings can fetch up to 700,000 yuan ($106,000).

To feed the booming industry, Chinese fishers are pillaging the South China Sea for the creatures. That's adding to the tension in the region, which is already a geopolitical flashpoint because of China's expansive territorial claims. As stocks dwindle, Chinese fishers are ranging more widely into disputed waters. Ed Gomez, a marine biologist at the University of the Philippines, Manila, says he has examined recent footage taken by divers showing Chinese fishers operating at Scarborough Shoal—claimed by China, Taiwan, and the Philippines—"digging

A dragon carved from a giant clam shell. Carvings can fetch more than $100,000.

PHOTOS: (TOP TO BOTTOM) AMAN SANTOS/CTI-SOUTHEAST ASIA/FLICKR; C. LARSON

Published by AAAS

up the reef looking for shells, and loading up huge cargo boats chock-full of giant clam shells."

The harvest damages reef ecosystems, biologists say. Giant clams, which may live for 80 or more years, are food for predators such as eels and starfish and provide shelter for fish and shrimp species. The clams are also a reservoir for specialized microalgae—zooxanthellae—that symbiotically help them glean energy from photosynthesis. A giant clam "is a whole ecosystem by itself, like a mini coral reef," Gomez says.

Giant clams are particularly vulnerable to depletion because the hermaphroditic creatures are slow to mature and reproduce. Although they can produce sperm at 2 or 3 years, they take up to 10 years to reach sexual maturity as a female. "Because they are being harvested at such a rapid rate, there is not time for them to naturally reproduce," Neo says. "If we don't have giant clams in the reefs, the reef's role will diminish with time," she says. "There will be a reduction in biodiversity."

Harvesting them inflicts collateral damage on reefs as well. When a giant clam is spotted, divers will push it to shallower water, dislodging coral and other species along the way, and then hoist it into a boat.

The illicit trade stays largely in China, which adds to the challenge of stopping it. Giant clams are protected under the Convention on International Trade in Endangered Species of Wild Fauna and Flora, but the treaty can't deter domestic traders or smugglers because it works mainly by requiring an export permit for trade in threatened species. "It's hard to use international obligations to stop [the trade]," Neo says. "It has to come from the Chinese side."

The Chinese government faces what Zhang calls "a great dilemma" in deciding how forcefully to crack down. China's own laws classify the giant clam as endangered, which makes it officially protected. On the other hand, he says, the fishers are pawns in the political drama playing out in the South China Sea. When President Xi Jinping visited Tanmen in April 2013, Zhang says, he encouraged the fishers to build bigger ships and range farther in the South China Sea.

In a hopeful development, Tanmen's government last March banned the harvest, transport, and sale of giant clams. One local trader says that police periodically inspect fishing vessels and seize the clams. But Tanmen's curio shops remain open, and another storeowner says she has no trouble buying raw giant clamshells. Overcoming patriotic fervor and market forces to save the embattled species will not be easy. ■

The University of Oxford received more research funds from a recent E.U. program than did any other U.K. university.

PHOTO: © JOHN ALEXANDER/ROBERT HARDING/CORBIS

EUROPEAN UNION

Debate sharpens over U.K. threat to leave Europe

Many researchers worry about a loss of funds and influence, but some say the fears are overblown

By **Tania Rabesandratana** *and* **Erik Stokstad**

After Britain's Conservative Party won a surprisingly large majority in the House of Parliament on 7 May last year, Prime Minister David Cameron promised a referendum on a contentious topic: Should the United Kingdom pull out of the European Union? Now, campaigners are gearing up for a major debate about the pros and cons of a "Brexit"—including its impact on British science.

Leading scientific institutions say that hundreds of millions of pounds in research funding are at stake, along with the country's influence on E.U. science programs. "The importance of engagement with Europe is paramount," Leszek Borysiewicz, vice-chancellor at the University of Cambridge in the United Kingdom, said on 19 January at a hearing of the science and technology committee of the House of Lords.

But a much smaller group of researchers says U.K. science would actually gain from leaving the European Union because it would escape bureaucracy and regulations, for instance on clinical trials. The campaign to stay in the Union has been "all emotion without thinking about the cold hard facts," says Angus Dalgleish, an oncologist at the University of London who represents Leave.EU, a pro-Brexit group.

The referendum could take place before the summer. A vote for departure would not affect U.K. membership in non-E.U. science organizations, such as CERN, the European Space Agency, and the European Molecular Biology Laboratory. Public opinion is split and could be influenced by the outcome of Cameron's negotiations with the European Union; at a summit with heads of state next month, he will seek concessions on issues such as curbs on welfare for migrants and more national sovereignty.

Advocates for staying in the European Union point out that U.K. research institutions have benefited greatly from access to the European Union's science programs. For instance, about €7 billion has flowed into the United Kingdom from across the English Channel as part of Framework Programme 7 (FP7), a grants scheme that ran from 2007 to 2013, according to the European Commission. U.K. applicants had a 22.8% success rate in FP7—higher than the E.U. average of 20.5%—and the United Kingdom ranked second among the Union's 28 member states in number of participants and cash received. A divorce would also reduce the United Kingdom's influence over E.U. science policies, says Mike Galsworthy, a science policy expert who leads the campaign Scientists for EU in London.

Dalgleish and other E.U. critics say that the money and influence come with oner-

Published by AAAS

ous strings attached—both regulatory constraints on research and bureaucratic inefficiencies in administration. They add that the United Kingdom's annual contribution to the European Union last year was approximately €14.5 billion greater than what came back overall; the net savings from leaving would more than replace any losses for research, they argue.

U.K. researchers could still take part in E.U. projects after a Brexit if the United Kingdom bought its way back into Horizon 2020, the successor to FP7, and any future programs. Currently, 13 non-E.U. members—including Israel, Norway, and Switzerland—have "association agreements" that allow them to participate in Horizon 2020 in return for a membership fee based on gross domestic product per capita. Such deals can pay off: Switzerland paid about €1.6 billion to become associated with FP7, but Swiss science won more than €1.8 billion in grants from the program. A buy-in deal could be even better, Brexit supporters say, if the United Kingdom were allowed to cherry-pick Horizon 2020 components in which its researchers are most successful, such as the European Research Council, which offers individual grants for basic scientists.

E.U. supporters dismiss these arguments as naïve. They say there are no guarantees that U.K. political leaders would redirect any savings toward research rather than toward paying down the national debt, for example, and a Brexit could spark economic turmoil that could strain government budgets. Nor would the European Union look kindly on a U.K. bid for association with selected research programs. "I wouldn't be sure that the E.U. would accept such 'picking the winners'" says Peter Tindemans, director of EuroScience, a science advocacy organization based in Strasbourg, France. A departure could also create resentment and an unfriendly negotiation climate in Brussels.

None of that scares Dalgleish. The United Kingdom is a global research powerhouse whose economic heft and vitality would add leverage in any negotiations, he says: "They need us more than we need them." But as the Russell Group, a lobbying association of top U.K. research universities, cautioned in a statement to the House of Lords last November: "We can only speculate about the impact of withdrawing from the E.U., since we have no precedent to guide us."

In the end, the impact on science will play only a small role in the outcome of any referendum. Rather than worry too much about research, Tindemans says, the European Union should "challenge the U.K. as to whether they want to be part of Europe or a fairly isolated country." ■

BIOMEDICAL RESEARCH

Biden seeks clear course for his cancer moonshot

Researchers have plenty of ideas for the vice president's bid to boost collaboration and improve treatments

By **Jocelyn Kaiser**, *in Washington, D.C., and* **Jennifer Couzin-Frankel**, *in Philadelphia, Pennsylvania*

Vice President Joseph Biden last week vowed to tackle "cancer politics" during an unusual roundtable with leading oncologists, where he elaborated on his plans for the cancer "moonshot" that President Barack Obama had highlighted 3 days earlier in the State of the Union address.

The 15 January roundtable was held in a cramped conference room at the Abramson Cancer Center at the University of Pennsylvania (UPenn)—the undergraduate alma mater, Biden pointed out, of his son Beau, who died last year of brain cancer at 46. Biden's goal, which he says he'll pursue well beyond the remaining year of his term, is to catalyze greater investment, coordination, and collaboration in a field marked by multiple initiatives, targeting a complex of many different diseases.

Seated next to Francis Collins, director of the National Institutes of Health (NIH), Biden seemed well aware that his moonshot metaphor has made many in the cancer world and beyond cringe. "I don't want the press saying, 'Biden is naïve and out to cure all cancer, and we can do it tomorrow,'" he said. "Sometimes … I wish we hadn't called it a moonshot," he added later.

Still, Biden said he's already consulted with some 200 cancer experts worldwide and is planning to set up a task force. At UPenn, he pressed the scientists about genomics, immunotherapy, and big data, sounding alternately humble—"[I'm] just an uninformed guy"—and challenging. "I met with two other researchers doing the exact same thing," Biden said to Robert Vonderheide, after the UPenn oncologist described work on a vaccine to prevent relapse in women carrying certain mutations that predispose to breast and ovarian cancers. "How do you guys communicate?"

Although detail about the initiative is scarce, Biden's interest is energizing the cancer research community. Biden's advisers are "talking to many of the right people, have taken the right approach (improve the research process rather than

Biden is seeking advice from researchers, including a group at UPenn last week, on targeting his moonshot.

PHOTO: STAR SHOOTER/MEDIAPUNCH/IPX

Published by AAAS

promise specific achievements by certain dates), and are already focused on some important things that could be accomplished within a year and without legislation," wrote Harold Varmus, a former National Cancer Institute (NCI) and NIH director now at Weill Cornell Medicine in New York City, in an email.

Biden's moonshot invites comparisons to the war on cancer that President Richard Nixon launched in 1971, and then-NCI Director Andrew von Eschenbach's 2003 call to eliminate suffering and death from cancer by 2015. Many scientists, however, oppose setting firm deadlines for biomedical research and in particular for ending cancer, which experts consider to be more than 200 diseases. "There's no one moon. There are many moons," says Bruce Chabner, director of clinical research at Massachusetts General Hospital in Boston.

At UPenn, Biden said he is seeking ideas for realistic, near-term goals as well as loftier ones. Asked what might be good focus for a "10-year moonshot," Vonderheide and UPenn oncologist Carl June both pointed to cancer prevention. Biden also appeared enthusiastic about the promise of immunotherapies; attending the event was a UPenn team, including June, that made breakthroughs in treating blood cancer with genetically modified T cells (*Science*, 28 June 2013, p. 1514).

> ***"I don't want the press saying, 'Biden is naïve and out to cure all cancer, and we can do it tomorrow.'"***
>
> **Joseph Biden**, vice president, United States

In a blog post, Biden said one of his goals is to "break down silos and bring all the cancer fighters together" in order to "make a decade worth of advances in 5 years." At UPenn, he said President Obama will be issuing an executive order that will enable Biden to build alliances among federal agencies. Another near-term step is likely to be a request for additional cancer funding in the White House's fiscal year 2017 budget proposal, due out 9 February. Researchers hope the request will help persuade Congress to maintain the momentum built by last year's 5% funding bump for NCI and 7% rise for NIH, which Biden backed. Collins and Douglas Lowy, NCI's acting director, last week told reporters that the money might support an industry-government partnership and build on NIH efforts to encourage researchers to share data.

Cancer researchers already have some data-sharing projects underway. The Association of American Cancer Researchers (AACR) is pooling patient genetic and clinical data from major cancer centers to learn how rare cancer-driving mutations influence a patient's response to treatments (*Science*, 3 November 2015, p. 730). Fifteen scientists affiliated with AACR discussed the project with Biden's staff during an 8 January meeting. "We all agree on the need to scale up," says Charles Sawyers of Memorial Sloan Kettering Cancer Center in New York City, one of the participants.

In a separate effort, NCI is launching the Genomic Data Commons, which aims to pool data on up to 50,000 cancer patients, Lowy noted. Biden wants to "change the incentives" so that even researchers without government funding will want to share data, said Biden policy chief Don Graves.

Researchers also hope Biden can help clear bureaucratic red tape that is one reason only 5% of cancer patients enroll in clinical trials, says the University of Nebraska, Omaha's Julie Vose, president of the American Society for Clinical Oncology. People on Medicare, for example, can enroll in a clinical trial only if they have a certain kind of coverage. Biden could also help persuade Medicare and other insurers to cover the costs of tumor DNA sequencing.

NIH officials are knocking down rumors that Biden's initiative will build on two other cancer moonshots. One, announced last week by Los Angeles, California, oncologist and billionaire Patrick Soon-Shiong, aims to bring together companies to test combinations of cancer immunotherapy drugs. NIH is "obviously interested in" such endeavors, Collins says, but Soon-Shiong's is not directly linked to Biden's effort.

Another moonshot was announced in 2012 by the MD Anderson Cancer Center in Houston, Texas, where Biden's son received treatment. It sets specific targets, such as cutting deaths from colon cancer by 30% over 10 years, and may have inspired the moonshot metaphor, suggests MD Anderson President Ronald DePinho, who said he has "had multiple conversations" with Biden.

Although Biden won't be in the White House much longer, Graves said the moonshot is meant to "[lay] the groundwork for meaningful advances ... that will pay out benefits in the coming years." Biden's journey, meanwhile, continues: On 19 January he was in Davos, Switzerland, hosting another cancer roundtable with a mix of prominent researchers, as he assesses how to get his moonshot launched. ■

CONSERVATION

Standoff imperils Oregon refuge

Takeover disrupts what observers call a model public-private restoration effort

By **Robert F. Service**

As an armed occupation of the Malheur National Wildlife Refuge in southeastern Oregon drags into its fourth week, the first casualty of the standoff could be the refuge's ecological health. "We've got a complete stand-down and delay," says Paul Henson of the U.S. Fish and Wildlife Service (FWS) in Portland, Oregon, which oversees the refuge and intensively manages it to maintain habitat and fight invasive species. "We're not allowed to go there," says Henson, FWS's Oregon supervisor.

The delay could soon become critical, Henson and others say. Beginning in early spring, FWS personnel regulate water flows throughout the refuge to safeguard habitat for the hundreds of thousands of migratory birds that use the 76,000-hectare refuge as a key stopover and nesting ground. Federal biologists are also in the midst of a 15-year effort to combat invasive carp that have largely destroyed the native aquatic ecosystem of the refuge's two massive, shallow lakes and the Blitzen River that feeds them from the south. "It will set us back," says Linda Beck, a FWS biologist fighting the carp, whose office at the refuge has been commandeered by militants.

The Malheur refuge was created in 1908 by President Theodore Roosevelt to protect lakes and wetlands that comprise a key oasis along the Pacific Flyway, the route followed by hundreds of bird species migrating between the tropics and the Arctic. In the mid-1800s, the region's water—in an otherwise arid landscape—also drew ranchers, who transformed the Blitzen River with myriad dykes, canals, and ditches to irrigate land for cattle, changes that have contributed to widespread invasions by exotic plants.

On 2 January, some 20 heavily armed militants took over unoccupied buildings at the refuge, demanding that all federally owned land in the West be turned over to

Published by AAAS

Livestock grazing continues to be controversial on most public lands in the West. But these cattle at the Malheur refuge help preserve bird nesting habitat.

PHOTO: © KENDALL GILBERT/CORBIS

local control for increased ranching, mining, and other so-called "beneficial" uses. Refuge personnel and law enforcement officials have backed off, wanting to avoid violence. For now, the militants show no signs of leaving, declaring they are committed to overturning federal land-use rules that they say are tone-deaf to the needs of families that have lived in the area for generations.

Ironically, the refuge—unlike others nearby—allows local ranchers access to graze their cattle. And both refuge managers and outside observers say cooperation between FWS and the local community has been strong. From 2008 through 2013, FWS employees held dozens of meetings with a range of stakeholders—local ranchers and business leaders; state, county, and tribal officials; and scientists and environmentalists—to assemble a Comprehensive Conservation Plan (CCP) for the refuge. The plan lays out a strategy for restoring the refuge to ecological health while recognizing the needs of locals.

"It's wholly ironic that [the refuge] has become a center for protest of heavy-handed government, when [it has] really been a model for cooperation with the local population," says Chad Boyd, a rangeland scientist with the U.S. Department of Agriculture's Agricultural Research Service in Burns, Oregon. Bob Sallinger, conservation director for the Audubon Society of Portland, agrees: "I would rate this as one of the most successful collaborative processes that I've ever been involved with." The alliance also earned praise from rancher Fred Otley, who lives near Malheur. "The refuge has really listened and taken a more collaborative approach," Otley told *The Seattle Times*.

When the CCP process began, Sallinger and others said they expected cattle grazing to be a flashpoint, as it has been on other Western refuges where the animals have destroyed vegetation and polluted streams. But the stakeholders agreed that invasive carp were a far bigger, and largely ignored, problem.

The carp were introduced into the 3200-hectare Malheur Lake in the 1920s and quickly spread. The fish forage in bottom sediments, turning normally clear waters black and wiping out aquatic plants and insects that serve as the base of the refuge's food chain. Today, Malheur Lake "is literally … a mud puddle," Beck says.

One result is that the refuge's duck population has plummeted by 90%. No one knows how many carp infest the refuge, but in 2009 alone biologists removed some 30,000, averaging between 4.5 to 7 kilograms each. Malheur "is the poster child of invasive species nightmares," says David Dobkin, an ecologist with the High Desert Ecological Research Institute in Bend, Oregon. "The entire food chain has been completely disrupted and transformed."

Cattle grazing seemed a lesser threat and could even be turned to advantage. FWS now limits cows to less sensitive portions of the refuge, and actually relies on grazing to prevent grasses and other vegetation from becoming unattractive to nesting birds. "It's a truly valuable tool," Henson says.

Today, refuge managers say their goal is to slowly restore the region's native ecology, continually adapting their management practices as they gain ground. They are installing fish screens to prevent carp from infesting the river's side channels and studying carp behavior, looking for better ways to combat them. This spring, commercial fishermen are slated to begin a 5-year carp harvesting effort expected to remove millions of kilograms of fish each year, to be processed into fertilizer for dairy cow fields. But as the occupation continues, all of these plans are on hold.

Henson says he's hopeful that the standoff won't spoil the refuge's good working relationship with local residents. "I've called a half a dozen ranchers and county commissioners," Henson says, and he says they've all assured him that they are committed to continuing to work together to improve the refuge. The standoff, he says, "might actually make our relationship stronger as we weather this together." ■

Published by AAAS

DATA CHECK

BEHIND THE NUMBERS

Tracking first jobs to measure the impact of research funding

By **Jeffrey Mervis**

Follow 3200 new Ph.D.s from eight major state universities into their first jobs, and what will you learn?

Mainstream media that covered the results, published last month in *Science*, focused on the unremarkable fact that those with engineering and computer science degrees were earning a lot more than those trained in the life sciences, and that corporate jobs pay much better than academic positions. But Midwestern policymakers may be surprised to learn that newly minted Ph.D.s from two of their flagship institutions are more likely to end up working in California than in their home states. (The universities are not identified to preserve the confidentiality of data records.) And for those who think about how public spending on research fosters innovation, the biggest news may be the study itself: It is based on an unprecedented blending of university administrative records with employment and earnings data collected for the U.S. Census Bureau.

The study marks a milestone in creating what former presidential science adviser John Marburger called "a science of science policy." It brings researchers one step closer to meeting Marburger's goal of making decisions about the size and scope of federal investments in research based on data rather than anecdotes.

The new study uses data from the Institute for Research on Innovation and Science (IRIS) at the University of Michigan, Ann Arbor. IRIS was formed last year to promote research on how basic research can foster economic development and benefit society, and the study is its first major product. IRIS's origins lie in a database of federal R&D expenditures, called STAR METRICS, created in response to Marburger's 2005 call for such research. A consortium of 15 Midwestern universities expanded the idea into a common data platform, called UMETRICS, using data they were required to compile on the impact of the massive 2009 federal stimulus spending package. More than two dozen major research universities pay annual dues to support IRIS and have access to its analyses.

"The goal of IRIS is to produce independent statistical evidence on how research investments work their way through the economy," explains co-author Julia Lane, an economist at New York University in New York City, who was the driving force behind STAR METRICS while working for the federal government. "I'm not a big fan of magical expenditure multipliers that lack any empirical basis," she adds, referring to a common but controversial method of measuring the economic impact of academic research.

The paper examines the immediate postgraduation employment of those who earned Ph.D.s between 2009 and 2011 from eight research-intensive public universities in the Midwest: Indiana, Ohio State, Pennsylvania State, and Purdue universities and the universities of Iowa, Michigan, Minnesota, and Wisconsin. Its title—"Wrapping it up in a person"—refers to the adage that the best way to turn basic research into new technologies and products is to hire the people who made those discoveries. All the graduate students had been part of a research grant, and the authors hypothesized that their first jobs might shed light on how—and where—Ph.D.s apply their new knowledge.

22 percent
Fraction of new Ph.D.s from eight major U.S. public research universities in the Midwest who took jobs in-state.

14 percent
Fraction of new Ph.D.s from that cohort who left the state for a job in California.

39 percent
Fraction who took jobs in industry.

Nearly three in five remained in academia, many presumably as postdocs, with salaries that reflect their lowly rank. But 39% took industry jobs, and disproportionately worked at companies that conduct research. A relative handful (4%) joined the government.

That's the national picture. But state officials typically want to know whether their state is getting a good return on its investment in higher education, including the extent to which graduates contribute to local economic development. So the researchers also studied how these doctoral recipients dispersed across the country after getting their degrees.

The results may be humbling to hometown boosters. Only 22% of the total cohort remained in-state, roughly half of them staying within 50 miles of their alma mater. The picture of those who left shows the powerful lure of the megastate of California, home to one in eight Americans. Propelled by Silicon Valley in the north and a large aerospace and biotech industry in the south, California receives a whopping 26% of the nation's R&D expenditures.

It also attracted 14.3% of this cohort of doctoral recipients. That's more than double the 6.7% who went to Minnesota, the next most popular state destination. Slicing the data in another way, California attracted 19% of those who left their home states. That puts it far ahead of Illinois, which attracted 7.3% of all Ph.D.s who relocated. New York, Texas, and North Carolina were the only other states that snared more than 5% of the mobile Ph.D. cohort.

The study does not explore whether having 22% of the cohort remain in-state after graduation is a "good" or "bad" outcome. And the data don't identify the factors causing graduates to stay or leave, admits co-author Bruce Weinberg, an economist at Ohio State University, Columbus. "There's no way from this study to quantify the effect of having a major research university in your state," he says. "And we can't run a randomized control trial—nobody wants to be told where to go after their degree." Nor does the study paint a picture of national mobility rates and employment patterns for this pool of talent.

Forthcoming papers may do that, Weinberg notes, and studies examining gender differences in the graduate training and early career paths of those in science and engineering fields are coming out shortly. "We're only getting started," Lane says. "The idea is get as many researchers as possible involved in the science of science policy." ■

DATA: *SCIENCE*, 11 DECEMBER 2015, P. 1367

Published by AAAS

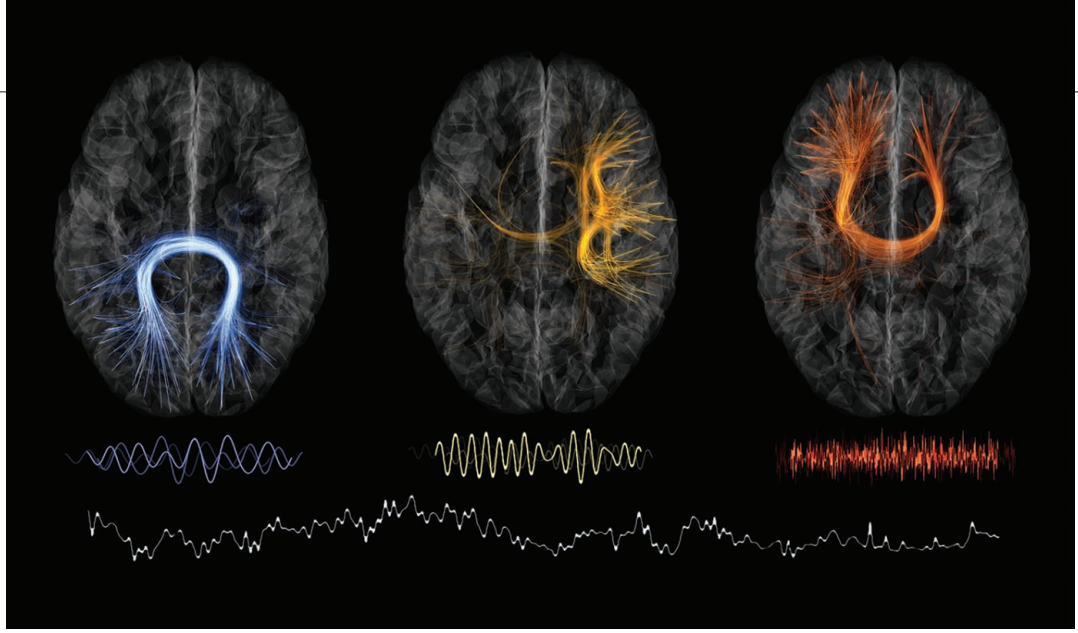

The Montreal Neurological Institute plans to free up its findings, including data that point to connections between brain regions communicating at different neural rhythms.

IMAGE: SEBASTIEN DERY, MCCONNELL BRAIN IMAGING CENTRE, MONTREAL NEUROLOGICAL INSTITUTE

DATA SHARING

Montreal institute going 'open' to accelerate science

Experiment aims to show whether forgoing patents and freeing up data can boost neuroscience research

By **Brian Owens**

Guy Rouleau, the director of McGill University's Montreal Neurological Institute (MNI) and Hospital in Canada, is frustrated with how slowly neuroscience research translates into treatments. "We're doing a really shitty job," he says. "It's not because we're not trying; it has to do with the complexity of the problem."

So he and his colleagues at the renowned institute decided to try a radical solution. Starting this year, any work done there will conform to the principles of the "open-science" movement—all results and data will be made freely available at the time of publication, for example, and the institute will not pursue patents on any of its discoveries. Although some large-scale initiatives like the government-funded Human Genome Project have made all data completely open, MNI will be the first scientific institute to follow that path, Rouleau says.

"It's an experiment; no one has ever done this before," he says. The intent is that neuroscience research will become more efficient if duplication is reduced and data are shared more widely and earlier. Opening access to the tissue samples in MNI's biobank and to its extensive databank of brain scans and other data will have a major impact, Rouleau hopes. "We think that it is a way to accelerate discovery and the application of neuroscience."

After a year of consultations among the institute's staff, pretty much everyone—about 70 principal investigators and 600 other scientific faculty and staff—has agreed to take part, Rouleau says. Over the next 6 months, individual units will hash out the details of how each will ensure that its work lives up to guiding principles for openness that the institute has developed. They include freely providing all results, data, software, and algorithms; and requiring collaborators from other institutions to also follow the open principles.

Staff at the institute were generally in favor of the plan, according to Lesley Fellows, a neurologist at MNI, though there were concerns about how to implement some aspects of it—such as how to protect patient confidentiality, and whether there would be sufficient financial support. Yet there is a "moral imperative," according to Fellows, for research to be shared as openly as possible.

"While the scale of 'open' that can be pursued right now may vary across research areas and will certainly depend on the resources that can be brought to bear, the practical challenges seem worth contending with," she says. Participation is voluntary, and researchers can pursue patents on their own, but MNI will not pay the fees or help with the paperwork.

Advocates of open science have welcomed MNI's move. Brian Nosek, a psychologist and director of the Center for Open Science at the University of Virginia in Charlottesville, says he is "very impressed" with the institute's plans. "It's clear they are looking to move the organization towards the ideals of science," he says.

Nosek says the decision to eschew patents is especially intriguing. "I haven't seen others do that before," he says. But it's not something that will necessarily work in other scientific fields, like engineering, Nosek predicts. "There is lots of debate in the life sciences now about what should and should not be patented, but that may not translate across disciplines smoothly."

Rouleau concedes that the patent ban might mean MNI has to forgo some future licensing income. But he says the kind of early-stage science that the institute does is not really worth protecting. "There is a fair amount of patenting by people at the institute, but the outcomes have not been very useful," he says, adding that the institute would rather provide data that others could use to develop patentable medicines. "It comes down to what is the reason for our existence? It's to accelerate science, not to make money."

The insistence that any organization or institute that collaborates with MNI will also have to follow open-science principles for that project could help to spread the approach, says Dan Gezelter, a chemist and open-science advocate at the University of Notre Dame in South Bend, Indiana. "It's a little bit viral. I've never seen that before," he says. Nosek agrees. "There is little that is more powerful in changing behavior than peer pressure," he says.

MNI is developing metrics to monitor its open-science experiment and determine whether it has the hoped-for impact. Officials will look at participation by the institute's own staff, how much their open resources are being used by other researchers, and whether new products or therapies are being developed more quickly. "In 5 years," Rouleau says, "we'll be able to say 'these things worked, and these things didn't.'" ■

Brian Owens is a writer based in St. Stephen, Canada.

Published by AAAS

NUMBER 9

A new giant planet, still unseen, appears to be shaping the orbits of objects beyond Neptune

By **Eric Hand**

The solar system appears to have a new ninth planet. This week, two scientists announced evidence that a body nearly the size of Neptune—but as yet unseen—orbits the sun every 15,000 years. During the solar system's infancy 4.5 billion years ago, they say, the giant planet was knocked out of the planet-forming region near the sun. Slowed down by gas, the planet settled into a distant elliptical orbit, where it still lurks today.

The claim is the strongest yet in the centuries-long search for a "Planet X" beyond Neptune. The quest has been plagued by far-fetched claims and even outright quackery. But the new evidence comes from a pair of respected planetary scientists, Konstantin Batygin and Mike Brown of the California Institute of Technology (Caltech) in Pasadena, who prepared for the inevitable skepticism with detailed analyses of the orbits of other distant objects and months of computer simulations. "If you say, 'We have evidence for Planet X,' almost any astronomer will say, 'This again? These guys are clearly crazy.' I would, too," Brown says. "Why is this different? This is different because this time we're right."

Outside scientists say their calculations stack up and express a mixture of caution and excitement about the result. "I could not imagine a bigger deal if—and of course that's a boldface 'if'—if it turns out to be right," says Gregory Laughlin, a planetary scientist at the University of California (UC), Santa Cruz. "What's thrilling about it is [the planet] is detectable."

Batygin and Brown inferred its presence from the peculiar clustering of six previously known objects that orbit beyond Neptune. They say there's only a 0.007% chance, or about one in 15,000, that the clustering could be a coincidence. Instead, they say, a planet with the mass of 10 Earths has shepherded the six objects into their strange elliptical orbits, tilted out of the plane of the solar system.

> ***"Killing Pluto was fun, but this is head and shoulders above everything else."***
>
> **Mike Brown**, Caltech

The orbit of the inferred planet is similarly tilted, as well as stretched to distances that will explode previous conceptions of the solar system. Its closest approach to the sun is seven times farther than Neptune, or 200 astronomical units (AUs). (An AU is the distance between Earth and the sun, about 150 million kilometers.) And Planet X could roam as far as 600 to 1200 AU, well beyond the Kuiper belt, the region of small icy worlds that begins at Neptune's edge about 30 AU.

If Planet X is out there, Brown and Batygin say, astronomers ought to find more objects in telltale orbits, shaped by the pull of the hidden giant. But Brown knows that no one will really believe in the discovery until Planet X itself appears within a telescope viewfinder. "Until there's a direct detection, it's a hypothesis—even a potentially very good hypothesis," he says. The team has time on the one large telescope in Hawaii that is suited for the search, and they hope other astronomers will join in the hunt.

Batygin and Brown published the result this week in *The Astronomical Journal*. Alessandro Morbidelli, a planetary dynamicist at the Nice Observatory in France, performed the peer review for the paper. In a statement, he says Batygin and Brown made a "very solid argument" and that he is "quite convinced by the existence of a distant planet."

CHAMPIONING A NEW NINTH PLANET is an ironic role for Brown; he is better known as a planet slayer. His 2005 discovery of Eris, a remote icy world nearly the

ILLUSTRATION: A. CUADRA/*SCIENCE*

Published by AAAS

The new giant planet (lower right) would be similar in size and appearance to Neptune.

same size as Pluto, revealed that what was seen as the outermost planet was just one of many worlds in the Kuiper belt. Astronomers promptly reclassified Pluto as a dwarf planet—a saga Brown recounted in his book *How I Killed Pluto*.

Now, he has joined the centuries-old search for new planets. His method—inferring the existence of Planet X from its ghostly gravitational effects—has a respectable track record. In 1846, for example, the French mathematician Urbain Le Verrier predicted the existence of a giant planet from irregularities in the orbit of Uranus. Astronomers at the Berlin Observatory found the new planet, Neptune, where it was supposed to be, sparking a media sensation.

Remaining hiccups in Uranus's orbit led scientists to think that there might yet be one more planet, and in 1906 Percival Lowell, a wealthy tycoon, began the search for what he called "Planet X" at his new observatory in Flagstaff, Arizona. In 1930, Pluto turned up—but it was far too small to tug meaningfully on Uranus. More than half a century later, new calculations based on measurements by the Voyager spacecraft revealed that the orbits of Uranus and Neptune were just fine on their own: No Planet X was needed.

Yet the allure of Planet X persisted. In the 1980s, for example, researchers proposed that an unseen brown dwarf star could cause periodic extinctions on Earth by triggering fusillades of comets. In the 1990s, scientists invoked a Jupiter-sized planet at the solar system's edge to explain the origin of certain oddball comets. Just last month, researchers claimed to have detected the faint microwave glow of an outsized rocky planet some 300 AU away, using an array of telescope dishes in Chile called the Atacama Large Millimeter Array (ALMA). (Brown was one of many skeptics, noting that ALMA's narrow field of view made the chances of finding such an object vanishingly slim.)

PODCAST

To hear a podcast with author Eric Hand, go to http://scim.ag/pod_6271

Brown got his first inkling of his current quarry in 2003, when he led a team that found Sedna, an object a bit smaller than both Eris and Pluto. Sedna's odd, far-flung orbit made it the most distant known object in the solar system at the time. Its perihelion, or closest point to the sun, lay at 76 AU, beyond the Kuiper belt and far outside the influence of Neptune's gravity. The implication was clear: Something massive, well beyond Neptune, must have been pulled Sedna into its distant orbit.

That something didn't have to be a planet. Sedna's gravitational nudge could have come from a passing star, or from one of the many other stellar nurseries that surrounded the nascent sun at the time of the solar system's formation.

Since then, a handful of other icy objects have turned up in similar orbits. By combining Sedna with five other weirdos, Brown says he has ruled out stars as the unseen influence: Only a planet could explain such strange orbits. Of his three major discoveries—Eris, Sedna, and now, potentially, Planet X—Brown says the last is the most sensational. "Killing Pluto was fun. Finding Sedna was scientifically interesting," he says. "But this one, this is head and shoulders above everything else."

BROWN AND BATYGIN were nearly beaten to the punch. For years, Sedna was a lone clue to a perturbation from beyond Neptune. Then, in 2014, Scott Sheppard and Chad Trujillo (a former graduate student of Brown's) published a paper describing the discovery of VP113, another object that never comes close to the sun. Sheppard, of the Carnegie Institution for Science in Washington, D.C., and Trujillo, of the Gemini Observatory in Hawaii, were well aware of the implications. They began to examine the

Pointing to Planet X

The bizarre orbits of six known worlds are clustered in a way that demands the existence of a giant planet 10 times the mass of Earth. Planet X spends most of its time in the outer reaches of its 15,000-year orbit, where the Subaru Telescope in Hawaii will look for it.

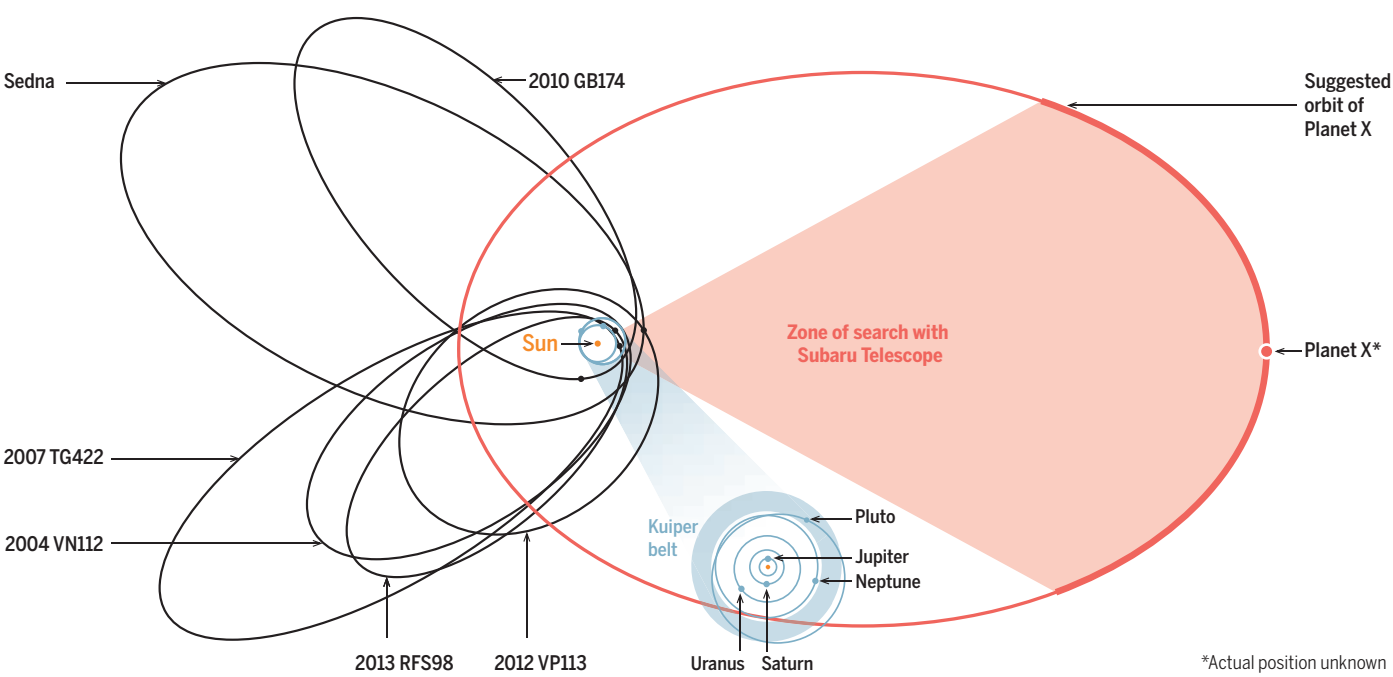

*Actual position unknown

CREDITS: (DATA) JPL; BATYGIN AND BROWN/CALTECH; (DIAGRAM) A. CUADRA/*SCIENCE*

Published by AAAS

orbits of the two objects along with 10 other oddballs. They noticed that, at perihelion, all came very near the plane of solar system in which Earth orbits, called the ecliptic. In a paper, Sheppard and Trujillo pointed out the peculiar clumping and raised the possibility that a distant large planet had herded the objects near the ecliptic. But they didn't press the result any further.

Later that year, at Caltech, Batygin and Brown began discussing the results. Plotting the orbits of the distant objects, Batygin says, they realized that the pattern that Sheppard and Trujillo had noticed "was only half of the story." Not only were the objects near the ecliptic at perihelia, but their perihelia were physically clustered in space (see diagram, p. 331).

The 8-meter Subaru Telescope atop Mauna Kea in Hawaii has a large field of view—enabling it to search efficiently for Planet X.

For the next year, the duo secretly discussed the pattern and what it meant. It was an easy relationship, and their skills complemented each other. Batygin, a 29-year-old whiz kid computer modeler, went to college at UC Santa Cruz for the beach and the chance to play in a rock band. But he made his mark there by modeling the fate of the solar system over billions of years, showing that, in rare cases, it was unstable: Mercury may plunge into the sun or collide with Venus. "It was an amazing accomplishment for an undergraduate," says Laughlin, who worked with him at the time.

Brown, 50, is the observational astronomer, with a flair for dramatic discoveries and the confidence to match. He wears shorts and sandals to work, puts his feet up on his desk, and has a breeziness that masks intensity and ambition. He has a program all set to sift for Planet X in data from a major telescope the moment they become publicly available later this year.

Their offices are a few doors down from each other. "My couch is nicer, so we tend to talk more in my office," Batygin says. "We tend to look more at data in Mike's." They even became exercise buddies, and discussed their ideas while waiting to get in the water at a Los Angeles, California, triathlon in the spring of 2015.

First, they winnowed the dozen objects studied by Sheppard and Trujillo to the six most distant—discovered by six different surveys on six different telescopes. That made it less likely that the clumping might be due to an observation bias such as pointing a telescope at a particular part of the sky.

Batygin began seeding his solar system models with Planet X's of various sizes and orbits, to see which version best explained the objects' paths. Some of the computer runs took months. A favored size for Planet X emerged—between five and 15 Earth masses—as well as a preferred orbit: antialigned in space from the six small objects, so that its perihelion is in the same direction as the six objects' aphelion, or farthest point from the sun. The orbits of the six cross that of Planet X, but not when the big bully is nearby and could disrupt them. The final epiphany came 2 months ago, when Batygin's simulations showed that Planet X should also sculpt the orbits of objects that swoop into the solar system from above and below, nearly orthogonal to the ecliptic. "It sparked this memory," Brown says. "I had seen these objects before." It turns out that, since 2002, five of these highly inclined Kuiper belt objects have been discovered, and their origins are largely unexplained. "Not only are they there, but they are in exactly the places we predicted," Brown says. "That is when I realized that this is not just an interesting and good idea—this is actually real."

Sheppard, who with Trujillo had also suspected an unseen planet, says Batygin and Brown "took our result to the next level. … They got deep into the dynamics, something that Chad and I aren't really good with. That's why I think this is exciting."

Others, like planetary scientist Dave Jewitt, who discovered the Kuiper belt, are more cautious. The 0.007% chance that the clustering of the six objects is coincidental gives the planet claim a statistical significance of 3.8 sigma—beyond the 3-sigma threshold typically required to be taken seriously, but short of the 5 sigma that is sometimes used in fields like particle physics. That worries Jewitt, who has seen plenty of 3-sigma results disappear before. By reducing the dozen objects examined by Sheppard and Trujillo to six for their analysis, Batygin and Brown weakened their claim, he says. "I worry that the finding of a single new object that is not in the group would destroy the whole edifice," says Jewitt, who is at UC Los Angeles. "It's a game of sticks with only six sticks."

At first blush, another potential problem comes from NASA's Wide-field Infrared Survey Explorer (WISE), a satellite that completed an all-sky survey looking for the heat of brown dwarfs—or giant planets. It ruled out the existence of a Saturn-or-larger planet as far out as 10,000 AU, according to a 2013 study by Kevin Luhman, an astronomer at Pennsylvania State University, University Park. But Luhman notes that if Planet X is Neptune-sized or smaller, as Batygin and Brown say, WISE would have missed it. He says there is a slim chance of detection in another WISE data set at longer wavelengths—sensitive to cooler radiation—which was collected for 20% of the sky. Luhman is now analyzing those data.

EVEN IF BATYGIN AND BROWN can convince other astronomers that Planet X exists, they face another challenge: explaining how it ended up so far from the sun. At such distances, the protoplanetary disk of dust and gas was likely to have been too thin to fuel planet growth. And even if Planet X did get a foothold as a planetesimal, it

PHOTO: SUBARU TELESCOPE, NAOJ

Published by AAAS

would have moved too slowly in its vast, lazy orbit to hoover up enough material to become a giant.

Instead, Batygin and Brown propose that Planet X formed much closer to the sun, alongside Jupiter, Saturn, Uranus, and Neptune. Computer models have shown that the early solar system was a tumultuous billiards table, with dozens or even hundreds of planetary building blocks the size of Earth bouncing around. Another embryonic giant planet could easily have formed there, only to be booted outward by a gravitational kick from another gas giant.

It's harder to explain why Planet X didn't either loop back around to where it started or leave the solar system entirely. But Batygin says that residual gas in the protoplanetary disk might have exerted enough drag to slow the planet just enough for it to settle into a distant orbit and remain in the solar system. That could have happened if the ejection took place when the solar system was between 3 million and 10 million years old, he says, before all the gas in the disk was lost into space.

Hal Levison, a planetary dynamicist at the Southwest Research Institute in Boulder, Colorado, agrees that something has to be creating the orbital alignment Batygin and Brown have detected. But he says the origin story they have developed for Planet X and their special pleading for a gas-slowed ejection add up to "a low-probability event." Other researchers are more positive. The proposed scenario is plausible, Laughlin says. "Usually things like this are wrong, but I'm really excited about this one," he says. "It's better than a coin flip."

Mike Brown (left) and Konstantin Batygin.

All this means that Planet X will remain in limbo until it is actually found.

ASTRONOMERS HAVE SOME GOOD IDEAS about where to look, but spotting the new planet won't be easy. Because objects in highly elliptical orbits move fastest when they are close to the sun, Planet X spends very little time at 200 AU. And if it were there right now, Brown says, it would be so bright that astronomers probably would have already spotted it.

Instead, Planet X is likely to spend most of its time near aphelion, slowly trotting along at distances between 600 and 1200 AU. Most telescopes capable of seeing a dim object at such distances, such as the Hubble Space Telescope or the 10-meter Keck telescopes in Hawaii, have extremely tiny fields of view. It would be like looking for a needle in a haystack by peering through a drinking straw.

One telescope can help: Subaru, an 8-meter telescope in Hawaii that is owned by Japan. It has enough light-gathering area to detect such a faint object, coupled with a huge field of view—75 times larger than that of a Keck telescope. That allows astronomers to scan large swaths of the sky each night. Batygin and Brown are using Subaru to look for Planet X—and they are coordinating their efforts with their erstwhile competitors, Sheppard and Trujillo, who have also joined the hunt with Subaru. Brown says it will take about 5 years for the two teams to search most of the area where Planet X could be lurking.

If the search pans out, what should the new member of the sun's family be called? Brown says it's too early to worry about that and scrupulously avoids offering up suggestions. For now, he and Batygin are calling it Planet Nine (and, for the past year, informally, Planet Phattie—1990s slang for "cool"). Brown notes that neither Uranus nor Neptune—the two planets discovered in modern times—ended up being named by their discoverers, and he thinks that that's probably a good thing. It's bigger than any one person, he says: "It's kind of like finding a new continent on Earth."

He is sure, however, that Planet X—unlike Pluto—deserves to be called a planet. Something the size of Neptune in the solar system? Don't even ask. "No one would argue this one, not even me." ■

Distant, dim, and elusive

The hunt for planets beyond Neptune has a long and checkered history.

1906
Percival Lowell founds an observatory in Flagstaff, Arizona, to search for the missing planet, which he calls Planet X.

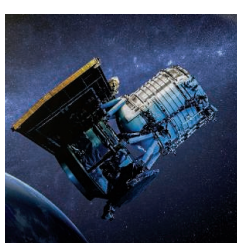

2014
An all-sky survey from the Wide-field Infrared Survey Explorer satellite rules out planets the size of Saturn or larger out to 10,000 astronomical units.

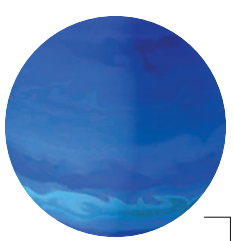

2015
Astronomers at the California Institute of Technology in Pasadena announce indirect evidence for a Neptune-sized planet with an orbit of 15,000 years.

1846
Neptune is discovered based on discrepancies in Uranus's orbit. Remaining anomalies suggest another planet lies farther out.

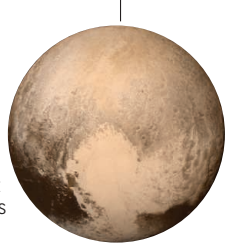

1930
At Lowell Observatory, Clyde Tombaugh discovers Pluto, but it is too small to affect Uranus.

1984
Scientists suggest that mass extinctions could be explained by a nearby dwarf star called Nemesis, which would shower Earth with comets.

1993
Refined calculations show no discrepancies in Uranus's orbit after all. The need for Planet X disappears.

1999
Astronomers say a bias in the orbits of some comets means a Jupiter-sized planet, called Tyche, lurks in the outer solar system.

2003
Sedna is discovered. Its strange 12,000-year orbit requires an outside nudge.

CREDITS: (IMAGES, TOP TO BOTTOM) LANCE HAYASHIDA/CALTECH; WIKIMEDIA COMMONS; NASA/JPL-CALTECH; A. CUADRA/*SCIENCE*; NASA/JHUAPL/SWRI; (DIAGRAM) A. CUADRA/*SCIENCE*

Published by AAAS

INSIGHTS

Wider combs for better timing *p. 340* ▸

One-step nitrifiers *p. 342* ▸

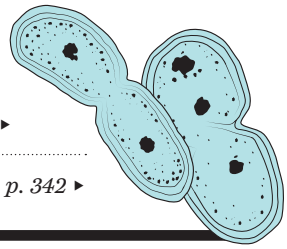

PERSPECTIVES

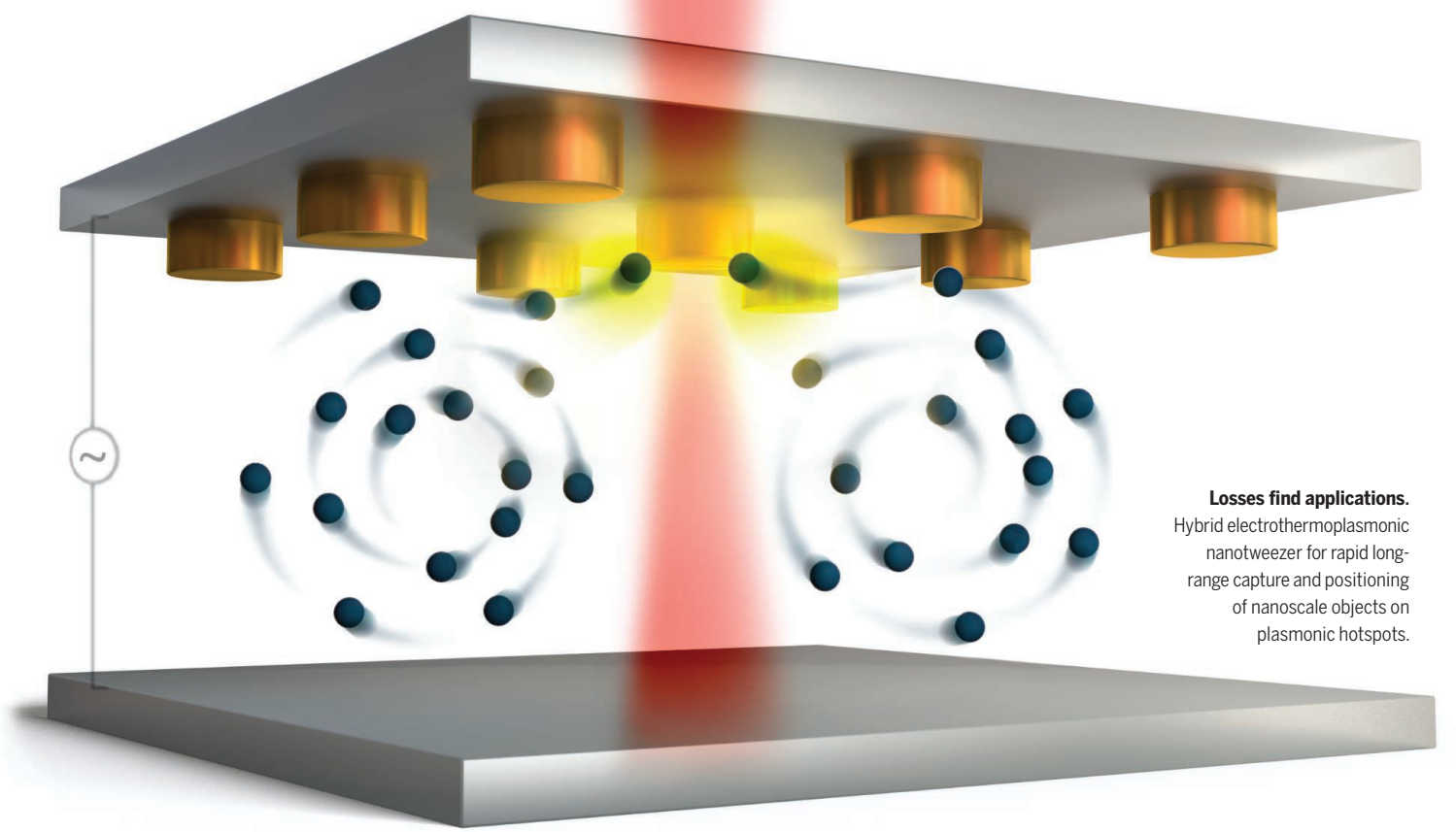

Losses find applications. Hybrid electrothermoplasmonic nanotweezer for rapid long-range capture and positioning of nanoscale objects on plasmonic hotspots.

APPLIED PHYSICS

Plasmonics—turning loss into gain

The optical losses usually associated with plasmonic materials could be used in applications

By **Justus C. Ndukaife,[1,2] Vladimir M. Shalaev,[1] Alexandra Boltasseva[1]**

The light-induced electronic excitations that occur at the surface of metals—plasmons—provide the extraordinary ability to confine electromagnetic energy to the subwavelength scale. Such extreme optical confinement can enhance the light-matter interaction and enable miniaturized optical and optoelectronic devices. However, this confinement requires that plasmonic materials possess free carriers, which unavoidably results in light being lost or absorbed in the system (*1*). This optical loss has hampered the realization of device designs with ultracompact, on-chip optical components and nanometer-scale resolution imaging. Because of the detrimental effects of plasmonic losses, several avenues are being explored to mitigate the high absorption, such as using gain to compensate for the losses, and synthesizing alternative low-loss plasmonic materials (*2*). Rather than continuing to pursue low-loss plasmonics approaches, we draw attention to the benefit of losses by high-

ILLUSTRATION: V. ALTOUNIAN/*SCIENCE*

Published by AAAS

lighting recent groundbreaking discoveries that were enabled by intrinsic losses in plasmonic systems.

A key consequence of losses in plasmonics is resonant absorption of incident photons to produce local heating of the plasmonic structure. Recently, loss-induced heating was used to address a long-standing challenge in the field of plasmon-enhanced optical tweezing—to dynamically and rapidly load the plasmonic trap on demand (*3*). The hybrid electrothermoplasmonic nanotweezer (*3*) combines plasmonic heating and ac electric fields for fast and precise delivery of nanometer-sized objects to plasmonic hotspots, where they are confined within a few seconds (see the first figure). This device could be used for trapping and analysis of virus and protein samples to improve the sensitivity of nanoscale sensors, as well as trapping and positioning quantum emitters such as quantum dots and nanodiamonds.

Loss-induced plasmonic heating could also play a role in optical data storage and encryption. Prior work has successfully harnessed polarization-dependent local heating and the reshaping of gold nanorods embedded in polyvinyl alcohol for five-dimensional optical recording of images (*4*). Optical data storage that is amenable to integration in optoelectronic devices was proposed (*5*) where heat-induced re-shaping of pillar bowtie nanoantennas was used to record images. Heat-assisted magnetic recording (HAMR) is a promising approach for increasing magnetic data storage that could push the limit of data storage beyond 1 Tb/in^2 (see the figure, panel B). The conventional design paradigm is to use plasmonic nanoantennas or near-field transducers (NFTs) to focus light onto a sub–50-nm spot that would be subsequently absorbed by the magnetic medium to temporarily heat it and reduce the coercivity in order to write the bits (*6*, *7*). In HAMR, the separation between the NFT and magnetic layer is a few nanometers, and because near-field radiative transfer can be much higher than predicted by the Stefan-Boltzmann law (*8*), it might be possible to harness near-field heat transfer from the hot NFT to the magnetic film for enhanced magnetic recording.

Plasmonic photothermal therapy represents another practical application of plasmonics that harnesses loss-induced heating of plasmonic nanoparticles to locally heat and destroy cancer cells (*9*) (see the figure, panel A). Quadrapeutics (*10*) combines encapsulated drugs, gold nanoparticles, near-infrared short pulses, and x-rays for cancer cell destruction. Central to this emerging technology is the plasmonic nanobubble, which is generated from resonant collective heating of embedded gold nanoparticles that have preferentially accumulated in the cancerous cells. Explosion of the bubble exerts mechanical pressure on cell walls to not only eject the drug payload into the cell cytoplasm but also to destroy the host cancer cells.

"Harnessing intrinsic loss in plasmonics could usher transformative technological innovations..."

Plasmonic heating could also become a crucial component in the renewable energy concept based on the conversion of solar energy to electricity. A key issue limiting the efficiency of solar cells is the loss of sub-bandgap photons, which are not absorbed by the solar cell material, and hence do not contribute to generation of the photocurrent in the cell. Broadband solar absorbers and emitters (*7*, *11*) made of plasmonic resonators can be used to absorb all energy within the solar spectrum and selectively emit to a narrow spectral window within the bandgap of the solar cell. Furthermore, the plasmonic absorbers and emitters could also be used to harvest waste heat. The hot electrons generated following the absorption of the incident photons in plasmonic nanoparticles could be used to enhance chemical reactions such as water splitting, and conversion of solar energy to chemical fuels, thus representing an emerging and actively investigated field with both fundamental and technological relevance (*12*).

Harnessing intrinsic loss in plasmonics could usher transformative technological innovations that would affect several fields, including information technology, life sciences, and clean energy. It is time for the plasmonic community to turn loss into gain. ■

REFERENCES AND NOTES

1. J. B. Khurgin, *Nat. Nanotechnol.* **10**, 2 (2015).
2. G. V. Naik, V. M. Shalaev, A. Boltasseva, *Adv. Mater.* **25**, 3264 (2013).
3. J. C. Ndukaife *et al.*, *Nat. Nanotechnol.* **11**, 53 (2016).
4. P. Zijlstra, J. W. M. Chon, M. Gu, *Nature* **459**, 410 (2009).
5. B. J. Roxworthy, A. M. Bhuiya, V. V. G. K. Inavalli, H. Chen, K. C. Toussaint, *Nano Lett.* **14**, 4687 (2014).
6. W. A. Challener *et al.*, *Nat. Photon.* **3**, 303 (2009).
7. U. Guler, V. M. Shalaev, A. Boltasseva, *Mater. Today* **18**, 227 (2014).
8. E. Rousseau *et al.*, *Nat. Photon.* **3**, 514 (2009).
9. L. R. Hirsch *et al.*, *Proc. Natl. Acad. Sci. U.S.A.* **100**, 13549 (2003).
10. E. Y. Lukianova-Hleb *et al.*, *Nat. Med.* **20**, 778 (2014).
11. A. Lenert *et al.*, *Nat. Nanotechnol.* **1**, 1 (2014).
12. M. L. Brongersma, N. J. Halas, P. Nordlander, *Nat. Publ. Gr.* **10**, 25 (2015).

ACKNOWLEDGMENTS

We acknowledge financial support from NSF Materials Research Science and Engineering Centers grant DMR- 1120923. J. C. N acknowledges partial support from the Purdue Water Institute.

10.1126/science.aad9864

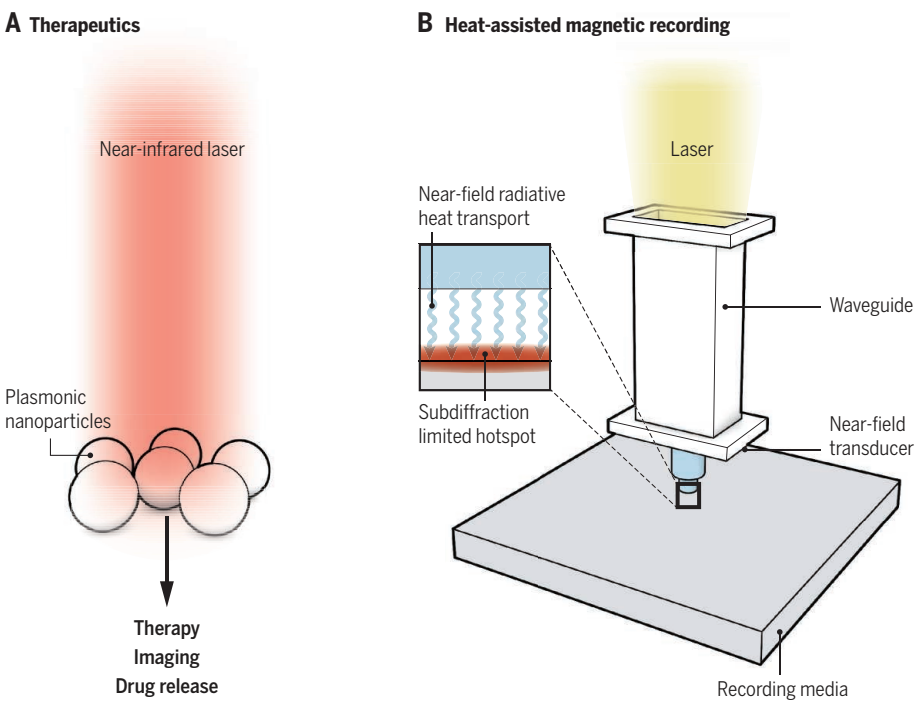

Losses find applications. (**A**) Application of local heating of plasmonic nanostructures for photothermal therapy imaging and drug release. (**B**) Heat-assisted magnetic recording scheme for data storage.

[1]*School of Electrical and Computer Engineering and Birck Nanotechnology Center, Purdue University, West Lafayette, IN 47907, USA.* [2]*Water Institute, Purdue University Calumet, Hammond, IN 46323, USA. E-mail: aeb@purdue.edu*

ILLUSTRATION: V. ALTOUNIAN/*SCIENCE*

Published by AAAS

MATERIALS CHEMISTRY

Interlacing molecular threads

Materials with a fabric-like microstructure are highly elastic

By **Enrique Gutierrez-Puebla**

The synthesis of organic materials has typically involved linking one or more types of discrete molecular building blocks to produce structures that are extended in three dimensions. For example, repeated addition of monomers results in the formation of organic polymers that have randomly packed structures and therefore form amorphous solid materials. If the building blocks repeat in an ordered sequence, crystalline solids are formed. The properties of the resulting solids are intimately related to both their network structure and their chemical components. On page 365 of this issue, Liu *et al.* report a material that has a fabric-like woven microstructure, giving it exceptional flexibility (*1*).

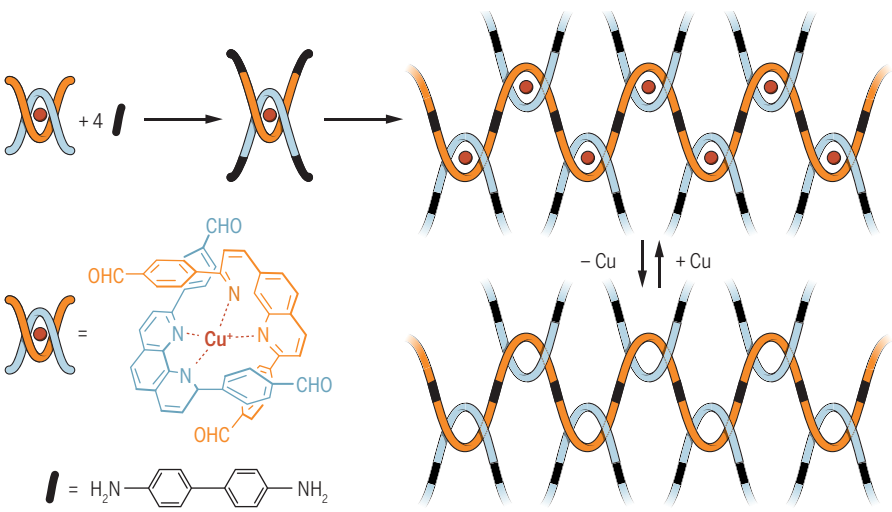

Molecular weaving. In a traditional COF material, organic building units are linked through covalent bonds to create rigid crystalline materials. Liu *et al.* report a COF material made from molecular threads that are connected through copper complexes. Removal of the copper ions results in a highly flexible and elastic material. This process is reversible.

A range of crystalline materials can be made by modifying or controlling the building units, resulting in materials with desired properties, such as high porosity, conductivity, and catalytic activity. Metal-organic frameworks (MOFs) (*2*) and covalent organic frameworks (COFs) (*3*) are two highly versatile classes of such materials. MOFs are constructed by joining inorganic clusters via organic linkers through coordination bonds; COFs consist of organic building units linked through strong covalent bonds (*4*). COFs are promising materials for storing gases such as hydrogen or methane and for use as catalysts and in optoelectronic applications.

However, these materials are all built through rigid, directional bonds between their components, restricting the range of their mechanical and elastic characteristics. Liu *et al.* now report the synthesis of COF materials from molecular threads (*1*). These threads are woven without chemical bonds between them, creating a structure in which molecular chains can slide past each other easily. The formation of materials from interlaced threads has long been sought because such solids are expected to have mechanical and other properties different from those of traditional materials (*5*). However, although there are many examples of materials that contain molecular chains, synthetic chemists had not previously found a way to interlace chains in a controlled manner.

To create such interlaced materials, Liu *et al.* rely on the synthesis of COFs to form crystalline materials with covalently bound organic molecules. The novel aspect is the selection of a Cu(I) complex as one building unit. This complex contains two identical molecules that are the starting point of independent threads in the COF. The metal cations act as templates that hold each thread-starting molecule in the correct position. Thus, the position of the metal centers precisely defines the points where the threads will be woven. The threads are extended by linking the thread-starting molecules with complementary linear molecules via imine bonds (a methodology extensively used in COF chemistry), resulting in a crystalline, open, extended structure denoted COF-505.

The copper cations can be easily removed, releasing the organic threads and providing them with a large degree of freedom (resulting in a loss of crystallinity). Upon elimination of the metal cations, the material undergoes a 10-fold increase in elasticity. The demetalation process is reversible, causing the solid to return to its previous crystalline state (see the figure). It is thus possible to modify the material's elastic properties through a simple process of metal complexation/decomplexation.

This synthetic approach based on the use of (removable) metal centers is comparable to the template synthesis of molecular rotaxanes, catenanes, and other materials based on interlocked rings (*6*, *7*). Nonetheless, COF-505 is very different from other materials with interpenetrated structures: Once the metal centers are removed, there are no interlocked rings in the structure. The material is exclusively made of interlaced molecular organic threads, similar to a woven fabric (see the figure), conferring it with unique flexibility as well as dynamic and elastic properties. These properties may, for example, be useful for designing materials that can transmit mechanical stimuli in a highly controllable chemical environment or in high-pressure applications that require materials capable of absorbing impacts or of deforming reversibly while preserving their chemical and structural integrity.

It should be possible to control the elasticity of COF-505 and of future related solids and to combine it with other properties already displayed by porous COFs. In addition, it may be possible to remetalate with cations other than copper, including catalytically active cations. This would extend the scope of these materials to many more chemical applications, for example, in catalysis, providing flexible reactive microenvironments. The materials may also find application as responsive molecular sponges—for example, for the sequestration of metal cations in liquid wastes. ■

Instituto de Ciencia de Materiales de Madrid, Consejo Superior de Investigaciones Científicas, Madrid 28049, Spain. E-mail: egutierrez@icmm.csic.es

REFERENCES

1. Y. Liu *et al.*, *Science* **351**, 365 (2016).
2. H. Furukawa, K. E. Cordova, M. O'Keeffe, O. M. Yaghi, *Science*, **341**, 1230444 (2013).
3. P. J. Waller, F. Gándara, O. M. Yaghi, *Acc. Chem. Res.* 10.1021/acs.accounts.5b00369 (2015).
4. H. M. El-Kaderi *et al.*, *Science* **316**, 268 (2007).
5. R. C. Ball, M. Doi, F. F. Edwards, M. Warner, *Polymer* **22**, 1010 (1981).
6. A. I. Prikhod'ko, F. Durola, J.-P. Sauvage, *J. Am. Chem. Soc.* **130**, 448 (2008).
7. E. V. Alexandrov, V. A. Blatov, D. M. Proserpio, *Acta Cryst. A* **68**, 484 (2012).

10.1126/science.aad9671

ILLUSTRATION: P. HUEY/*SCIENCE*

Published by AAAS

Editing policy to fit the genome?

Framing genome editing policy requires setting thresholds of acceptability

By **R. Isasi,[1,2]* E. Kleiderman,[2] B. M. Knoppers[2]**

Balancing therapeutic prospects brought by scientific advances with regulation to address highly contested socioethical issues is the ultimate challenge in dealing with disruptive science. Human genome editing is a powerful tool that offers great scientific and therapeutic potential (*1*, *2*). Yet, it rejuvenates socioethical and policy questions surrounding the acceptability of germline modification.

POLICY

The first national research application for licensing genome editing in human embryos is about to be filed in the United Kingdom (*3*). This is a country offering robust oversight, while also adopting a bold approach toward innovative science. At the same time, a revised pan-European regulation on clinical trials will come into effect in May of 2016 that would continue a prohibition on carrying out gene therapy clinical trials that "result in modifications to the subject's germ line genetic identity" (*4*). "Genetic identity," however, has yet to be defined, and we need to look for an approach to genome editing that can lead toward compromise or consensus.

Defining the contours and diversity of national policy frameworks governing the human germ line is difficult. The permissibility of conducting research on clinical applications of genome editing on early human development is often considered part of the regulatory approaches to assisted human reproductive technologies, stem cells, or genomic research. Similarities and differences between approaches also need to be considered. Internationally, policies extend across a continuum that distinguishes between degrees of permissiveness, that is, between legally binding legislation and regulatory and/or professional guidance or research versus clinical applications. We drew on a representative sample of 16 countries to provide a global "snapshot" of the spectrum of policy and legislative approaches (restrictive to permissive) regarding human germline editing, human embryonic stem cell research, human reproductive cloning, human research cloning, human somatic gene therapy, and pre-implantation genetic diagnosis (see the figure). Our sample also represents countries in which innovative research in the fields of genomics and stem cells is being carried out and/or that are hot spots for stem cell and reproductive tourism. For each technology, we showed whether it is being governed by laws (legislation) or by normative documents and policies (regulatory).

Where legislation has been adopted either prohibiting or restricting germline interventions, it is mostly accompanied by criminal sanctions ranging from hefty imprisonment terms to fines (e.g., Australia, Belgium, Brazil, Canada, France, Germany, Israel, Netherlands, and United Kingdom). However, such restrictive legislation frequently requires that there be intentionality on the part of the individual (*mens rea*). For example, legislation adopted in Australia targets the intentional alteration of "the genome of a human cell in such a way that the alteration is heritable by descendants or the human whose cell was altered" (*5*, *6*). It further criminalizes intentionally placing "an embryo in the body of a woman knowing that, or reckless as to whether, the embryo is a prohibited embryo." Under Australian law, an embryo with an altered germ line or an embryo created solely for research purposes is considered a "prohibited embryo" (*5*, *6*). The intentionality provision has created a degree of policy uncertainty, particularly in terms of downstream restrictions on certain applications, such as clinical uses.

> ***"the thresholds the PGD model delineates...represent a robust approach to regulation."***

Restrictive policy approaches also usually include upstream limitations, which outlaw a technology or an application regardless of its purpose by means of tight regulations, blanket prohibitions, or moratoria. These types of restrictions are exemplified in broad, bottom-up bans on human embryo and/or germline manipulations, embryo genetic testing, and somatic cell nuclear transfer technologies. Germany and Canada have adopted upstream criminal bans on germline interventions and also restrict embryo research.

Nonetheless, some enacted prohibitions can be rendered ineffective or inadequate in practice, such as when the scope of laws focuses on a particular technology that is later outpaced by scientific developments. Similarly, prohibitions will be limited if exceptions are allowed. This is the case for provisions that, although aiming to adopt a restrictive approach toward embryo research, allow for interventions deemed therapeutically beneficial to the embryo or necessary for the preservation of its life, or are required in order to achieve a pregnancy (e.g., Belgium, Germany, and France). The vague language of such provisions means they would become obsolete once the particular intervention is considered standard clinical practice (*7*, *8*). Legal uncertainty comes into play when dealing with medical innovation.

Finally, restrictive policies signal a critical attitude toward science because of fears of commodification of potential human life, and they advocate for strong government intervention in the regulation of research.

The most frequent approach is intermediate. Hereunder, the application of genomic technologies in embryos and germ cells is allowed but closely monitored by governments (*8*) with the goal of providing efficient and safe mechanisms for conducting research. In the context of genome editing, a particular technology or an intervention is not banned per se. Rather, specific downstream applications are forbidden, such as attempting to initiate a human pregnancy with an embryo or a reproductive cell whose germ line has been intentionally altered (e.g., France, Israel, Japan, and Netherlands). In sum, reproductive purposes are typically outlawed, whereas scientific research activities, such as investigating basic biology or aspects of the methodology itself are generally permitted.

A few countries have permissive approaches that aim to promote scientific progress with the belief that it is beneficial for humanity. Here, a wide range of activities are permitted, provided that governance is observed, mostly by means of *de facto* or case-by-case approval by a licensing authority. Illustrative examples of this approach are found in policies adopted in the United Kingdom and China, where conducting research for reproductive purposes is permitted and potential clinical applications are not

[1]*Dr. John T. MacDonald Foundation Department of Human Genetics, University of Miami, Miami, FL 33136, USA.* [2]*Centre of Genomics and Policy, Department of Human Genetics, Faculty of Medicine, McGill University, Montreal, Quebec H3A 1A4, Canada.* **Corresponding author. E-mail: rosario.isasi@icloud.com*

Published by AAAS

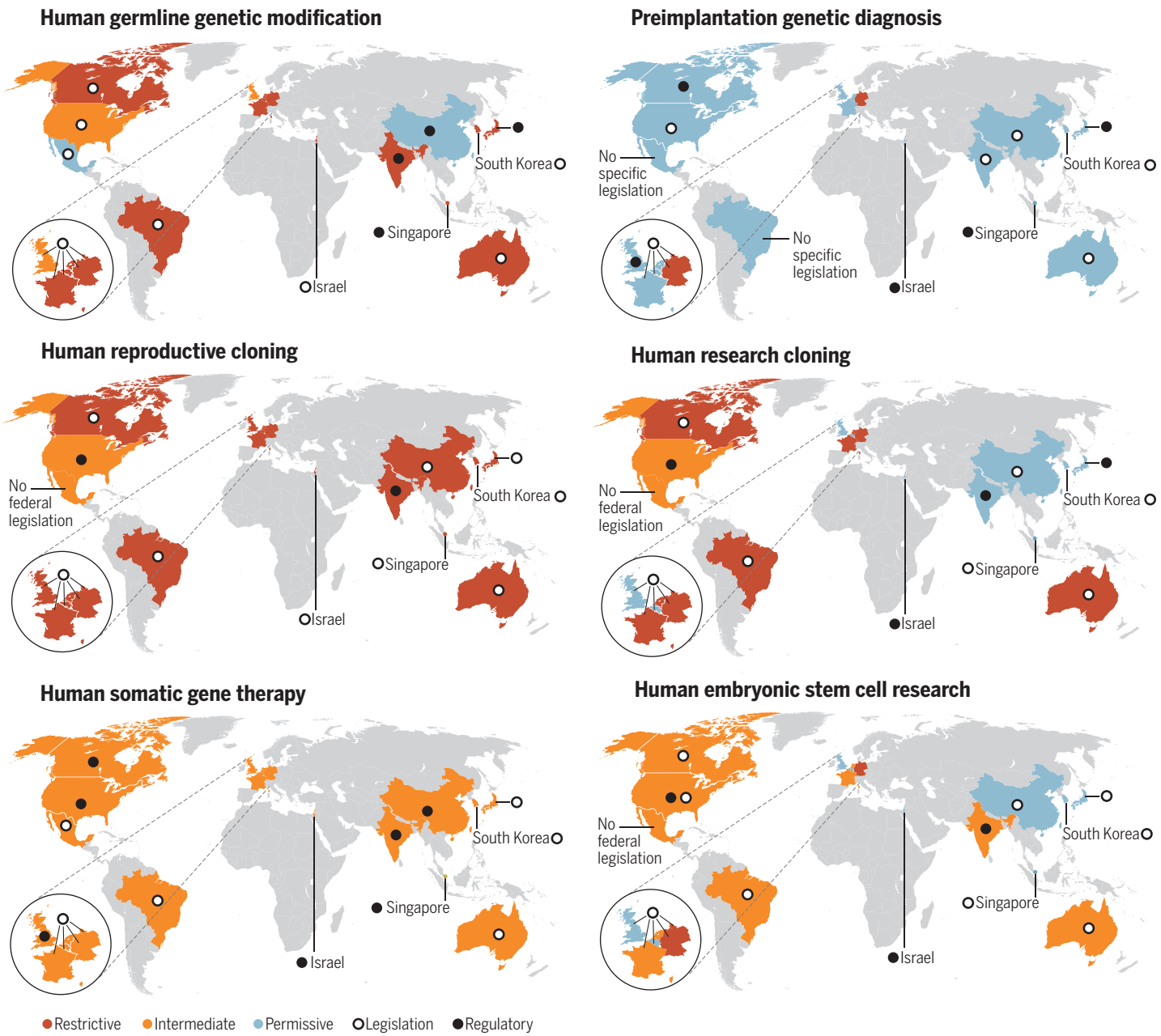

Representative country policies toward genome-related technologies. The sources for all the information shown are listed in the supplementary materials.

explicitly outlawed. Given that governance depends on different approvals or licensing agencies deciding on a case-by-case basis, there is a risk of arbitrary applications or inconsistencies. In addition, when governed by guidelines or professional codes alone, without effective enforcement mechanisms, the risk is to end up (or to be perceived) as self-serving and as following a consumer model (e.g., Mexico, or state–level regulations found in the United States) (*7*).

OVERARCHING ISSUES. One problem that can be seen in all of the approaches described is vagueness in distinctions between clinical and research applications, as well as in basic definitions. There is considerable uncertainty over whether already existing bans on genome editing in embryos and germ cells for clinical purposes (e.g. to induce a pregnancy) also encompass a prohibition to conduct research, including reproductive research (such uncertainties can be found in the laws of China, France, Israel, Netherlands, South Korea, and United Kingdom). Israeli legislation forbids "using reproductive cells that have undergone a permanent intentional genetic modification (germline gene therapy) in order to cause the creation of a person" (*9*) although a license may still be obtained "for certain types of genetic intervention" provided that "human dignity will not be prejudiced" (*9*). In the United Kingdom "altering the genetic structure of any cells while it forms part of an embryo" (*10*) is banned unless licensed.

In the majority of cases, we have analyzed, vague or narrow terminology has inadvertently created barriers or ambiguities that may allow for interpretations or practices to circumvent or hinder the intent of the policy, without violating its literal interpretation. For example, legislation adopted in Belgium prohibits carrying out "research or treatments of eugenic nature that is to say, focused on the selection or amplification of non-pathological genetic characteristics of

ILLUSTRATION: P. HUEY/*SCIENCE*

Published by AAAS

the human species" (*11*). In turn, French law creates a new category of criminal offense, typified as "crimes against the human species" (*12, 13*). To that end, it states that "no person may undermine the integrity of the human species" and bars "carrying out a eugenic practice aimed at organizing the selection of persons" (*12, 13*). However, no further guidance is provided as to what constitutes a eugenic practice or what should be the spectrum of permissibility (if any) with regards to the selection of human traits.

Terminological debates on what constitutes a "human embryo" or a "reproductive cell" are ongoing in many countries (*8*). As a result, in some jurisdictions a human embryo is an entity determined by a particular point in time (e.g., Australia, Canada, Singapore) or, established by its capacity to develop into an individual or a human being (e.g., Belgium, Japan, Germany, Netherlands). Similar scenarios are present with respect to what constitutes a germ line. We believe that scientific understanding and precision in legal definitions of what constitutes a human embryo and/or its germ line are essential to developing coherent policies.

SETTING THRESHOLDS. The recent spate of policy activity by professional organizations, funding and regulatory agencies appears to be converging on an intention to "advance cautiously." What this entails has yet to be clearly articulated. For some, caution means maintaining a vigilant attitude while evidence mounts for the benefits and risks of the technology together with their social implications. For others, caution entails adopting tiered approaches, for example, by temporary, self-regulatory moratoria or funding restrictions (*14–16*). What remains elusive is the determination of thresholds for acceptability (*17, 18*).

Preimplantation genetic diagnosis (PGD) was first regarded as highly controversial (*19*) and now is mainly governed within the general biomedical research context. Many countries allow genetic testing in preimplantation embryos subject to governance and according to substantive, medically determined requirements [see figure and (*19*)]. The development and evolution of PGD policies, together with their medical and social uptake, may provide a suitable model for defining research and, eventually, clinical reproductive applications of genome editing.

Medical determinations for PGD have most commonly depended on the "gravity" of the genetic condition (i.e., "serious" or "severe") or whether the condition is "untreatable." This gravity threshold was adopted in Mexican legislation in the context of criminalizing genetic manipulation. Under the Penal Code of the Federal District of Mexico, human genetic manipulation is prohibited when its purpose is other than "the elimination or reduction of serious diseases or defects" (*20*). Similarly, the Singaporean Bioethics Advisory Committee in 2015 reiterated "that the clinical practice of germline modification be prohibited, pending scientific evidence that techniques to prevent or eliminate serious genetic disorders have been proven effective" (*21*).

Some countries (e.g., United Kingdom, Canada, Australia, Israel, Netherlands, and Japan) (*19*, *22*) have added a "substantial risk" of occurence qualifier to the determination of gravity for PGD, which imposes another filter affecting acceptability. The degree or probability of risk has not been further defined in any jurisdiction. Even more controversial is the requirement of allowing PGD only to prevent the risk of transmission of "untreatable" and "incurable" diseases to descendants. These concepts remain vaguely articulated in both professional guidelines and in national legislation.

The Hinxton Group has proposed a self-regulatory approach that indirectly applies this PGD model to genome editing. The group, without endorsing any particular intervention, or particular policy model, maintains that a plausible spectrum of permissibility might range from correction of serious, early-onset or late-onset disease-causing mutations (e.g., Tay-Sachs, cystic fibrosis, or Huntington's disease), through the introduction of known disease-preventing changes (e.g., against HIV infection), to non-medical enhancements (e.g., increased muscle mass) (*23*).

In a recent statement, the International Summit on Gene Editing noted a proposed array of applications for germline editing in clinical research and therapy. They ranged from the avoidance of severe inherited diseases to "enhancement" of human capabilities. The statement concluded that it would "be irresponsible to proceed with any clinical use of germline editing unless and until (i) the relevant safety and efficacy issues have been resolved…and (ii) there is broad societal consensus about the appropriateness of the proposed application." Ongoing appraisal of scientific advances and societal views was also recommended (*16*).

We maintain that the thresholds the PGD model delineates for medical determinations and substantial risk of occurrence (albeit still relatively flawed and contentious) represent a robust approach to regulation. However, precision in language and understanding will also be necessary in order to move forward in this context.

Many questions still remain to be addressed. Are there defensible uses for genome editing so as to select, or deselect, certain human traits? Will conferring immunity against disease or the reparation of a deleterious gene be considered enhancement? Are there any thresholds for nonmedical interventions?

Public acceptance may change as the benefits of genome editing emerge for disease prevention. Eventually, as we move from research to the clinic, the collective sum of individual decisions could constitute a de facto policy. However, we believe that the task of adopting policy guidance for the acceptability (if at all) of germline interventions is more than just editing policy to fit individual genomes or circumstances. ■

REFERENCES AND NOTES

1. J. S. LaFountaine, K. Fathe, H. D. Smyth, *Int. J. Pharm.* **494**, 180 (2015).
2. J. A. Doudna, E. Charpentier, *Science* **346**, 1258096 (2014).
3. D. Cressey, A. Abott, H. Ledford, *Nature*. 10.1038/nature.2015.18394.
4. Regulation No. 536/2014 of the European Parliament and the Council of 16 April 2014 on clinical trials on medicinal products for human use, and repealing Directive 2001/20/EC… (2014).
5. Australia, Prohibition of Human Cloning for Reproduction and the Regulation of Human Embryo Research Amendment Act, Act no. 172 (2006).
6. Australia, Prohibition of Human Cloning for Reproduction Act 2002 (last amended by Act no. 144), (2008).
7. R. M. Isasi, B. M. Knoppers, *Hum. Reprod.* **21**, 2474 (2006).
8. R. M. Isasi, B. M. Knoppers, *Eur. J. Health Law* **13**, 9 (2006).
9. Israel, Prohibition of Genetic Intervention (Human Cloning and Genetic Manipulation of Reproductive Cells) Law (1999) (last renewed), (2009).
10. United Kingdom, Human Fertilisation Act (1990) (last amended), (2008).
11. Belgium, Act on Research on Embryos in Vitro–Loi du 11 Mai Relative a la Recherché sur les Embryons in Vitro (2003).
12. France, Bioethics Law/Loi No. 2004-800 du 6 août 2004 relative à la bioéthique (last amended), (2009).
13. France, Code Civil (1804) re the Bioethics Law (last amended), (2015).
14. D. Baltimore *et al*., *Science* **348**, 36 (2015).
15. E. Lanphier, F. Urnov, S. E. Haecker, M. Werner, J. Smolenski, *Nature* **519**, 410 (2015).
16. Organizing Committee for the International Summit on Human Gene Editing, International Summit Statement, 1 to 3 December 2015, Washington, DC (National Academies, Washington, DC, 2015) http://www8.nationalacademies.org/onpinews/newsitem.aspx?RecordID=12032015a.
17. A. L. Caplan, B. Parent, M. Shen, C. Plunkett, *EMBO Rep.* **16**, 1421 (2015).
18. J. Sugarman, *EMBO Rep.* **16**, 879 (2015).
19. B. M. Knoppers, R. M. Isasi, *Hum. Reprod.* **19**, 2695 (2004).
20. Penal Code of the Federal District of Mexico (Mexico DF) (2002) (last amended), (2014).
21. Bioethics Advisory Committee of Singapore, Ethics Guidelines for Human Biomedical Research (Singapore, 2015).
22. B. M. Knoppers, S. Bordet, R. M. Isasi, *Annu. Rev. Genomics Hum. Genet.* **7**, 201 (2006).
23. The Hinxton Group, Statement on Genome Editing Technologies and Human Germline Modification (2015); www.hinxtongroup.org/hinxton2015_statement.pdf.

ACKNOWLEDGMENTS

Partially supported by the EUCelLEX EU-FP7 Program, Grant Agreement No. 601806 and the Canada Research Chair in Law and Medicine, McGill University. We thank S. L. Züchner for comments and suggestions. The opinions expressed above are those of the authors alone.

SUPPLEMENTARY MATERIALS

www.sciencemag.org/content/351/6271/337/suppl/DC1

10.1126/science.aad6778

Published by AAAS

APPLIED OPTICS

How Cherenkov radiative losses can improve optical frequency combs

Broader optical frequency combs on a photonic chip can help refine time standards

By **N. Akhmediev** *and* **N. Devine**

The idea of a frequency comb seems relatively simple, yet substantial technical efforts are required for one to be generated with the high accuracy and stability needed for metrology applications. The ideal frequency comb would be a set of discrete equidistant frequency (f) components separated by intervals Δf. Typically Δf is in the microwave range so that the separation of the comb "teeth" can be measured and controlled electronically. However, stabilization of Δf is not sufficient for applications; having a nearly octave-wide comb is necessary for "self-referencing" the comb (*1*, *2*). On page 357 of this issue, Brasch *et al.* (*3*) show how to create a wideband comb spectrum to help realize this goal.

For absolute measurements of optical frequency, the position of each element of the comb must be fixed (*1*, *2*), which can be done by using nonlinear optics to relate any two distant components of the comb. The simplest route to synchronization is the generation of an optical second harmonic $2f_0$ matched with one of the higher-frequency teeth of the comb, while the fundamental frequency f_0 is synchronized to another lower frequency (see the figure, panel A). However, this technique requires the width of the comb to be at least one octave (the comb shown in red has insufficient width). Other nonlinear optical effects may allow this range to be smaller (*4*).

A frequency comb can be based on pulses circulating in an optical cavity, such as an optical fiber loop coupled to an output fiber that extracts a small part of the pulse energy at each round trip to form a train of equidistant identical pulses (panel D of the figure shows the 100-μm ring resonator fabricated by Brasch *et al.* on a silicon substrate). The energy loss at the coupler must be compensated by an external pump. The latter is provided either by an amplification of the pulse within the loop (for example, as in a passively mode-locked laser) or by a continuous wave (CW) at fixed frequency that may enter the loop through the same coupler forming a parametric oscillator.

Optical solitons, predicted by Hasegawa and Tappert (*5*), are pulses of electromagnetic radiation that keep constant shape through the balance between nonlinearity and dispersion, and were observed experimentally in a fiber by Mollenauer *et al.* (*6*). Kerr nonlinearity (changing the refractive index of the medium with an applied electric field) converts the pulse circulating within the cavity into a soliton with the duration much shorter than the period of circulation. The frequency of circulation is the same as Δf, whereas the duration of the pulse is inversely proportional to the width of the generated spectrum (red comb in panel B of the figure). The spectrum usually contains thousands of discrete components that are not shown explicitly in the figure.

In recent years, frequency comb devices have become substantially smaller as they have moved from optical tables to being fabricated on a chip (*7*), potentially being integrated with pumping lasers. Stability of the soliton in the loop is crucial for the accuracy of the frequency comb. In a lossless medium such as an optical fiber, solitons can propagate for kilometers without changing their shape, but dissipative solitons circulating in a loop require a continuous energy supply from the pump. Energy gained by the pulse in each round trip is dissipated through the coupler to balance consumption and disposal and fixes the amplitude and shape of the soliton (*8*).

The use of dissipative solitons in microresonators substantially improves the characteristics of the frequency comb (*9*, *10*). Brasch *et al.* now show how

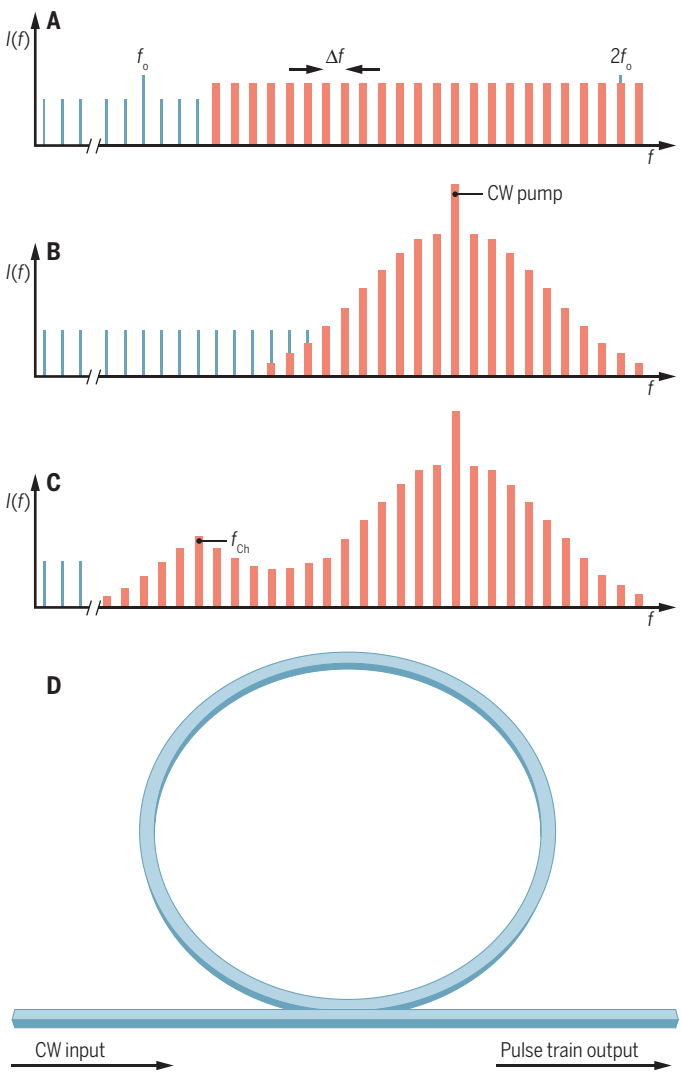

Creating a wider comb. (**A**) An "ideal" rectangular frequency comb where $I(f)$ is intensity of spectral components. (**B**) A bell-shaped finite-width frequency comb resulting from the dissipative soliton circulation in the ring. (**C**) Fully coherent frequency comb extended by using Cherenkov radiation. (**D**) Schematic of the microring Kerr resonator.

ILLUSTRATION: P. HUEY/*SCIENCE*

Optical Sciences Group, Research School of Physics and Engineering, Australian National University, Canberra, ACT 2600, Australia. E-mail: nail.akhmediev@anu.edu.au

Published by AAAS

losses in the form of Cherenkov radiation, initially thought to be destructive for solitons, can extend the frequency range of the comb. Such radiation is emitted in presence of the third-order dispersion in their specially engineered microring. The frequency of Cherenkov radiation f_{Ch} is defined by the total dispersion (*11*) and can be placed at a distance from the central frequency of the soliton (see the figure, panel C). Losses are usually detrimental for the accuracy of oscillations, including those in atomic clocks. The coherence of Cherenkov radiation with the primary optical field was also found in the so-called Fermi-Pasta-Ulam recurrence effect in optical fibers (*12*). In fact, the losses caused by the third-order dispersion can be either reversible or irreversible (*12*).

The microring resonator engineered by Brasch *et al.* allows the radiation to remain coherent with the frequency comb and extends it considerably at the red side of the spectrum. Radiation circulation in the ring adds comb components around it, and all of the comb components are indeed coherent, so that the total spectrum is wider than the one produced solely by the soliton. Remarkably, the duration of the soliton in this device is nearly a record low—only six optical cycles—which makes the comb spectrum sufficiently wide already. Using the Cherenkov radiation allowed Brasch *et al.* to reach the two-thirds of an octave that is fully coherent and self-referenced. The spectrum from 150 to 225 THz obtained is an exceptional technical achievement. The relative accuracy reached in this device is a stunning 3×10^{-15}.

Frequency combs have a myriad of applications (*13*). Frequency standards, matching optical and radio frequencies, measurements of fundamental constants, modern astronomy, and digital telecommunications rely on these devices. They are used for synchronization of atomic clocks, providing us with accurate time standards. High-precision spectroscopy and precise GPS technology are two other applications that we cannot live without today. Intensive research efforts will bring us chip-based frequency comb devices for uses beyond the laboratory environment. ■

REFERENCES

1. S. T. Cundiff, J. Ye, *Rev. Mod. Phys.* **75**, 325 (2003).
2. D. J. Jones *et al.*, *Science* **288**, 635 (2000).
3. V. Brasch *et al.*, *Science* **351**, 357 (2016).
4. H. R. Telle *et al.*, *Appl. Phys. B* **69**, 327 (1999).
5. A. Hasegawa, F. Tappert, *Appl. Phys. Lett.* **23**, 142 (1973).
6. L. F. Mollenauer *et al.*, *Phys. Rev. Lett.* **45**, 1095 (1980).
7. J. S. Levy *et al.*, *Nat. Photon.* **4**, 37 (2010).
8. P. Grelu, N. Akhmediev, *Nat. Photon.* **6**, 84 (2012).
9. T. Herr *et al.*, *Phys. Rev. Lett.* **113**, 123901 (2014).
10. T. Herr *et al.*, *Nat. Photon.* **8**, 145 (2014).
11. N. Akhmediev, M. Karlsson, *Phys. Rev. A* **51**, 2602 (1995).
12. A. Mussot *et al.*, *Phys. Rev. X* **4**, 011054 (2014).
13. N. R. Newbury, *Nat. Photon.* **5**, 186 (2011).

10.1126/science.aad8694

NEURODEVELOPMENT

Oligodendrocytes follow blood vessel trails in the brain

Brain microvasculature is a scaffold for neuroglial migration

By **Elisabetta Dejana**[1,2,3] *and* **Christer Betsholtz**[1,4]

The mammalian brain is probably the most complex organ generated by evolution so far. It is composed of more distinct cell types than any other organ (*1*), including those that protrude myriads of processes to make the connections that define brain function. Brain development requires that differentiated cells become dispersed and positioned correctly, which demands that progenitor cells migrate—often over very long distances—from sites of origin in the early neural tube to final sites of differentiation in the multilayered brain tissue. Oligodendrocytes, the cells that myelinate axons, are perhaps the most migratory of all the brain's cell types, but their paths have remained ill defined (*2*). On page 379 of this issue, Tsai *et al.* (*3*) report that oligodendrocyte precursor cells (OPCs) migrate along blood vessels, and define a signaling pathway involved in the process. The findings are exciting not only for their pathological implications, but because they add to the emerging picture that blood vessels do much more than provide oxygen and nutrients to the developing or regenerating tissue—a concept sometimes referred to as angiocrine signaling (*4*, *5*).

OPCs originate in the ventral ventricular zone of the mammalian embryonic spinal cord and of the forebrain, and migrate over relatively large distances to reach their specific target areas and to complete their maturation (*6*). The motility of these precursors is regulated by intrinsic and extracellular factors. Tsai *et al.* observed in embryonic mice that OPCs establish an intimate interaction with the brain's microvasculature. Using a live-imaging technique, the authors noticed that OPCs appear to crawl along the vessels and, occasionally, jump from one vessel to another. The authors also show that coverage of the vessels with pericytes (cells that wrap around the endothelial cells of blood vessels) is irrelevant for OPC migration, whereas destruction of the basic endothelial architecture of the vascular system [through inactivating G protein–coupled receptor 124 (Gpr124) (*7*, *8*)] prevented OPCs from exiting their zone of origin. Gpr124 is required for neovascularization of the central nervous system. It is also a coactivator for signaling triggered by the secreted protein Wnt in developing and mature vascular endothelial cells. Tsai *et al.* propose that the molecular mechanism underlying OPC attraction to the brain vasculature involves the observed increase in expression of chemokine (C-X-C motif) receptor 4 (Cxcr4) by the OPCs through autocrine canonical Wnt signaling, and by the interaction of Cxcr4 with its ligand, stromal-derived factor 1 (Sdf-1), which is produced by endothelial cells. Importantly, strict interaction with the vessels maintains the undifferentiated state of OPCs during migration. Upon arrival at specific targets, OPCs detach from the vasculature and undergo full maturation (see the figure).

[1]*Department of Immunology, Genetics and Pathology, Rudbeck Laboratory, Uppsala University, Uppsala, Sweden.* [2]*FIRC Institute of Molecular Oncology, Milan, Italy.* [3]*Department of Oncology and Hemato-Oncology, Milan University, Milan, Italy.* [4]*Department of Medical Biochemistry and Biophysics, Karolinska Institutet, Stockholm, Sweden. E-mail: elisabetta.dejana@igp.uu.se; christer.betsholtz@igp.uu.se*

> ***"...blood vessels do much more than provide oxygen and nutrients to...tissue..."***

Several aspects of the study by Tsai *et al.* need further investigation—for instance, the role of the vasculature, which may be more complex than simply acting as a trail for OPC migration. Vascular cells, and in particular the endothelium, produce several growth and differentiation factors that likely create a favorable niche for OPC migration and maturation. The niche is impaired when the vessels are altered, such as in absence of Gpr124, and may act independently of a direct physical interaction of OPCs with the vessels.

Another important consideration is that endothelial cells present a different and highly specialized functional behavior in different types of vessels. This is particularly true for the brain vasculature, which can vary in many aspects in different regions of the brain (*9*). The type of interaction of OPCs with the vascular cells may therefore depend on the adhesive membrane proteins expressed by endothelial cells, local extracellular matrix proteins, or on biologically active factors

Published by AAAS

produced by the endothelium. It is unclear why the OPCs detach from the vessels in particular locations and start to differentiate. It will be interesting to learn if blood vessel factors or properties play an active role also in oligodendrocyte differentiation through, for example, changes in adhesive properties or the expression of specific differentiation-promoting or -inhibiting factors. Similarly, local differences in the vasculature may explain the phenomenon of OPC jumping from one vessel to another. This could be due to a set of adhesive proteins or chemotactic agents differentially expressed by the vessels.

OPCs themselves may also modify the behavior of the vasculature by modulating angiogenesis and, importantly, differentiation of the blood-brain barrier. OPCs produce high amounts of Wnt7a and Wnt7b, which are major inducers of the barrier properties of the brain microcirculation (*10*). Although direct evidence is missing, it is conceivable that OPCs may contribute substantially to the full differentiation of the brain vasculature.

At a more general level, the study of Tsai *et al.* introduces a novel paradigm—the role of the vasculature in guiding migratory neuroglial cells to their target area. Understanding the molecular basis of this interaction and its functional importance requires further work, but it is tempting to extend this observation to other cell types. For instance, some of the physiological mechanisms of cell-to-cell interaction described by Tsai *et al.* may be present during the dissemination of glioblastoma cells in the brain. These tumor cells resemble OPCs by marker expression and by their propensity to migrate over long distances, essentially eliminating any prospects for radical surgery (*11*). Interestingly, recent work suggests that glioblastoma cells migrate along blood vessels and disrupt the blood-brain barrier en route (*12*).

Are the observations of Tsai *et al.* relevant in demyelination pathology? Although OPC migratory activity is inhibited at maturation, these precursor cells reacquire this property after pathological demyelination in the adult. This process plays a crucial role in inhibiting the onset and progression of diseases such as multiple sclerosis. It is therefore conceivable that any condition that affects OPC migration, such as local alteration or dismantling of the vasculature, may also strongly impair the capacity of the organism to repair neural injuries. ■

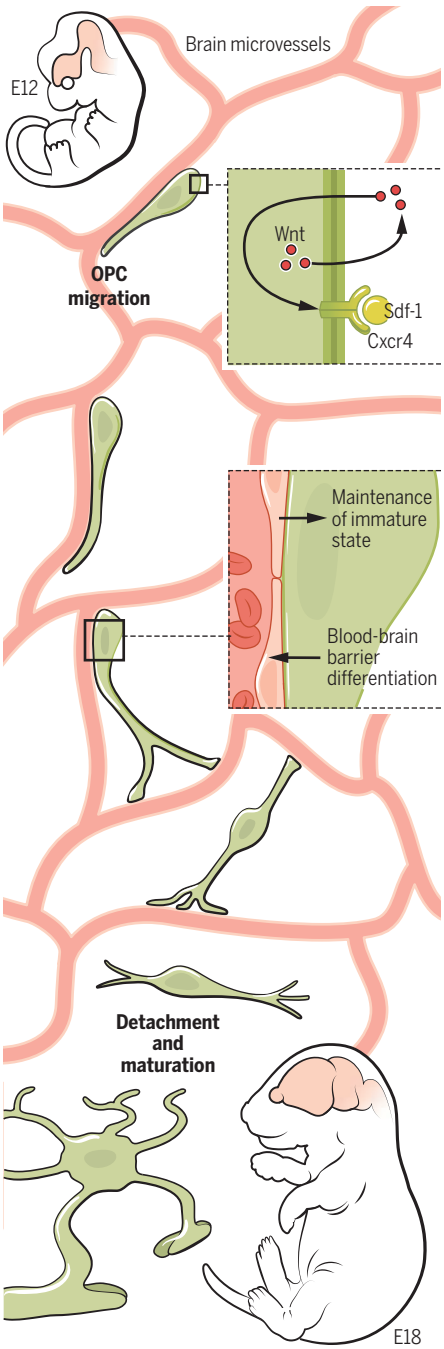

Vascular guidance. OPCs migrate along brain microvessels to reach specific target areas. Migration is directed by increased Wnt-induced expression of the receptor Cxcr4, which binds to the chemokine Sdf-1 (embryonic mouse shown). Cross talk between endothelial cells and OPCs may influence their reciprocal functions. At arrival, OPCs detach from blood vessels and mature.

REFERENCES AND NOTES

1. A. Zeisel *et al.*, *Science* **347**, 1138 (2015).
2. U. Funfschilling *et al.*, *Nature* **485**, 517 (2012).
3. H.-H. Tsai *et al.*, *Science* **351**, 379 (2016).
4. E. Lammert *et al.*, *Science* **294**, 564 (2008).
5. G. Nikolova *et al.*, *Dev. Cell* **10**, 397 (2006).
6. N. Kessaris *et al.*, *Nat. Neurosci.* **9**, 173 (2006).
7. F. Kuhnert *et al.*, *Science* **330**, 985 (2010).
8. B. Vanhollebeke *et al.*, *eLife* **8**, 4 (2015).
9. Y. Zhou *et al.*, *J. Clin. Invest.* **124**, 3825 (2014).
10. J. M. Stenman *et al.*, *Science* **322**, 1247 (2008).
11. G. P. Dunn *et al.*, *Genes Dev.* **26**, 756 (2012).
12. S. Watkins *et al.*, *Nat. Commun.* **5**, 4196 (2014).

ACKNOWLEDGMENTS

E.D. and C.B. are supported by the European Research Council (268870, 294556), the Swedish Science Council, and Wallenberg Foundation. E.D. is supported by the Italian Association for Cancer Research and Telethon Foundation (GGP14149). C.B. is supported by the Leducq Foundation and Swedish Cancer Foundation.

10.1126/science.aaf1139

MICROBIOLOGY

The do-it-all nitrifier

The discovery of bacteria that can oxidize both ammonia and nitrite upends a long-held dogma

By **Alyson E. Santoro**

With numerous amendments to the microbial nitrogen cycle over the past two decades, it seems at times that nothing is certain. Yet one aspect of the nitrogen cycle seemed clear: that the labor of nitrification—the oxidation of ammonia (NH_3) to nitrite (NO_2^-) and ultimately nitrate (NO_3^-)—is divided between two separate groups of microorganisms. Sergei Winogradsky first showed this in the late 1800s when he isolated the organisms responsible for the two steps of nitrification, ammonia oxidizers and nitrite oxidizers. But a series of recent papers upends this 100-year-old dogma with the description of three different cultivated bacteria (*1*, *2*) and an uncultivated bacterium (*3*) that can each carry out the complete oxidation of ammonia to nitrate.

We should know by now that if a reaction is thermodynamically possible, microbes will find a way. A complete nitrifier should gain more energy per mole of substrate (*1*), but may grow at a slower rate, than organisms carrying out the individual steps of the pathway. Ten years ago, Costa *et al.* (*4*) modeled the trade-off between growth rate (favored by short metabolic pathways) and growth yield (favored by longer pathways). They found that this trade-off should favor the existence of a complete nitrifier when microbes grow slowly in clonal colonies. Such conditions are found in the biofilms that cover many natural and engineered surfaces.

It is perhaps no surprise, then, that the complete ammonia oxidizers, or comammox bacteria, come from biofilms in an aquaculture treatment system (*1*), a deep subsurface pipe (*2*), and a bioactive filter at a drinking water treatment plant (*3*). In all cases, the comammox bacteria belong to the genus *Nitrospira*, members of which were until recently believed to rely on nitrite for growth.

Horn Point Laboratory, University of Maryland Center for Environmental Science, Cambridge, MD 21613, USA. E-mail: asantoro@umces.edu

ILLUSTRATION: K. SUTLIFF/*SCIENCE*

Published by AAAS

In one of the studies, van Kessel *et al.* (*1*) enriched two *Nitrospira* bacteria using a bioreactor fed with a steady stream of low concentrations of ammonium. The resulting consortium contained the anammox (anaerobic ammonium-oxidizing) bacteria *Brocadia* as well as two newly discovered *Nitrospira* bacteria, provisionally named "*Candidatus* N. nitrosa" and "*Ca.* N. nitrificans."

The genomes of the two *Nitrospira* species contain the genes necessary for ammonia oxidation, including ammonia monooxygenase (*amo*) and hydroxylamine oxidoreductase (*hao*), and for nitrite oxidation, including the molybdoprotein nitrite oxidoreductase (*nxr*). Careful stable-isotope and radioisotope incubations confirmed ammonia oxidation and carbon fixation. Using the newfound *amo* sequences to probe public databases, the researchers discovered an entire clade of putative comammox *amo* sequences previously identified as particulate methane monooxygenase (*pmo*). These findings suggest that the newly discovered bacteria were previously detected in the environment but had been mistakenly identified as methane-oxidizing bacteria.

Similarly, Daims *et al.* (*2*) enriched a thermophilic comammox bacterium, "*Ca.* Nitrospira inopinata," in coculture with a proteobacterium. The authors sequenced the complete genome of *Ca.* N. inopinata and combined this analysis with proteomics to show that both ammonia- and nitrite-oxidizing enzymes are abundant during growth. They further explored whether ammonia-oxidizing capability was lost by extant *Nitrospira* species that are capable of nitrite oxidation only, or whether the newly discovered comammox *Nitrospira* acquired ammonia-oxidizing capability through lateral gene transfer. Nucleotide usage in the *amo* gene sequences is different from the rest of the genome, suggesting acquisition of the *amo* genes through a recent lateral gene transfer event.

The newly cultivated comammox bacteria provide support for comammox potential in uncultivated bacteria, such as the *Nitrospira* genome assembled by Pinto *et al.* (*3*). As with its cultivated counterparts, this genome contains genes for the transport and degradation of urea, potentially providing an additional source of ammonia for energy and biosynthesis.

These discoveries contribute to a growing appreciation that nitrifiers are more than we believed them to be (see the figure). Historically characterized as reliant on ammonia or nitrite for energy and inorganic carbon fixation, both ammonia oxidizers and nitrite oxidizers have been proven by recent research to be much more metabolically versatile. Select nitrite oxidizers, such as *Nitrobacter*, can use acetate or pyruvate for growth in the absence of nitrite. Ammonia-oxidizing thaumarchaea not only transport organic carbon sources (*5*) but may even require these sources (*6*). Thaumarchaea may also use cyanate (*7*) as a source of ammonia to fuel growth. Nitrite-oxidizing *Nitrospira* may degrade urea or cyanate to feed ammonia oxidizers, which in turn feed the *Nitrospira* with nitrite (*7*, *8*). Perhaps the most surprising recent finding is that some *Nitrospira* grow not as nitrite oxidizers but as aerobic hydrogen oxidizers (*9*). The implication is that the carbon and nitrogen cycles are entwined in complex ways.

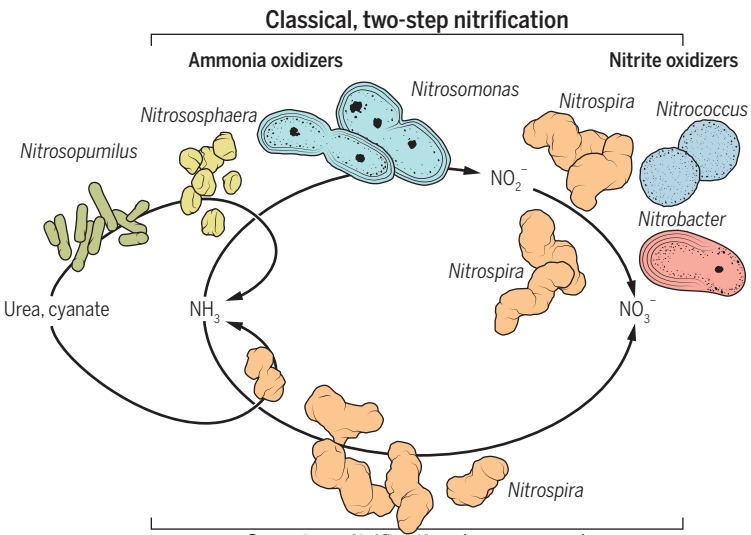

Metabolic diversity of nitrifiers. Nitrification has long been held to be a two-step process divided between two groups of organisms, some representatives of which are shown. Recent studies (*1*–*3*) have uncovered nitrifiers that are capable of complete nitrification, as well as novel substrates for the generation of ammonium.

The approach used to uncover these complete nitrifiers highlights an elegant combination of an old strategy—enrichment of microbial consortia—with the latest bioinformatic techniques for reconstructing complete genomes from uncultivated organisms. This strategy enables researchers to mimic conditions in the environment, where both substrates and products are kept at low concentrations by other members of the consortium. It thus allows for the cultivation of novel organisms that may be missed when high concentrations of substrate are provided (*10*). Comammox *Nitrospira*, like other recently described nitrite oxidizers (*11*), require ammonium for biosynthesis, meaning that they would have been missed by typical strategies enriching for nitrite oxidizers using nitrite as the sole nitrogen source. Comammox bacteria and nitrite oxidizers may actually compete with ammonia oxidizers (their previously assumed partners) for ammonium, highlighting a potentially underappreciated role for competition in the nitrogen cycle (*12*).

How does the discovery of comammox change our perception of the global nitrogen cycle? Conventional methods of measuring nitrification rates in the environment likely capture the activity of these organisms, and nitrification is already treated as a one-step process in many global biogeochemical models. It is uncertain, however, whether existing measurement methods capture direct nitrification from the organic nitrogen pool. Nitrification is a major source of nitric oxide (NO) and the greenhouse gas nitrous oxide (N_2O) to the atmosphere; it remains to be shown whether comammox organisms make either of these compounds, and if so, under what conditions. Irrespective of their quantitative importance, the discovery of comammox emphasizes that our perception of nitrification (and of many other biogeochemical processes) is based on physiological characterization of a small fraction of extant microbial diversity. ■

REFERENCES AND NOTES

1. M. A. H. J. van Kessel *et al.*, *Nature* 10.1038/nature16459 (2015).
2. H. Daims *et al.*, *Nature* 10.1038/nature16461 (2015).
3. A. J. Pinto *et al.*, *mSphere* 10.1128/mSphere.00054-15 (2015).
4. E. Costa, J. Perez, J. U. Kreft, *Trends Microbiol.* **14**, 213 (2006).
5. M. Li *et al.*, *Nat. Commun.* **6**, 8933 (2015).
6. W. Qin *et al.*, *Proc. Natl. Acad. Sci. U.S.A.* **111**, 12504 (2014).
7. M. Palatinszky *et al.*, *Nature* **524**, 105 (2015)
8. H. Koch *et al.*, *Proc. Natl. Acad. Sci. U.S.A.* **112**, 11371 (2015).
9. H. Koch *et al.*, *Science* **345**, 1052 (2014).
10. A. E. Santoro *et al.*, *Proc. Natl. Acad. Sci. U.S.A.* **112**, 1173 (2015).
11. D. Y. Sorokin *et al.*, *ISME J.* **6**, 2245 (2012).
12. J. L. Penn, T. S. Weber, C. A. Deutsch, American Geophysical Union Fall Meeting, San Francisco, 15 to 19 December 2014, abstract B33I-08; http://adsabs.harvard.edu/abs/2014AGUFM.B33I..08P.

ACKNOWLEDGMENTS

W. Haskell provided feedback on the figure. C. Deutsch provided early access to modeling results. A.E.S. is an associate fellow in the Integrated Microbial Biodiversity program of the Canadian Institute for Advanced Research and is partially supported by United States National Science Foundation award OCE-1260006.

10.1126/science.aad9671

ILLUSTRATION: P. HUEY/*SCIENCE*

Published by AAAS

EDUCATION AND DEVELOPMENT

Knowledge capital, growth, and the East Asian miracle

Access to schools achieves only so much if quality is poor

By **Eric A. Hanushek**[1]* *and* **Ludger Woessmann**[2]

With per-capita gross domestic product (GDP) growing by an average of 4.5% annually since 1960, people in East Asia are about nine times as prosperous as two generations ago. By contrast, the average person in Latin America is only about two and a half times as prosperous. Over the past quarter-century, both theoretical and empirical analyses of possible drivers of the different growth rates seen around the world invariably assign an important role to human capital (*1*–*4*). This has led to development policies focused on increasing enrollment and retention in schools. We argue, however, that too much attention is paid to the time spent in school, and too little is paid to the quality of the schools and the types of skills developed there.

EDUCATION

Differences in school attainment cannot account for the East Asian miracle or the Latin American puzzle. When plotting the marginal effect of years of schooling attained in 1960 (*5, 6*) against annual growth rates between 1960 and 2000 [see the chart, (A)], East Asian countries are systematically above the schooling-growth line, which indicates that they grew faster than expected by their school attainment. Latin American countries, lying below the line, grew slower than expected. [Details of all analyses are in the supplementary materials (SM).]

Empirical analyses of growth have attempted to deal with these and other anomalies by adding geographic, institutional, and cultural factors in addition to school attainment and by taking different approaches to the form and estimation of the models. Nonetheless, skepticism about the validity of such estimates has grown because the impact of various factors has been sensitive to the specification of the model (*7*), because of suspicion of reverse causality, i.e., growth causes more schooling rather than the other way around (*8*), and because other factors, such as culture or institutions, may drive both schooling and growth (*9*).

Our prior analysis (*10*–*12*) emphasizes linkage between growth and the skills of the population measured by cognitive tests and shows that the main questions about empirical growth models are greatly lessened once skills are appropriately measured. Here, we build upon that work to demonstrate how the apparent growth anomalies mentioned above are consistent with this perspective, and we sketch implications for current development policy.

MEASURING SKILLS. Measuring a nation's human capital by school attainment suffers from two major problems: (i) the assumption that the amount of learning associated with each year of schooling is the same across the world; (ii) the assumption that other factors affecting human capital development—families, health, and the like—are either unimportant or uncorrelated with school attainment. On the surface, neither is plausible. On international math and science tests given at around 9th grade, Honduras lags Singapore by some 2.3 standard deviations (*13*), which suggests that the average 9th-grade student in Honduras is more than 6 years behind the aver-

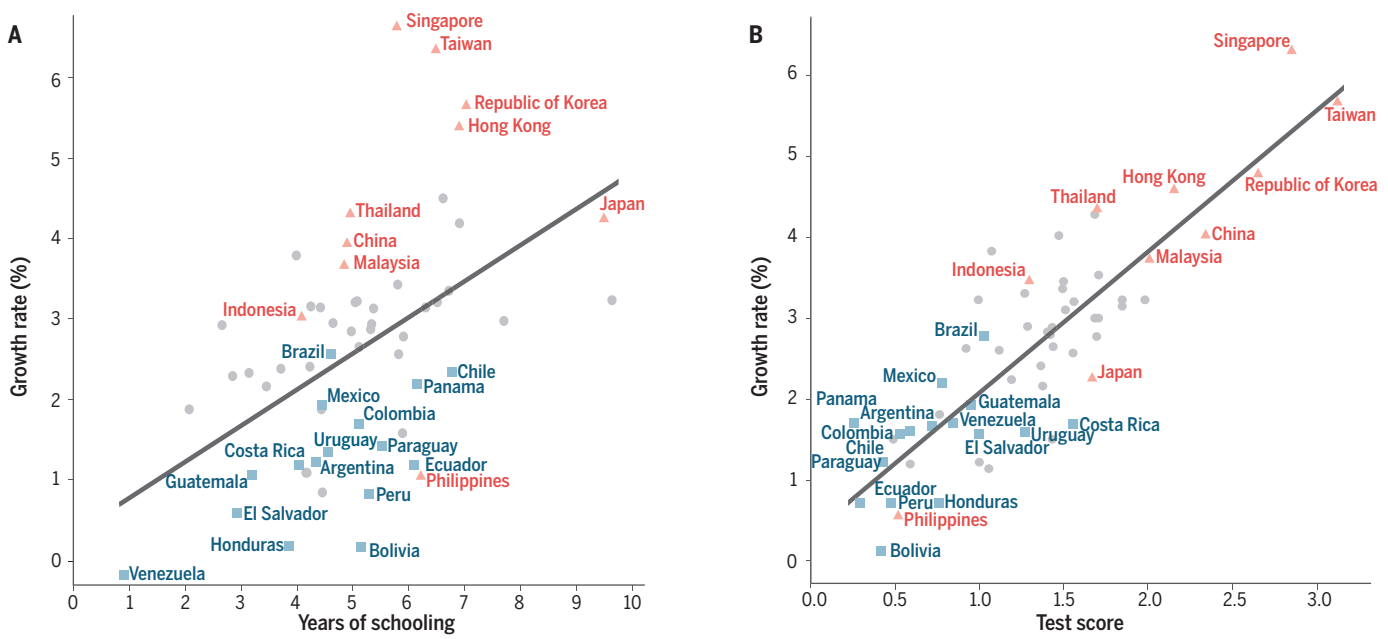

Knowledge capital accounts for apparent growth mysteries in East Asia and Latin America. (**A**) Differences in years of school attainment cannot account for either the strong East Asian growth or the weak Latin American growth. (**B**) Differences in average math and science test scores can account for both phenomena. Both figures refer to the average annual rate of growth of real GDP per capita in 1960–2000, conditional to the initial level of real GDP per capita (both panels, which reflects that countries that start behind can grow faster because it is easier to imitate than to innovate) and to initial years of school attainment (B only). We stop the analysis in 2000 to avoid potential bubbles building up before the 2008 global recession, as well as its aftermath, but results are similar when extended to 2007 or 2009. Each point represents one of the 59 countries for which both economic outcomes over time and international test scores are available. Test score refers to the natural exponential function of the average math and science scores on international tests between 1964 and 2003. Lines are lines of best fit based on a linear regression of the depicted conditional variables. See SM for details. [Source (*14*)]

ILLUSTRATION: N. CARY/*SCIENCE*

Published by AAAS

age 9th-grade student in Singapore.

We combine all available results for each country from international math and science tests taken between 1964 and 2003 (extended with Latin American regional tests) into a single direct measure of human capital [see SM], which, in the aggregate, we call the knowledge capital of a nation. Our work provides an approach for aggregating scores across previously unintegrated tests (*14*). This combines skills developed in schools and also in families, among peers, and through cultures.

The importance of more appropriately measuring skills is seen in the chart (B). The knowledge capital–growth relationship suggests little mystery for East Asia, Latin America, or other regions: Growth rates are accounted for by cognitive skills.

Four things stand out from underlying regressions of GDP growth involving years of schooling and test scores (table S2). (i) Cognitive skills are highly related to growth—in terms of both magnitude and statistical significance. (ii) In the presence of the achievement measure, school attainment has no independent effect on growth. (iii) The growth in East Asia and Latin America and the impact of knowledge capital are no different from that in the rest of the world. (iv) Considering knowledge capital dramatically increases our ability to account for differences in growth. A regression including years of schooling accounts for 25% of the variance in country growth rates, compared with 79% when test scores are included.

Although it is impossible to erase all concerns about causality in empirical growth models, the most commonly raised issues can be plausibly addressed. A detailed analysis of causation can be found in (*14*), but it is useful to summarize the range of tests. Perhaps the most obvious issue is that achievement is measured over the same period as growth. This is motivated by the fact that nations' test outcomes have not changed much over time, with 73% of the variation in test scores reflecting overall country differences as opposed to measurement errors or changes over time (SM). However, it opens the possibility of simple reverse causation. Nevertheless, tests are available since 1964 for 25 countries. If achievement tested before 1985 is related to subsequent growth to 2000 (or 2009), a stronger relation is found for countries with early tests.

Moreover, analyses show that the strong estimated impact of knowledge capital is insensitive to the addition of commonly suggested alternative factors, including geography, institutions, and physical capital; to the specific set of countries; or to the precise time period of study (*14*). Considering merely variations in cognitive skills due to school institutions (such as use of school exit exams or the degree of school choice and competition) shows the same impact on growth as the overall difference in scores and also suggests that school policy matters.

We also investigate labor market performance of immigrants to the United States to rule out the possibility that the knowledge capital–growth relationship reflects a nation's culture or other institutions (*14*). Cognitive skills that immigrants to the United States are estimated to bring from their home country have direct rewards in the U.S. labor market, whereas immigrants from the same countries schooled in the United States are not rewarded according to the knowledge capital of the home country, which suggests independence of any home country institutions or culture. Finally, we find that the observed changes in test scores over time are related to changes in growth rates over time (*14*). These tests with consistent results about the knowledge capital–growth relationship, although not separately conclusive, make a prima facie case that this truly is a causal relationship.

"Gains from providing... universal...basic skills are projected to be six times those of just providing universal access to schools."

REORIENT POLICY. These results have direct implications for policy discussions around the world. Clearly, many factors in addition to schools enter into achievement levels, including parental inputs, health, and preschool programs, but schools offer one important place where public policy can improve the situation.

School-quality issues are clearly important for the United States (*15, 16*), which currently falls 29th in the world in terms of scores on the Programme for International Student Assessment (PISA) mathematics and science tests. But the implications are strongest for developing countries. For more than two decades, there has been a concerted effort to expand access to schooling in developing countries with the United Nations Millennium Development Goals (MDGs) and the Education for All initiative of the United Nations Organization for Education, Science, and Culture, the World Bank, and others. Both efforts called for all children to complete primary schooling beginning in 2015—something not accomplished.

There has been substantial expansion of schooling under the MDGs; e.g., primary school enrollment in sub-Saharan Africa went up from 60% in 2000 to 80% in 2015 (*17*). But without a quality focus, the levels of achievement remained incredibly low (*18*). The MDG experience suggests that going to school without learning has no impact on economic outcomes.

A new set of post-2015 Sustainable Development Goals has recently been established, again focusing on school completion, acknowledging the importance of school quality, but stopping short of quantified quality targets. Lower-income countries (with available test data) generally average only 80% enrollment in lower secondary schools. Projections based on the presented growth model indicate that GDP gains from lifting just the 80% currently enrolled children to basic skill levels are three times the gains from enrolling 100% of children in schools of current quality (*13*). Gains from providing both universal access and basic skills for all are projected to be six times those of just providing access. If there is going to be inclusive economic development across the world, attention must focus on school quality and having all students achieve basic skills. ■

[1]Stanford University, Stanford, CA 94305, USA. [2]Ifo Institute and Ludwig Maximilians University Munich, 80539 Munich, Germany. *Corresponding author. E-mail: hanushek@stanford.edu

REFERENCES AND NOTES

1. R. J. Barro, *Q. J. Econ.* **106**, 407 (1991).
2. P. Romer, *Carnegie-Rochester Conf. Ser. Public Policy* **32**, 251 (1990).
3. D. Acemoglu, *Introduction to Modern Economic Growth* (Princeton Univ. Press, Princeton, NJ, 2009).
4. P. Aghion, P. Howitt, *The Economics of Growth* (MIT Press, Cambridge, MA, 2009).
5. The measure "years of schooling" is constructed from national census data on completion rates of education levels weighted by the typical length of each level for individual countries. [For details, see SM and (*6*).]
6. R. J. Barro, J. W. Lee, *Education Matters: Global Schooling Gains from the 19th to the 21st Century* (Oxford Univ. Press, Oxford, 2015).
7. R. Levine, D. Renelt, *Am. Econ. Rev.* **82**, 942 (1992).
8. M. Bils, P. J. Klenow, *Am. Econ. Rev.* **90**, 1160 (2000).
9. D. Acemoglu, S. Johnson, J. A. Robinson, in *Handbook of Economic Growth*, P. Aghion, S. N. Durlauf, Eds. (North Holland, Amsterdam, 2005), vol. 1A, pp. 385–472.
10. E. A. Hanushek, D. D. Kimko, *Am. Econ. Rev.* **90**, 1184 (2000).
11. E. A. Hanushek, L. Woessmann, *J. Econ. Lit.* **46**, 607 (2008).
12. E. A. Hanushek, L. Woessmann, *J. Econ. Growth* **17**, 267 (2012).
13. E. A. Hanushek, L. Woessmann, *Universal Basic Skills: What Countries Stand to Gain* (Organization for Economic Co-operation and Development, Paris, 2015).
14. E. A. Hanushek, L. Woessmann, *The Knowledge Capital of Nations: Education and the Economics of Growth* (MIT Press, Cambridge, MA, 2015).
15. E. A. Hanushek, P. E. Peterson, L. Woessmann, *Endangering Prosperity: A Global View of the American School* (Brookings Institution Press, Washington, DC, 2013).
16. J. I. Klein, C. Rice, J. Levy, *U.S. Education Reform and National Security* (Council on Foreign Relations, Washington, DC, 2012).
17. United Nations, *The Millennium Development Goals Report 2015* (United Nations, New York, 2015).
18. L. Pritchett, *The Rebirth of Education: Schooling Ain't Learning* (Center for Global Development, Washington, DC, 2013).

SUPPLEMENTARY MATERIALS

www.sciencemag.org/content/351/6271/344/suppl/DC1

10.1126/science.aad7796

Published by AAAS

The enormous *Amorphophallus titanum* emits a fetid stench reminiscent of decaying meat when in bloom.

PLANT SCIENCE

The beauty of botanicals

A naturalist takes a round-the-world romp through the plants that have helped shape human history

By **Helen Anne Curry**

No doubt we all stop on occasion to admire a spectacular plant such as a glamorous rose blushing in a neighbor's garden or a sugar maple ablaze with color in autumn. Perhaps a little less often, we pause to appreciate more common plant denizens, from the trees we use for lumber or shade to the fruits and grains that comprise our daily meals.

Less often still do we stop to do what the eminent British nature writer Richard Mabey exhorts in *The Cabaret of Plants*: to cease thinking of plants simply as pleasurable sights and useful objects and to instead appreciate them as "vital, autonomous beings" that conduct their affairs with little regard for human concerns. Doing so, he argues, will rekindle our collective wonder about these marvelous creatures and their manifold modes of surviving and thriving on an ever-changing planet—and perhaps even help us learn to live among them more benignly.

That reorientation may seem daunting, but Mabey's book serves as a field guide for the novice appreciator of plant autonomy. The 29 chapters teem with examples of plants that have captured the imaginations of human observers, from the rumored half-plant, half-animal "vegetable lamb" of early modern travel narratives; to the colossal Titan arum, whose fetid phallic inflorescence titillated Victorian audiences; to the elusive epiphytic moonflower cactus of the Amazon.

Mabey narrates the lives of these species by drawing on the words and images produced by those who encountered them. He invites the reader to sit alongside Paleolithic cave dwellers and view prehistoric vegetation through their etchings of leafs and twigs. The writings of the Romantics introduce the dancing daffodils that engulfed their senses and graced their poems. Mabey looks to Impressionist painters to capture the inexpressible iridescent animation of an olive grove.

Naturalists and other scientists are perhaps his most common interlocutors. Their efforts to understand plants on their own terms—to ponder the evolutionary turns that resulted in subterranean orchids and bulbous baobab trees, to prod tropical flowers into blooming in inhospitable environments, and to probe the still-mysterious modes of plant communication—provide the backbone of knowledge that should serve not to explain away the apparent ingenuity of plants but instead to heighten our awe of it.

In a few instances, Mabey himself is the observer—and what a treat that is, given Mabey's lifetime of botanical adventures and his elegant, exuberant prose. Even his engagements with plants that disappoint him nonetheless captivate the reader. "What unnerved me was how *dull* I was finding the Great Yew," he writes of seeing the famous Fortingall Yew, which at 2000 to 3000 years old is sometimes proclaimed the oldest tree in Britain. "It had none of the panache and power and narrative fascination of deciduous trees one twentieth its age. It had no great burrs where branches had been lopped, no self-pleachings, no cryptic caverns." Yet this experience underscores the central lesson of the book: It doesn't matter what Mabey, or for that matter anyone, thinks of the tree. In Mabey's words, "plants have agendas of their own," and as long as humans continue to leave space for the Fortingall Yew and others like it, these ancient organisms will keep on living and adapting just as they have done for millennia.

Mabey worries that our species will not leave such space. He mourns a perceived loss of interest and excitement about the "vegetable world's alternative solutions to living" and laments that today, even conservationists resort to emphasizing plants' economic benefits rather than their intrinsic interest and value.

He intends for his spirited book to serve as a corrective to this narrowed vision and the limited imperative for plant preservation it conveys. Who could feel anything but delight in the Madagascan Star of Bethlehem, an orchid whose nectar lies at the bottom of a foot-long channel, accessible only to a species of hawkmoth with a foot-long tongue? Or anything but astonishment in learning of the "King's Holly" of Tasmania, a shrub whose clonal community is an estimated 43,600 years old and extends more than half a mile? Or anything but a desire to protect and preserve the varied ecosystems that allow plants as diverse as the lovely British bird's-eye primrose, the towering primordial sequoia of California, and the sensational Amazonian water lily to endure?

Whether depicting the bizarre, the beautiful, or something else altogether, *The Cabaret of Plants* provides ample opportunities to pause and share the wonder of many past observers—and to take a step toward being the kind of plant appreciator whose existence appears increasingly endangered.

The reviewer is in the Department of History and Philosophy of Science, University of Cambridge, Cambridge CB2 3RH, UK. E-mail: hac44@cam.ac.uk

The Cabaret of Plants
Richard Mabey
Norton, 2016. 384 pp.

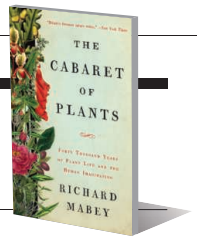

10.1126/science.aad9074

PHOTO: © PATRICK STRAUB/EPA/CORBIS

Published by AAAS

EXHIBITION

The damage we do

A new exhibition explores how we remember, record, and recover from trauma

TRAUMA
Built to Break
Science Gallery Dublin
Through 21 February 2016
www.sciencegallery.com

By **Giovanni Frazzetto**

From schedules of torture and close-ups of physical injury to the timbre of war, the disfigurement of land, and the resonance of mental illness and abuse, the works on display in a new exhibition at the Science Gallery Dublin visualize trauma in palpable and concealed guises

In David Cotterrell's triptych of pictures entitled *Supernumerary*, trauma is disclosed in frightening realism. Raw, and at first sight repelling, the images are authentic scenes from inside the emergency operating theater of a military hospital in Afghanistan. While exposing broken flesh, blood, and surgery equipment, the shots immortalize medical staff's frantic attempts to save lives. In all its screaming urgency, the view is solemn and quiet and, like the students in Rembrandt's *The Anatomy Lesson*, leaves the viewer in search of reassurance amid the mystery of fatality and survival.

With the help of goggles and headphones, the interactive piece *Project Syria* takes visitors to the streets of Aleppo, where they are exposed to the chaos, danger, and discomfort of a rocket explosion. Users then find themselves in the middle of a refugee camp. Bringing us a little closer to the stark reality of the Syrian crisis, the piece is disturbingly persuasive.

Continuous loud music. Extended sleep deprivation. Starvation. Waterboarding. These are some of the so-called "enhanced interrogation techniques" endured over a period of 50 days by Guantanamo detainee Mohammed al-Qahtani. Artist Stefanie Posavec and neuroscientist Shane O'Mara sensitively visualize this harrowing experience on a wide tableau. Each day of detention is shown as a vertical bar. The hours are filled with color-coded rectangles that build a revealing gradient of interrogation sessions. The aesthetic result is a seemingly benign palette of colors—of vague Mondrianesque appearance—that belies a humiliating and deplorable regimen of torture.

Be it in landscapes, buildings, public plots, or private homes, trauma is traceable in spaces that are paced, deserted, or transformed by human action. In a pair of arresting black and white photographs entitled *SILENCE, After a Kneecapping* and *ENCLAVE, Dividing Wall*, Northern Irish artist Willie Doherty captures the chilling reverberation of violence that ignited and shook the city of Derry during the late-20th-century ethnonationalist conflict known as "The Troubles." Parking lots, streets, walls, stairs, fences, and passageways look desolate but bear the signature of aggressive disturbance.

Sightlines 1 **depicts an operating theater in Helmand Province, Afghanistan.**

Chernobyl's Herbarium, by Anaïs Tondeur, highlights another spatial victim of trauma. The images feature imprints of vegetation that grew in the 30-kilometer radius surrounding Chernobyl's nuclear plant after the explosion in 1986. By using the photogram technique, in which images are captured by placing an object directly onto light-sensitive paper, Tondeur catches the trauma endured by the flora samples. Reminiscent of atomic shadows, the stems, leaves, and flowers of the plants shine in an archival sepia tone.

Art is inimitable at articulating the mind of trauma sufferers. When the very first pictures of psychiatric patients were printed in medical journals at the end of the 19th century, they served both as new means of diagnosis and as windows into a patient's condition. Evocative of the shriveled bodies and diaphanous faces in the art of the tormented Viennese painter Egon Schiele (1890–1918), four *Self-Portraits* by William Utermohlen (1933–2007) conjure the artist as patient and endurer of pain. Created over a 5-year period, the portraits depict the progression of Alzheimer's disease. The artist's identity appears to gradually fade, and each piece is imbued with an agonizing awareness of impending physical and existential decay.

Hysteria, a video installation realized by dancer and choreographer Maurice Kelliher, is the most lyrical and intimate piece in the exhibition. Once considered a condition of broad aetiology and exclusively linked to women, hysteria was postulated to have origins in unresolved unconscious conflicts. Sigmund Freud suggested that the symptomatic spectrum manifested among hysterics was a bodily and behavioral response to memories either too shameful or too distressing to face. In other words, the illness was an outcome of trauma and a refuge from it.

Kelliher subtly visualizes this split. The video consists of a dancer, behind whom plays original footage documenting "war neurosis"—a form of hysteria diagnosed in World War I soldiers. The rawness of a haunting condition is rendered as a choreographic artifice in which details of soldiers' facial twitching, tremors, heavy breathing, and frenetic gait are mirrored by equally stuttering but graceful dance movements. At once hypnotizing and dreamful, *Hysteria* is projected onto a large wall and is visible to street passers-by, even when the gallery is closed.

At a time when terrorism, forced migration, ideologies of hatred, and the risk of war put our civilization and mental well-being to test, a creative reflection on the science and experience of trauma is obliging. Despite its gruesome theme, TRAUMA is shrouded in compassion and optimism, which point the way to recovery. We are vulnerable to trauma, but we are also pliable to overcome it.

10.1126/science.aad9278

PHOTOS: (LEFT TO RIGHT) *SIGHTLINES 1* BY DAVID COTTERRELL AS PART OF TRAUMA: BUILT TO BREAK AT SCIENCE GALLERY AT TRINITY COLLEGE DUBLIN; *PRIMITIVE REFLEX* BY GRÁINNE TYNAN AS PART OF TRAUMA: BUILT TO BREAK AT SCIENCE GALLERY AT TRINITY COLLEGE DUBLIN

The reviewer is the author of Joy, Guilt, Anger, Love *(Penguin, 2014) and is a visiting research fellow at Trinity College Dublin. E-mail: gio@giovannifrazzetto.com*

Published by AAAS

LETTERS

Edited by **Jennifer Sills**

Editorial expression of concern

ON 7 MAY 2004, *Science* published the Report "RNA-Mediated Metal-Metal Bond Formation in the Synthesis of Hexagonal Palladium Nanoparticles" by Lina A. Gugliotti, Daniel L. Feldheim, and Bruce E. Eaton (*1*). An investigation by the U.S. National Science Foundation's (NSF's) Office of Inspector General determined that the authors falsified research data published in the paper. Although the NSF did not find that the authors' actions constituted misconduct, it nonetheless concluded that they "were a significant departure from research practices" (*2*). *Science* is working with the authors to understand their response to the NSF final ruling. Depending on the outcome of this discussion, *Science* will issue either a Retraction or a (further) correction to the paper, as allowed under the NSF ruling. In the meantime, this Editorial Expression of Concern serves to alert readers to the conclusions of the investigation.

Marcia McNutt
Editor-in-Chief

REFERENCES

1. L. A. Gugliotti, D. L. Feldman, B. E. Eaton, *Science* **304**, 850 (2004).
2. NSF Office of Inspector General, Closeout Memorandum (www.nsf.gov/oig/case-closeout/A06110054.pdf).

Eradicating polio: A balancing act

THE EDITORIAL "ERADICATING polio" by A. Adams and D. M. Salisbury (6 November 2015, p. 609) presented great news about the progress of polio eradication: Efforts led by the World Health Organization (WHO) resulted in only 70 cases of paralytic poliomyelitis caused by wild polioviruses of serotype 1 (WPV1) in 2015 (*1*), whereas disease caused by WPV2 or WPV3 has not been registered since 2012.

These statistics, however, omit another important source of infection and disease. Highly pathogenic vaccine-derived polioviruses (VDPVs) continue to cause outbreaks worldwide (*2*) and are chronically excreted by a small number of immune-compromised individuals, sometimes for many years (*3*). The overwhelming majority of poliovirus infections are asymptomatic, leading to silent circulation detectable only by environmental surveillance, which is not performed globally. Thus, it is impossible to ensure that the virus is truly absent, requiring continued immunization. It is recognized that eradication of polio will never be possible as long as the current live vaccine strains are in use (*4*), leading WHO to plan a phased, globally synchronized withdrawal of the live vaccine, ultimately replacing it with safer, inactivated vaccine. This transition will not be possible or sustainable without development and introduction of a new generation of safer, more effective and affordable vaccines and treatment options for chronic excretors.

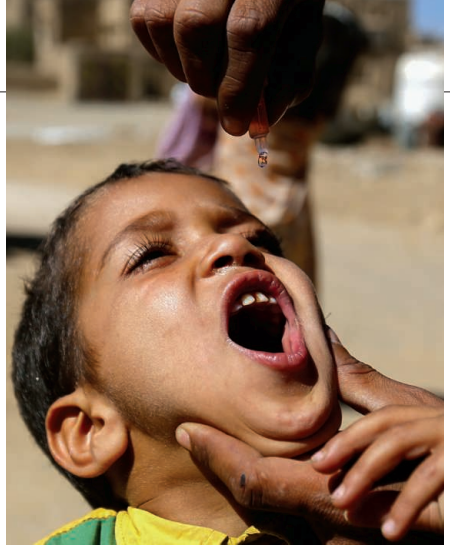

A child receives an oral polio vaccine in Sana'a, Yemen.

The major message of the Editorial is that "all polioviruses (wild and vaccine strains) in laboratory, research, and manufacturing facilities will have to be destroyed or securely contained" in order to prevent inadvertent release. Strict and premature containment will severely hinder the availability of new vaccines and therapeutics (*5*) currently under development, supported by WHO and the Bill & Melinda Gates Foundation. Thus, a careful balance between containment and research/product development must be applied during this transition.

Vadim Agol,[1,2] Jeronimo Cello,[3] Konstantin Chumakov,[4]* Ellie Ehrenfeld,[5] Eckard Wimmer[3]

[1]M. P. Chumakov Institute of Poliomyelitis and Viral Encephalitides, Moscow, 142782, Russia. [2]A. N. Belozersky Institute of Physical-Chemical Biology, M. V. Lomonosov Moscow State University, Moscow, 119899, Russia. [3]Department of Molecular Genetics and Microbiology, School of Medicine, Stony Brook University, Stony Brook, NY 11794, USA. [4]Center for Biologics Evaluation and Research, U.S. Food and Drug Administration, Silver Spring, MD 20903, USA. [5]NIAID, NIH, Bethesda, MD 20892, USA.

*Corresponding author.
E-mail: Konstantin.Chumakov@fda.hhs.gov

REFERENCES AND NOTES

1. Polio Eradication, Data and Monitoring (www.polioeradication.org/Dataandmonitoring.aspx).
2. O. M. Diop *et al.*, *Morb. Mortal. Wkly. Rep.* **64**, 640 (2015).
3. G. Dunn *et al.*, *PLOS Pathog.* **11**, e1005114 (2015).
4. W. R. Dowdle, E. de Gourville, O. M. Kew, M. A. Pallansch, D. J. Wood, *Rev. Med. Virol.* **13**, 277 (2003).
5. A. S. Bandyopadhyay, J. Garon, K. Seib, W. A. Orenstein, *Future Microbiol.* **10**, 791 (2015).
6. The opinions expressed in this Letter are solely of its authors and may not reflect the official position of the Food and Drug Administration.

Practicalities of political agency

THANK YOU TO K. O'Brien for her exuberant call for a deeper form of political agency to tackle climate change ("Political agency: The key to tackling climate change," Perspectives, 4 December 2015, p. 1170). O'Brien hopes that each person will be inspired to change him- or herself and others, allowing us to "depend on individuals expressing political agency." Although this would work well in an ideal world, its practical implementation runs into reality.

Much research demonstrates that collectives can display political agency far exceeding the sum of "reflection and collaborative action" from individuals. From the *Madness of Crowds* (*1*) to *The Wisdom of Crowds* (*2*), extensive empirical evidence demonstrates that it is not necessarily "individuals who will ultimately decide the future." Constructive group dynamics, as opposed to groupthink, produce a collective achieving far more effective action than a collection of individuals (*3*).

Meanwhile, the current political realities in some parts of the world mean that taking individual stances to change society can be dangerous. Many are imprisoned and executed precisely because they are "participating in grassroots community initiatives" or "engaging…through art and literature." As the climate justice movement has shown (*4*), not all individuals are treated fairly.

Placing increased responsibility on individuals implies that collectives such as governments and corporations can do less. The burden for resolving societal ills thus falls on individuals, irrespective of their power, resources, or capabilities (*5*). Instead, without neglecting the long-standing science of extensively documented cases where collections of individual power achieved transformative change (*6*, *7*), we must recognize that real inequalities and power relations dominate political agency. We must also accept the essential role played by the power of human collectives beyond a collection of individuals.

Ilan Kelman

Institute for Risk and Disaster Reduction and Institute for Global Health, University College London, London, WC1E 6BT, UK and Norwegian Institute of International Affairs, Oslo, 0033, Norway.
E-mail: ilan_kelman@hotmail.com

PHOTO: © YAHYA ARHAB/EPA/CORBIS

Published by AAAS

REFERENCES

1. C. Mackay, *Extraordinary Popular Delusions and the Madness of Crowds* (Bentley, London, 1841).
2. J. Surowiecki, *The Wisdom of Crowds* (Random House, New York, 2004).
3. D. Forsyth, *Group Dynamics* (Wadsworth, Belmont, ed. 5, 2009).
4. H. Shue, *Climate Justice: Vulnerability and Protection* (Oxford Univ. Press, 2014).
5. A. Parr, *The Wrath of Capital: Neoliberalism and Climate Change Politics* (Columbia Univ. Press, New York, 2013).
6. E. C. Stanton *et al.*, Eds., *History of Woman Suffrage*, Volumes 1 to 6 (Fowler & Wells, New York, 1881–1922).
7. D. H. Smith, *Southern Speech J.* **34**, 8 (1968).

Response

KELMAN MAKES AN important point about the power of constructive group dynamics in collective action, and he emphasizes the drawbacks of placing responsibility on individuals. He is not alone; Shove is also critical of limiting climate policy objectives to individual attitudes, behaviors, and choices (*1*). However, the purpose of my Perspective was not to prioritize individual action over collective action, but rather to discuss the relationship between individual and collective change.

In the piece, I support a more expansive view of political agency, which recognizes that individuals are socially embedded and that social relationships influence the dynamics of collective action and transformative change (*2*). I emphasized the importance of questioning beliefs, particularly those that form part of shared knowledge and that inform social practices, as this can be a powerful force for structural and systemic change (*3*).

There is no doubt that individual actions and grassroots initiatives can be dangerous, especially when they challenge norms, interests, and the status quo. However, individual actions are rarely isolated—they are embedded in a social, material, and cultural context. Agency can both create and be influenced by social structures (*3*). This is not to imply that all individuals are the same or have the same capacities and opportunities to influence outcomes. Challenging inequalities, addressing power differentials, or questioning development paradigms demands a level of awareness and social consciousness that goes beyond a limited sense of self and an isolated sense of individuality (*4*). This is something that can be cultivated, not the least through education.

Climate change is a collective action problem, and political agency is essential to global sustainability. Yet leaving political agency to state actors and denying individuals an active role as agents of change risks subjecting ourselves to a world where global average temperatures rise to dangerous levels, contributing to risks of severe, widespread, and irreversible impacts globally (*5*). To support transformations to sustainability, we may first have to overcome the dualisms and dichotomies that separate individual action from collective action.

Karen O'Brien

Department of Sociology and Human Geography, University of Oslo, Oslo, 0317, Norway.
E-mail: karen.obrien@sosgeo.uio.no

REFERENCES

1. E. Shove, *Environ. Plan.* **42**, 1273 (2010).
2. B. Maiguashca, *Contemporary Political Agency: Theory and Practice*, B. Maiguashca, R. Marchetti, Eds. (Routledge, London, 2013), pp. 118–136.
3. A. Wendt, *Social Theory of International Politics* (Cambridge Univ. Press, 1999).
4. M. M. Schlitz, C. Vieten, E. M. Miller, *J. Consciousness Stud.* **17**, 18 (2010).
5. IPCC, *Climate Change 2014: Synthesis Report. Contribution of Working Groups I, II and III to the Fifth Assessment Report of the Intergovernmental Panel on Climate Change*, R. K. Pachauri, L. A. Meyer, Eds. (IPCC, Geneva, 2014).

REVIEW SUMMARY

SOLAR ENERGY

Research opportunities to advance solar energy utilization

Nathan S. Lewis*

BACKGROUND: Despite providing a relatively small percentage of total global energy supply, solar energy systems generally receive enthusiastic support from technologists, regulators, politicians, and environmental groups. The energy in sunlight can be converted into electricity, heat, or fuel. Although the costs of solar panels have declined rapidly, technology gaps still exist for achieving cost-effective scalable deployment combined with storage technologies to provide reliable, dispatchable energy.

ADVANCES: The costs of Si-based solar panels have declined so rapidly that panel costs now make up <30% of the costs of a fully installed solar-electricity system. Research and development (R&D) opportunities hence lie in the development of very high efficiency conversion materials, to advantageously leverage the associated reduction in area-related balance-of-systems costs. Such materials would optimally either leverage or mate with existing, low-cost Si photovoltaic (PV) technology. Ultralightweight, flexible, robust, and efficient materials could also greatly reduce the installation costs and could allow for enhanced automation and inexpensive support structures.

The development of cost-effective persistent grid-scale storage to compensate for the intermittency of sunlight is a major area for R&D. Possibilities include new types of batteries and flow batteries, as well as geologic storage of hydrogen, methane, or compressed air.

Opportunities also exist to improve the capabilities of concentrated solar power systems that convert sunlight into heat. Improved thermal storage fluids would provide longer-term storage to compensate for cloudy days in areas of high direct insolation. Thermoelectrics, in principle, could replace engines to provide efficient conversion systems that have no moving parts. New thermochemical cycles could allow for the highly efficient, cost-effective conversion of solar heat into fuels by promoting endothermic reactions, such as water splitting, carbon dioxide reduction, or thermochemical conversion of feedstocks, such as methane to high energy-density liquid hydrocarbon fuels that are needed in the transportation sector.

ON OUR WEB SITE

Read the full article at http://dx.doi.org/10.1126/science.aad1920

Artificial photosynthetic systems that directly produce fuel from sunlight are in the proof-of-concept stage. Such technologies offer the potential to provide renewable hydrogen by solar-driven water splitting or to produce hydrocarbons directly from sunlight, water, and CO_2. Key goals for R&D are development of materials that can absorb and convert sunlight efficiently that are seamlessly integrated with catalysts that promote the production of fuel, with the production of O_2 from water also required to complete a sustainable, scalable chemical cycle. Systems must simultaneously be efficient, robust, cost-effective, and safe.

OUTLOOK: Considerable opportunities for cost reduction that can achieve both evolutionary and revolutionary performance improvements are present for all types of solar energy–conversion technologies. Learning by doing and R&D will both be needed to produce an innovation ecosystem that can sustain the historical rate of cost reductions in PVs and concentrated solar thermal technology. Disruptive approaches to storage technologies are needed to compensate for the intermittency of sunlight and allow for development of a full clean-energy system. Solar fuels technology contains abundant opportunities for discovery of new materials and systems that will allow for deployable, cost-effective routes to the direct production of fuels from sunlight. ■

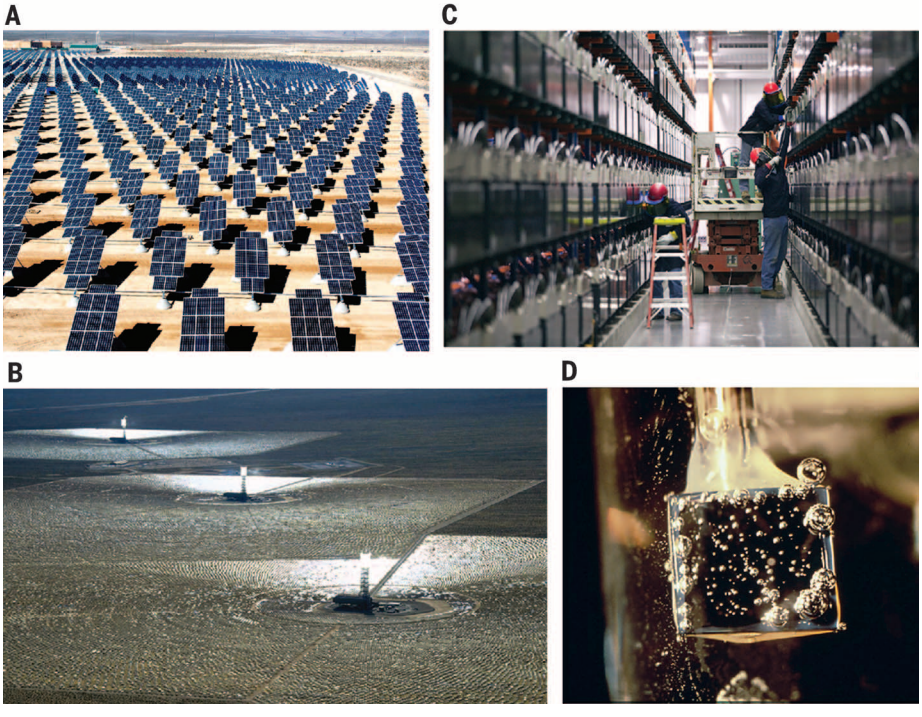

Solar energy–conversion and storage technologies. (**A**) Nellis Solar Power Station, a 14-MW PV installation at Nellis Air Force Base, NV. (**B**) Concentrated solar thermal power 392-MW installation at Ivanpah, CA. (**C**) World's largest battery (NiCd) storage installation (40 MW for 7 min, 26 MW for 15 min), Fairbanks, AK. (**D**) Solar fuels demonstration of a photoelectrode evolving hydrogen gas. [Image sources: (A) Nellis Air Force Base PV installation, https://commons.wikimedia.org/wiki/Category:Nellis_Solar_Power_Plant. (B) Ivanpah solar electric generation installation, http://i.ytimg.com/vi/M5yzgfCNpvM/maxresdefault.jpg. (C) Fairbanks battery installation, http://blog.gvea.com/wordpress/?p=1677]

The list of author affiliations is available in the full article online.
*Corresponding author. E-mail: nslewis@caltech.edu
Cite this article as: N. S. Lewis, *Science* 351, aad5117 (2016). DOI: 10.1126/science.aad5117.

REVIEW

SOLAR ENERGY

Research opportunities to advance solar energy utilization

Nathan S. Lewis*

Major developments, as well as remaining challenges and the associated research opportunities, are evaluated for three technologically distinct approaches to solar energy utilization: solar electricity, solar thermal, and solar fuels technologies. Much progress has been made, but research opportunities are still present for all approaches. Both evolutionary and revolutionary technology development, involving foundational research, applied research, learning by doing, demonstration projects, and deployment at scale will be needed to continue this technology-innovation ecosystem. Most of the approaches still offer the potential to provide much higher efficiencies, much lower costs, improved scalability, and new functionality, relative to the embodiments of solar energy-conversion systems that have been developed to date.

Because of its unmatched resource potential, solar energy utilization has been the subject of intense research, development, and deployment efforts that have accelerated during the past decade (*1*). Efforts have focused on the development of photovoltaics (PVs) for production of solar electricity, on conversion of solar energy into electricity or heat, and on artificial photosynthetic systems that directly produce fuels from sunlight. The dramatic increases in deployment and concomitant decreases in the cost of solar energy-conversion systems in the past decade attest to the importance of investments in innovation (*1*).

The cost-effectiveness of terrestrial solar energy systems is dictated by two fundamental constraints. First, as compared with fossil fuels or nuclear fission, the relatively low average terrestrial power density of sunlight, typically ~200 to 250 W/m^2, requires very inexpensive materials and systems to cost-effectively cover the large areas needed to capture and convert solar power on a terawatt global scale (*2*, *3*). Second, the intermittency of sunlight requires cost-effective energy-storage technologies to provide energy on demand with high reliability. This review provides an update on many of the developments that have occurred during the past decade (*4*) and identifies some of the promising opportunities for further research and development (R&D) in light of the present status and economics of solar energy-conversion technologies.

Solar electricity

Photoactive materials

Solar cells can be conveniently categorized on the basis of the type of light-absorbing material in the photoactive layer (Table 1). Devices based on crystalline silicon rely on a p-n junction formed through spatially directed doping of a

210 Noyes Laboratory, 127-72, Division of Chemistry and Chemical Engineering, Beckman Institute and Kavli Nanoscience Institute, California Institute of Technology, Pasadena, CA 91125, USA.
*Corresponding author. E-mail: nslewis@caltech.edu

Table 1. List of PV materials and defining commercial and technical attributes. n/a, not applicable.

PV material	Maturity	2013 production (GWp)	Efficiency [best module (*35*), highest reported cell (*7*)]; attributes
CdTe	Commercial	1.9	17.5%, 21.5%; thin film, sublimes congruently and enables monolithic module manufacturing
a-Si:H	Commercial	0.8	12.3%, 13.6%; flexible modules when material is deposited onto stainless steel substrates; efficiency decays with time
$CuInGaSe_2$	Commercial	0.8	17.5%, 21.7%; requires stringent process control to maintain stoichiometry of four-element material over large areas
Mono-Si	Commercial	13.9	22.9%, 25%; highest Si module efficiencies; implements technology for extensive control of bulk and surface recombination losses; high efficiency yields reduced area-related balance-of-systems costs
Multi-Si	Commercial	21.3	18.5%, 20.8%; market leader
Ribbon Si	Commercial	0	Continuous instead of batch process to make the Si substrate
GaAs	Demo	n/a	24.1%, 28.8%; thin-film epitaxial layers require facile removal from the lattice-matched, expensive substrate; radiation tolerance and light weight are advantageous for space power applications
Multijunction (high concentration PV)	Demo	0.05	38.9%, 46%; high efficiency; limited to high locations with high direct normal irradiance, optimal performance requires complex dual-axis tracking and optical focusing
Organic PVs	R&D	n/a	8.3%, 11.5%; readily processable, flexible cells; modest cell efficiencies; long-term decay of efficiency;
Quantum dots			n/a, 9.9%; potential for very high efficiencies through multiple exciton generation processes; growth of large single crystals not required
Perovskites			n/a, 20.1%; very rapid increase in demonstrated cell efficiency; stability unproven; soluble, toxic Pb salt; material dissolves in water
Dye-sensitized solar cells			n/a, 11.9%; wet chemical processing of titania substrate followed by adsorption of dye; fabrication of cell requires sealing gel or liquid electrolyte; small improvement in efficiency over past decade

planar silicon (Si) structure to effect charge separation and to allow for efficient production of photocurrent and photovoltage (Fig. 1) (*5*, *6*). The cost of Si solar panels, measured in dollars per peak watt ($/Wp) has decreased by ~20% for each doubling in cumulative global module production (*2*, *3*). Commercially available Si panels, which accounted for ~90% of total solar panel production in 2013, now have an energy payback period of <2.5 years and ~16 to 21% power-conversion efficiencies (*2*, *3*). The dramatic reductions in panel cost have been realized largely through sustained, systemic reductions in specific manufacturing costs, including those of the polymer encapsulant, the screen-printing of the silver electrical contacts, and even the production of the Si wafers themselves, along with economies of scale enabled by construction of very large panel-production facilities. Research opportunities to further lower costs include methods to integrate higher band-gap materials with Si to create a high-efficiency tandem device in a scalable, cost-effective process that is compatible with existing Si PV manufacturing methods.

Gallium arsenide and other "III–V" single-junction and multijunction PV devices (*7*–*10*) are highly efficient and used on satellites but are currently only considered cost-effective for terrestrial applications by combining small device areas with high-concentration-factor optics that utilize active solar tracking and optical concentrating systems. Opportunities exist for obtaining improved efficiencies through spectral-splitting approaches (*11*, *12*), as well as through novel designs for both one-dimensional (1D) and 2D optical concentration and tracking systems and structures, as well as in development of new approaches to the low-cost growth of high-quality, high-performance III–V monolithic devices and structures.

In contrast to active materials based on single-crystal substrates, thin-film materials, such as cadmium telluride (CdTe), $CuInGaSe_2$, amorphous hydrogenated Si, and organic PVs can provide flexible, lightweight modules that could result in reduced system installation costs. Engineered CdS/CdTe heterostructures provide control over junction recombination at the metallurgical interface (*3*). Toxicity concerns related to release of Cd into the environment have been raised, especially in Europe, but have been addressed by rigorous encapsulation of the active material, in conjunction with proposed panel-recycling programs (*13*). Scarcity issues related to the availability of Te may preclude scaling of CdTe PV technology to terawatt levels (*14*), but the lower CdTe module efficiencies of <15%, as compared with 16 to 21% efficiencies for Si panels, are presently more important considerations in determining the cost-competitiveness of the various PV panel technologies. Research opportunities involve grain-boundary passivation to allow thin films to exhibit the high mobilities and efficiencies of single crystals. Solar cells based on perovskites formed from lead salts with organic ammonium cations have demonstrated that extraordinary performance can be obtained using simple deposition techniques in novel materials systems (*7*, *15*–*17*). The long-term stability of these materials at the highest reported efficiencies remains to be established (*17*, *18*). Intense efforts are currently being devoted to understanding the fundamental behavior of such systems, as well as to discover other similarly behaving classes of materials that are environmentally benign, do not release toxic lead ions upon dissolution in water, and combine efficiency with stability. Such considerations underscore the complex technological, political, and economic aspects associated with the development a sustainable, cost-effective solar energy-utilization system (*1*).

Earth-abundant light absorbers that could provide alternative materials options for solar absorbers, including Zn_3P_2 (*19*, *20*), $ZnSnN_2$ (*21*, *22*), and Cu_2O (*23*, *24*), are receiving renewed interest after preliminary investigations in the early 1980s (*25*, *26*). Research opportunities involve control over the bulk and surface properties of such materials to obtain high efficiencies, preferably in thin-film form.

The performance of organic PV cells, such as those based on composites of poly-phenylenevinylene (PPV) with a functionalized C60 that serves as the light absorber (*27*–*30*), in principle, can be systematically varied by chemical control over the composition and structure of the components of the device (*29*). Radical-related side reactions under visible and ultraviolet illumination of the organic materials that form the active components of the device structure must be minimized to obtain long-term stability while preserving high efficiency. Research opportunities for dye-sensitized solar cells include the development of molecular sensitizers that exhibit improved photovoltages, as well as enhanced stability, while retaining device efficiency (*31*, *32*).

Quantum-confined systems, including inorganic quantum dots, can provide multiple electrons upon absorption of a photon having an energy greater than twice the band gap of the absorber (*33*). Organic materials exhibit an analogous process denoted as singlet fission (*34*). Both phenomena could form the basis for solar cells that exhibit efficiencies in excess of the conventional, Shockley-Queisser (S-Q), theoretical limit of 32% for a single–band gap material under unconcentrated sunlight (*33*). Research opportunities involve incorporation of this phenomenon into operational devices that exhibit high photovoltages in conjunction with quantum yields in excess of unity for photocurrent production. These materials systems will ultimately have to compete with other approaches to obtain device efficiencies that exceed the S-Q limit, such as multijunction cells, which have already exhibited efficiencies >40% under high concentration (*7*, *35*).

Balance of systems

The cost of Si solar panels now constitutes ~30% of the cost of a fully installed utility-scale system (Fig. 2) (*36*, *37*). The "hard" materials costs, including the inverter, support structures, and electrical wiring, make up ~30% of the system costs. "Soft" costs, including installation labor, permitting, inspection and interconnection, financing, and customer acquisition, make up ~40% of the installed system costs. These balance-of-systems costs have not declined nearly as rapidly as module costs.

For an installation having a specific peak output power, increases in module efficiency would correspondingly reduce the area-related balance-of-systems cost (Fig. 2B). Any viable alternative to Si, or any PV technology that leverages or mates with Si PV technology will ultimately have to exhibit long-term stability and superior efficiency at competitive manufactured panel costs. Improvements in efficiency, especially through R&D, that result in the development of new materials and PV systems having efficiencies higher than the S-Q limit, would have more of an impact on lowering the cost of installed solar electricity than proportionate reductions in the manufacturing costs of present Si-based panels, as shown in Fig. 3.

To be certified for sale in the marketplace, solar panels are required to contain protective glass that can survive a hailstorm. The cost of the float-glass material is relatively low (*38*), but the stiffness and weight of the resulting panels produces sizable costs for shipping, requires the use of costly support structures, and produces substantial labor costs for installation. Soft costs are lower in Germany and Australia than in the United States, because permitting and installation processes and protocols have been streamlined (*39*, *40*). Obtaining much lower installed PV system costs will not only require ultralight-weight, flexible, robust, and efficient materials

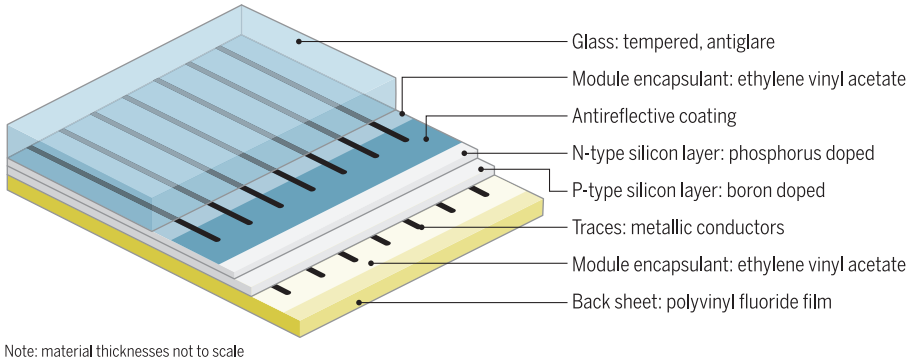

Note: material thicknesses not to scale

Fig. 1. Components of a typical silicon solar cell. The diagram shows the absorber layer, the p-n junction, antireflection coating, grid and contact lines, encapsulation, and glass support structures.

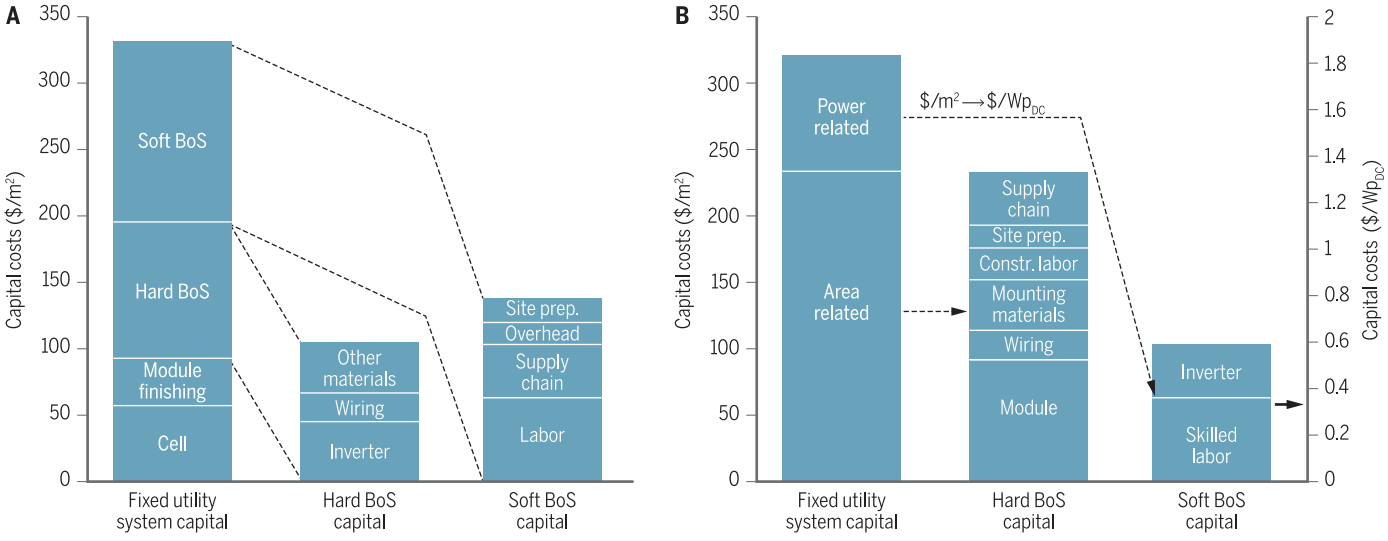

Fig. 2. Breakdown of capital costs for installed utility-scale PV systems. (**A**) Costs of finished modules (panels) made from Si solar cells, as well as hard and soft balance-of-systems (BoS) costs as tabulated by Goodrich *et al*. (*35*). The solar cell and module costs have been updated from those listed in (*35*) to reflect the rapidly declining price of these components (*36*). (**B**) Breakdown of the same capital costs for installed utility-scale PV systems as in (A), except that the costs are broken down into items that scale with the area of the installation (and hence, panel efficiency) and (area-independent) items that are related to the power produced by the installation and described in terms of dollars per peak watt of direct current.

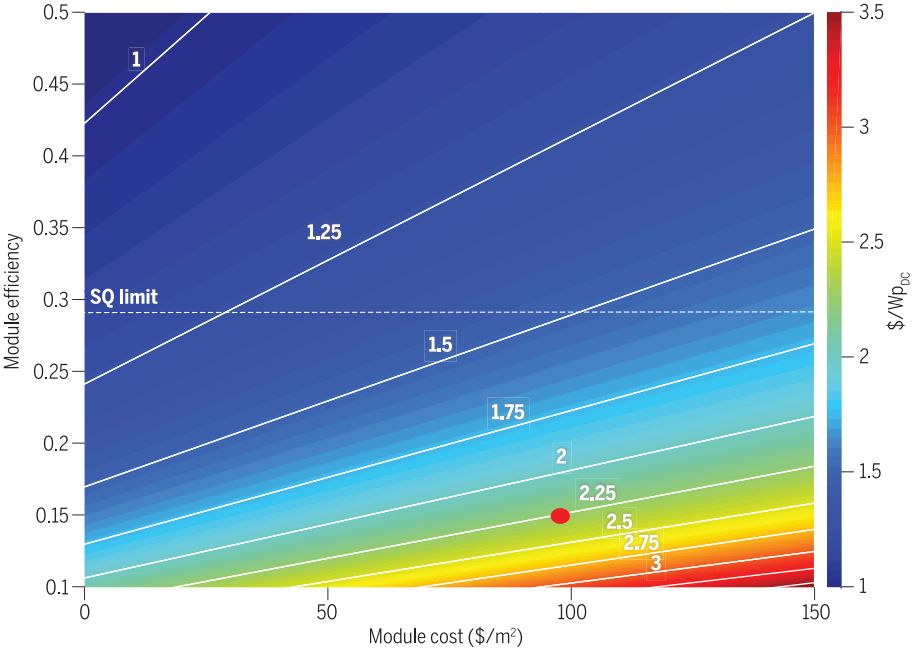

Fig. 3. Costs for installed utility-scale PV projects as a function of module efficiency and module cost. Movement parallel to the abscissa assumes that all costs are held constant other than the module cost (Fig. 2A), whereas movement parallel to the ordinate is based on the assumption that there is a linear proportionality of all area-related costs (Fig. 2B) to the module efficiency. The red dot is representative as an example of recent utility-scale projects for which citable data are available (*38*, *39*) with 15% efficient Si-based panels at a cost of $90/m^2 and with a total installed project fixed capital cost of $2.25/Wp. Utility-scale projects have been chosen because they are less expensive per Wp and less variable than rooftop installations, which have similar Si module costs but had, at the time, fully installed project costs of ~ $4.90/Wp in California as compared with $2.20/Wp in Germany, with the difference caused primarily by differences in permitting, labor, inspection, and other soft costs.

and panel technology in the photoactive, encapsulating, and structural components, but also will require disruptive engineering approaches, including very inexpensive support structures, increasing automation, and streamlined protocols that minimize the skill level and effort associated with system installation (Fig. 3) (*6*).

Although the capital costs can be firmly established for a given PV installation (for example, Figs. 2 and 3), the levelized cost of electricity (LCOE) depends on the deployment site, which dictates the electrical energy that is produced by the panels over their useful lifetime and requires assumptions involving the discount rate (i.e., the time value of money), useful system life, and operating costs. For utility-scale Si PV systems having fully installed costs of $1.80/Wp, conventional assumptions yield LCOEs of $0.10 to $0.15/kWh, with the lower value for favorable sites, such as in California (*41*). In 2014, the average U.S. electricity price for large industrial customers, including generation, transmission, and distribution costs, as well as profit, was ~$0.07/kWh (*42*).

Grid integration and energy storage

Regardless of the competitiveness on a levelized cost basis of solar electricity relative to fossil-based or nuclear-based electricity, the value of electricity produced from an intermittent resource is not the same as the value of energy that can be provided on demand. In some market scenarios, such as residential installations in areas with high peak electricity pricing, PV currently has a favorable value proposition, especially with tax incentives or other subsidies (*41*, *43*). The full costs of solar electricity must also eventually include costs associated with grid integration, as

well as the accompanying cost of energy storage to compensate for daily, weekly, and seasonal variability in insolation (2, 41). To ensure reliability, utilities currently back up intermittent renewables, including solar and wind installations, to nearly their full rated peak capacity with dispatchable generation, generally derived from natural-gas-fired power plants. The cost of persistent grid-scale storage currently far exceeds the levelized cost of solar electricity (43, 44).

Pumped hydroelectricity is near its technoeconomic potential globally (44). Compressed-air energy storage will require cost-effective technologies to create robust, full-volume seals in very large underground geological cavities, such as salt caverns (44). Superconducting magnetic-energy storage and flywheels are best suited for high-power, low-energy applications (44, 45).

Batteries currently are expensive grid-scale electrical energy–storage technologies, especially when the costs are amortized over the >30-year lifetime of an installed solar electricity system (44). If one assumes a 15- to 20-year battery lifetime with one cycle per day, conventional or advanced lead-acid batteries have a levelized cost of energy storage (LCES) (not including generation costs) for renewable energy storage and/or time-shifting applications of $0.80 to 1.0/kWh and $0.40 to 0.50/kWh, respectively (46). Under the same assumptions, Na-S batteries, which require operation at ~350°C to obtain sufficient conductivity through the beta-alumina solid electrolyte that separates the liquid sodium negative electrode from the positive electrode composed of a surrounding layer of sulfur, have an LCES of $0.30 to $0.40/kWh (46). Capital costs of $250/kWh for the battery cells are part of the $1000/kWh current cost of a fully installed secondary lithium-ion (Li-ion) battery system for PV storage applications, which results in an LCES of $0.49/kWh, if one assumes a 10-year service life, one cycle per day, a 10% discount rate, a linear capacity decline to 80% of rated capacity at the end of life, 92% charge-discharge energy-storage efficiency, and no operating costs (46, 47). Although the underlying battery chemistry and materials have been relatively unchanged for more than 20 years, Li-ion cells are following an ~25% learning curve, as calculated from sales and production data spanning 2000 to the present (48).

Given current average cell costs of $270/kWh, at the historical rate of cost decline, obtaining a $100/kWh Li-ion cell cost would require production and learning for >25 years, if one assumes a fixed 100 GWh worldwide annual capacity during that time, in accord with expectations for Li-ion battery-production capacity when new, large-production-capacity additions that are currently under construction become operational (48). Chemical reactions between the electrolyte and solvent in current Li-ion batteries fundamentally limit the useful lifetime of such batteries (49), regardless of the depth of discharge or power-management technology incorporated into the system. The costs associated with battery-pack integration and management, inverters, and other hardware and labor costs that dominate the total installed system costs are currently much higher than the battery cell costs. Lithium-air (50), lithium sulfur (51), zinc-air (52), solid-state Li (53), and advanced Li-ion battery chemistries (53), among others, are all being explored.

Flow batteries, based on electrically charging an anolyte and catholyte and storing the fluids in separate holding tanks until discharge, are a focus of major early-stage R&D efforts (44, 54). Electrochemical couples being developed include aqueous vanadium as $V^{3+/2+}$, Zn-Br, V-Cr, Fe-Cr, or H_2/Br_2 systems (54), as well as quinone-hydroquinone redox species (55). Relatively large storage volumes are required because the energy density of flow batteries is typically 20 Wh/liter, compared with an energy density of >200 Wh/liter for Li-ion batteries and >12,000 Wh/liter for liquid hydrocarbon fuels, such as gasoline. If one assumes a 20-year lifetime and one cycle per day, at typical 65 to 75% charge-discharge efficiencies, Fe/Cr and V-based redox flow batteries have an estimated LCES of $0.20 to $0.30 and $0.30 to $0.40/kWh, respectively, with the latter costs resulting from higher materials costs for the V-based system relative to the Fe/Cr or Zn-Br systems (46). Electrically discharging the contents of the holding tanks rapidly will require pumping large quantities of liquid into effective contact with highly porous, high–surface area electrodes, which will add to the system cost. Notwithstanding associated carbon emissions, cost-effective generation technology to compensate for the intermittency of solar electricity and to provide back-up and firming capabilities for daily and seasonal variability in new solar generation capacity currently uses natural-gas plants (46), with costs expected to remain low where shale gas is abundant.

Solar thermal systems

The four main types of solar collectors are parabolic trough collectors, linear Fresnel reflectors, power towers (i.e., central receiver systems), and dish-engine systems, which produce local temperatures of 550°C, 550°C, >1000°C, and 1200°C, respectively (56–58). To generate electricity, either an oil or a molten salt heat-storage fluid, typically an eutectic mixture of 60 weight % (wt %) sodium nitrate to 40 wt % potassium nitrate, known as solar salt, is heated. The heat then is exchanged to produce steam, which is used to drive a turbine to generate electricity (Fig. 4) (5). Power conversion units are either separate or combined Rankine-Brayton cycles. As of 2014, the installed global capacity of PV was 177 GWp, as compared with <5 GWp of solar thermal capacity (59, 60). Solar thermal installations are preferably sited in regions with a high direct normal irradiance value, typically in desert regions of the southwestern United States or Australia, or, for example, Morocco or southern Spain (61).

Although large-scale solar thermal electricity projects were planned both in the United States and in Morocco, driven by mandates, renewable portfolio standards, and low-carbon electricity incentives, the generation costs have proven to be greater than $0.15/kWh when all installation and operational expenses are included (62, 63).

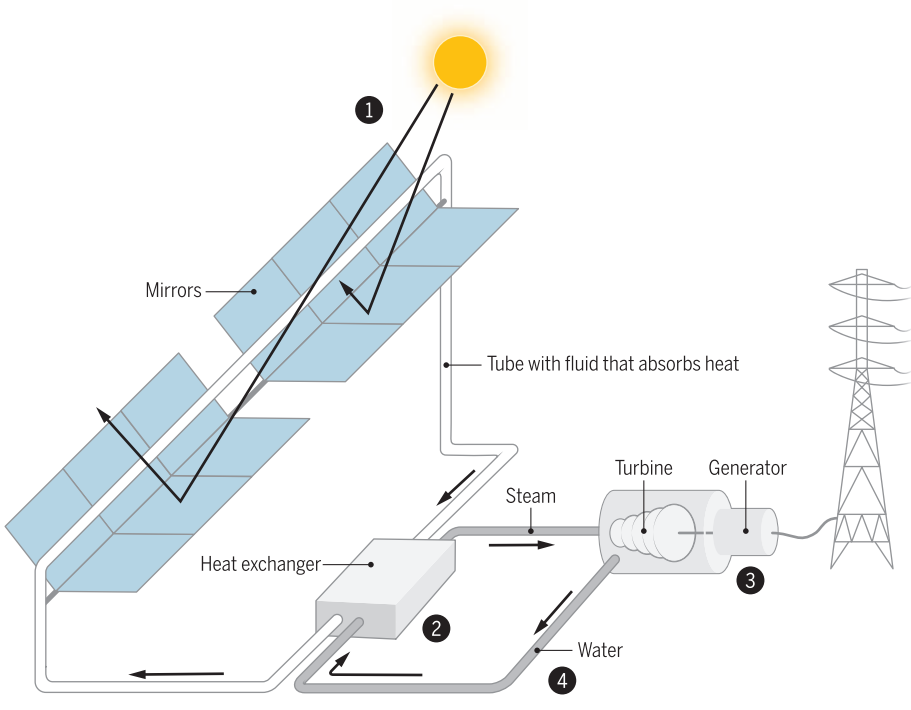

Fig. 4. Schematic of a typical 1D concentrating solar thermal system. The sunlight is focused along one dimension to heat up a thermal fluid—typically, either an oil or a molten salt—which is then passed through a heat exchanger to produce steam that is used in a turbine to produce electricity.

Between 6 and 8 hours of storage can be obtained by use of molten salts as the thermal fluid, but compensation for cloudy days requires 36 hours, or more, of storage. Improved thermal storage fluids are an active area of R&D (*64*). The all-inclusive costs for solar thermal systems have not declined substantially since the early 1980s (*62*) (Fig. 5), in contrast to the costs of PV modules and installed PV systems. For example, the Ivanpah Solar Electric Generation system commissioned in 2013 in the Mojave Desert of California is an air-cooled, 392 MW capacity, power-tower system consisting of 300,000 mirrors and three towers. The project had a capital cost of $2.2 billion and is producing electricity under a 25-year power purchase agreement for a price estimated as >$0.13/kWh to the cognizant utilities (*41*). Research efforts include development of power cycles that allow for higher-temperature operation, along with the development of advanced materials for the fabrication of the collectors (*65*), in conjunction with new engineering approaches to the design of the collectors and integration with the rest of the plant (*66*–*68*). Thermoelectrics could also serve as the technology that converts heat into electricity, provided that their performance can be improved to the necessary levels under the high temperatures that are produced in an operational solar thermal system (*5*, *69*).

Extensive deployment of either PV or solar thermal electricity-generating systems in remote regions with high direct insolation would require installation of new transmission lines. The Sunrise Powerlink—a 117-mile-long, 1-GW capacity, 500-kV, >90% above-ground transmission line built between 2010 and 2012 to provide solar and wind power from the Imperial Valley to San Diego—had a project cost of $1.9 billion (*70*). Concentrated solar power can also be used to provide a source of heat to drive endothermic chemical reactions. In one demonstration system, solar heat is used as a supplement to process heat, to produce synthetic fuel from CO and H_2 (syngas) by using the Fischer-Tropsch process (*71*). For the solar-driven process to be economically viable, the cost of solar-derived heat must be less than the cost of heat derived from combustion of fossil energy, such as natural gas. The capital costs of the solar thermal part of the facility—including the costs associated with siting constraints, as well as underutilization of the plant during night time and periods of off-peak insolation—must be covered by the value of the solar-derived heat production.

Solar-derived heat can also be used to promote the formation of fuels, such as H_2 produced through solar-driven water splitting (*72*). In an exemplary two-step cycle, CeO_2 is first reduced thermally to Ce_2O_3 with the production of O_2, followed by the thermally driven oxidation of Ce_2O_3 by water to produce CeO_2 and H_2 (*73*). Other thermochemical cycles are based on sulfur iodine, hybrid sulfur, photolytic sulfur ammonia, zinc oxide, cadmium oxide, or $FeAl_2O_4$ (*74*). Generally, the cycles exploit temperature swings to evolve O_2 and H_2 separately, which creates research opportunities to explore methods of obtaining high levels of heat recovery so as to ensure high system efficiencies. Isothermal redox cycles have been proposed to alleviate heat-rejection issues, by use of an open system in which a partial pressure change promotes the evolution of O_2 by the thermal reaction of $CoFe_2O_4$ with Al_2O_3, and the $CoAl_2O_4$ and $FeAl_2O_4$ then react with steam to produce H_2 and close the chemical cycle (*75*). Many of these thermochemical water-splitting cycles are also of interest for the production of H_2 from the heat produced by gas-cooled nuclear fission reactors.

These thermochemical cycles to date have been demonstrated in process steps at the laboratory or pilot scales. Implementation of these thermochemical processes in deployed solar thermal systems will require R&D that enables the needed mass flows of reagents into the reactor while allowing facile product egress from the reactor, in addition to effectively confining the heat in the reactor while allowing for the optical excitation to enter, but not leave, the reactor. The reactor

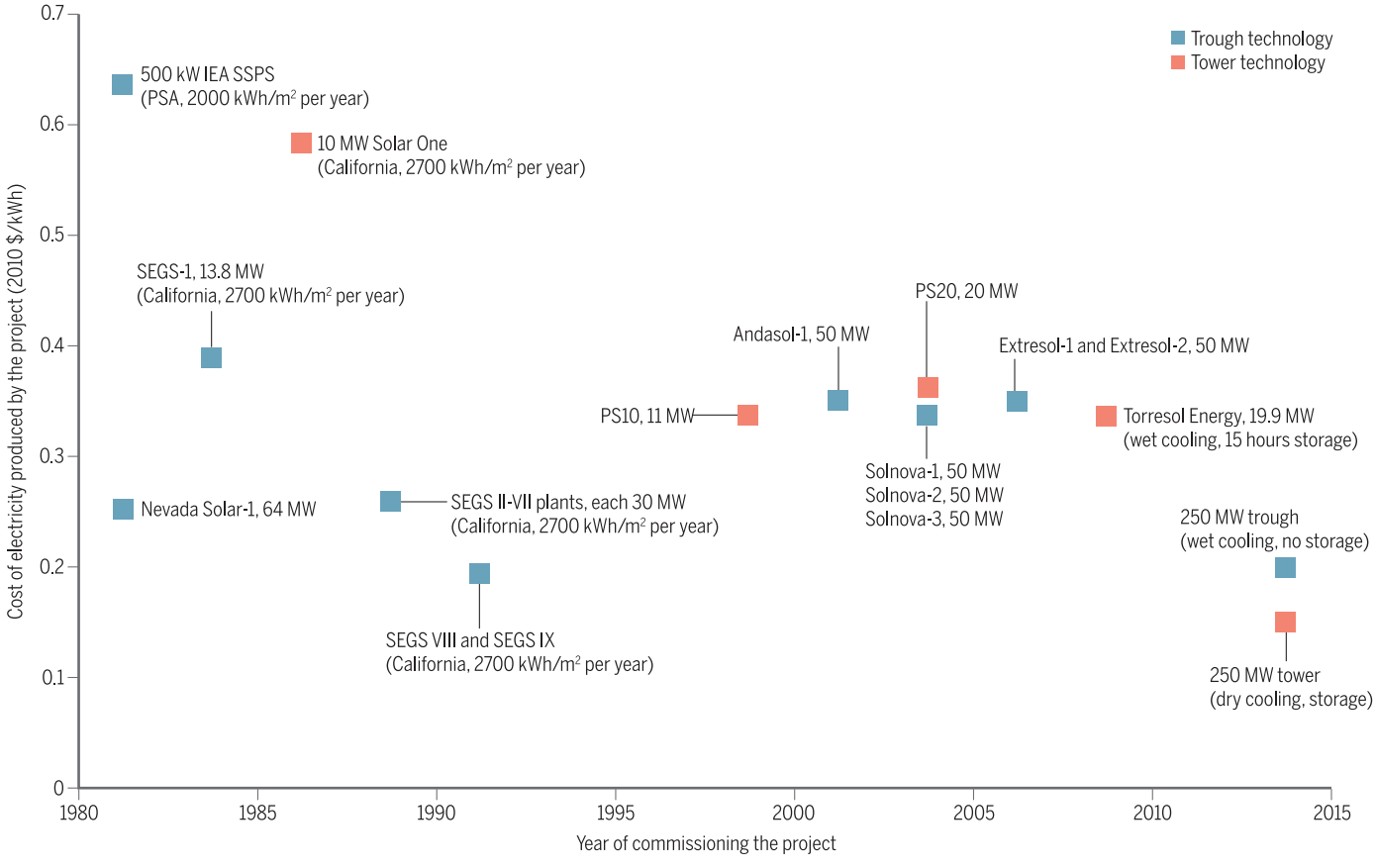

Fig. 5. Chronology of the total installed cost for some large solar thermal projects. Names of projects and rated capacity of each installation. IEA SSPS, International Energy Agency Small Solar Power Systems (Europe); SEGS, Solar Energy Generating Systems (California); P10 (Spain).

Table 2. List of solar fuel systems and their defining technical attributes.

Solar fuels system	State of development	Example systems
Molecular systems	Persistent charge separation demonstrated; fuel-producing systems, including efficient, stable molecular electrocatalysts, must be discovered	Porphyrins linked to quinones either in diads, triads, or tetrads; Ru-bipyridyl inorganic chromophores linked to Pt particles or hydrogenases, and linked to molecular catalysts for water oxidation
Inorganic semiconductor particles	Solar-driven water-splitting devices demonstrated; efficiency, safety, stability need to be addressed simultaneously	GaN:ZnO w/ RuO_2, Cr_2O_3-coated Rh cocatalysts (*123*)
Semiconductor photoelectrodes	Efficient, safe systems demonstrated; long-term stability, cost-effectiveness need to be improved	$Si/Al_{0.15}Ga_{0.85}As$ (*124*), $GaAs/GaInP_2$ (*100*)
Photovoltaic electrolysis	Demo	Si PV coupled to electrolyzer (*125*, *126*)

materials must also be cost-effective, efficient, and robust under extreme operating conditions and environments (*5*, *76*).

Solar Fuels

The direct production of fuels from sunlight could provide a scalable grid storage technology. Liquid fuels are required for ships, aircraft, and heavy-duty trucks, which collectively total 40% of current global transportation fuel demand. Solar fuels technology has thus received recent attention at the proof-of-concept R&D stage in various laboratories worldwide (*5*). The status of various approaches to solar fuels generation is summarized in Table 2. Exquisite chemical synthetic methods have been used to assemble various chlorophyll-based and -related light absorbers in conjunction with precisely connected electron donors and acceptors, to achieve separation of the light-induced electron-hole pairs produced by the chromophore of interest (*5*, *77*, *78*). The existence of the natural photosynthetic system implies that it ought to be possible to assemble a fully nonbiological photosynthetic assembly, which provides a goal for research efforts in synthetic organic, inorganic, and materials chemistry. Particles of inorganic semiconductors, in conjunction with heterogeneous cocatalysts, have been shown to act as artificial photosynthetic systems (*5*, *79*). A research goal is to develop an efficient, stable photocatalytic system that does not produce stoichiometric, flammable mixtures of H_2 and O_2 (*79*).

In artificial photosynthetic systems based on photoelectrochemical (PEC) cells, (Fig. 6), the charge separation is facilitated by an electric field that is formed at or near a semiconductor-liquid interface (*79*, *80*). Production of fuel generally requires coupling of the separated electrical charges with multielectron catalysts for the half-reactions of interest. In many respects, PEC cells represent the integration of a discrete PV module with an electrolyzer to achieve the conversion of sunlight into H_2 and O_2 by solar-driven water splitting (*79*, *81*). Regardless of how it is produced, the solar H_2 could be used in a turbine or fuel cell for grid storage, and could be used as a transportation fuel either directly as H_2, or indirectly by reacting the H_2 with CO_2 or other carbon-based feedstocks, such as biomass, to produce methanol or other reduced carbon-based fuels (*82*, *83*). Additionally, solar-derived H_2 could readily be used as a feedstock to produce ammonia, for use in agriculture, as well as in commerce and transportation.

For a solar-driven PEC-based water-splitting system to be deployed in the marketplace, the PEC system must be advantageous in cost relative to the established, discrete PV + electrolyzer (E) combination that provides the same system-level functionality (*79*). The levelized cost of H_2 (LCH) from a discrete PV+E system has been estimated to be $7 to $20/kg (*84*, *85*), because of the relatively high cost of electricity from PV in conjunction with a low capacity factor for utilization of the electrolysis unit. In contrast, the LCH produced by steam reforming of natural gas is only $2/kg (*86*). Research opportunities involve the development of a disruptive technology for electrolytic H_2 generation, noting that the chlor-alkali electrolysis process has been practiced at scale for more than a century (*87*). Storage in geologic formations has been proposed for renewable hydrogen produced by electrolysis (*88*).

In state-of-the-art polymer-electrolyte-membrane (PEM) electrolyzers, the cost of the noble metal catalysts is <6% of the total system costs (*89*). Even less expensive catalysts—based on Ni-Mo and related alloys on the cathode and mixed Ni (Fe, La, and so on) oxides on the anode—are used in alkaline electrolysis (*90*), with a facility rated to produce 100 MW of electricity constructed in the 1980s at Aswan Dam (*91*). Moreover, available electrocatalysts in acidic or alkaline media display much lower overpotentials (*92*) than available electrocatalysts operated at near-neutral pH (*93*–*95*). Hence, an integrated photoelectrochemical system must take advantage of substantial cost reductions enabled by integration, other than purely a reduction in catalyst cost, to be advantageous in cost relative to a discrete PV+E combination. Opportunities for such cost reduction are provided by synergistic integration of very inexpensive materials in novel form factors and geometries, such as arrays of semiconducting microwires in flexible polymeric membranes (*96*, *97*) coupled to earth-abundant electrocatalysts, with the system able to take up water from the atmosphere as an input feedstock (*98*).

A technology for an integrated solar fuels generator must be robust, efficient, safe, and cost-effective. At present, viable integrated systems can simultaneously meet at most three of these desiderata. Systems that are very efficient and stable are currently made from expensive, complex materials assemblies, such as a high-efficiency III–V PV tandem cell connected electrically in series with, but isolated physically from, an electrolysis cell (*99*). Use of an analogous multijunction III–V cell as a photoelectrode in an aqueous electrolyte in either a wired or wireless configuration produces H_2 transiently, because integration results in corrosion of the photoelectrode by the electrolyte (*100*, *101*). Electrodes that are cheap and robust—such as spray-painted coatings of iron oxide as photoelectrodes by themselves or with coatings of electrocatalysts—are inefficient (*5*). Electrolysis or photoelectrolysis under bulk near-neutral pH conditions (*93*, *102*–*104*) is inefficient and/or produces potentially explosive, stoichiometric mixtures of H_2 and O_2 over active catalysts for recombination of the products (*95*, *105*–*108*).

Photocathodes made from p-type indium phosphide coated with nearly transparent noble metal electrocatalyst films have yielded >13% ideal regenerative cell efficiencies for the production of H_2 from 1 M HCl (aqueous) (*109*), which illustrates the possibilities for obtaining efficient and stable photoelectrodes for solar fuels production. Operation in acidic or alkaline liquid or polymeric electrolytes is important because intrinsically safe, efficient solar-driven water-splitting systems can be built in these media (*81*, *110*). Some recent examples along this R&D path include the discovery of earth-abundant alternatives to Pt that are stable and highly active for H_2 evolution in acidic media (*111*) and the integration of earth-abundant electrocatalysts into Si microwire arrays for efficient H_2 production from acidic media (*112*). Research opportunities include methods to minimize the obscuring of light associated with typical metal and metal oxide electrocatalysts for fuel-forming half-reactions (*113*).

Porous films allow electrolyte to permeate to the underlying semiconductor and, thus, only partially mitigate deleterious corrosion or passivation processes (*114*). For oxidative processes, amorphous TiO_2 films in conjunction with Ni oxide islands (*115*), or alternatively the use of reactively sputtered Ni oxide films, have recently been shown to provide extended stability for photoanodes

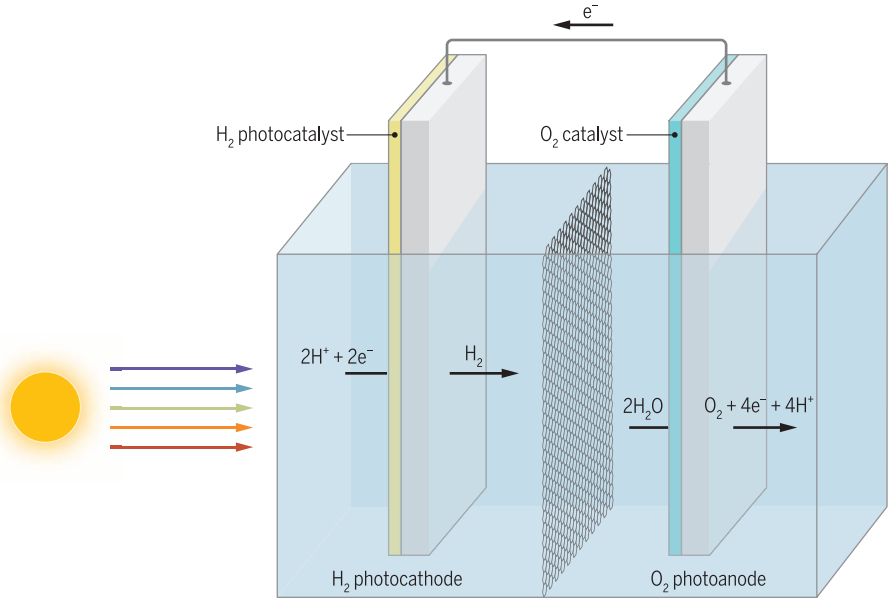

Fig. 6. Schematic of a tandem photoelectrochemical cell. The photocathode where H_2O, or H_2O and CO_2, are reduced to a fuel, and the photoanode, where water is oxidized to produce O_2. The electrodes also generally have electrocatalysts to facilitate the desired multielectron half-reactions, and the membrane is present to ensure intrinsically safe operation as well as to facilitate beneficial collection of the H_2 under a pressure differential to ensure its flow into a pipeline collection system.

performing water oxidation in alkaline media (*114*, *116*, *117*). These approaches to photoanode protection, which have shown operational stability and efficiency for water oxidation while operating continuously for thousands of hours under simulated sunlight, i.e., passing the charge equivalent to >1 year of outdoor operation (*114*), may allow for new combinations of materials to be utilized. These components will have to be combined with other materials and components at scale to realize the full potential of an integrated approach to solar fuels generation. Research opportunities also lie in the development of a cost-effective balance-of-plant that would provide feedstock water of the requisite purity, as well as facilitate the safe, cost-effective collection of the solar-derived H_2 over relatively large areas for distribution and end-use, either as H_2 or by conversion to carbon-containing fuels through known thermochemical conversion processes.

The multielectron reduction of CO_2 to a liquid fuel will require the development of entirely new, unprecedented families of catalysts to effect such a transformation in an energy-efficient and selective fashion. To date, metal electrodes require high overpotentials, are generally unstable at the required reducing potentials, and also produce a wide array of trace organic products (*118*) that would require an expensive and energy-intensive process step to separate and concentrate the products. On specific electrode surfaces, substituted pyridiniums yield partial formation of methanol and other alcohols (*119*). An engineered bacterial system has been used to produce low concentrations of isopropanol from electrolytically generated H_2 (*120*), complementing previous studies that have coupled the enzyme formate dehydrogenase to a semiconductor electrode to demonstrate the direct enzyme-catalyzed photoelectrochemical production of fuel (*121*). Extensive research efforts aim to extend the stability of such enzymes in vitro.

Other challenges for CO_2 reduction involve the flux limitations associated with utilization of atmospheric CO_2 as a sustainable CO_2 source, as well as the expense of concentration of CO_2 for use as a reagent (*122*). In conjunction with advances in materials and methods, additional systems-based technoeconomic analysis is required to ascertain whether an artificial system can be constructed, in principle, with much higher efficiency, lower cost, and utility than either natural photosynthesis or direct or indirect solar H_2 production followed by thermochemical conversion of H_2 with N_2, CO_2, or other carbon-containing reactants, such as ethylene or biofuels, to produce value-added, energy-rich fuels and/or chemicals.

Promise and potential

The remarkable progress that has been made in cost reduction and commercial deployment of solar energy technologies underscores the benefits of investment in R&D and indicates the promise of, and necessity for, continued innovation to produce further advances in the field. Both evolutionary and revolutionary technology development, involving foundational research, applied research, learning by doing, demonstration projects, and deployment at scale will be needed to continue this technology-innovation ecosystem. Relative to the embodiments of solar energy–conversion systems that have been developed to date, higher efficiencies, lower costs, improved scalability, and new functionality are in principle achievable. Hence, research, engineering and manufacturing will need to be pursued in harmony and in a sustained fashion to allow realization of the full potential of solar energy utilization, and to allow the energy in sunlight to make a material, and perhaps dominant, contribution to a sustainable, cost-effective, global energy system.

REFERENCES AND NOTES

1. C. Zheng, D. M. Kammen, An innovation-focused roadmap for a sustainable global photovoltaic industry. *Energy Policy* **67**, 159–169 (2014). doi: 10.1016/j.enpol.2013.12.006
2. J. Jean, P. R. Brown, R. L. Jaffe, T. Buonassisi, V. Bulovic, Pathways for solar photovoltaics. *Energy Environ. Sci.* **8**, 1200–1219 (2015). doi: 10.1039/C4EE04073B
3. I. S. E. Fraunhofer, *Photovoltaics Report* (2014); https://www.ise.fraunhofer.de/de/downloads/pdf-files/aktuelles/photovoltaics-report-in-englischer-sprache.pdf.
4. N. S. Lewis, Toward cost-effective solar energy use. *Science* **315**, 798–801 (2007). doi: 10.1126/science.1137014; pmid: 17289986
5. N. S. Lewis, G. Crabtree, *Basic Research Needs for Solar Energy Utilization: Report of the Basic Energy Sciences Workshop of Solar Energy Utilization*, 21 to 15 April 2005, Washington, DC [Office of Basic Energy Science, U.S. Department of Energy (DOE), Washington, DC, 2005].
6. DOE, SunShot Vision Study (2012); http://energy.gov/sites/prod/files/2014/01/f7/47927.pdf.
7. National Renewable Energy Laboratory, Efficiency chart (NREL, Golden, CO, 2015); http://www.nrel.gov/ncpv/images/efficiency_chart.jpg.
8. D. Manners, Alta devices ramping GaAs solar cells with 29% efficiency [blog], *Electronics Weekly*, 29 October 2012; http://www.electronicsweekly.com/blogs/mannerisms/manufacturing/alta-devices-ramping-gaas-sola-2012-10/.
9. M. A. Green, K. Emery, Y. Hishikawa, W. Warta, E. D. Dunlop, Solar cell efficiency tables (version 40). *Prog. Photovolt. Res. Appl.* **20**, 606–614 (2012). doi: 10.1002/pip.2267
10. Sharp Corporation, Sharp develops concentrator solar cell with world's highest conversion efficiency of 44.4% [news release] (Sharp Corp., 2013): http://www.sharp-world.com.
11. A. Polman, H. A. Atwater, Photonic design principles for ultrahigh-efficiency photovoltaics. *Nat. Mater.* **11**, 174–177 (2012). doi: 10.1038/nmat3263; pmid: 22349847
12. J. M. Russo *et al.*, Spectrum splitting metrics and effect of filter characteristics on photovoltaic system performance. *Opt. Express* **22** (Suppl 2), A528–A541 (2014). doi: 10.1364/OE.22.00A528; pmid: 24922262
13. California Energy Commission, Recycling of CdTe Thin Film Photovoltaic Panels (2012); http://docketpublic.energy.ca.gov/PublicDocuments/Compliance/09-AFC-6C%20Blythe/TN%2067267%2009-24-12%20Recycling%20of%20CdTe%20Thin%20Film%20Photovoltaic%20Panels.pdf.
14. C. Candelise, M. Winskel, R. Gross, Implications for CdTe and CIGS technologies production costs of indium and tellurium scarcity. *Prog. Photovolt. Res. Appl.* **20**, 816–831 (2012). doi: 10.1002/pip.2216
15. M. Gunther, Meteoric rise of perovskite solar cells under scrutiny over efficiencies. *Chem. World*, 2 March 2015.
16. M. A. Green, K. Emery, Y. Hishikawa, W. Warta, E. D. Dunlop, Solar cell efficiency tables (version 45). *Prog. Photovolt. Res. Appl.* **23**, 1–9 (2015). doi: 10.1002/pip.2573
17. M. A. Green, A. Ho-Baillie, H. J. Snaith, The emergence of perovskite solar cells. *Nat. Photonics* **8**, 506–514 (2014). doi: 10.1038/nphoton.2014.134
18. X. Li *et al.*, Improved performance and stability of perovskite solar cells by crystal crosslinking with alkylphosphonic acid ω-ammonium chlorides. *Nat. Chem.* **7**, 703–711 (2015). doi: 10.1038/nchem.2324; pmid: 26291941
19. E. J. Luber, M. H. Mobarok, J. M. Buriak, Solution-processed zinc phosphide (α-Zn_3P_2) colloidal semiconducting nanocrystals for thin film photovoltaic applications. *ACS Nano* **7**, 8136–8146 (2013). doi: 10.1021/nn4034234; pmid: 23952612
20. O. Vazquez-Mena *et al.*, Performance enhancement of a graphene-zinc phosphide solar cell using the electric field-effect. *Nano Lett.* **14**, 4280–4285 (2014). doi: 10.1021/nl500925n; pmid: 25058004
21. L. Lahourcade *et al.*, Structural and optoelectronic characterization of RF sputtered $ZnSnN_{(2)}$. *Adv. Mater.* **25**,

2562–2566 (2013). doi: 10.1002/adma.201204718; pmid: 23386387

22. N. Feldberg *et al.*, $ZnSnN_2$: A new earth-abundant element semiconductor for solar cells. *2012 38th IEEE Photovolt. Spec. Conf. (PVSC)*, 3 to 8 June, Austin, TX, (IEEE, 2012), pp. 2524–2527.
23. S. S. Wilson *et al.*, Interface stoichiometry control to improve device voltage and modify band alignment in ZnO/Cu_2O heterojunction solar cells. *Energy Environ. Sci.* **7**, 3606–3610 (2014). doi: 10.1039/C4EE01956C
24. T. Minami, Y. Nishi, T. Miyata, Heterojunction solar cell with 6% efficiency based on an n-type aluminum-gallium-oxide thin film and p-type sodium-doped Cu_2O sheet. *Appl. Phys. Express* **8**, 022301 (2015). doi: 10.7567/APEX.8.022301
25. A. E. Rakhshani, Preparation, characteristics and photovoltaic properties of cuprous-oxide—a review. *Solid-State Electron.* **29**, 7–17 (1986). doi: 10.1016/0038-1101(86)90191-7
26. M. Bhushan, A. Catalano, Polycrystalline Zn_3P_2 Schottky-barrier solar-cells. *Appl. Phys. Lett.* **38**, 39–41 (1981). doi: 10.1063/1.92124
27. A. J. Heeger, 25th anniversary article: Bulk heterojunction solar cells: understanding the mechanism of operation. *Adv. Mater.* **26**, 10–28 (2014). doi: 10.1002/adma.201304373; pmid: 24311015
28. L. Dou *et al.*, 25th anniversary article: A decade of organic/polymeric photovoltaic research. *Adv. Mater.* **25**, 6642–6671 (2013). doi: 10.1002/adma.201302563; pmid: 24105687
29. H. Hoppe, N. S. Sariciftci, Organic solar cells: An overview. *J. Mater. Res.* **19**, 1924–1945 (2004). doi: 10.1557/JMR.2004.0252
30. A. J. Heeger, Semiconducting polymers: The third generation. *Chem. Soc. Rev.* **39**, 2354–2371 (2010). doi: 10.1039/b914956m; pmid: 20571667
31. A. Hagfeldt, G. Boschloo, L. Sun, L. Kloo, H. Pettersson, Dye-sensitized solar cells. *Chem. Rev.* **110**, 6595–6663 (2010). doi: 10.1021/cr900356p; pmid: 20831177
32. N. Sharifi, F. Tajabadi, N. Taghavinia, Recent developments in dye-sensitized solar cells. *ChemPhysChem* **15**, 3902–3927 (2014). doi: 10.1002/cphc.201402299; pmid: 25277957
33. A. J. Nozik, Multiple exciton generation in semiconductor quantum dots. *Chem. Phys. Lett.* **457**, 3–11 (2008). doi: 10.1016/j.cplett.2008.03.094
34. M. B. Smith, J. Michl, Singlet fission. *Chem. Rev.* **110**, 6891–6936 (2010). doi: 10.1021/cr1002613; pmid: 21053979
35. M. A. Green, K. Emery, Y. Hishikawa, W. Warta, E. D. Dunlop, Solar cell efficiency tables (version 46). *Prog. Photovolt. Res. Appl.* **23**, 805–812 (2015). doi: 10.1002/pip.2637
36. A. Goodrich, T. James, M. Woodhouse, *Residential, Commercial, and Utility-Scale Photovoltaic (PV) System Prices in the United States: Current Drivers and Cost-Reduction Opportunities* (NREL, Golden, CO 2012).
37. P. V. Spot Price, (2015); http://pv.energytrend.com/pricequotes.html.
38. A. Goodrich *et al.*, A wafer-based monocrystalline silicon photovoltaics road map: Utilizing known technology improvement opportunities for further reductions in manufacturing costs. *Sol. Energy Mater. Sol. Cells* **114**, 110–135 (2013). doi: 10.1016/j.solmat.2013.01.030
39. K. Calhoun, K. Crofton, J. Goodman, R. McIntosh, *Lessons from Australia—Reducing Solar PV Costs Through Installation Labor Efficiency* (Rocky Mountain Institute and Georgia Tech Research Institute, Boulder, CO, 2014).
40. J. Morris, K. Calhoun, D. Seif, *Reducing Solar PV Soft Costs—A Focus on Installation Labor* (Rocky Mountain Institute and Georgia Tech Research Institute, Boulder, CO, 2013).
41. R. Schmalansee, *The Future of Solar Energy* (Massachusetts Institute of Technology, Cambridge, MA, 2015).
42. Energy Information Association, "Electric Power Monthly" (Energy Information Association, June 2015); http://www.eia.gov/electricity/monthly/.
43. B. Kaun, *Cost-Effectiveness of Energy Storage in California* [Electric Power Research Institute (EPRI), 2013].
44. A. A. Akhil, G. Huff, A. B. Currier, B. C. Kaun, D. M. Rastler, S. B. Chen, A. L. Cooper, D. T. Bradshaw, W. D. Gauntlett, *DOE/EPRI 2013 Electricity Storage Handbook in Collaboration with NRECA* (Sandia National Laboratories, Albuquerque, NM, 2013).
45. V. A. Boicea, Energy storage technologies: The past and the present. *Proc. IEEE* **102**, 1777–1794 (2014). doi: 10.1109/JPROC.2014.2359545
46. D. M. Rastler, *Electricity Energy Storage Technology Options* (EPRI, 2011).
47. E. Musk, Powerwall: Energy Storage for a Sustainable Home (Tesla Motors, 2015); https://www.teslamotors.com/powerwall.
48. C. Pillot, "The rechargeable battery market and main trends 2014–2025," presentation at 31st International Battery Seminar, Fort Lauderdale, 9 to 12 March 2015 (Avicenne Energy, 2015).
49. A. Barré *et al.*, A review on lithium-ion battery ageing mechanisms and estimations for automotive applications. *J. Power Sources* **241**, 680–689 (2013). doi: 10.1016/j.jpowsour.2013.05.040
50. A. C. Luntz, B. D. McCloskey, Nonaqueous Li-air batteries: A status report. *Chem. Rev.* **114**, 11721–11750 (2014). doi: 10.1021/cr500054y; pmid: 25376975
51. A. Manthiram, Y. Fu, S. H. Chung, C. Zu, Y. S. Su, Rechargeable lithium-sulfur batteries. *Chem. Rev.* **114**, 11751–11787 (2014). doi: 10.1021/cr500062v; pmid: 25026475
52. Y. Li, H. Dai, Recent advances in zinc-air batteries. *Chem. Soc. Rev.* **43**, 5257–5275 (2014). doi: 10.1039/C4CS00015C; pmid: 24926965
53. N. Alias, A. A. Mohamad, Advances of aqueous rechargeable lithium-ion battery: A review. *J. Power Sources* **274**, 237–251 (2015). doi: 10.1016/j.jpowsour.2014.10.009
54. A. Z. Weber *et al.*, Redox flow batteries: A review. *J. Appl. Electrochem.* **41**, 1137–1164 (2011). doi: 10.1007/s10800-011-0348-2
55. B. Huskinson *et al.*, A metal-free organic-inorganic aqueous flow battery. *Nature* **505**, 195–198 (2014). doi: 10.1038/nature12909; pmid: 24402280
56. Solar Power Authority, High-temperature solar thermal (HTST) technology: An overview and evaluation (Cleantech Authority, 2010); http://solarpowerauthority.com/high-temperature-solar-thermal/.
57. C. Richter, S. Teske, R. Short, *Concentrating Solar Power: Global Outlook 2009* (SolarPACES, ESTELA, Greenpeace International, 2009).
58. Wyld Group, High temperature solar thermal technology roadmap (2008); http://solarpowerauthority.com/high-temperature-solar-thermal/.
59. Photovoltaic Power Systems Programme, International EnergyAgency, *2014 Snapshot of Global PV Markets* (PVPS, IEA, Paris, 2015).
60. IEA, Solar Thermal Electricity, Technology Roadmap (IEA, Paris, 2014).
61. Solar GIS, World Map of Direct Normal Irradiation (2015); http://solargis.info/doc/_pics/freemaps/1000px/dni/SolarGIS-Solar-map-DNI-World-map-en.png.
62. America's Energy Future Panel on Electricity from Renewable Resources, *Electricity from Renewable Resources: Status, Prospects, and Impediments* (National Academy Press, Washington, DC, 2010).
63. California Council on Science and Technology, *California's Energy Future—The View to 2050* (CCST, Sacramento, CA, 2011); https://ccst.us/publications/2011/2011energy.php.
64. T. Kousksou, P. Bruel, A. Jamil, T. El Rhafiki, Y. Zeraouli, Energy storage: Applications and challenges. *Sol. Energy Mater. Sol. Cells* **120**, 59–80 (2014). doi: 10.1016/j.solmat.2013.08.015
65. H. Ghasemi *et al.*, Solar steam generation by heat localization. *Nat. Commun.* **5**, 4449 (2014). doi: 10.1038/ncomms5449; pmid: 25043613
66. Y. M. Kim, C. G. Kim, D. Favrat, Transcritical or supercritical CO_2 cycles using both low- and high-temperature heat sources. *Energy* **43**, 402–415 (2012). doi: 10.1016/j.energy.2012.03.076
67. G. Augsburger, *Thermo-Economic Optimisation of Large Solar Tower Power Plants`* (École Polytechnique Fédérale de Lausanne, Lausanne, 2013).
68. M. Joly *et al.*, Novel black selective coating for tubular solar absorbers based on a sol–gel method. *Sol. Energy* **94**, 233–239 (2013). doi: 10.1016/j.solener.2013.05.009
69. D. Kraemer *et al.*, High-performance flat-panel solar thermoelectric generators with high thermal concentration. *Nat. Mater.* **10**, 532–538 (2011). doi: 10.1038/nmat3013; pmid: 21532584
70. SDG&E Sunrise Powerlink, SDG&E Energizes Sunrise Powerlink [news release] (2012); http://regarchive.sdge.com/sunrisepowerlink/release26.html.
71. J. Kim, T. A. Johnson, J. E. Miller, E. B. Stechel, C. T. Maravelias, Fuel production from CO_2 using solar-thermal energy: System level analysis. *Energy Environ. Sci.* **5**, 8417 (2012). doi: 10.1039/c2ee21798h
72. A. Meier, A. Steinfeld, in *Solar Energy*, C. Richter, D. Lincot, C. A. Gueymard, Eds. (Springer, New York, 2013), pp. 521–552.
73. S. Abanades, G. Flamant, Thermochemical hydrogen production from a two-step solar-driven water-splitting cycle based on cerium oxides. *Sol. Energy* **80**, 1611–1623 (2006). doi: 10.1016/j.solener.2005.12.005
74. R. Perret, *Solar Thermochemical Hydrogen Production Research (STCH)* (Sandia National Laboratories, Albuquerque, NM, 2011).
75. C. L. Muhich *et al.*, Efficient generation of H_2 by splitting water with an isothermal redox cycle. *Science* **341**, 540–542 (2013). pmid: 23908235
76. A. W. Weimer *et al.*, *Development of a Solar-Thermal ZnO/Zn Water-Splitting Thermochemical Cycle* (NREL, Golden, CO, 2009).
77. D. Gust, T. A. Moore, A. L. Moore, Mimicking photosynthetic solar energy transduction. *Acc. Chem. Res.* **34**, 40–48 (2001). doi: 10.1021/ar9801301; pmid: 11170355
78. M. R. Wasielewski, Photoinduced electron transfer in supramolecular systems for artificial photosynthesis. *Chem. Rev.* **92**, 435–461 (1992). doi: 10.1021/cr00011a005
79. B. D. James, G. N. Baum, J. Perez, K. N. Baum, *Technoeconomic Analysis of Photoelectrochemical (PEC) Hydrogen Production* (DOE, Washington, DC, 2009).
80. M. G. Walter *et al.*, Solar water splitting cells. *Chem. Rev.* **110**, 6446–6473 (2010). doi: 10.1021/cr1002326; pmid: 21062097
81. J. R. McKone, N. S. Lewis, H. B. Gray, Will solar-driven water-splitting devices see the light of day? *Chem. Mater.* **26**, 407–414 (2014). doi: 10.1021/cm4021518
82. National Research Council, National Academy of Engineering, in *The Hydrogen Economy* (National Academies Press, Washington, DC, 2004), chap 1; http://www.nap.edu/read/10922/chapter/1.
83. G. A. Olah, Towards oil independence through renewable methanol chemistry. *Angew. Chem. Int. Ed. Engl.* **52**, 104–107 (2013). doi: 10.1002/anie.201204995; pmid: 23208664
84. J. I. Levene, M. K. Mann, R. Margolis, A. Milbrant, *An Analysis of Hydrogen Production from Renewable Electricity Sources* (NREL, Golden, CO, 2005).
85. R. Van Noorden, 'Artificial leaf' faces economic hurdle. *NATNEWS* (2012). doi: 10.1038/nature.2012.10703
86. S. Dillich, T. Ramsden, M. Melaina, *Hydrogen Production Cost Using Low-Cost Natural Gas: DOE Hydrogen and Fuel Cells Program Record* (DOE, Washington, DC, 2012).
87. T. F. O'Brien, T. V. Bommaraju, F. Hine, *Handbook of Chlor-Alkali Technology*. (Springer, 2005), vol. 1.
88. W. Leighty, Running the world on renewables: Hydrogen transmission pipelines and firming geologic storage. *Int. J. Energy Res.* **32**, 408–426 (2008). doi: 10.1002/er.1373
89. DOE, *FY 2014 Progress Report for the DOE Hydrogen and Fuel Cells Program* (DOE, Washington, DC, 2014).
90. K. Ayers, C. Capuano, "Economical production of hydrogen through development of novel, high-efficiency electrocatalysts for alkaline membrane electroysis," in *Proton Energy Systems, 2014 DOE Annual Progress Report: Hydrogen Production* (DOE, Washington, DC, 2014).
91. J. O. M. Bockris, B. E. Conway, E. Yeager, R. E. White, *Electrochemical Processing: Comprehensive Treatise of Electrochemistry* (Plenum Press, 1981), vol. 2.
92. C. C. McCrory *et al.*, Benchmarking hydrogen evolving reaction and oxygen evolving reaction electrocatalysts for solar water splitting devices. *J. Am. Chem. Soc.* **137**, 4347–4357 (2015). doi: 10.1021/ja510442p; pmid: 25668483
93. C. R. Cox, J. Z. Lee, D. G. Nocera, T. Buonassisi, Ten-percent solar-to-fuel conversion with nonprecious materials. *Proc. Natl. Acad. Sci. U.S.A.* **111**, 14057–14061 (2014). doi: 10.1073/pnas.1414290111; pmid: 25225379
94. M. W. Kanan, D. G. Nocera, In situ formation of an oxygen-evolving catalyst in neutral water containing phosphate and Co^{2+}. *Science* **321**, 1072–1075 (2008). doi: 10.1126/science.1162018; pmid: 18669820
95. A. Minguzzi, F.-R. F. Fan, A. Vertova, S. Rondinini, A. J. Bard, Dynamic potential–pH diagrams application to electrocatalysts for wateroxidation. *Chem. Sci.* **3**, 217–229 (2012). doi: 10.1039/C1SC00516B
96. J. M. Spurgeon *et al.*, Flexible, polymer-supported, Si wire array photoelectrodes. *Adv. Mater.* **22**, 3277–3281 (2010). doi: 10.1002/adma.201000602; pmid: 20589771
97. M. R. Shaner *et al.*, Photoelectrochemistry of core–shell tandem junction n-p^+-Si/n-WO_3 microwire array photoelectrodes. *Energy Environ. Sci.* **7**, 779–790 (2014). doi: 10.1039/C3EE43048K
98. J. M. Spurgeon, N. S. Lewis, Proton exchange membrane electrolysis sustained by water vapor. *Energy Environ. Sci.* **4**, 2993–2998 (2011). doi: 10.1039/c1ee01203g

99. S. Licht *et al*., Over 18% solar energy conversion to generation of hydrogen fuel; theory and experiment for efficient solar water splitting [reprinted from *J. Phys. Chem. B*, **104**, 8920-8924 (2000)]. *Int. J. Hydrogen Energy* **26**, 653–659 (2001). doi: 10.1016/S0360-3199(00)00133-6
100. O. Khaselev, J. A. Turner, A monolithic photovoltaic-photoelectrochemical device for hydrogen production via water splitting. *Science* **280**, 425–427 (1998). doi: 10.1126/science.280.5362.425; pmid: 9545218
101. S. S. Kocha, D. Montgomery, M. W. Peterson, J. A. Turner, Photoelectrochemical decomposition of water utilizing monolithic tandem cells. *Sol. Energy Mater. Sol. Cells* **52**, 389–397 (1998). doi: 10.1016/S0927-0248(97)00245-6
102. S. Y. Reece *et al*., Wireless solar water splitting using silicon-based semiconductors and earth-abundant catalysts. *Science* **334**, 645–648 (2011). doi: 10.1126/science.1209816; pmid: 21960528
103. F. F. Abdi *et al*., Efficient solar water splitting by enhanced charge separation in a bismuth vanadate-silicon tandem photoelectrode. *Nat. Commun.* **4**, 2195 (2013). doi: 10.1038/ncomms3195; pmid: 23893238
104. J. B. Gerken *et al*., Electrochemical water oxidation with cobalt-based electrocatalysts from pH 0-14: The thermodynamic basis for catalyst structure, stability, and activity. *J. Am. Chem. Soc.* **133**, 14431–14442 (2011). doi: 10.1021/ja205647m; pmid: 21806043
105. J. Newman, Scaling with Ohm's Law: Wired vs. wireless photoelectrochemical cells. *J. Electrochem. Soc.* **160**, F309–F311 (2013). doi: 10.1149/2.020304jes
106. J. Jin *et al*., An experimental and modeling/simulation-based evaluation of the efficiency and operational performance characteristics of an integrated, membrane-free, neutral pH solar-driven water-splitting system. *Energy Environ. Sci.* **7**, 3371–3380 (2014). doi: 10.1039/C4EE01824A
107. E. A. Hernández-Pagá *et al*., Resistance and polarization losses in aqueous buffer-membrane electrolytes for water-splitting photoelectrochemical cells. *Energy Environ. Sci.* **5**, 7582–7589 (2012). doi: 10.1039/c2ee03422k
108. J. O. Bockris, B. Dandapani, D. Cocke, J. Ghoroghchian, On the splitting of water. *Int. J. Hydrogen Energy* **10**, 179–201 (1985). doi: 10.1016/0360-3199(85)90025-4
109. E. Aharon-Shalom, A. Heller, Efficient p-InP(Rh-H Alloy) and p-InP(Re-H alloy) hydrogen evolving photocathodes. *J. Electrochem. Soc.* **129**, 2865–2866 (1982). doi: 10.1149/1.2123695
110. S. Haussener *et al*., Modeling, simulation, and design criteria for photoelectrochemical water-splitting systems. *Energy Environ. Sci.* **5**, 9922–9935 (2012). doi: 10.1039/c2ee23187e
111. J. F. Callejas *et al*., Electrocatalytic and photocatalytic hydrogen production from acidic and neutral-pH aqueous solutions using iron phosphide nanoparticles. *ACS Nano* **8**, 11101–11107 (2014). doi: 10.1021/nn5048553; pmid: 25250976
112. C. W. Roske *et al*., Comparison of the performance of CoP-coated and Pt-coated radial-junction n^+p-silicon microwire-array photocathodes for the sunlight-driven reduction of water to H_2 gas. *J. Phys. Chem. Lett.* **6**, 1679–1683 (2015).
113. L. Trotochaud, T. J. Mills, S. W. Boettcher, An optocatalytic model for semiconductor–catalyst water-splitting photoelectrodes based on in situ optical measurements on operational catalysts. *J. Phys. Chem. Lett.* **4**, 931–935 (2013). doi: 10.1021/jz4002604; pmid: 26291358
114. K. Sun *et al*., Stable solar-driven oxidation of water by semiconducting photoanodes protected by transparent catalytic nickel oxide films. *Proc. Natl. Acad. Sci. U.S.A.* **112**, 3612–3617 (2015).pmid: 25762067
115. S. Hu *et al*., Amorphous TiO_2 coatings stabilize Si, GaAs, and GaP photoanodes for efficient water oxidation. *Science* **344**, 1005–1009 (2014). doi: 10.1126/science.1251428; pmid: 24876492
116. K. Sun *et al*., Stable solar-driven water oxidation to O_2(g) by Ni-oxide-coated silicon photoanodes. *J. Phys. Chem. Lett.* **6**, 592–598 (2015). doi: 10.1021/jz5026195; pmid: 26262472
117. B. Mei *et al*., Protection of p^+-n-Si photoanodes by sputter-deposited Ir/IrO_x thin films. *J. Phys. Chem. Lett.* **5**, 1948–1952 (2014). doi: 10.1021/jz500865g; pmid: 26273878
118. E. E. Benson, C. P. Kubiak, A. J. Sathrum, J. M. Smieja, Electrocatalytic and homogeneous approaches to conversion of CO_2 to liquid fuels. *Chem. Soc. Rev.* **38**, 89–99 (2009). doi: 10.1039/B804323J; pmid: 19088968
119. G. Seshadri, C. Lin, A. B. Bocarsly, A new homogeneous electrocatalyst for the reduction of carbon dioxide to methanol at low overpotential. *J. Electroanal. Chem.* **372**, 145–150 (1994). doi: 10.1016/0022-0728(94)03300-5
120. J. P. Torella *et al*., Efficient solar-to-fuels production from a hybrid microbial-water-splitting catalyst system. *Proc. Natl. Acad. Sci. U.S.A.* **112**, 2337–2342 (2015). doi: 10.1073/pnas.1424872112; pmid: 25675518
121. B. A. Parkinson, P. F. Weaver, Photoelectrochemical pumping of enzymatic CO_2 reduction. *Nature* **309**, 148–149 (1984). doi: 10.1038/309148a0
122. American Physical Society Panel on Public Affairs, *Direct Air Capture of CO_2 with Chemicals: A Technology Assessment for the APS Panel on Public Affairs* (Office of Public Affairs, APS, Washington, DC, 2011); http://www.aps.org/policy/reports/assessments/upload/dac2011.pdf).
123. K. Maeda, K. Domen, Photocatalytic water splitting: Recent progress and future challenges. *J. Phys. Chem. Lett.* **1**, 2655–2661 (2010). doi: 10.1021/jz1007966
124. S. Licht *et al*., Efficient solar water splitting, exemplified by RuO_2-catalyzed AlGaAs/Si photoelectrolysis. *J. Phys. Chem. B* **104**, 8920–8924 (2000). doi: 10.1021/jp002083b
125. Schatz Solar Hydrogen Project, 2015); http://www.schatzlab.org/projects/archive/schatz_solar.html.
126. L. Arriaga, W. Martinez, U. Cano, H. Blud, Direct coupling of a solar-hydrogen system in Mexico. *Int. J. Hydrogen Energy* **32**, 2247–2252 (2007). doi: 10.1016/j.ijhydene.2006.10.067

ACKNOWLEDGMENTS

We acknowledge the NSF, CHE-1214152; the DOE Office of Science through the Joint Center for Artificial Photosynthesis, grant DE-SC0004993; and the DOE Office of Science, grant DE-FG02-03ER15483; and the Gordon and Betty Moore Foundation, grant 1225; for support that enabled the preparation of this Review, and M. Shaner for assistance in the preparation of this manuscript.

10.1126/science.aad1920

REPORTS

RADIO ASTRONOMY

Real-time detection of an extreme scattering event: Constraints on Galactic plasma lenses

Keith W. Bannister,[1]* Jamie Stevens,[1] Artem V. Tuntsov,[2] Mark A. Walker,[2] Simon Johnston,[1] Cormac Reynolds,[3] Hayley Bignall[3]

Extreme scattering events (ESEs) are distinctive fluctuations in the brightness of astronomical radio sources caused by occulting plasma lenses in the interstellar medium. The inferred plasma pressures of the lenses are ~10^3 times the ambient pressure, challenging our understanding of gas conditions in the Milky Way. Using a new survey technique, we discovered an ESE while it was in progress. Here we report radio and optical follow-up observations. Modeling of the radio data demonstrates that the lensing structure is a density enhancement and the lens is diverging, ruling out one of two competing physical models. Our technique will uncover many more ESEs, addressing a long-standing mystery of the small-scale gas structure of our Galaxy.

Distinctive variations in the radio light curves of quasars were first identified during routine astrometric observations with the Green Bank Interferometer (*1*); these variations were named extreme scattering events (ESEs). It was immediately recognized that the cause of the ESEs could not be intrinsic to the quasar but rather must be a foreground propagation phenomenon. The presumed model was occulting clouds at a distance of ~1 kpc, with a size of ~10^{14} cm and a high free-electron density of ~10^3 cm^{-3}. These observations revealed an immediate problem: The combination of high density and ionized gas implies pressures that are three orders of magnitude larger than the typical pressure in the diffuse interstellar medium (ISM) (*2*). Although such pressures have been observed in a very small fraction of interstellar gas (*3*, *4*), the fact that ESEs are relatively common raises the question of how such structures can form and live long enough to be detected as ESEs. There is general agreement (*5*, *6*) [with some exceptions (*7*)] that Kolmogorov turbulence in the ISM cannot generate such large, discrete, and long-lived overpressured regions, so two competing physical models have been proposed: Plasma sheets seen edge-on (*5*, *8*) provide the required column density variation but yield light curves that are at odds with the data (*9*), whereas models of cold self-gravitating clouds (*9*–*11*) solve the pressure problem but, in turn, imply that the clouds must make up a substantial fraction of the Galaxy's mass.

The interpretation of ESEs remains uncertain because existing narrow-band radio monitoring has only limited use in determining the lens properties and because no ESEs have been detected in progress at any other wavelength or modality. To date, only one ESE has been subject to follow-up observations while in progress: Q1741–038 showed no changes in H I absorption (*12*) or rotation measures (*13*), whereas very-long-baseline interferometry (VLBI) (*14*) revealed a marginal increase in the observed size of the source. To date, no observations of ESEs have been made at optical, infrared, or x-ray wavelengths.

Historically, ESEs have been difficult to find, requiring large investments in telescope time for only a limited number of detections. Lazio *et al.* (*15*), building on the work of Fiedler *et al.* (*16*), searched the largest available data set for ESEs. Their data contained dual-frequency observations of 149 sources every ~2 days, spanning 17 years. With a total of ~1200 source-years of observations, they had discovered merely ~15 events. Only a handful of other events have been discovered serendipitously (*17*–*22*), but no follow-up observations were made to shed light on the physical nature of the lensing structures.

Real-time detection of ESEs is the key to their understanding, as most properties of the lens are measurable only with intensive follow-up observations while the ESE is in progress. For example, well-sampled radio light curves permit determination of the electron column density profile. VLBI can be used to measure the angular scale and geometry of the lens in the plane of the

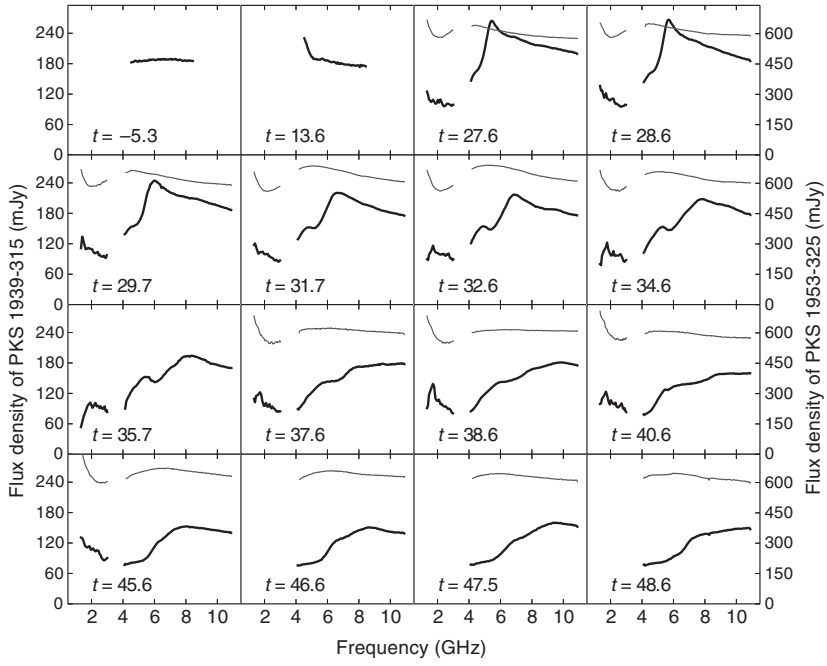

Fig. 1. The first 16 ATCA radio spectra of PKS 1939–315 (thick black lines) and near-simultaneous spectra of ATCA calibrator PKS 1953–325 (thin gray lines). t = MJD − 56800 is the observing day. The first survey spectrum at t = −5.3 showed no evidence of an ESE in PKS 1939–315, whereas the discovery spectrum during the survey on t = 13.6 showed strong evidence, with a sharp uptick below 5 GHz. On t = 27.6, we started wide-band, regular monitoring of PKS 1939–315 and an ATCA calibrator, PKS 1953–325. Where both sources were observed, they were viewed within 20 min of each other. PKS 1953–325 was not observed on the first two epochs and is weakly variable in the monitoring. All spectra have been averaged to 64-MHz channels. Measurement errors from thermal noise in each spectrum are 0.5 millijansky (mJy) (1 Jy = 10^{-26} W m^{-2} Hz^{-1}) root mean square, less than the thickness of the lines. ATCA receivers do not cover the frequencies 3.1 to 3.9 GHz.

[1]Commonwealth Scientific and Industrial Research Organisation Astronomy and Space Science, PO Box 76, Epping, New South Wales 1710, Australia. [2]Manly Astrophysics, 3/22 Cliff Street, Manly, New South Wales 2095, Australia. [3]International Centre for Radio Astronomy Research–Curtin University, Perth, Western Australia 6102, Australia.
*Corresponding author. E-mail: keith.bannister@csiro.au

sky. Temporary reddening of the background source at optical wavelengths can reveal the presence of dust in the lens, and absorption lines against the background source can measure the composition and physical conditions in the lens. Finally, changes in rotation measure can probe the lens's magnetic field. A measurement of any of these properties would represent a breakthrough and would help to explain the origin of these lenses, as well as how they form and survive. Real-time detection is required to maximize the effectiveness of follow-up resources.

We have developed an efficient technique for finding ESEs in real time, by exploiting the wideband receiver and correlator on the Australia Telescope Compact Array (ATCA) (*23*). The key to our technique is as follows: When a plasma lensing event is in progress, the radio spectrum of the background source changes from a featureless continuum to one that is highly structured. This is a result of the λ^2 dependence of the plasma refractive index (*24*), which moves the lens focus closer to the observer at some frequencies versus others. We selected a sample (*25*) of ~1000 active galactic nuclei (AGN) and observed this sample once per month, obtaining spectra in the range of 4 to 8 GHz. With only 50 s on target, we obtain a spectrum with a signal-to-noise ratio >50 in a 64-MHz channel. This is sufficient to identify an ESE in progress, simply by searching for a spectrum that is not well modeled by a smooth power law and that has changed considerably between epochs. Each survey run requires 24 hours of observation time to acquire spectra for all targets. Instantaneous identification is the key requirement for follow-up studies, which yield more useful data when initiated early in the event. The false detection rate is low, as the ESE signature depends much more on frequency than intrinsic AGN variability, which is generally modeled as broad-band synchrotron emission (*26*).

We discovered an ESE toward PKS 1939–315 on 5 June 2014 [modified Julian date (MJD) 56813], 2 months after beginning our survey, when it showed a substantial change in spectral shape near 4.5 GHz. A power-law fit to this discovery spectrum has a $\chi^2/N_{\mathrm{d.o.f.}} = 12.3$ (where $N_{\mathrm{d.o.f.}}$ is the number of degrees of freedom) (Fig. 1), indicating that an ESE was potentially in progress. Upon discovery of this ESE, we began high-cadence monitoring observations with the ATCA, made over a wider frequency range (2 to 11 GHz) than is possible in the survey mode. This monitoring revealed a double-horned light curve (Fig. 2) between time t = 0 to 100 days (t = MJD – 56800), with variations of almost a factor of three at some frequencies. The shape of this light curve is markedly similar to the light curves of some previous ESEs, although it does not have the short-lived spikes at 8 GHz that were observed for the archetypal ESE toward Q0954+658 (*1*). These data reveal strong time variability, as is typical for ESEs. Some spectra are complex, occasionally containing two distinct peaks between 4 and 8 GHz (Fig. 1).

PKS 1939–315 has been identified with a V = 20 mag (V-band magnitude) quasi-stellar object (*27*) with unknown redshift. To check for temporary reddening from dust associated with the lens, we obtained g', r', and i' band images with the Gemini South 8-m telescope. The observations bracketed the second magnification event (t = 60 to 100 days) and revealed no variability in any band within a 3σ limit of 0.5 mag (*25*). We also obtained 16 optical observations with the Small and Medium Research Telescope System (SMARTS) 1.3-m telescope on a 3-day cadence during the second magnification event, in Johnston V and Cousins R and I bands. These images also showed no evidence of variability within ~0.3 mag (3σ) (*25*).

To measure the geometry and angular scale of the lens, we obtained high-resolution, phase-referenced VLBI images with the Very Long Baseline Array (VLBA). We made observations in four bands in the range of 4 to 8 GHz with a ~2-day cadence, sampling the second magnification event. We also obtained a 12-hour observation with the Australian Long Baseline Array during the first magnification event. Each VLBI image contained only one image of the background source. We detected significant ($P = 6 \times 10^{-4}$), long-term astrometric shifts of the radio source during the ESE, which we conclude are on the order of ~1 milli-arc sec (*25*).

The wide bandwidth of the ATCA radio data permits the study of the lens over a factor of ~10 in wavelength. This corresponds to a factor of ~10^2 in the strength of the lens and provides strong constraints on lens models. Rather than restricting attention to a specific geometry and functional form for the electron column density (N_e) profile of the lens [e.g., a one-dimensional (1D) Gaussian (*28*)], we have developed a method for computing a 1D slice through the lens N_e, assuming only a geometry (*25*, *29*). The method relies on the fact that certain characteristic curves drawn through the dynamic spectrum each correspond to the same position in the lens plane. The lens properties can therefore be determined from the parameters of this family of curves.

We have applied this method, assuming two different geometries (fig. S6): a highly anisotropic geometry (appropriate for modeling an edge-on sheet) and an axially symmetric geometry (appropriate for modeling a spherical cloud or shell). We assume a distance of 1 kpc (*1*) and an effective transverse velocity of 50 km s^{-1} (*30*) for conversion to physical units.

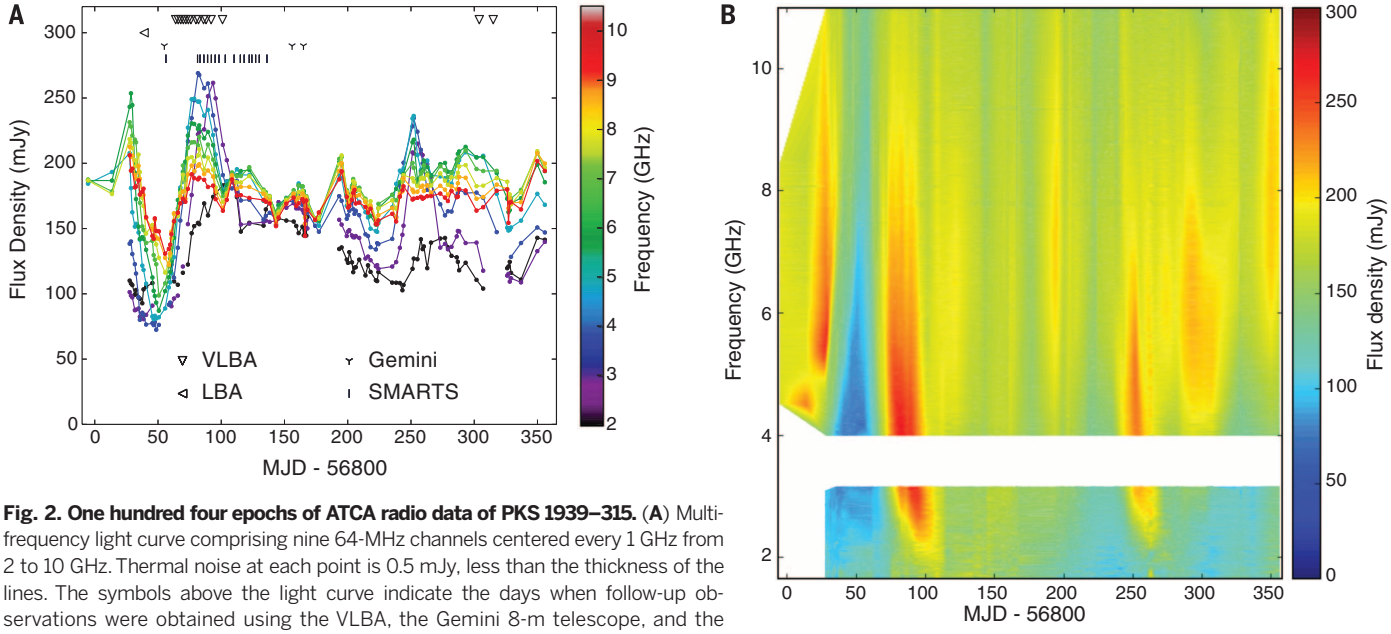

Fig. 2. One hundred four epochs of ATCA radio data of PKS 1939–315. (**A**) Multi-frequency light curve comprising nine 64-MHz channels centered every 1 GHz from 2 to 10 GHz. Thermal noise at each point is 0.5 mJy, less than the thickness of the lines. The symbols above the light curve indicate the days when follow-up observations were obtained using the VLBA, the Gemini 8-m telescope, and the SMARTS 1.3-m telescope. (**B**) Dynamic spectrum averaged to 4-MHz frequency resolution, sampled on a 1-day grid, and linearly interpolated between observing epochs. The thermal noise at each spectral point is 2 mJy. ATCA receivers do not cover the frequencies 3.1 to 3.9 GHz.

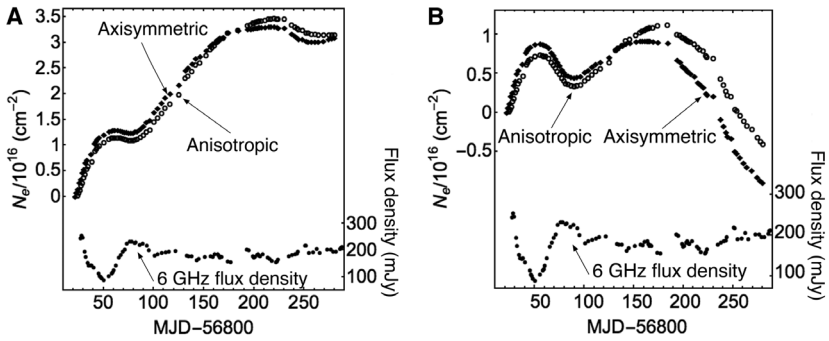

Fig. 3. Electron column density profile of the plasma lens. These column densities were constructed by modeling the ATCA photometry (supplementary materials), assuming axisymmetric and highly anisotropic geometries, a distance of 1 kpc, and transverse velocity V_{eff} = 50 km s^{-1}. To facilitate comparison with the light curve, the density profiles are shown as a function of the position that each density measurement projects to at the source at 6 GHz. Profiles as a function of the lens coordinates are shown in fig. S8. Each point corresponds to a "characteristic" drawn through the dynamic spectrum (fig. S6), which has been identified with a particular position in the lens plane. The bottom plots are identical in both panels and trace the 6-GHz light curve. (**A**) Modeled electron column density. (**B**) Electron column density with a linear trend removed to emphasize electron column density excursions. The main ESE event, centered on t = 50 days, corresponds to a local maximum in N_e, implying a divergent lens. The linear trends are 5.9 × 10^{16} and 5.2 × 10^{16} cm^{-2} year^{-1} for the axisymmetric and extremely anisotropic cases, respectively. The gradient changes from −4.3 × 10^{16} cm^{-2} year^{-1} (both geometries) to 2.4 × 10^{17} (or 1.9 × 10^{17}) cm^{-2} year^{-1} for the axisymmetric (or anisotropic) geometry. This corresponds to a change in the deflection angle of 0.43 (or 0.35) milli–arc sec under the distance and velocity assumptions.

The data do not distinguish between the two geometries. The resulting 1D slice through the electron column density of the lens looks very similar in both cases (Fig. 3). The modeled electron column density increases approximately linearly with time, with the flux density variations being produced by the small-scale electron column density variations on top of a mean gradient. In both geometries, the structure responsible for the deep flux minimum near t = 50 days is robustly modeled by a local maximum in the electron column, corresponding to a diverging lens. An overfocused, converging lens would simultaneously create a flux maximum and a focus at the higher frequencies within our observing band—a possibility that is clearly excluded by our data.

For the axisymmetric model, the impact parameter is weakly constrained to be t = 0 ± 10 days, corresponding to the lens centroid crossing the background source almost exactly. The most likely impact epoch is $t \approx -10$, and it is firmly earlier than $t \approx 0$. The peak in the N_e profile is offset from this position, which implies either a shell-like or aligned cylindrical morphology of the structure responsible for the ESE, rather than the density peaking at the symmetry center. However, because the impact parameter is zero, the relative orientation of the effective velocity vector and the plasma density contours is constant, similar to the highly anisotropic case.

We were unable to infer the geometry of the lens from the VLBI data, as multiple images of the background source were never observed, and the sizes of any time-dependent shifts were too small to be reliably detected. However, the long-lived shift of 1 milli–arc sec is comparable to the shift inferred from the change in the gradient of N_e (Fig. 3) under our distance and velocity assumptions.

Hereafter, we consider the implications of modeling the dynamic spectrum under both geometric assumptions. Under the anisotropic assumption, modeling shows that the lens is diverging rather than an overfocused converging one, which conclusively rules out the underdense current-sheet model (*8*). An overdense sheet is consistent with the data. The conclusions under the axisymmetric assumption are less clear. A spherical cloud model would appear to be discounted, owing to the offset between the peak in the column density and the center of symmetry. But although a shell-like morphology implied in the axisymmetric model is qualitatively consistent with the cold-cloud prediction, where a cloud of self-gravitating neutral gas is surrounded by an ionized shell (*9*–*11*), how the mean gradient fits into that picture is unclear.

Our best lens models exhibit column density changes of ~10^{16} cm^{-2} over transverse scales of ~10^{13} cm [20 days at 50 km s^{-1} in Fig. 2, or see (*25*) or (*29*)], yielding gradients of ~10^{3} cm^{-3}. If the plasma structure responsible for the lensing is not highly elongated along the line of sight, that gradient should be comparable to the volume density of electrons in the plasma. For the material to be thermally ionized, its temperature must be $T \gtrsim 3 \times 10^3$ K, which yields a plasma pressure of $2n_eT \gtrsim 6 \times 10^6$ K cm^{-3} (where n_e is the volume density of electrons), in accordance with previous estimates of ESEs and ~2 × 10^{3} higher than the typical pressure in the diffuse interstellar medium (*2*).

In the case of PKS 1939–315, we have ruled out a converging lens, measured a VLBI astrometric shift, and determined the form of the column density profile. Our work, combined with future surveys, should generate a statistically significant sample of well-studied lenses, which will determine the overall covering fraction, optical depth, and spatial distribution of ESE lenses. Some fraction of those ESEs should create multiple images of the background source resolvable with VLBI, which will enable the geometry to be unambiguously determined. Such surveys may unveil a substantial component of the Milky Way ISM.

REFERENCES AND NOTES

1. R. L. Fiedler, B. Dennison, K. J. Johnston, A. Hewish, *Nature* **326**, 675–678 (1987).
2. S. R. Kulkarni, C. Heiles, in *Neutral Hydrogen and the Diffuse Interstellar Medium* (Springer, 1988), pp. 95–153.
3. E. B. Jenkins, T. M. Tripp, *Astrophys. J. Suppl. Ser.* **137**, 297–340 (2001).
4. E. B. Jenkins, T. M. Tripp, *Astrophys. J.* **734**, 65 (2011).
5. R. W. Romani, R. D. Blandford, J. M. Cordes, *Nature* **328**, 324–326 (1987).
6. B. J. Rickett, A. G. Lyne, Y. Gupta, *Mon. Not. R. Astron. Soc.* **287**, 739–752 (1997).
7. M. Hamidouche, J.-F. Lestrade, *Astron. Astrophys.* **468**, 193–203 (2007).
8. U.-L. Pen, L. King, *Mon. Not. R. Astron. Soc.* **421**, L132–L136 (2012).
9. M. A. Walker, in *SINS - Small Ionized and Neutral Structures in the Diffuse Interstellar Medium*, M. Haverkorn, W. M. Goss, Eds. [Astronomical Society of the Pacific (ASP) Conference Series, ASP, 2007], vol. 365, p. 299.
10. R. N. Henriksen, L. M. Widrow, *Astrophys. J.* **441**, 70–76 (1995).
11. M. Walker, M. Wardle, *Astrophys. J.* **498**, L125–L128 (1998).
12. T. J. W. Lazio *et al.*, *Astrophys. J.* **546**, 267–272 (2001).
13. A. W. Clegg, A. L. Fey, R. L. Fiedler, *Astrophys. J.* **457**, L23 (1996).
14. T. J. W. Lazio *et al.*, *Astrophys. J.* **534**, 706–717 (2000).
15. T. J. W. Lazio *et al.*, *Astrophys. J. Suppl. Ser.* **136**, 265–392 (2001).
16. R. Fiedler, B. Dennison, K. J. Johnston, E. B. Waltman, R. S. Simon, *Astrophys. J.* **430**, 581–594 (1994).
17. I. Cognard *et al.*, *Nature* **366**, 320–322 (1993).
18. G. Cimò *et al.*, *Publ. Astron. Soc. Aust.* **19**, 10–13 (2002).
19. V. Maitia, J.-F. Lestrade, I. Cognard, *Astrophys. J.* **582**, 972–977 (2003).
20. T. Savolainen, Y. Y. Kovalev, *Astron. Astrophys.* **489**, L33–L36 (2008).
21. C. E. Senkbeil *et al.*, *Astrophys. J.* **672**, L95–L98 (2008).
22. A. B. Pushkarev *et al.*, *Astron. Astrophys.* **555**, A80 (2013).
23. W. E. Wilson *et al.*, *Mon. Not. R. Astron. Soc.* **416**, 832–856 (2011).
24. T. H. Stix, *Waves in Plasmas* (American Institute of Physics, 1992).
25. Materials and methods are available as supplementary materials on *Science* Online.
26. E. Valtaoja *et al.*, *Astron. Astrophys.* **254**, 71–79 (1992).
27. E. K. Mahony *et al.*, *Mon. Not. R. Astron. Soc.* **417**, 2651–2675 (2011).
28. A. W. Clegg, A. L. Fey, T. J. W. Lazio, *Astrophys. J.* **496**, 253–266 (1998).
29. A. V. Tuntsov *et al.*, http://arxiv.org/abs/1512.03411 (2015).
30. B. J. Rickett, L. Kedziora-Chudczer, D. L. Jauncey, *Astrophys. J.* **581**, 103–126 (2002).

ACKNOWLEDGMENTS

We thank R. Ekers for valuable discussions in the preparation of this paper, P. Edwards for scheduling the ATCA and Australian Long Baseline Array observations, J. Ogle for scheduling the VLBA observations, and the staff at the Narrabri facility for facilitating access to the ATCA. Full acknowledgments are available in the supplementary materials. All data described in this paper are attached to the supplementary materials. We report no conflicts of interest.

SUPPLEMENTARY MATERIALS

www.sciencemag.org/content/351/6271/354/suppl/DC1
Materials and Methods
Supplementary Text
Figs. S1 to S9
Table S1
References (*31*–*43*)
Data Files and Analysis Script

10 June 2015; accepted 2 December 2015
10.1126/science.aac7673

APPLIED OPTICS

Photonic chip–based optical frequency comb using soliton Cherenkov radiation

V. Brasch,[1] M. Geiselmann,[1] T. Herr,[1]* G. Lihachev,[2,3] M. H. P. Pfeiffer,[1] M. L. Gorodetsky,[2,3] T. J. Kippenberg[1]†

Optical solitons are propagating pulses of light that retain their shape because nonlinearity and dispersion balance each other. In the presence of higher-order dispersion, optical solitons can emit dispersive waves via the process of soliton Cherenkov radiation. This process underlies supercontinuum generation and is of critical importance in frequency metrology. Using a continuous wave–pumped, dispersion-engineered, integrated silicon nitride microresonator, we generated continuously circulating temporal dissipative Kerr solitons. The presence of higher-order dispersion led to the emission of red-shifted soliton Cherenkov radiation. The output corresponds to a fully coherent optical frequency comb that spans two-thirds of an octave and whose phase we were able to stabilize to the sub-Hertz level. By preserving coherence over a broad spectral bandwidth, our device offers the opportunity to develop compact on-chip frequency combs for frequency metrology or spectroscopy.

Optical solitons are propagating pulses of light that retain their temporal and spectral shape as the result of a balance between nonlinearity and dispersion (*1*). In the presence of higher-order dispersion, optical solitons can emit soliton Cherenkov radiation (*2*, *3*). This process, also known as dispersive wave generation, is one of the key nonlinear frequency conversion mechanisms of coherent supercontinuum generation (*4*), which allows a substantial increase in the spectral bandwidth of pulsed laser sources. The generation of a coherent supercontinuum from a pulsed laser propagating through a photonic crystal fiber has enabled the first self-referenced optical frequency combs (*5*, *6*) and has given access to coherent broadband spectra for frequency combs with repetition rates up to ~10 GHz.

One route to broadband frequency combs with higher repetition rates was established with the discovery of microresonator (Kerr) frequency combs (*7*, *8*). Since then, the field of microresonator frequency combs has made substantial advances (*9*–*11*), including frequency comb generation in complementary metal-oxide semiconductor (CMOS)–compatible silicon nitride (Si_3N_4, henceforth SiN) photonic chips (*12*, *13*) and a detailed understanding of the comb formation process (*14*–*17*). However, it has been a challenge to achieve broadband frequency combs that are coherent (*18*, *19*). Recently, temporal dissipative Kerr solitons (DKSs)—analogous to dissipative cavity solitons (*20*, *21*) in fiber loop cavities—have been observed in crystalline microresonators (*19*), leading to coherent frequency combs. These solitons, which balance dispersion and loss via the Kerr nonlinearity, can be generated spontaneously from chaotic Kerr frequency combs when tuning the pump laser through the cavity resonance (*19*). Recent numerical simulations (*16*, *17*, *19*) have predicted that such solitons in the presence of soliton Cherenkov radiation (*3*, *16*, *22*) can provide a path to the reliable generation of broadband and coherent frequency combs, which can even span a full octave.

The resonance frequencies of one mode family in a microresonator can be approximated around ω_0 as a Taylor series:

$$\omega_\mu = \omega_0 + \sum_{j=1} \frac{D_j \mu^j}{j!} \quad (1)$$

where $\mu \in Z$ is the relative mode number, $D_1/2\pi$ is the free spectral range of the resonator, D_2 is related to the group velocity dispersion (GVD) parameter β_2 by $D_2 = -(c/n)D_1^2\beta_2$, and D_3, D_4, ... are related to higher-order dispersion. Figure 1E shows the integrated dispersion $D_{int}(\mu)$ relative to the pump mode at $\mu = 0$; that is,

$$D_{int}(\mu) \equiv \omega_\mu - (\omega_0 + D_1\mu) = \frac{D_2\mu^2}{2!} + \frac{D_3\mu^3}{3!} + \ldots \quad (2)$$

When pumping a microresonator with a continuous wave (CW) laser with frequency ω_P near ω_0, the dynamics of this system can be described by a master equation,

$$\frac{\partial A}{\partial t} + i\sum_{j=2} \frac{D_j}{j!}\left(\frac{\partial}{i\partial\varphi}\right)^j A - ig\left(1 + \frac{iD_1}{\omega_0}\frac{\partial}{\partial\varphi}\right)|A|^2 A = -\left[\frac{\kappa}{2} + i(\omega_0 - \omega_P)\right]A + \sqrt{\frac{\kappa\eta P_{in}}{\hbar\omega_0}} \quad (3)$$

(*14*, *17*, *22*), where

$$A(\varphi, t) = \sum_\mu A_\mu \exp[i\mu\varphi - i(\omega_\mu - \omega_0)t] \quad (4)$$

is the slowly varying field amplitude; φ is the azimuthal angular coordinate inside the resonator, corotating with a soliton; $g = \hbar\omega_0^2 c n_2 / n^2 V_{eff}$ is the nonlinear (per photon) Kerr coupling coefficient [where $\hbar$ is Planck's constant divided by 2π, c is the speed of light in vacuum, n and n_2 are the linear and nonlinear (Kerr) refractive indices of the material, and $V_{eff} = A_{eff}L$ is the effective nonlinear mode volume (where A_{eff} is the effective nonlinear mode area and L is the cavity length)]; κ is the cavity decay rate; η is the coupling efficiency; and P_{in} is the pump power inside the bus waveguide. Formally, this equation is identical to the Lugiato-Lefever equation (*16*, *17*) (a damped, driven nonlinear Schrödinger equation). For anomalous GVD and in the absence of third- and higher-order dispersion, approximate solutions can correspond to bright temporal solitons superimposed on a CW background:

$$A(\varphi) \approx A_{CW} + A_1 \sum_{j=1}^{N} \mathrm{sech}\left[\sqrt{\frac{2(\omega_0 - \omega_P)}{D_2}}(\varphi - \varphi_j)\right] \exp(i\psi_0) \quad (5)$$

with φ_j corresponding to the relative angular position of the jth soliton. Amplitude A_1, phase ψ_0, and background A_{CW} are determined by the system's parameters. The minimal pulse duration is given by

$$\Delta t_{min} \approx 2\sqrt{\frac{nD_2}{cD_1^2}\frac{1}{\gamma\mathcal{F}P_{in}}} \quad (6)$$

(*19*), where $\mathcal{F}$ is the resonator finesse and $\gamma = \omega n_2 / c A_{eff}$. These temporal dissipative Kerr solitons have been generated in fiber cavities (*21*) and have been observed in crystalline microresonators recently (*19*). When higher-order dispersion terms are present, the shape and velocity of the stationary solitons change as they develop radiative tails (*3*, *23*, *24*). The spectrum of such a perturbed soliton becomes asymmetric, with its maximum shifted away from the pump frequency and an additional, local maximum (Fig. 1E) is generated (also called a dispersive wave). Because the radiative tail is emitted from the soliton, an analogy to Cherenkov radiation can be drawn (*3*).

The spectral position of the Cherenkov radiation is approximately given by the linear phase-matching condition (*2*, *25*) $D_{int}(\mu_{DW}) = 0$ at $\mu_{DW} = (-3D_2/D_3)$ for $D_4 = 0$. In the presence of D_4, two peaks of Cherenkov radiation may occur at

$$\mu_{DW} = \frac{-2D_3}{D_4} \pm \sqrt{\left(\frac{2D_3}{D_4}\right)^2 - \frac{12D_2}{D_4}} \quad (7)$$

Our experimental platform is based on silicon nitride optical microresonators, which are very suitable for nonlinear optical applications (*13*, *26*). We used SiN ring resonators (thickness 800 nm, diameter 238 μm) embedded in SiO_2 (Fig. 1, A to

[1]École Polytechnique Fédérale de Lausanne (EPFL), CH-1015 Lausanne, Switzerland. [2]Russian Quantum Center, Skolkovo 143025, Russia. [3]Faculty of Physics, M. V. Lomonosov Moscow State University, Moscow 119991, Russia.
*Present address: Centre Suisse d'Electronique et Microtechnique SA (CSEM), CH-2002 Neuchâtel, Switzerland. †Corresponding author. E-mail: tobias.kippenberg@epfl.ch

D), resulting in anomalous GVD for wavelengths around 1.5 μm. The microresonator fabrication was optimized so as to mitigate avoided crossings of different mode families that can locally alter dispersion (*27*, *28*). Measurements of the dispersion (*28*) revealed that around the pump wavelength, the mode structure closely approaches a purely anomalous GVD (Fig. 2B and fig. S2), with a measured $D_2/2\pi$ = 2.4 ± 0.1 MHz, in close agreement with finite element method modeling that yields $D_2/2\pi$ = 2.6 MHz (*28*). When pumping the resonator's TM_{00} mode family at 1560 nm via the bus waveguide, we observed discontinuities in the cavity transmission and converted frequency comb light (figs. S1 and S5A) as well as a narrowing of the repetition rate beat note (fig. S1, C and D), signatures previously associated with dissipative Kerr soliton formation (*19*).

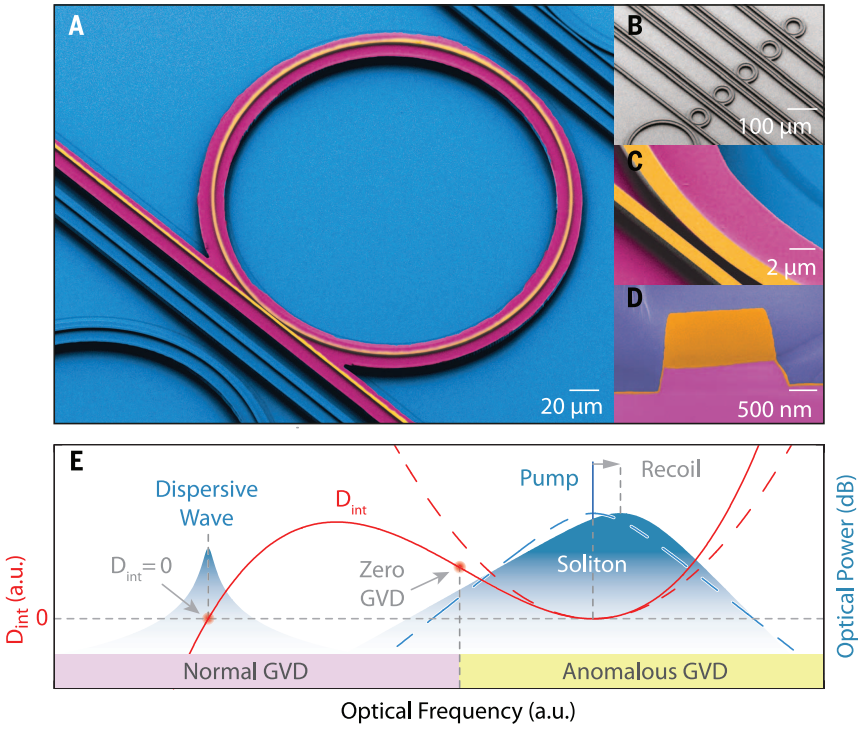

Fig. 1. Temporal soliton generation and soliton Cherenkov radiation in a planar SiN microresonator on a photonic chip. (**A**) Colored scanning electron microscopy images of a SiN optical microresonator with the same geometry as the one used but without the SiO_2 encapsulation. Blue, silicon substrate; magenta, SiO_2 pedestal; orange, SiN waveguide. (**B**) An image of resonators at lower magnification. (**C**) A close-up of the coupling region between bus waveguide and resonator (similar geometry as used, but the two waveguides have the same width in the sample used in this work). (**D**) A cross section of a device that also shows the top cladding (SiO_2, colored purple). (**E**) A schematic of the integrated dispersion $D_{int}(\mu)$ and the associated soliton dynamics with the Cherenkov radiation at D_{int} = 0. Regions with positive curvature have anomalous group velocity dispersion (GVD); regions with negative curvature have normal GVD. Around the pump $D_{int}(\mu)$ can be approximated by a parabola (red dashed line) as it is dominated by quadratic, anomalous GVD.

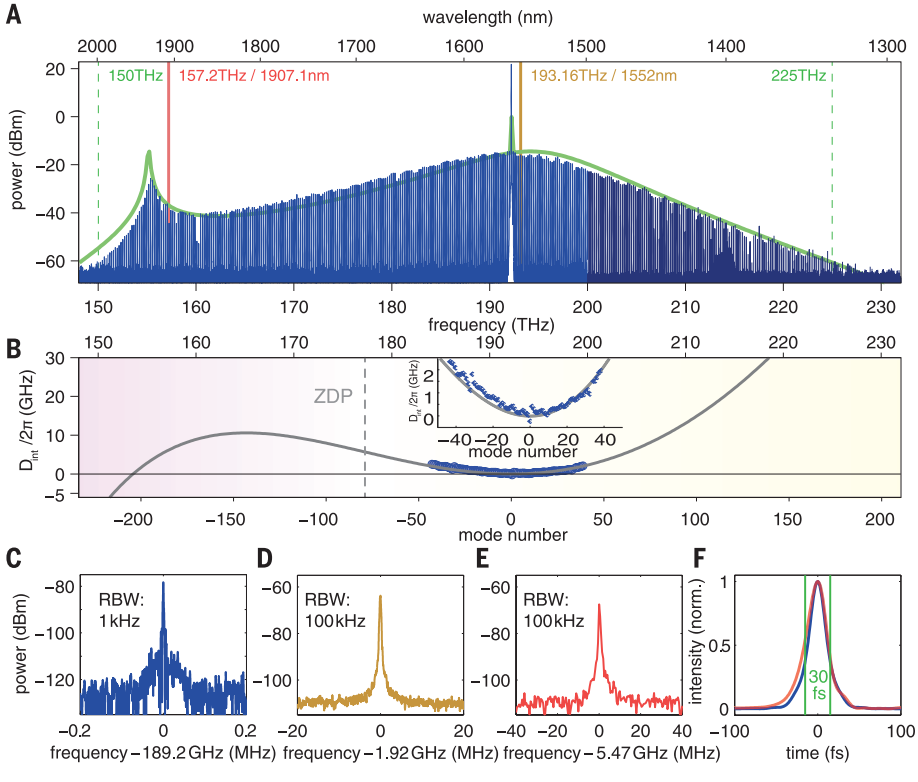

Fig. 2. Single optical dissipative Kerr soliton and soliton Cherenkov radiation in a SiN chip based optical microresonator. (**A**) The optical spectrum shows the $sech^2$ shape of a single soliton (with a 3-dB width of 10.8 THz) and the soliton Cherenkov radiation at 155 THz. The green dashed lines mark a span of two-thirds of an octave. The green solid line denotes the simulated spectral envelope. The different blue colors indicate measurements done with two different optical spectrum analyzers. (**B**) The integrated dispersion D_{int} from finite element method simulations for the measured resonator geometry (gray solid line). The gray dashed line indicates the zero dispersion point. The blue dots around 0 (inset shows a zoom-in) are measured positions of around 80 resonances which show good agreement with the simulated dispersion. (**C**) The repetition rate beat note of the frequency comb at the line spacing of 189.22 GHz shows a narrow linewidth of ~1 kHz. (**D** and **E**) The measured beat note of the generated frequency comb with a narrow linewidth reference laser positioned at 1552.0 nm [(D), orange line in (A)] and at 1907.1 nm [(E), red line in (A)]. (**F**) The intensity profile of the soliton pulse inside the resonator estimated from the measured spectrum (blue) and taken directly from the numerical simulation, with full width at half maximum (FWHM) below 30 fs. The red profile shows a small asymmetry due to the effect of the Cherenkov radiation.

To access the soliton states in a steady state, we developed a laser tuning technique to overcome instabilities associated with the discontinuous transitions of the soliton states (*28*), allowing stable soliton operation for hours (fig. S7). The optical single-soliton spectrum with $P_{in} \approx 2$ W shown in Fig. 2A has several salient features: (i) It covers a bandwidth of two-thirds of an octave. (ii) It exhibits the characteristic sech^2 spectral envelope near the pump that is associated with temporal solitons. The 3-dB bandwidth of 10.8 THz corresponds to 29-fs optical pulses. (iii) The sharp feature around 1930 nm (155 THz) corresponds to the soliton Cherenkov radiation (*16*, *22*). Figure 2B shows the measured and simulated dispersion. The spectral position of the Cherenkov radiation at $\mu = -195$ is in good agreement with the linear phase-matching condition that occurs for $D_{int}(\mu_{DW}) = 0$ at $\mu_{DW} = -200$ with the simulated parameters $D_2/2\pi = 2.6$ MHz, $D_3/2\pi = 24.5$ kHz, and $D_4/2\pi = -290$ Hz (fig. S8).

Also shown in Fig. 2A is a numerically simulated spectrum [based on coupled mode equations (*28*)]. It shows only small deviations from the experimental spectrum, caused by effects that are not included in the simulations (*28*). In particular, the absence of the soliton recoil (Fig. 1E), which is associated with the formation of a dispersive wave (*23*, *24*), is attributed to the cancellation via the soliton Raman self-frequency shift (*28*, *29*). The good agreement with the experimental data establishes numerical simulations as a powerful predictive tool for soliton dynamics in microresonators.

To investigate a key property of a frequency comb, its coherence, we first measured the repetition rate beat note of 189.2 GHz on a photodiode by means of amplitude modulation downmixing (*28*, *30*) (fig. S5B). Figure 2C shows the resulting beat note, which exhibits a narrow linewidth and a signal-to-noise ratio of 40 dB in 100 kHz bandwidth, demonstrating the coherent nature of the spectrum. We also recorded the low-frequency intensity noise of the transmitted light of the soliton state and found no excess noise relative to the pump laser noise (fig. S4). To locally investigate the coherence of the Cherenkov radiation, we carried out additional CW heterodyne beat note measurements at 1907 nm, which exhibited a narrow linewidth around 1 MHz (Fig. 2E). Simultaneously with the beat at 1907 nm, we measured the beat with a laser at 1552 nm. The resulting beat note was similar in width to the in-loop beat of the frequency-stabilized pump laser (~300 kHz). These measurements prove that the entire spectrum is coherent, in contrast to earlier reports (*18*). It is useful to contrast the single-soliton state to the incoherent high-noise state; we observed in the high-noise case a spectrum that markedly deviates from the single-soliton spectrum in terms of the shape of the Cherenkov radiation peak and the shape of the spectrum around the pump (fig. S4K).

Our system also allows us to access states with multiple solitons in the resonator. Figure 3, A to C, shows the optical spectra of three multisoliton states, which are coherent (fig. S3) and stable for hours (fig. S7). The generated spectra show pronounced variations in the spectral envelope that arise from the interference of the Fourier components of the individual solitons, as described by the spectral envelope function

$$I(\mu) = \left| \sum_{j=1}^{N} \exp(i\varphi_j \mu) \right|^2 \quad (8)$$

The insets of Fig. 3, A to C, show the reconstructed relative positions of the solitons inside the resonator for the different spectra (*28*). Figure 3B shows the case where two solitons are almost perfectly opposite to each other in the resonator, resulting in an effectively doubled line spacing. Figure 3C shows that a higher number of cavity solitons ($N = 3$) results in a spectrum with more complex spectral modulations.

To prove the usability of our system for metrological applications, we implemented a full phase stabilization of the spectrum by phase-locking the pump laser and the repetition rate of the SiN comb to a common radio-frequency reference. For absolute frequency stabilization of

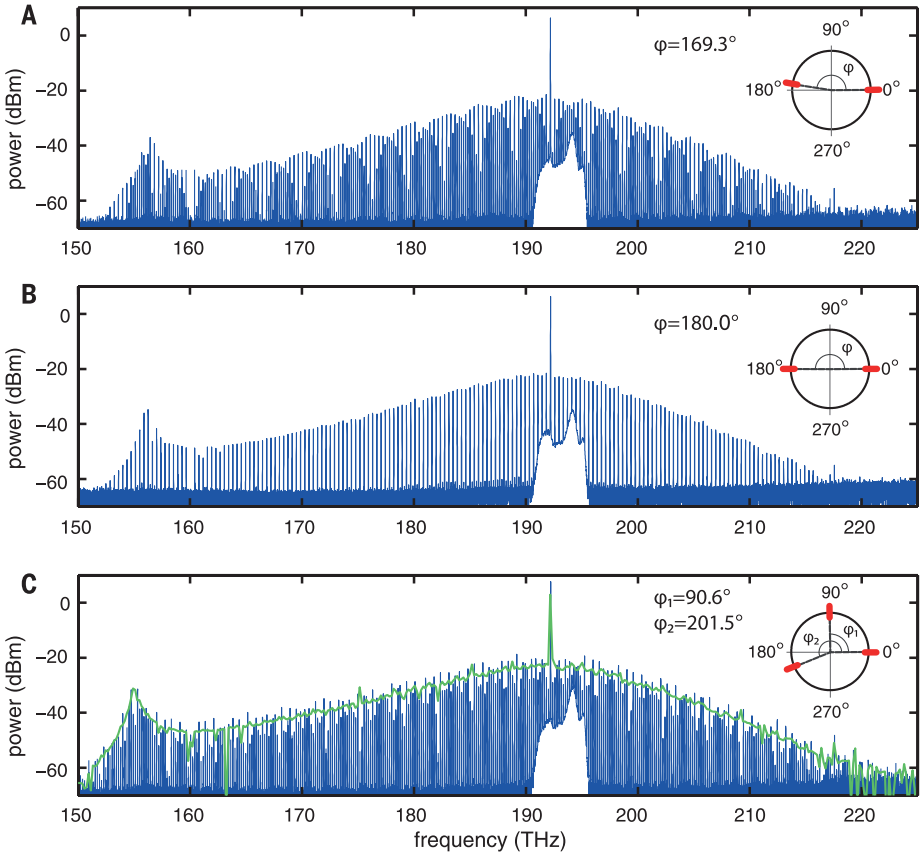

Fig. 3. Multisoliton states in a planar SiN microresonator on a photonic chip. (**A** to **C**) Spectra for multisoliton states and the relative phase position of the solitons inside the microresonator shown in the insets according to the field autocorrelation (Fourier transform of the intensity spectrum). (A) and (B) show two-soliton states; (C) shows a three-soliton state with the derived single-soliton spectral envelope (solid green line).

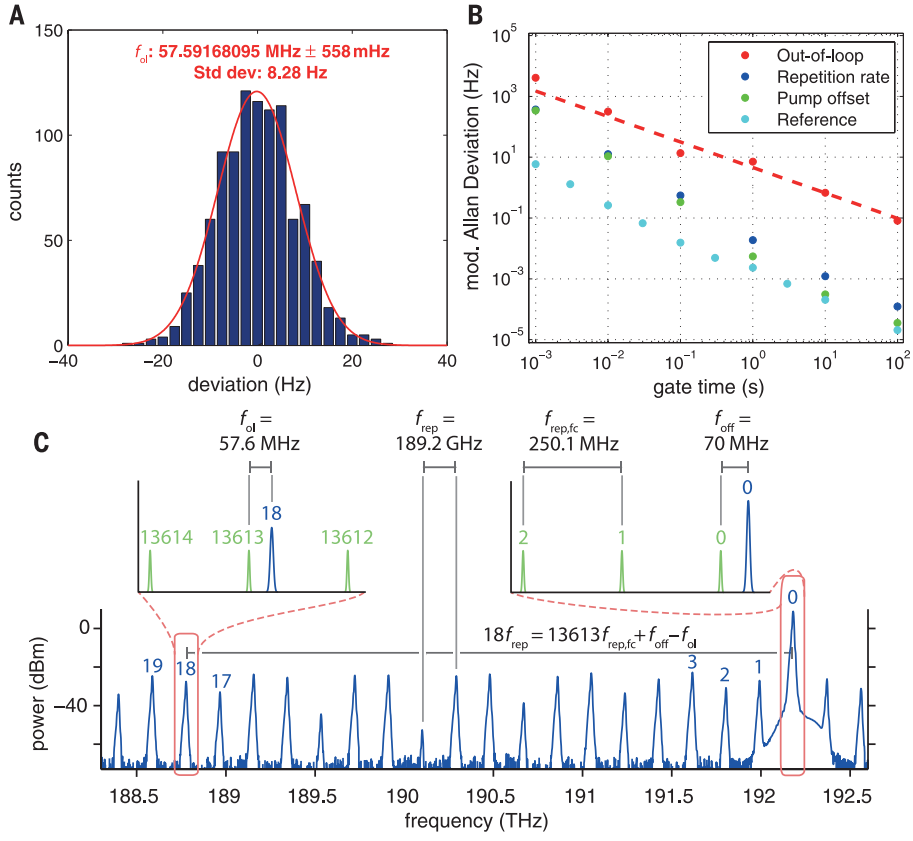

Fig. 4. Full phase stabilization and absolute frequency accuracy measurement of dissipative Kerr solitons in a SiN microresonator. (**A**) Histogram of the frequency counter measurement for the out-of-loop beat of the stabilized microresonator frequency comb with a commercial fiber laser frequency comb. Gate time is 1 s. The Gaussian fit gives the exact frequency of the beat (f_{ol}). The stabilized state shown here is a two-soliton state. (**B**) The modified Allan deviation of the out-of-loop beat as well as the in-loop signals for the two locks of the repetition rate and the pump laser offset of the microresonator frequency comb. All signals average down over the gate time, as expected for coherent signals. (**C**) A scheme highlighting the principle of the frequency accuracy measurement referenced to a self-referenced fiber frequency comb. The out-of-loop beat is between the 18th line on the red side of the pump of the microresonator frequency comb and the 13,613th line of the reference comb counted from the line to which the pump laser is locked.

the pump laser, we used an offset lock to a self-referenced fiber laser frequency comb (*28*, *31*). In Fig. 4B, we show the modified Allan deviation of the in-loop signals and an out-of-loop signal that consists of the beat of one comb tooth of the SiN comb (mode number –18) with one tooth of the reference comb. For all three signals, the modified Allan deviation averages down with increasing gate time.

The out-of-loop measurement also allows us to compare the absolute frequency accuracy of the soliton Cherenkov radiation–based comb state with the fiber laser reference comb. Taking into account all locked frequencies as shown in Fig. 4C, and extracting the center frequency of the out-of-loop signal from frequency counter measurements shown in Fig. 4A, we derive a frequency difference of $\Delta = (18 \times f_{rep}) - (13{,}613 \times f_{rep,fc}) - f_{off} + f_{ol} = 25 \pm 558$ mHz for the 1000-s measurement. We therefore validate the accuracy of the SiN soliton frequency comb to the sub-Hz level and verify the relative accuracy (with respect to the optical carrier) to 3×10^{-15}.

The observation of soliton Cherenkov radiation in a photonic chip–based microresonator provides a path to numerically predictable, fully coherent frequency comb spectra, with increased bandwidth that extends into the normal GVD regime. The currently achieved coherent two-thirds of an octave can be self-referenced by doubling and tripling the high and low end of the spectrum, respectively (*2f-3f* technique), and the bandwidth can be extended to a full octave with modified dispersion designs.

REFERENCES AND NOTES

1. A. Hasegawa, M. Matsumoto, *Optical Solitons in Fibers* (Springer, 2003).
2. P. K. Wai, C. R. Menyuk, Y. C. Lee, H. H. Chen, *Opt. Lett.* **11**, 464–466 (1986).
3. N. Akhmediev, M. Karlsson, *Phys. Rev. A* **51**, 2602–2607 (1995).
4. D. V. Skryabin, A. V. Gorbach, *Rev. Mod. Phys.* **82**, 1287–1299 (2010).
5. T. Udem, R. Holzwarth, T. W. Hänsch, *Nature* **416**, 233–237 (2002).
6. S. T. Cundiff, J. Ye, *Rev. Mod. Phys.* **75**, 325–342 (2003).
7. P. Del'Haye *et al.*, *Nature* **450**, 1214–1217 (2007).
8. T. J. Kippenberg, R. Holzwarth, S. A. Diddams, *Science* **332**, 555–559 (2011).
9. F. Ferdous *et al.*, *Nat. Photonics* **5**, 770–776 (2011).
10. S. B. Papp *et al.*, *Optica* **1**, 10–14 (2014).
11. J. Pfeifle *et al.*, *Nat. Photonics* **8**, 375–380 (2014).
12. J. S. Levy *et al.*, *Nat. Photonics* **4**, 37–40 (2010).
13. D. J. Moss, R. Morandotti, A. L. Gaeta, M. Lipson, *Nat. Photonics* **7**, 597–607 (2013).
14. A. B. Matsko *et al.*, *Opt. Lett.* **36**, 2845–2847 (2011).
15. T. Herr *et al.*, *Nat. Photonics* **6**, 480–487 (2012).
16. S. Coen, H. G. Randle, T. Sylvestre, M. Erkintalo, *Opt. Lett.* **38**, 37–39 (2013).
17. Y. K. Chembo, C. R. Menyuk, *Phys. Rev. A* **87**, 053852 (2013).
18. P. Del'Haye *et al.*, *Phys. Rev. Lett.* **107**, 063901 (2011).
19. T. Herr *et al.*, *Nat. Photonics* **8**, 145–152 (2014).
20. N. Akhmediev, A. Ankiewicz, *Dissipative Solitons: From Optics to Biology and Medicine* (Springer-Verlag, 2008).
21. F. Leo *et al.*, *Nat. Photonics* **4**, 471–476 (2010).
22. M. R. E. Lamont, Y. Okawachi, A. L. Gaeta, *Opt. Lett.* **38**, 3478–3481 (2013).
23. C. Milián, D. V. Skryabin, *Opt. Express* **22**, 3732–3739 (2014).
24. J. K. Jang, M. Erkintalo, S. G. Murdoch, S. Coen, *Opt. Lett.* **39**, 5503–5506 (2014).
25. M. Erkintalo, Y. Q. Xu, S. G. Murdoch, J. M. Dudley, G. Genty, *Phys. Rev. Lett.* **109**, 223904 (2012).
26. M. A. Foster *et al.*, *Opt. Express* **19**, 14233–14239 (2011).
27. T. Herr *et al.*, *Phys. Rev. Lett.* **113**, 123901 (2014).
28. See supplementary materials on *Science* Online.
29. C. Milián, A. V. Gorbach, M. Taki, A. V. Yulin, D. V. Skryabin, *Phys. Rev. A* **92**, 033851 (2015).
30. P. Del'Haye, S. B. Papp, S. A. Diddams, *Phys. Rev. Lett.* **109**, 263901 (2012).
31. P. Del'Haye, O. Arcizet, A. Schliesser, R. Holzwarth, T. J. Kippenberg, *Phys. Rev. Lett.* **101**, 053903 (2008).

ACKNOWLEDGMENTS

Supported by European Space Agency contracts ESTEC CN 4000108280/12/NL/PA and ESTEC CN 4000105962/12/NL/PA, the Swiss National Science Foundation, and contract W911NF-11-1-0202 from the Defense Advanced Research Projects Agency, Defense Sciences Office. This material is based on work supported by the Air Force Office of Scientific Research, Air Force Material Command, under award FA9550-15-1-0099. M.L.G. and G.L. were supported by Russian Foundation for Basic Research grant 13-02-00271 and the Ministry of Education and Science of the Russian Federation project 4.585.21.0005. M.G. acknowledges support from the Hasler foundation and the MSCA-COFUND program at EPFL. All samples were fabricated at the Centre for MicroNanotechnology (CMi) at EPFL.

SUPPLEMENTARY MATERIALS

www.sciencemag.org/content/351/6271/357/suppl/DC1
Materials and Methods
Supplementary Text
Figs. S1 to S8
References (*32*–*41*)

18 September 2015; accepted 3 December 2015
Published online 31 December 2015
10.1126/science.aad4811

ELECTROCHEMISTRY

Active sites of nitrogen-doped carbon materials for oxygen reduction reaction clarified using model catalysts

Donghui Guo,[1] Riku Shibuya,[2] Chisato Akiba,[2] Shunsuke Saji,[2] Takahiro Kondo,[1]* Junji Nakamura[1]*

Nitrogen (N)–doped carbon materials exhibit high electrocatalytic activity for the oxygen reduction reaction (ORR), which is essential for several renewable energy systems. However, the ORR active site (or sites) is unclear, which retards further developments of high-performance catalysts. Here, we characterized the ORR active site by using newly designed graphite (highly oriented pyrolitic graphite) model catalysts with well-defined π conjugation and well-controlled doping of N species. The ORR active site is created by pyridinic N. Carbon dioxide adsorption experiments indicated that pyridinic N also creates Lewis basic sites. The specific activities per pyridinic N in the HOPG model catalysts are comparable with those of N-doped graphene powder catalysts. Thus, the ORR active sites in N-doped carbon materials are carbon atoms with Lewis basicity next to pyridinic N.

The oxygen reduction reaction (ORR) is a key reaction for fuel cells and other renewable energy technologies such as metal-air batteries and dye-sensitized solar cells. Nitrogen-doped carbon materials as nonmetal catalysts exhibit high electrocatalytic activity for the ORR (*1*, *2*) and high durability, even under acidic conditions (*3*). Nitrogen-doped carbon materials are thus among the most promising candidates as alternatives to high-cost Pt catalysts for fuel cell applications. To be developed as high-performance catalysts, they should be engineered to contain a high concentration of active sites without inactive components. Hence, it is imperative to identify the active sites of nitrogen-doped carbon materials for the ORR, albeit still under debate. Currently, the debate focuses on whether the active sites are created by pyridinic N (pyri-N, N bonded to two carbon atoms) or graphitic N (grap-N, N bonded to three carbon atoms, also called substituted N or quaternary N) (*4*–*13*).

The controversy can be ascribed to two reasons. One is the mixing of different types of nitrogen species in the carbon materials, which is inevitable in the doping processes (e.g., by annealing under NH_3 atmosphere). The other lies in the inhomogeneities associated with the morphology and the graphitization level of the evaluated samples, which leads to inhomogeneous sizes of the π-conjugated system. Indeed, the size of nitrogen-doped graphene quantum dots has been reported to affect the ORR performance (*14*). Thus, it is difficult to determine which type of nitrogen creates the active site for the ORR by comparing samples subjected to treatment or pyrolysis at different temperatures because the size of the π-conjugated system is also dependent on the annealing temperature.

To determine the active site conclusively, we develop four types of model catalysts with well-defined π conjugation based on highly oriented pyrolytic graphite (HOPG): (i) pyridinic N-dominated HOPG (*pyri*-HOPG); (ii) graphitic N-dominated HOPG (*grap*-HOPG), and for comparison, (iii) edges patterned on the surface without N (*edge*-HOPG); and (iv) *clean*-HOPG (see supplementary methods and fig. S1). The active sites and adsorption properties of the nitrogen-doped carbon surfaces are examined by ORR, post-ORR x-ray photoelectron spectroscopy (XPS), and CO_2 temperature programmed desorption (TPD) measurements.

Of the four types of prepared HOPG model catalysts, preparation of the pyridinic N–dominated HOPG model catalyst is the most challenging because pyridinic N atoms are preferentially located at the edges of graphite. We thus designed an edge-patterned surface by Ar^+ etching through a mask. Figure 1 (A to D) shows surface morphological characterization of a typical edge-patterned model catalyst. The ordered uniform rectangular groove structures were distributed over the surface in a wide range. The atomic force microscopy (AFM) image presented in Fig. 1B shows dark regions corresponding to the grooves etched through the slits of the mask by ion beam and bright regions that correspond to nonetched surfaces. The surface of the bright region is intact and is basically flat. The profile of the blue line in Fig. 1B shows that the depth of the grooves is about 1200 ± 80 nm for this sample (Fig. 1D), which could be varied from about 100 nm to more than 2 μm by manipulating the etching energy and duration.

Figure 1E shows XPS N 1s spectra for *clean*-HOPG, *edge*-HOPG, *grap*-HOPG, and *pyri*-HOPG (C 1s and survey spectra are shown in fig. S2). The nondoped samples (*clean*-HOPG and *edge*-HOPG)

[1]Faculty of Pure and Applied Sciences, University of Tsukuba, 1-1-1 Tennodai, Tsukuba, Ibaraki 305-8573, Japan. [2]Graduate School of Pure and Applied Sciences, University of Tsukuba, 1-1-1 Tennodai, Tsukuba, Ibaraki 305-8573, Japan. *Corresponding author. E-mail: takahiro@ims.tsukuba.ac.jp (T.K.); nakamura@ims.tsukuba.ac.jp (J.N.)

Table 1. Comparison of specific activity per pyridinic N of HOPG model catalysts (in Fig. 2) and N-GNS powder catalysts (in Fig. 4).

Sample	Nitrogen concentration (at. %)*	Pyridinic N concentration (at. %)*	|*j*| at 0.5 V (mA cm^{-2})†	Specific activity per pyridinic N at 0.5 V ($e^- s^{-1}$ *pyri*-N^{-1})‡
Model HOPG-4	0.60	0.57	0.00041	0.12
Model HOPG-5	4.9	2.2	0.00090	0.066
Model HOPG-6	5.5	3.1	0.0016	0.082
Model HOPG-7	13	3.9	0.0026	0.11
Model HOPG-8	11	6.5	0.0055	0.14
N-GNS-1	1.7	0.72	0.085	0.07
N-GNS-2	2.4	1.9	0.37	0.11
N-GNS-3	8.1	6.3	1.4	0.13

*Nitrogen concentration evaluated by XPS. †ORR current density obtained from current divided by geometric area of electrode surface. ‡Activity derived from ORR current density (|*j*|), i.e., number of electrons converted by oxygen reduction per pyridinic N per second ($e^- s^{-1}$ pyri-N), as follows:

$$\text{Activity per pyridinic N} = \frac{\text{number of electrons per sec per cm}^2\text{ of electrode surface}}{\text{number of pyridinic N per cm}^2\text{ of electrode surface}}$$

are indeed free of N, whereas N 1s peaks are observed for *grap*-HOPG and *pyri*-HOPG. The N concentrations of *grap*-HOPG and *pyri*-HOPG are 0.73 atomic % (82% for grap-N and 5% for pyri-N) and 0.60 atomic % (95% for pyri-N and 5% for grap-N), respectively, as estimated by the analysis of the peak areas for each element (N, C) by considering the atomic sensitivity of XPS. The N 1s spectra were analyzed by least-squares fitting analysis, which includes the components of pyridinic N (398.5 eV), graphitic N (401.1 eV), pyrrolic N (400.1 eV), and oxidic N (403.2 eV) (*15*–*18*).

The catalytic performance was measured by cyclic voltammetry (CV) in acidic electrolyte (0.1 M H_2SO_4) (electrode preparation is shown in fig. S3). Figure 1F shows the ORR curves obtained under oxygen-saturated conditions with the subtraction of data under nitrogen-saturated conditions as the background, in which the currents are divided by the geometric surface areas of electrodes (the same as the exposed catalyst surface areas) as described in the experimental method of the supplementary materials. Figure 1F shows that the *pyri*-HOPG model catalyst displays high activity at high voltages, compared to the very low ORR activities of the N-free model catalysts. The *pyri*-HOPG sample with lower N concentration (N: 0.60 at. %) is much more active than the *grap*-HOPG sample with higher N concentration (N: 0.73 at. %). Since the *pyri*-HOPG sample is nearly free of graphitic N, the ORR results indicate that pyridinic N rather than graphitic N reduces the ORR overpotential and creates the active site. The activity of the *grap*-HOPG sample could also be ascribed to the presence of pyridinic N as a minor component (0.04 at. %).

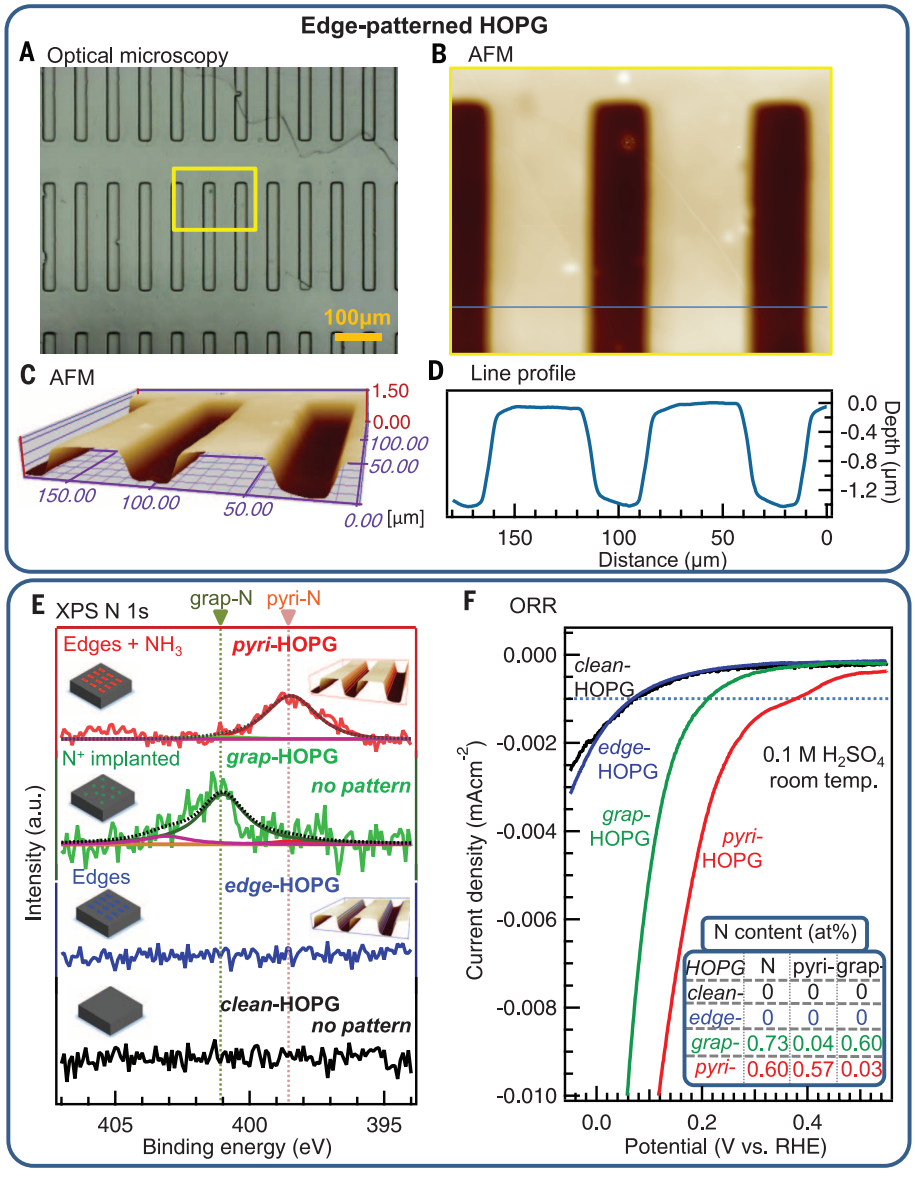

Fig. 1. Structural and elemental characterization of four types of N-HOPG model catalysts and their ORR performance. (**A**) Optical image of patterned *edge-N*$^+$-HOPG. (**B**) The AFM image obtained for the region indicated by the yellow rectangle in (A). (**C**) Three-dimensional representation of (B). (**D**) Line profile of the AFM image obtained along the blue line in (B). (**E**) N 1s XPS spectra of model catalysts. (**F**) ORR results for model catalysts corresponding to (E). Nitrogen contents of the model catalysts are shown as the inset in (F).

The dependence of the ORR activity of the catalyst on the concentration of pyridinic N was investigated and is presented in Fig. 2. Patterned HOPG model catalysts with higher nitrogen concentrations (*edge-N*$^+$-HOPG) were prepared by N^+ ion beam etching through a Ni mask, which contain mixtures of different types of nitrogen (fig. S4 for N 1s and fig. S5 for survey and C 1s spectra). The ORR activities differed because of the different nitrogen-doping conditions (Fig. 2A). The current densities at a specific potential [potential versus reversible hydrogen electrode (RHE)] for each ORR were extracted and plotted versus the corresponding concentrations of pyridinic N and graphitic N. Figure 2B illustrates the linear relationship between the current densities and concentration of pyridinic N at each investigated potential, independent of the preparation method, indicating that the ORR activity is determined solely by the pyridinic N concentration. This linear dependence also suggests that the inhomogeneities in the graphitization and size of the π-conjugation system in the samples were overcome successfully in the HOPG model catalysts by applying the same annealing temperature of 973 K. In contrast, there is no correlation between the current density and the concentration of graphitic N (fig. S6). As a result, the onset potential (potential versus RHE at current density of 1 μA cm^{-2}) increases with increasing concentration of pyridinic N (Fig. 2C).

We further investigated the intermediates of the ORR by ex situ post-ORR XPS measurements of the HOPG model, which reflects the steady-state surface of the N-HOPG model catalyst under ORR and provides mechanistic information about the active sites. Figure 3A illustrates a significant change in the N 1s peak (fig. S7 for C 1s) after the ORR half-cell measurement in acidic conditions, in which the concentration of pyridinic N (398.5 eV) decreased from 54 to 38%, and the concentration of the component corresponding to the 400.1 eV peak (either pyrrolic N or pyridonic N) increased from 11 to 29%, whereas the sum of the pyridinic N and pyrrolic/pyridonic N components remained largely constant (from 65 to 67%). By contrast, an N-HOPG sample after immersion in 0.1 M H_2SO_4 solution without the ORR scanning exhibited a negligible change in N 1s spectrum (fig. S8). The difference in the composition of nitrogen species before and after the ORR suggests that the carbon atoms next to pyridinic N react with OH species with consequent transformation of the pyridinic N to pyridonic N, as shown in Fig. 3B, suggesting that the active sites are the carbon atoms next to the pyridinic N rather than pyridinic N themselves.

Furthermore, we experimentally evaluated the relationship between the basicity and the activity of the HOPG model catalysts. Recently reported density functional theoretical (DFT) calculations

suggested that carbon nanostructures containing pyridinic N possess Lewis basicity (*19*). Based on local scanning tunneling microscopy/spectroscopy (STM-STS) measurements combined with DFT calculations, it has also been reported that carbon atoms adjacent to pyridinic N possess a localized density of states in the occupied region near the Fermi level (*20*). This suggests that the carbon atoms can behave as Lewis bases owing to the possibility of electron pair donation. We thus examined the adsorption of CO_2 as a probe of the Lewis base site. Figure 3C shows the profiles for TPD of CO_2 from the HOPG model catalysts on which CO_2 was adsorbed at room temperature (fig. S9 shows N 1s XPS spectra). It is found that acidic CO_2 molecule is adsorbed only on the ORR-active *pyri*-HOPG catalyst, which proves that the Lewis basic site is created by pyridinic N on the HOPG surface. It is generally known that oxygen molecules can be adsorbed on Lewis base sites (*21*). Because O_2 adsorption is the initial step of the ORR, the Lewis base site created by pyridinic N is thus suggested to be the active site for ORR.

To compare the HOPG model catalysts with powder catalysts, we prepared nitrogen-doped graphene nanosheets (N-GNS) and measured their ORR activities by the rotating disc method in 0.1 M H_2SO_4. Here, the N-GNS catalysts were prepared by the reaction of GNS with NH_3 at 973 K, which is the same temperature applied in the preparation of the HOPG model catalysts. Figure 4A shows the N 1s XPS profiles of the prepared N-GNS powder catalysts. The powder catalysts have high percentages of pyridinic N, and the pyridinic N concentration increases from N-GNS-1 (0.7 at. %) to N-GNS-2 (1.9 at. %) to N-GNS-3 (6.3 at. %), whereas the graphitic N concentrations are as low as 0.4 to 0.8 at. %. Figure 4B shows the ORR performances of the N-GNS powder catalysts, in which the currents are divided by the geometric electrode surface area (0.283 cm^2), with a loading amount of 0.02 mg. The ORR activity increases with increasing nitrogen concentration; e.g., the onset potential increases from

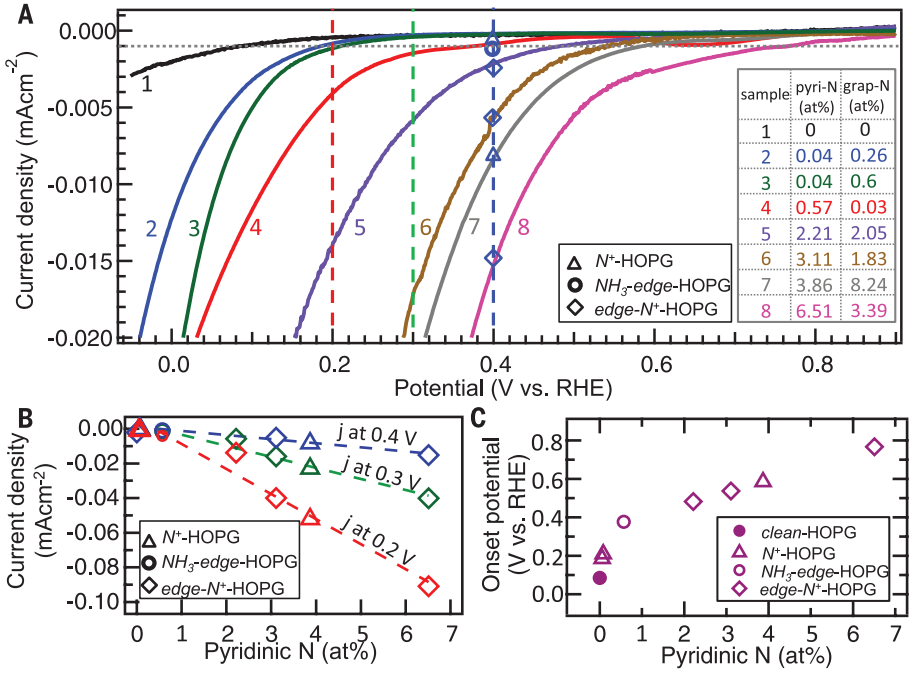

Fig. 2. Catalytic performance of N-HOPG model catalysts. (**A**) ORR results obtained for the model catalysts with different N concentrations. (**B**) Correlation between current densities of ORR at 0.2, 0.3, and 0.4 V versus RHE and the pyridinic N concentrations. (**C**) Correlation between onset potentials at 1 μA cm^{-2} and the pyridinic N concentrations. Different markers indicate different sample preparation methods. Nitrogen contents of the HOPG model catalysts are shown as the inset in (A).

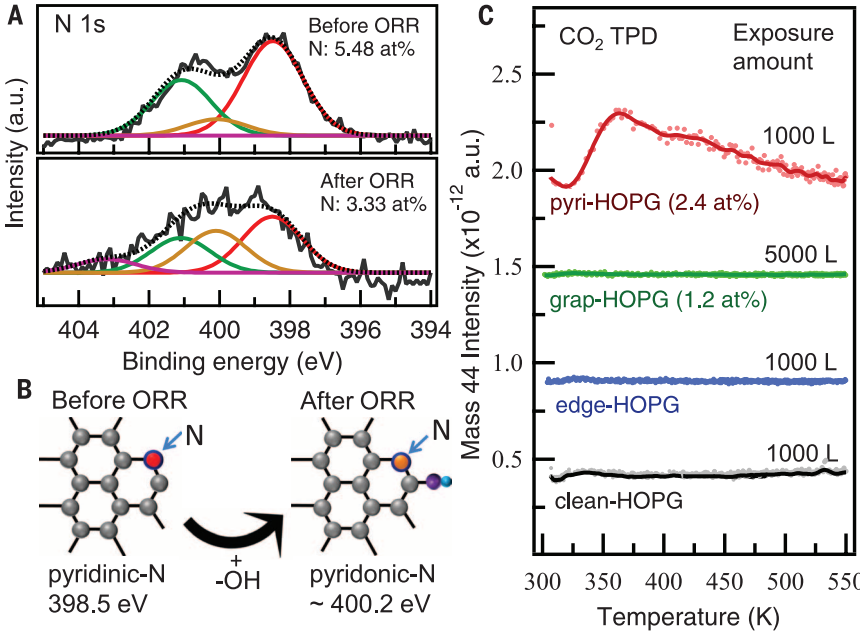

Fig. 3. Post-ORR XPS analysis and CO_2-TPD of the N-HOPG model catalysts. (**A**) N 1s XPS spectra of the N-HOPG model catalyst before and after ORR, respectively. (**B**) Schematic images of the formation of pyridonic N by the attachment of OH to the carbon atom next to pyridinic N. (**C**) CO_2-TPD results for the HOPG model catalysts.

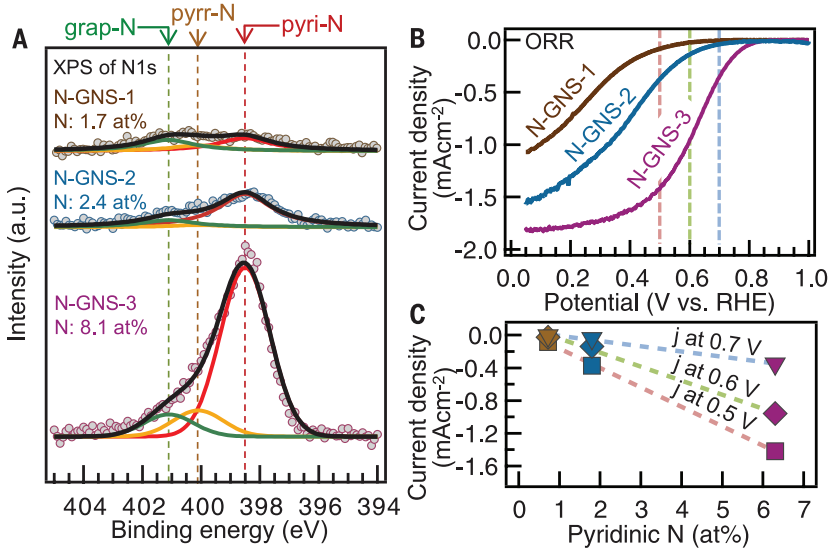

Fig. 4. N 1s XPS spectra and ORR performance of N-GNS powder catalysts. (**A** and **B**) N 1s XPS spectra of N-GNS powder catalysts with different nitrogen concentrations and the corresponding ORR results. (**C**) Correlation between current densities of ORR at 0.5, 0.6, and 0.7 V versus RHE and pyridinic N concentrations.

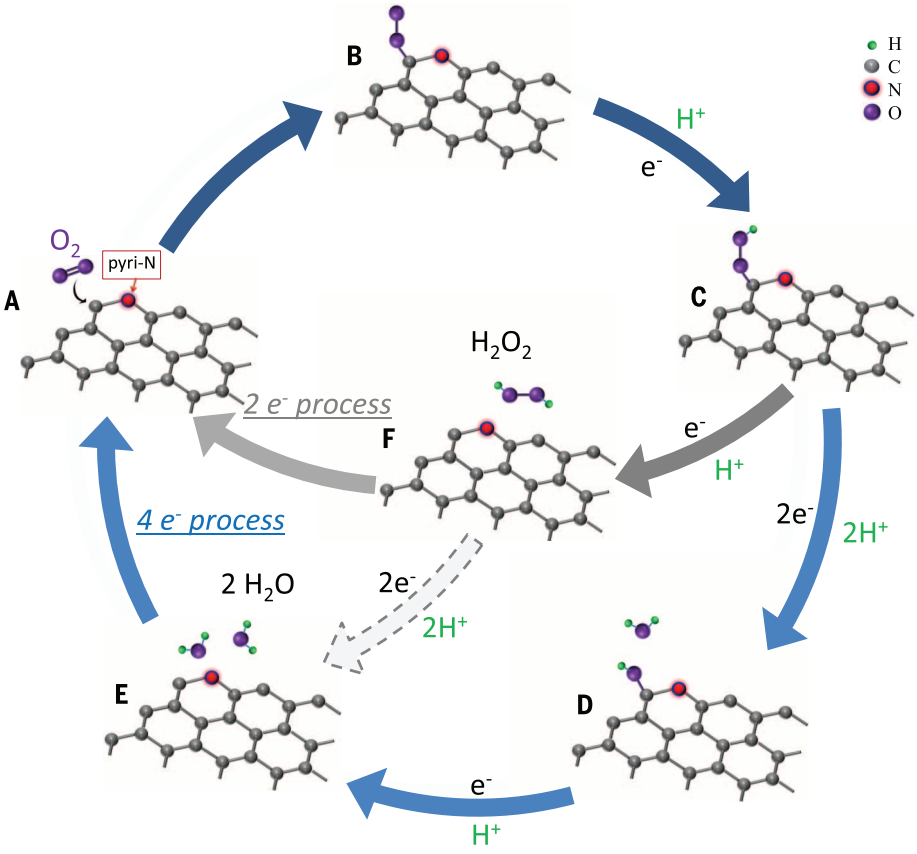

Fig. 5. Schematic pathway for oxygen reduction reaction on nitrogen-doped carbon materials.

0.77 V for N-GNS-1 to 0.91 V for N-GNS-3. The ORR activity was further examined in terms of the current densities at different potentials (0.5, 0.6, and 0.7 V versus RHE). The correlation between the ORR activities and the concentration of nitrogen species was examined for pyridinic N (Fig. 4C) and graphitic N (fig. S10). Linear relationships between the ORR activities at three different potentials and the concentration of pyridinic N were obtained (Fig. 4C), consistent with the linear relationships for the HOPG model catalysts (Fig. 2). It is thus confirmed that pyridinic N creates the active site for ORR in the N-GNS powder catalysts.

We further compared the ORR specific activities of the N-HOPG model catalysts (in Fig. 2) and the N-GNS powder catalysts (in Fig. 4). The activities were evaluated by using the current densities at 0.5 V, at which the oxygen diffusion effect is not so pronounced for N-GNS and the current density is not so small for the N-HOPG model catalysts (comparison at 0.6 V is shown in table S1). As shown in Table 1, the current densities at 0.5 V (absolute value, $|j|$) for the N-HOPG model catalysts are approximately three orders of magnitude lower than those for the N-GNS powder catalysts, which can be attributed to the difference in the absolute number of active sites per 1 cm^2 of the geometric surface area of the electrodes. The N-HOPG model catalyst is simply a plate with a very low graphite surface area of about 0.1 cm^2, identical to the geometric electrode surface area. By contrast, the BET (Brunauer-Emmett-Teller) surface areas of the N-GNS catalysts on the electrode (0.283 cm^2) are about 80 cm^2 (see supplementary materials). As the pyridinic N creates the active site for ORR, we calculated the specific activities per pyridinic N for the model and powder catalysts and compared them by taking into account the BET surface area (400 $m^2\ g^{-1}$) for N-GNS (see supplementary methods for detailed calculation). The specific activities per pyridinic N are similar, at ~0.1 $e^-\ s^{-1}$ pyri-N^{-1} for both types of catalysts (0.07 to 0.14 $e^-\ s^{-1}$ pyri-N^{-1}). The agreement in the specific activity per pyridinic N indicates that, in general, the active sites of ORR for various kinds of nitrogen-doped carbon materials are created by pyridinic N.

Finally, we propose a possible mechanism for the ORR on nitrogen-doped carbon materials (Fig. 5). As the Lewis base site is created by pyridinic N, the oxygen molecule is first adsorbed at the carbon atom next to the pyridinic N followed by protonation of the adsorbed O_2. Two pathways are then possible: One is the four-electron mechanism taking place at a single site, and the other is the 2 + 2–electron mechanism, which does not always take place at a single site. In the four-electron mechanism, the other two protons attach to the two oxygen atoms, leading to breakage of the O-OH bond and formation of OH species ("D" in Fig. 5) as observed in post-ORR

XPS (Fig. 3). The additional proton then reacts with the adsorbed OH to form H_2O ("E" in Fig. 5). In the 2 + 2–electron pathway, H_2O_2 is formed by reaction of the adsorbed OOH species with another proton ("F" in Fig. 5), followed by readsorption of H_2O_2 and its reduction by two protons to generate H_2O. The OH species detected in the post-ORR XPS measurement may arise from the four-electron mechanism, but it is also possible that the OH species next to the pyridinic N may arise from the reaction with H_2O_2 in the 2 + 2–electron mechanism. In either pathway, the carbon atoms next to pyridinic N with Lewis basicity play an important role as the active sites at which oxygen molecules are adsorbed as the initial step of the ORR.

In summary, we have demonstrated that pyridinic N in nitrogen-doped graphitic carbons creates the active sites for ORR under acidic conditions, based on studies of HOPG model catalysts and N-GNS powder catalysts. Carbon atoms next to pyridinic N are suggested to be the active sites with Lewis basicity at which O_2 molecules are adsorbed as the initial step of the ORR.

REFERENCES AND NOTES

1. K. Gong, F. Du, Z. Xia, M. Durstock, L. Dai, *Science* **323**, 760–764 (2009).
2. L. Dai, Y. Xue, L. Qu, H.-J. Choi, J.-B. Baek, *Chem. Rev.* **115**, 4823–4892 (2015).
3. J. Shui, M. Wang, F. Du, L. Dai, *Sci. Adv.* **1**, e1400129 (2015).
4. H.-W. Liang, X. Zhuang, S. Brüller, X. Feng, K. Müllen, *Nat. Commun.* **5**, 4973 (2014).
5. L. Qu, Y. Liu, J.-B. Baek, L. Dai, *ACS Nano* **4**, 1321–1326 (2010).
6. C. V. Rao, C. R. Cabrera, Y. Ishikawa, *J. Phys. Chem. Lett.* **1**, 2622–2627 (2010).
7. T. Xing *et al*., *ACS Nano* **8**, 6856–6862 (2014).
8. R. Liu, D. Wu, X. Feng, K. Müllen, *Angew. Chem.* **49**, 2565–2569 (2010).
9. H. Niwa *et al*., *J. Power Sources* **187**, 93–97 (2009).
10. H. Kim, K. Lee, S. I. Woo, Y. Jung, *Phys. Chem. Chem. Phys.* **13**, 17505–17510 (2011).
11. N. P. Subramanian *et al*., *J. Power Sources* **188**, 38–44 (2009).
12. L. Lai *et al*., *Energy Environ. Sci.* **5**, 7936–7942 (2012).
13. W. Ding *et al*., *Angew. Chem. Int. Ed.* **52**, 11755–11759 (2013).
14. Q. Li, S. Zhang, L. Dai, L. S. Li, *J. Am. Chem. Soc.* **134**, 18932–18935 (2012).
15. S. Maldonado, S. Morin, K. J. Stevenson, *Carbon* **44**, 1429–1437 (2006).
16. E. Raymundo-Piñero *et al*., *Carbon* **40**, 597–608 (2002).
17. J. R. Pels, F. Kapteijn, J. A. Moulijn, Q. Zhu, K. M. Thomas, *Carbon* **33**, 1641–1653 (1995).
18. I. Kusunoki *et al*., *Surf. Sci.* **492**, 315–328 (2001).
19. B. Li, X. Sun, D. Su, *Phys. Chem. Chem. Phys.* **17**, 6691–6694 (2015).
20. T. Kondo *et al*., *Phys. Rev. B* **86**, 035436 (2012).
21. H. Metiu, S. Chrétien, Z. Hu, B. Li, X. Sun, *J. Phys. Chem. C* **116**, 10439–10450 (2012).

ACKNOWLEDGMENTS

This work was financially supported by the New Energy and Industrial Technology Development Organization and partially supported by the Japan Science and Technology Agency–Precursory Research for Embryonic Science and Technology (JST-PRESTO) program, "New Materials Science and Element Strategy." We thank T. Kashiwagi and K. Kadowaki for support with sample etching and AFM measurements. The advice of T. Okajima and T. Ohsaka concerning the electrode preparation methods for the HOPG model catalysts is gratefully acknowledged. We thank X. Hao for assistance with sample preparation by photolithography. We thank all staff of BL07LSU of Spring-8 for assistance with surface analysis of the HOPG model catalysts. J.N. supervised the project. D.G. and C.A. prepared the model catalysts and performed XPS, AFM, and ORR measurements. R.S. performed CO_2-TPD analysis and S.S. prepared the N-GNS powder catalysts and performed ORR measurements. All authors discussed the results and D.G., T.K., and J.N. wrote the paper. The authors declare no competing financial interests.

SUPPLEMENTARY MATERIALS

www.sciencemag.org/content/351/6271/361/suppl/DC1
Materials and Methods
Supplementary Text
Figs. S1 to S10
Table S1

23 July 2015; accepted 8 December 2015
10.1126/science.aad0832

MOLECULAR FRAMEWORKS

Weaving of organic threads into a crystalline covalent organic framework

Yuzhong Liu,[1]* Yanhang Ma,[2]* Yingbo Zhao,[1]* Xixi Sun,[1] Felipe Gándara,[3] Hiroyasu Furukawa,[1] Zheng Liu,[4] Hanyu Zhu,[5] Chenhui Zhu,[6] Kazutomo Suenaga,[4] Peter Oleynikov,[2] Ahmad S. Alshammari,[7] Xiang Zhang,[5,8] Osamu Terasaki,[2,9]† Omar M. Yaghi[1,7]†

A three-dimensional covalent organic framework (COF-505) constructed from helical organic threads, designed to be mutually weaving at regular intervals, has been synthesized by imine condensation reactions of aldehyde functionalized copper(I)-bisphenanthroline tetrafluoroborate, $Cu(PDB)_2(BF_4)$, and benzidine (BZ). The copper centers are topologically independent of the weaving within the COF structure and serve as templates for bringing the threads into a woven pattern rather than the more commonly observed parallel arrangement. The copper(I) ions can be reversibly removed and added without loss of the COF structure, for which a tenfold increase in elasticity accompanies its demetalation. The threads in COF-505 have many degrees of freedom for enormous deviations to take place between them, throughout the material, without undoing the weaving of the overall structure.

Weaving, the mutual interlacing of long threads, is one of the oldest and most enduring methods of making fabric, but this important design concept has yet to be emulated in extended chemical structures. Learning how to link molecular building units by strong bonds through reticular synthesis (*1*) into weaving forms would be a boon to making materials with exceptional mechanical properties and dynamics. To successfully design weaving of chains into two- and three-dimensional (2D and 3D) chemical structures (Fig. 1, A and B), long threads of covalently linked molecules (i.e., 1D units) must be able to cross at regular intervals. It would also be desirable if such crossings serve as points of registry, so that the threads can have many degrees of freedom to move away from and back to such points without collapsing the overall structure. Structures have been made by weaving metal-organic chains (*2*), but designing well-defined materials and assembling their structures by weaving is challenging, and weaving in crystalline inorganic or covalent organic extended structures is undeveloped.

We report on a general strategy and its implementation for the designed synthesis of a woven material [covalent organic framework-505 (COF-505)]. This COF has helical organic threads interlacing to make a weaving crystal structure with the basic topology of Fig. 1B, and we show that this material has an unusual behavior in elasticity. Although terms such as interweaving (*3*), polycatenated (*2*), and interpenetrating (*4*–*6*) have been used to describe interlocking of 2D and 3D extended objects (Fig. 1, C and D), most commonly found in MOFs, we reserve the term "weaving" to describe exclusively the interlacing of 1D units to make 2D and 3D structures (Fig. 1, A and B). Weaving differs from the commonly observed interpenetrating and polycatenated frameworks because the latter are topologically interlocking

[1]Department of Chemistry, University of California, Berkeley, Materials Sciences Division, Lawrence Berkeley National Laboratory, and Kavli Energy NanoSciences Institute, Berkeley, CA 94720, USA. [2]Department of Materials and Environmental Chemistry, Stockholm University, SE-10691 Stockholm, Sweden. [3]Department of New Architectures in Materials Chemistry, Materials Science Institute of Madrid, Consejo Superior de Investigaciones Científicas, Madrid 28049, Spain. [4]Nanomaterials Research Institute, National Institute of Advanced Industrial Science and Technology (AIST), Tsukuba 305-8565, Japan. [5]NSF Nanoscale Science and Engineering Center (NSEC), University of California at Berkeley, 3112 Etcheverry Hall, Berkeley, CA 94720, USA. [6]Advanced Light Source, Lawrence Berkeley National Laboratory, Berkeley, CA 94720, USA. [7]King Abdulaziz City of Science and Technology, Post Office Box 6086, Riyadh 11442, Saudi Arabia. [8]Material Sciences Division, Lawrence Berkeley National Laboratory, 1 Cyclotron Road, Berkeley, CA 94720, USA. [9]School of Physical Science and Technology, ShanghaiTech University, Shanghai 201210, China.
*These authors contributed equally to this work. **†Corresponding author. E-mail: terasaki@mmk.su.se (O.T.); yaghi@berkeley.edu (O.M.Y.)**

(i.e., interlocking rings) (Fig. 1, C and D, insets), whereas the weaving constructs that we envision have many more degrees of freedom for enormous spatial deviations, by each of the threads, to take place independently and still preserve the underlying topology. Such freedom may enable reversible control over the mechanical properties of materials.

Our synthetic strategy is shown in Fig. 2, where we start with the aldehyde functionalized derivative of the well-known complex salt Cu(I)-bis[4,4'-(1,10-phenanthroline-2,9-diyl)dibenzaldehyde] tetrafluoroborate, $Cu(PDB)_2(BF_4)$ (Fig. 2A). The position of the aldehyde groups approximates a tetrahedral geometry and can be used in reticular synthesis as a building block to be linked with benzidine (BZ) and make an imine-bonded PDB-BZ threads weaving arrangement, with the tetrafluoroborate anions occupying the pores (Fig. 2B). The orientation of the PDB units in a mutually interlacing fashion ensures that the threads produced from linking the building units are entirely independent, with the Cu(I) ions serving as templates (points of registry) to bring those threads together in a precise manner at well-defined intervals. Because the PDB-BZ threads are topologically independent of the Cu(I) ions, the resulting woven structure is formally a COF (termed COF-505). The overall tetrahedral geometry of the aldehyde units ensures the assembly of the threads into a 3D framework (Fig. 2B). The topology of this framework is that of diamond, as expected from the principles of reticular chemistry (*1*). We show that when we remove the Cu(I) ions, the structure and its topology remain intact regardless of how the threads deviate from their points of registry, and upon remetalating, the overall structure is reversibly restored. We find a tenfold increase in elasticity when going from the metalated to the demetalated forms of the material.

The copper(I)-bisphenanthroline core of the $Cu(PDB)_2$ (without the aldehyde functionality) has been studied extensively as a discrete molecule for the formation of supramolecular complexes (*7*–*9*); however, as yet it has not been used to make extended structures, especially of the type discussed here. The tolerance for robust reaction conditions (*7*, *10*) makes this complex suitable for imine COF synthesis, especially in weak acidic conditions. Thus, the tetrahedral building unit, $Cu(PDB)_2$, was designed bearing aldehyde groups in the para positions of the two phenyl substituents (Fig. 2A). The synthesis of $Cu(PDB)_2(BF_4)$ molecular complex was carried out by air-free Cu(I) complexation of 4,4'-(1,10-phenanthroline-2,9-diyl)dibenzaldehyde, according to a previously reported procedure (*11*). The single-crystal structure of this complex revealed a distorted tetrahedral geometry around the Cu(I) center, with a dihedral angle of 57° between the two phenanthroline planes. This distortion likely arises from the π-π interaction between the phenanthroline and neighboring phenyl planes (*12*, *13*).

We synthesized COF-505 via imine condensation reactions by combining a mixture of $Cu(PDB)_2(BF_4)$ (15 mg, 0.016 mmol) and BZ (6.0 mg, 0.032 mmol) in tetrahydrofuran (THF, 1 mL) and aqueous acetic acid (6 mol/L, 100 μL). The reaction mixture was sealed in a Pyrex tube and heated at 120°C for 3 days. The resulting precipitate was collected by centrifugation, washed with anhydrous THF, and then evacuated at 120°C for 12 hours to yield 18.7 mg [94.4%, based on $Cu(PDB)_2(BF_4)$] of a dark brown crystalline solid (COF-505), which was insoluble in common polar and nonpolar organic solvents.

Fourier-transform infrared spectroscopy (FT-IR) and solid-state nuclear magnetic resonance (NMR) spectroscopy studies were performed on COF-505 to confirm the formation of imine linkages. A molecular analog of COF-505 fragment, Cu(I)-bis[(1,10-phenanthroline-2,9-diyl)bis(phenylene)bis(biphenyl)methanimine)] tetrafluoroborate, $Cu(PBM)_2(BF_4)$, was used as a model compound and synthesized by condensation of $Cu(PDB)_2(BF_4)$ and 4-aminobiphenyl (*12*). The FT-IR spectrum of COF-505 shows peaks at 1621 and 1196 cm^{-1} [1622 and 1197 cm^{-1} for $Cu(PBM)_2(BF_4)$], which are characteristic C=N stretching modes for imine bonds (*14*, *15*). Furthermore, the ^{13}C cross-polarization with magic-angle spinning (CPMAS) solid-state NMR spectrum acquired for COF-505 displays a series of peaks from 140 to 160 part per million, similar in shape and occurring at chemical shifts characteristic of those expected for C=N double bonds. To differentiate imine bonds from C=N double bonds of the phenanthroline unit, a cross-polarization and polarization inversion (CPPI) technique was applied, which leaves the signal for quaternary ^{13}C groups unchanged, whereas the residual tertiary ^{13}CH signal should approach zero (*16*). The decreased intensity of the ^{13}CH signal under these conditions confirmed the existence of imine CH=N double bond. Overall, these observations served as initial confirmation of having covalently linked imine extended threads in COF-505.

Before determining the single-crystal structure of COF-505, we studied the morphology and purity of the as-synthesized material. We found, using scanning electron microscopy (SEM), crystallites of ~200 nm are aggregated into spheres of 2 μm in diameter (Fig. 3A), which possibly arises from weak interactions of the synthesized material with the solvent, THF. No other phase was observed from SEM images taken throughout the material (*12*).

A single submicrometer-sized crystal (Fig. 3B) from this sample was studied by 3D electron diffraction tomography (3D-EDT) (*17*–*19*). One EDT data set was collected from the COF-505 (Fig. 3C) by combining specimen tilt and electron-beam tilt in the range of –41.3° to +69.1° with a beam-tilt step of 0.2°. From the acquired data set, 3D reciprocal lattice of COF-505 was constructed that was identified as a *C*-centered orthorhombic Bravais lattice. The unit-cell parameters were a = 18.9 Å, b = 21.3 Å, c = 30.8 Å, and V = 12399 $Å^3$, which were used to index reflections observed in both powder x-ray diffraction (PXRD) pattern and Fourier diffractograms of high-resolution transmission electron microscopy (HRTEM) images (Fig. 3D to F). The unit-cell parameters were further refined to be a = 18.6 Å, b = 21.4 Å, c = 30.2 Å, and V = 12021 $Å^3$ by Pawley refinement of PXRD pattern (Fig. 3G). The observed reflection conditions were summarized as *hkl*: $h+k = 2n$; *hk*0: $h,k = 2n$; *h*0*l*: $h = 2n$; and 0*kl*: $k = 2n$, which suggests five possible space groups—*Cm*2*a* (no. 39), *Cmma* (no. 67), *Cmca* (no. 64), *Cc*2*a* (no. 41), and *Ccca* (no. 68). Three of them—*Cm*2*a*, *Cmma*, and *Ccca*—were excluded because their projected plane group symmetries along [1-10] did not coincide with that of the HRTEM image, *pgg* (Fig. 3E). Furthermore, by performing Fourier analysis of the HRTEM images and imposing symmetry to the reflections, Cu(I) positions were

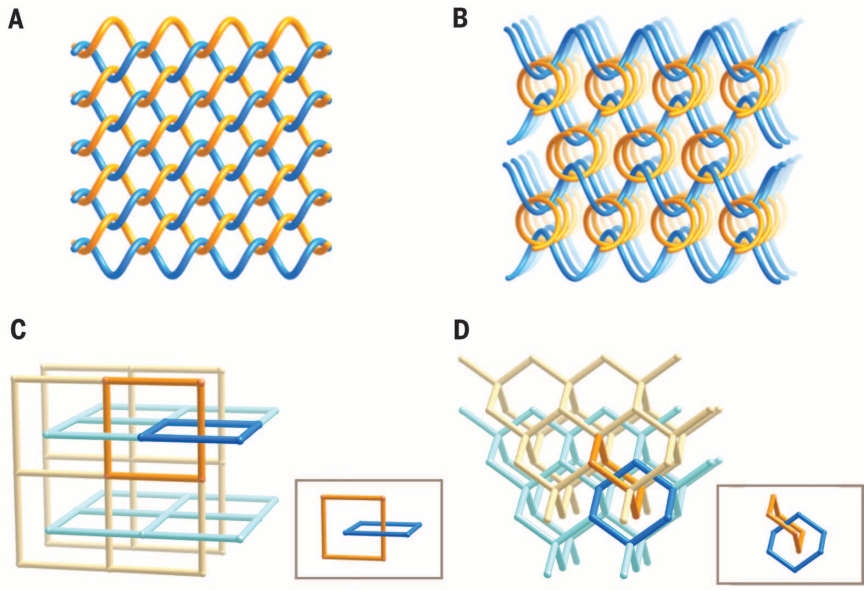

Fig. 1. Weaving and entanglement. Illustrations of weaving of threads in two (**A**) and three (**B**) dimensions, compared with entanglements of sheets (**C**), 3D arrangements (**D**), and their interlocking of rings (insets).

determined from the reconstructed 3D potential map (Fig. 3F). The structure of COF-505 was built in Materials Studio by putting $Cu(PDB)_2$ units at copper positions and connecting them through biphenyl (reacted BZ) molecules. The chemical compositions were determined by elemental analysis; therefore, once the number of copper atoms in one unit cell was obtained, the numbers of other elements in one unit cell were also determined, which indicates that the unit-cell framework is constructed by 8 $Cu(PDB)_2$ and 16 biphenyl units. However, symmetry operations of the space group *Cmca* require two PDB units connected to one copper onto a mirror plane perpendicular to *a* axis, which is not energetically favorable geometry. The final space group determined, *Cc2a*, was used to build and optimize a structure model. The PXRD pattern calculated from this model is consistent with the experimental pattern of activated COF-505 (*12*).

According to the refined model, COF-505 crystallizes in a diamond (**dia**) network with the distorted tetrahedral building units $Cu(PBD)_2$ and biphenyl linkers BZ linked through trans imine bonds. As a result, covalently linked adamantane-like cages 19 by 21 by 64 Å are obtained and elongated along the *c* axis (dimensions are calculated based on Cu-to-Cu distances). This size allows two diamond networks of identical frameworks to form the crystal. These frameworks are mutually interpenetrating (when the Cu centers are considered) in COF-505 crystals along the *c* direction, where the frameworks are related by a C_2 rotation along the *b* axis, leaving sufficient space for BF_4^- counterions (*20*). We note that when the structure is demetalated, as demonstrated below, the COF is mutually woven (Fig. 2B).

Fundamentally, each of the threads making up the framework is a helix (Fig. 4A). For clarity, only a fragment of one weaving framework is shown. The helices are entirely made of covalently linked organic threads. As expected, they are weaving and being held by Cu(I) ions at their points of registry (Fig. 4B). These threads are propagating in two different directions along [110] and [–110]. Although the helices are chemically identical, they have opposite chirality, giving rise to an overall racemic weaving framework (Fig. 4, C and D) of the same topology as in Fig. 1B. We note that in the context of reticular chemistry, the points of registry play an important role in crystallizing otherwise difficult-to-crystallize threads and to do so into 2D or 3D frameworks. This arrangement is in stark contrast to the parallel manner in which such 1D objects commonly pack in the solid state.

The COF-505 structure is a woven fabric of helices, so we sought to remove the Cu centers and examine the properties of the material before and after demetalation. Heating COF-505 in a KCN methanol-water solution (*8*) yielded a demetalated material. Using inductively coupled plasma (ICP) analysis, we found that 92 to 97% of the Cu(I) copper ions had been removed (*12*). The dark brown color of COF-505 [from the copper-phenanthroline metal-to-ligand charge transfer (MLCT) (*21*)] changed to pale yellow as

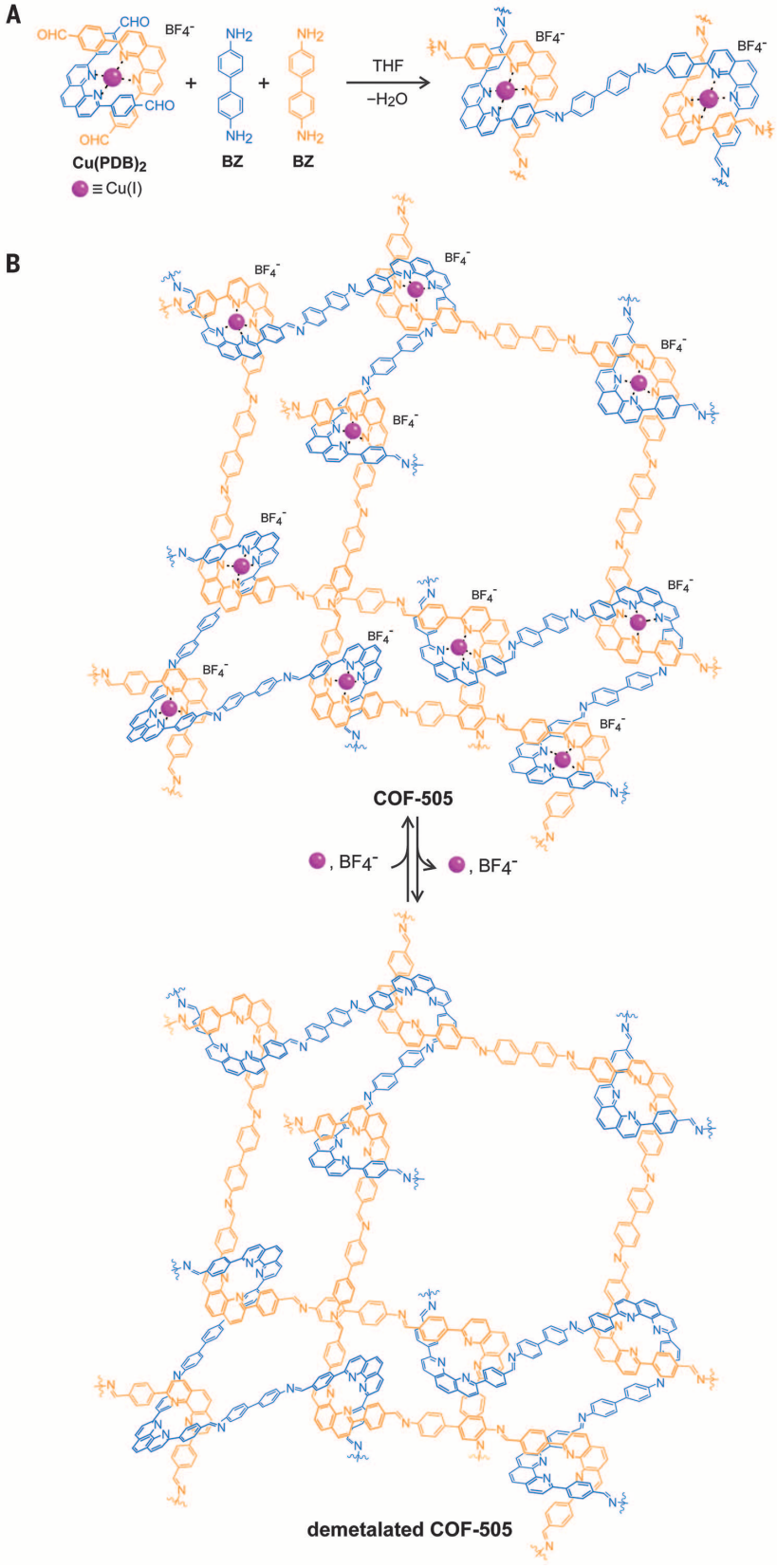

Fig. 2. A general strategy for the design and synthesis of weaving structures. COF-505 was constructed from organic threads using copper(I) as a template (**A**) to make an extended weaving structure (**B**), which can be subsequently demetalated and remetalated.

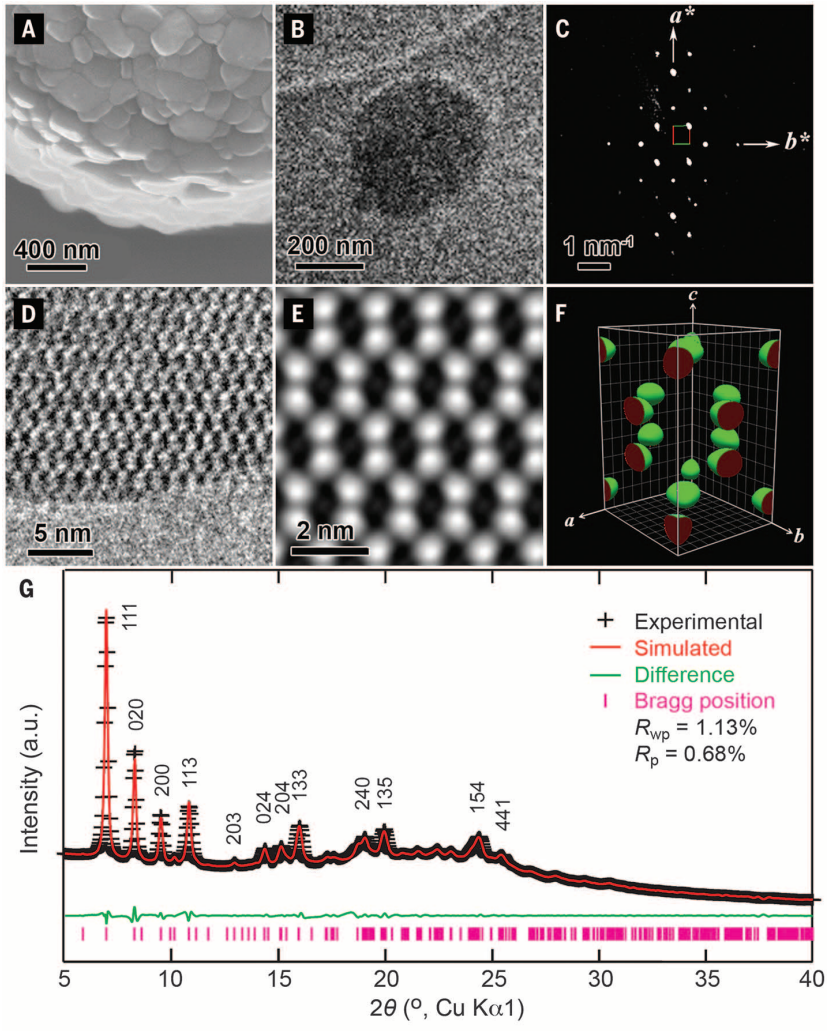

Fig. 3. Morphology and electron microscopy studies of COF-505. (**A**) Crystallites aggregated on a crystalline sphere observed by SEM. (**B**) TEM image of a single sub-μm crystal used for 3D-EDT. (**C**) 2D projection of the reconstructed reciprocal lattice of COF-505 obtained at 298 K from a set of 3D-EDT data. (**D**) HRTEM image of COF-505 taken with the [1-10] incidence. (**E**) 2D projected potential map obtained by imposing *pgg* plane group symmetry on Fig. 1D. (**F**) Reconstructed 3D electrostatic potential map (threshold, 0.8). (**G**) Indexed PXRD pattern of the activated sample of COF-505 (black) and the Pawley fitting (red) from the modeled structure.

demetalation proceeded (*12*). Although the crystallinity of demetalated material decreased compared with COF-505, SEM images show similar morphology before and after demetalation (*12*). Additionally, the imine linkages were also maintained; the FT-IR peaks at 1621 and 1195 cm^{-1} (*12*) are consistent with those of COF-505 (1621 and 1196 cm^{-1}, respectively). Furthermore, the material could be remetalated with Cu(I) ions by stirring in a $CH_3CN/CHCl_3$ solution of $Cu(CH_3CN)_4(BF_4)$ to give back crystalline COF-505. This remetalated COF-505 has identical crystallinity to the original as-synthesized COF-505, as evidenced by the full retention of the intensity and positions of the peaks in the PXRD (*12*). In the FT-IR spectrum, the peak representing imine C=N stretch was retained (*12*), indicating that the framework is chemically stable and robust under such reaction conditions.

Given the facility with which demetalation can be carried out and the full retention of the structure upon remetalation can be achieved, we examined the elastic behavior of the metalated and demetalated COF-505. A single particle of each of these two samples was indented by a conical tip of an atomic force microscope (AFM), and the load-displacement curves were recorded for both loading and unloading process (*22*). The effective Young's moduli (neglecting the anisotropy of the elasticity) of the two COF-505 materials was ~12.5 and 1.3 GPa for the metalated and demetalated particles, respectively (*12*). Notably, this tenfold ratio in elasticity upon demetalation of COF-505 is similar to the elasticity ratio for porous MOFs to polyethylene (*23*). The distinct increase of elasticity could be attributed to the loose interaction between the threads upon removal of copper. Moreover, the elasticity of the original COF-505 could be fully recovered after the process of demetalation and remetalation, being facilitated by the structure of weaving helical threads that easily "zip" and "unzip" at their points of registry. The large difference in elasticity modulus is caused by loss of Cu(I) ions, which in total only represent a minute mole percentage (0.67 mol%) of the COF-505 structure.

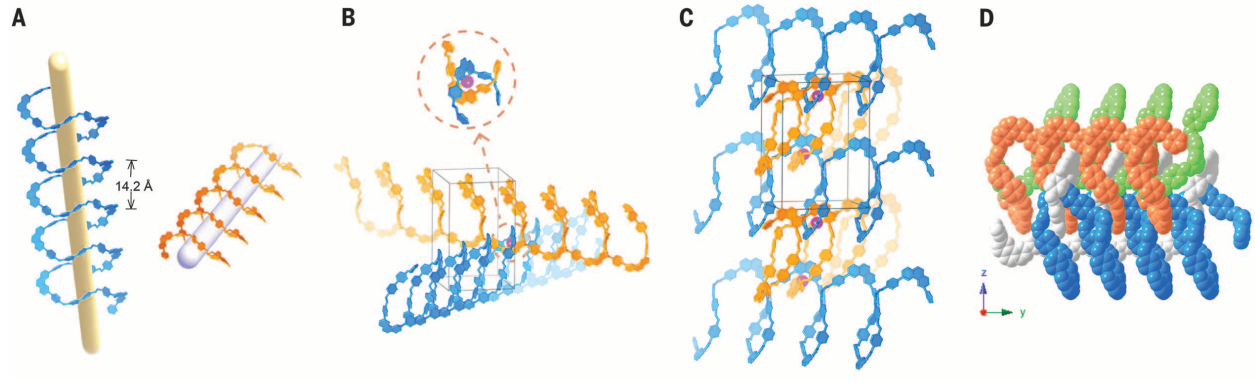

Fig. 4. Single-crystal structure of COF-505. The weaving structure of COF-505 consists of chemically identical helices (marked in blue and orange because they are of opposite chirality) with the pitch of 14.2 Å (**A**). The orange helices propagate in the [1-10] direction, whereas the blue helices propagate in the [110] direction with copper (I) ions as the points of registry (**B**). Neighboring blue helices are woven with the orange helices to form the overall framework (**C**). Blue and orange helices and their C_2 symmetry-related green and gray copies are mutually woven (**D**). Additional parallel helices in (C) and (D) are omitted for clarity.

REFERENCES AND NOTES

1. O. M. Yaghi *et al.*, *Nature* **423**, 705–714 (2003).
2. L. Carlucci, G. Ciani, D. M. Proserpio, *Coord. Chem. Rev.* **246**, 247–289 (2003).
3. B. Chen, M. Eddaoudi, S. T. Hyde, M. O'Keeffe, O. M. Yaghi, *Science* **291**, 1021–1023 (2001).
4. V. A. Blatov, L. Carlucci, G. Ciani, D. M. Proserpio, *Cryst. Eng. Comm.* **6**, 378–395 (2004).
5. S. R. Batten, R. Robson, *Angew. Chem. Int. Ed.* **37**, 1460–1494 (1998).
6. T. K. Maji, R. Matsuda, S. Kitagawa, *Nat. Mater.* **6**, 142–148 (2007).
7. C. O. Dietrich-Buchecker, J.-P. Sauvage, *Angew. Chem. Int. Ed. Engl.* **28**, 189–192 (1989).
8. C. O. Dietrich-Buchecker, J.-P. Sauvage, J. M. Kern, *J. Am. Chem. Soc.* **106**, 3043–3045 (1984).
9. M.-C. Jiménez, C. Dietrich-Buchecker, J.-P. Sauvage, *Angew. Chem. Int. Ed.* **39**, 3284–3287 (2000).
10. S. V. Pakhomova, M. A. Proskurnin, V. V. Chernysh, M. Y. Kononets, E. K. Ivanova, *J. Anal. Chem.* **56**, 910–917 (2001).
11. M. Linke *et al.*, *J. Am. Chem. Soc.* **122**, 11834–11844 (2000).
12. Materials and methods are available as supplementary materials on *Science* Online.
13. M. T. Miller, P. K. Gantzel, T. B. Karpishin, *Inorg. Chem.* **37**, 2285–2290 (1998).
14. Y.-B. Zhang *et al.*, *J. Am. Chem. Soc.* **135**, 16336–16339 (2013).
15. F. J. Uribe-Romo *et al.*, *J. Am. Chem. Soc.* **131**, 4570–4571 (2009).
16. X. Wu, K. W. Zilm, *J. Magn. Reson.* **102**, 205–213 (1993).
17. M. Gemmi, P. Oleynikov, *Z. Kristallogr.* **228**, 51–58 (2013).
18. E. Mugnaioli *et al.*, *Angew. Chem. Int. Ed.* **51**, 7041–7045 (2012).
19. Q. Sun *et al.*, *J. Mater. Chem. A* **2**, 17828–17839 (2014).
20. E. V. Alexandrov, V. A. Blatov, D. M. Proserpio, *Acta Crystallogr. A* **68**, 484–493 (2012).
21. D. V. Scaltrito, D. W. Thompson, J. A. O'Callaghan, G. J. Meyer, *Coord. Chem. Rev.* **208**, 243–266 (2000).
22. W. C. Oliver, G. M. Pharr, *J. Mater. Res.* **19**, 3–20 (2004).
23. J. C. Tan, A. K. Cheetham, *Chem. Soc. Rev.* **40**, 1059–1080 (2011).

ACKNOWLEDGMENTS

The structures of COF-505 and Cu(PDB)$_2$(BF$_4$) are available free of charge from the Cambridge Crystallographic Data Centre under the reference numbers CCDC-1434851 and CCDC-1434852, respectively. This research was supported by BASF SE (Ludwigshafen, Germany) for synthesis and basic characterization, and the U.S. Department of Defense, Defense Threat Reduction Agency (HDTRA 1-12-1-0053) for mechanical properties. We thank C. Canlas for his assistance with solid-state NMR and A. Schöedel (Yaghi group), B. Zhang, and Y. Liu (Molecular Foundry, Lawrence Berkeley National Laboratory) for helpful discussions. This work was also supported by the Spanish Ministry of Economy and Competitiveness through the Juan de la Cierva program (F.G.); a Grant-in-Aid for Scientific Research (C) (25390023) and JST Research Acceleration Program (Z.L. and K.S.); grants from Vetenskapsrådet (Y.M. and P.O.) and JEOL Ltd (P.O.), Japan; EXSELENT and 3DEM-Natur, Sweden (O.T.); and BK21Plus, Korea (O.T.). Beamline 7.3.3 of the Advanced Light Source is supported by the Director of the Office of Science, Office of Basic Energy Sciences, of the U.S. Department of Energy under contract DE-AC02-05CH11231. The AFM study was supported by the National Science Foundation (NSF) (grant DMR-1344290). The data reported in the paper are presented in the supplementary materials.

SUPPLEMENTARY MATERIALS

www.sciencemag.org/content/351/6271/365/suppl/DC1
Materials and Methods
Figs. S1 to S21
Tables S1 to S4
Reference (*24*)

8 September 2015; accepted 25 November 2015
10.1126/science.aad4011

PHOTOPHYSICS

Direct observation of triplet energy transfer from semiconductor nanocrystals

Cédric Mongin,[1] Sofia Garakyaraghi,[1] Natalia Razgoniaeva,[2] Mikhail Zamkov,[2] Felix N. Castellano[1]*

Triplet excitons are pervasive in both organic and inorganic semiconductors but generally remain confined to the material in which they originate. We demonstrated by transient absorption spectroscopy that cadmium selenide semiconductor nanoparticles, selectively excited by green light, engage in interfacial Dexter-like triplet-triplet energy transfer with surface-anchored polyaromatic carboxylic acid acceptors, extending the excited-state lifetime by six orders of magnitude. Net triplet energy transfer also occurs from surface acceptors to freely diffusing molecular solutes, further extending the lifetime while sensitizing singlet oxygen in an aerated solution. The successful translation of triplet excitons from semiconductor nanoparticles to the bulk solution implies that such materials are generally effective surrogates for molecular triplets. The nanoparticles could thereby potentially sensitize a range of chemical transformations that are relevant for fields as diverse as optoelectronics, solar energy conversion, and photobiology.

Semiconductor nanocrystals represent an important class of stable light-emitting materials that can be systematically tuned as a result of size-dependent quantum confinement, producing intense absorptions and photoluminescence ranging from the ultraviolet (UV) to the near-infrared (near-IR) (*1*, *2*). Their prominence continues to expand, owing to extensive optoelectronic, photochemical, and biomedical applications (*3*–*9*). Substantial research effort has been expended on funneling energy into these nanomaterials to produce enhanced photoluminescence via Förster transfer and on exploiting the energized semiconductor nanocrystals to deliver or accept electrons from substrates (*10*–*14*), sometimes en route to solar fuels photosynthesis (*15*–*18*). Tabachnyk *et al.* and Thompson *et al.* independently demonstrated the reverse triplet energy transfer process to that described here, wherein molecular organic semiconductors transfer their triplet energy to PbSe and PbS nanocrystals in thin films that interface both materials (*19*, *20*). However, the extraction of triplet excitons from semiconductor quantum dots and related inorganic nanomaterials remains largely unexplored. Semiconductor nanocrystals potentially offer considerable advantages over molecular photosensitizers in terms of facile preparative synthesis, photostability, size-tunable electronic and photophysical properties, high molar extinction coefficients, and trivial postsynthesis functionalization. Moreover, the inherently large (and energy-consuming) singlet-triplet energy gaps characteristic of molecular sensitizers can be circumvented by using nanomaterials with ill-defined spin quantum numbers and closely spaced (1 to 15 meV) excited-state energy levels (*21*–*24*). The broadband light-absorption properties of inorganic semiconductors are extendable into the near-IR region and can potentially be exploited for numerous triplet excited-state reactions, thus enabling stereoselective photochemical synthesis, photoredox catalysis, singlet oxygen generation, photochemical upconversion, and excited-state electron transfer. Here we provide definitive experimental evidence that triplet energy transfer proceeds rapidly and efficiently from energized semiconductor nanocrystals to surface-anchored molecular acceptors. Specifically, CdSe nanocrystals are shown to serve as effective surrogates for molecular triplet sensitizers and can readily transfer their triplet excitons to organic acceptors at the interface with near-quantitative efficiency.

The nanoparticle-to-solution triplet exciton transfer strategy that we implemented is shown schematically in Fig. 1; this diagram depicts all of the relevant photophysical processes and the associated energy levels promoting material-to-molecule triplet exciton migration. We employed oleic acid (OA)–capped CdSe nanocrystals (CdSe-OA) as the light-absorbing triplet sensitizer in conjunction with 9-anthracenecarboxylic acid (ACA) and 1-pyrenecarboxylic acid (PCA) as triplet acceptors in toluene. The carboxylic acid functionality enables adsorption of these chromophores on the CdSe surface through displacement of the OA capping ligands; subsequent washing steps isolate the desired CdSe/ACA or CdSe/PCA donor/acceptor systems. Selective green light excitation of CdSe/ACA or CdSe/PCA sensitizes triplet exciton migration from the semiconductor to the surface-bound molecular acceptor. We directly visualized this interfacial Dexter-like

[1]Department of Chemistry, North Carolina State University, Raleigh, NC 27695-8204, USA. [2]Department of Physics and Center for Photochemical Sciences, Bowling Green State University, Bowling Green, OH 43403, USA.
***Corresponding author. E-mail: fncastel@ncsu.edu**

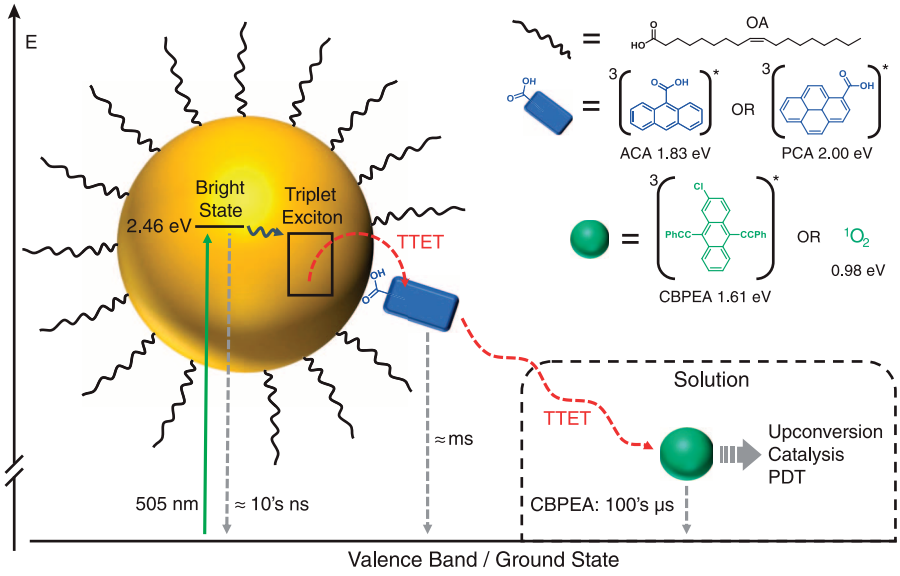

Fig. 1. Illustration of nanocrystal-to-solution triplet energy transfer, the associated energy levels, and the various TTET and decay pathways investigated in this study. PDT, photodynamic therapy.

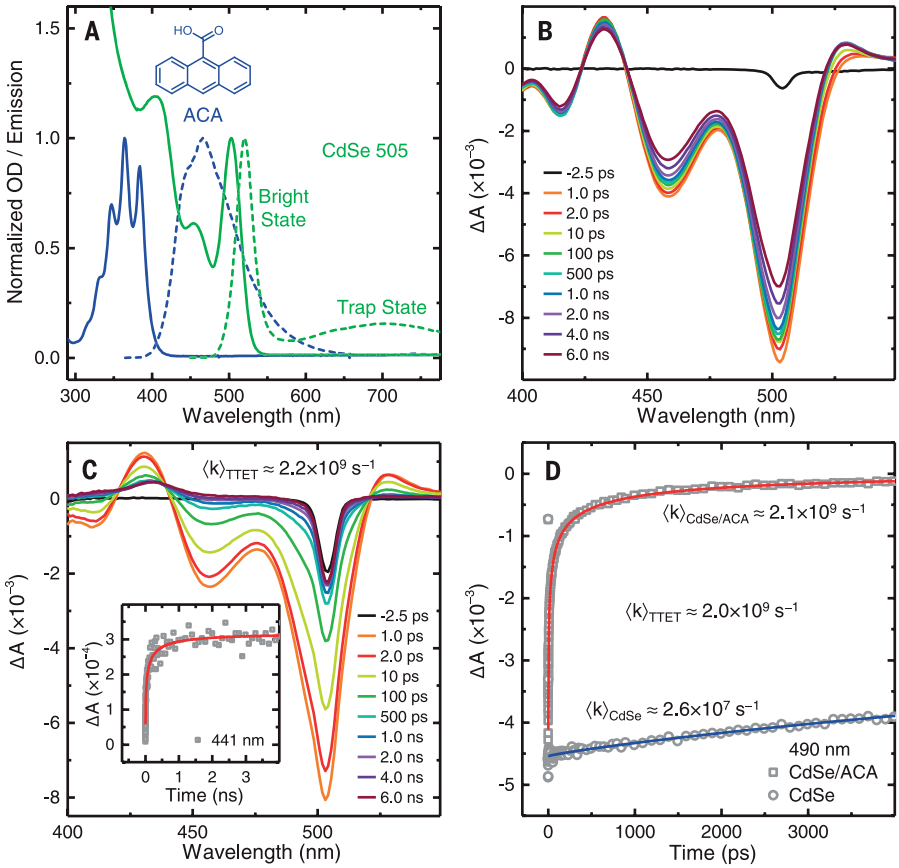

Fig. 2. Ultrafast spectroscopic evidence for triplet energy transfer from optically excited CdSe nanocrystals to surface-bound ACA. (**A**) Normalized electronic absorption (solid lines) and emission spectra (dashed lines) of ACA (blue) and CdSe nanocrystals (green) in toluene (OD, optical density). (**B** and **C**) Ultrafast TA difference spectra of CdSe-OA nanocrystals in toluene solution upon selective excitation of CdSe, using 500-nm pulsed laser excitation [0.05 µJ per pulse, 100 fs full width at half maximum (FWHM)], in (B) the absence and (C) the presence of surface-anchored ACA in toluene (ΔA, change in absorbance; $\langle k \rangle$, average rate constant). The inset in (C) shows TA kinetics monitored for the growth of ^{3}ACA at 441 nm. (**D**) Ground-state recovery of CdSe monitored by kinetics at 490 nm, illustrating quantitative quenching of CdSe in the presence of surface-anchored ACA. Complementary data for PCA are shown in figs. S2 to S4.

triplet-triplet energy transfer (TTET) by monitoring the kinetic growth of the characteristic triplet-to-triplet ($T_1 \rightarrow T_n$) absorptions in ACA and PCA (wavelength of maximum absorbance = 430 nm) using ultrafast transient absorption (TA) spectroscopy (*25*, *26*). The long-lived ACA and PCA localized triplets furthermore enabled exothermic triplet energy transfer to freely diffusing 2-chlorobisphenylethynylanthracene (CBPEA) and dioxygen.

CdSe-OA suspended in toluene was prepared as described in the supplementary materials. The first exciton band in these samples was located at 505 nm (2.46 eV; molar extinction coefficient at 505 nm, 59,200 M^{-1} cm^{-1}); using an established empirical equation (*27*), the average diameter of these nanoparticles was estimated to be 2.4 nm, in good agreement with transmission electron microscopy results (fig. S1). The CdSe-OA photoluminescence features, including the spectrally narrow band-gap "bright state" and the lower-energy "trap state" emissions, are shown in Fig. 2A (*28*). Triplet excitons derived from these excited states (2.40 eV and 2.30 to 1.40 eV, respectively) are suitable for exothermic TTET to ACA (lowest triplet state energy, E_T = 1.83 eV) and PCA (E_T = 2.00 eV) (*25*, *29*). We observed no evidence of triplet energy transfer from the CdSe-OA nanoparticles to anthracene (E_T = 1.85 eV), 9,10-diphenylanthracene (E_T = 1.77 eV), or pyrene (E_T = 2.10 eV) acceptors (*29*), despite thermodynamic expectations that such transfers should be exothermic. Unlike ACA and PCA, these acceptors lack the carboxylate functionality to coordinate directly to the nanoparticle surface. In these cases, the putative bimolecular transfer rate through the intervening OA layer appears to be slower than the excited-state lifetime of the nanoparticle.

Photoluminescence from CdSe-OA was quantitatively quenched by ACA and PCA (fig. S5). The nanocrystals bearing surface-anchored molecular acceptors were purified by successive precipitation and centrifugation cycles, after which the final ratio of acceptor to CdSe was determined to be ~12:1 (fig. S6). Ultrafast TA experiments were performed on the quantitatively quenched CdSe-OA/ACA materials to establish the mechanism and time scale for the semiconductor-to-molecule triplet exciton transfer process. Control experiments with CdSe-OA in toluene were also performed in the absence of ACA (Fig. 2B). In all cases, symmetric decay of the transient signal was observed over the first few picoseconds, which is consistent with multi-exciton annihilation within the nanocrystals (*30*), and was confirmed by laser power dependence experiments (fig. S7). With surface-anchored ACA (Fig. 2C), decay of the CdSe excited state was observed within 2 ns, coinciding with the growth of an absorption band centered at 433 nm, which was assigned to the $T_1 \longrightarrow T_n$ transitions of ACA (*25*). These results confirm direct TTET (no intermediates) from the selectively excited CdSe nanocrystals to the surface-anchored ACA chromophores. The possibility of an electron transfer mechanism was eliminated, based on the absence of

the ACA radical cation band that would be expected near 750 nm (figs. S8 to 11A) (*31*). Singlet-singlet energy transfer is not thermodynamically favorable, and no transient signals corresponding to singlet ACA (^{1}ACA*) were observed. Transient kinetics were monitored at 441 nm, where an isosbestic point was present in the CdSe-OA control difference spectra (Fig. 2B). In the presence of ACA (Fig. 2C), this isosbestic point shifts because of the overlapping ACA $T_1 \rightarrow T_n$ absorption band (fig. S12); thus, any new absorption feature observed at 441 nm (Fig. 2C, inset) can be attributed to triplet ACA (^{3}ACA*). The quantum efficiency for TTET from CdSe-OA to surface-anchored ACA was determined to be 0.92 from TA experiments (fig. S12B). Therefore, most of the excited states produced within CdSe can be extracted as long-lived molecular triplets that are suitable for subsequent chemical reactions. Variable rates of energy transfer were anticipated, depending on the initially populated CdSe excited states. Accordingly, following a published precedent (*11*, *32*), a stretched exponential function was determined to best model the interfacial TTET dynamics (eqs. S1 to S3). Kinetic analysis at 441 nm revealed a rise time associated with the ^{3}ACA* absorption with an average rate constant of 2.2×10^9 s^{-1}. Additionally, the rise of ^{3}ACA* was correlated to the ground-state recovery of CdSe (TA probe wavelength: 480, 490, and 510 nm) (Fig. 2D and fig. S13). Rate constants between 2.0×10^9 and 2.8×10^9 s^{-1} (table S1) were measured, in good agreement with the formation rate of ^{3}ACA*. TTET also occurred, with similar efficiencies but slower kinetics, when PCA was used as the surface-bound molecular acceptor (figs. S3 to S5). This is consistent with the lower TTET driving force associated with that process.

The $T_1 \rightarrow T_n$ absorption centered near 430 nm that was observed in the ultrafast TA experiments (Fig. 2C), which is characteristic of ^{3}ACA*, appeared as a prompt signal in nanosecond flash photolysis (Fig. 3A). Complementary data for PCA show similar results and are presented in Fig. 3B. The transient signals of the acceptor $T_1 \rightarrow T_n$ decay to the ground state over the next several milliseconds, illustrating that excitons can indeed be harvested from these semiconductor nanomaterials, resulting in an excited-state lifetime enhancement of six orders of magnitude.

The CdSe/ACA and CdSe/PCA materials also sensitized the production of $^1O_2$* when the solutions were aerated, evidenced by its characteristic photoluminescence centered at 1277 nm in the near-IR region (fig. S14). This is a unique example of $^1O_2$* sensitization through metal chalcogenide nanocrystals enabled by a mechanism distinct from that of Förster transfer (*33*–*35*). To further illustrate that excitons could be transferred away from the CdSe interface into the bulk solution, a second molecular triplet acceptor (CBPEA) was added to the CdSe/acceptor solution. CBPEA possesses a low-lying triplet state (E_T < 1.61 eV), facilitating exothermic TTET from energized acceptor chromophores, and is readily discernible by its distinct $T_1 \rightarrow T_n$ excited-state absorption, centered at 490 nm (*36*). Figure 3C presents the TA difference spectra measured at 3 μs and 200 μs after 505-nm pulsed nanosecond laser excitation of the CdSe/ACA solution in the presence of 6 μM CBPEA (Fig. 3D shows the complementary data for PCA as the acceptor). At early delay times, the ^{3}ACA* absorption spectrum dominates (Fig. 3C, blue line), eventually giving way quantitatively (quantum efficiency for TTET ~ 1.0) to a spectrum characteristic of triplet CBPEA (^{3}CBPEA*) at longer delay times (Fig. 3C, red line). By 3 ms after the laser pulse, the sample completely relaxed to the ground state (Fig. 3C, green line). These data demonstrate that the formation of ^{3}ACA* on the CdSe surface is followed by diffusion-controlled triplet-triplet energy transfer to CBPEA (fig. S15; rate constant for energy transfer, 1.2×10^9 M^{-1} s^{-1}), effectively transferring the triplet exciton into the bulk solution. The dynamics of this energy migration were captured in the single-wavelength absorption transients measured at 430 and 490 nm after the 505-nm excitation pulse (Fig. 3C, inset). The promptly formed transient absorption signal at 430 nm from ^{3}ACA* (red squares) exhibits an excited-state decay that is kinetically correlated with the formation of ^{3}CBPEA* (blue circles) at 490 nm. These experiments illustrate that bimolecular excited-state chemistry readily proceeds from the CdSe/acceptor materials, exhibiting behavior characteristic of a donor/acceptor TTET molecular system.

The results presented here provide proof-of-concept that excitons can be extracted from this particular semiconductor through direct TTET, but it stands to reason that this general strategy is probably also applicable to a plethora of associated materials. In this regard, molecular triplet-triplet annihilation processes can be sensitized by energized semiconductor nanocrystals (*23*, *37*, *38*). Although this investigation specifically targeted mechanistic insights into the TTET process along with chemically relevant triplet exciton decay pathways, we expect related photochemistry to promote similar triplet energy transfer phenomena in solid-state optoelectronic devices.

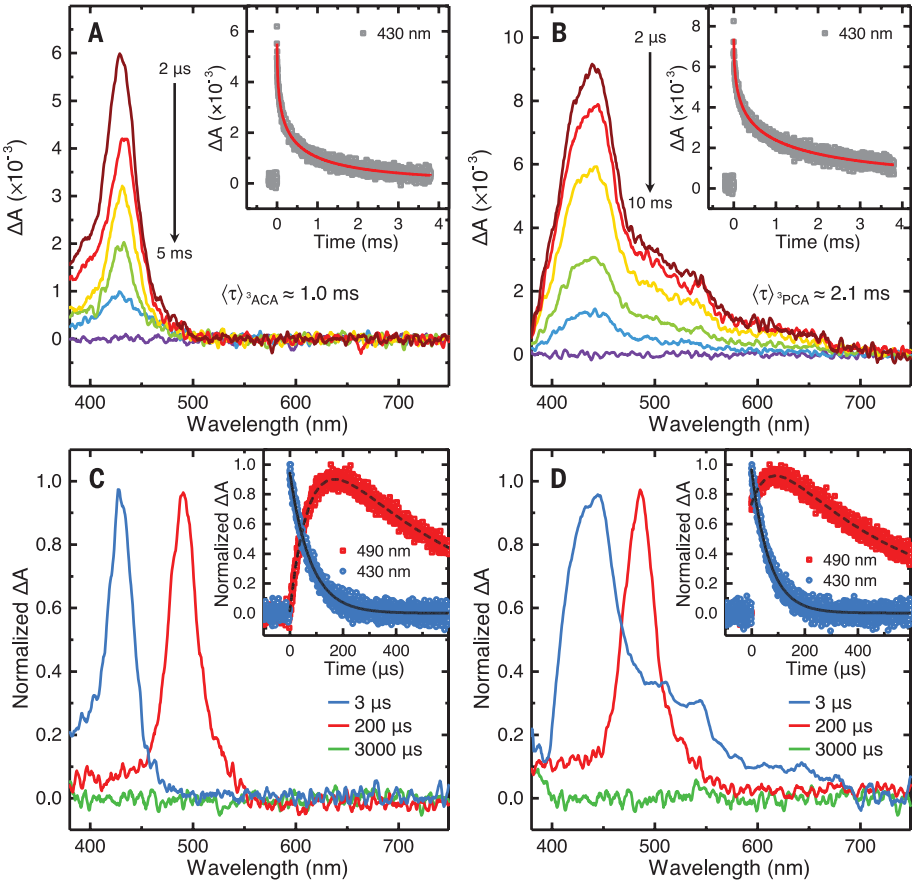

Fig. 3. Kinetic profiles and quenching studies of ACA and PCA triplet states populated from excited CdSe nanocrystals. TA difference spectra of a toluene solution of (**A**) CdSe/ACA (8 μM) measured from 2 μs to 5 ms and (**B**) CdSe/PCA (8 μM) measured from 2 μs to 10 ms after a 505-nm laser pulse (1 mJ, 5 to 7 ns FWHM; ⟨τ⟩, average lifetime). The insets show TA decay kinetics at 430 nm (gray squares) and their respective fits to eq. S1, illustrating the triplet decay. (**C** and **D**) TA difference spectra (excitation wavelength, 505 nm; 5 to 7 ns FWHM; 1 mJ) measured at selected delay times after the laser pulse in (C) CdSe/ACA (5 μM) and CBPEA (6 μM) and (D) CdSe/PCA (5 μM) and CBPEA (6 μM) in deaearated toluene at room temperature. The insets show TA decay kinetics at 430 nm (red circles) and the rise and decay at 490 nm (blue squares), with their respective biexponential fit lines (solid and dashed), illustrating the triplet energy transfer reaction between ^{3}ACA* and CBPEA.

REFERENCES AND NOTES

1. C. B. Murray, D. J. Norris, M. G. Bawendi, *J. Am. Chem. Soc.* **115**, 8706–8715 (1993).
2. M. L. Landry, T. E. Morrell, T. K. Karagounis, C.-H. Hsia, C.-Y. Wang, *J. Chem. Educ.* **91**, 274–279 (2014).
3. I. L. Medintz, H. T. Uyeda, E. R. Goldman, H. Mattoussi, *Nat. Mater.* **4**, 435–446 (2005).
4. M. Bruchez Jr., M. Moronne, P. Gin, S. Weiss, A. P. Alivisatos, *Science* **281**, 2013–2016 (1998).
5. I. Gur, N. A. Fromer, M. L. Geier, A. P. Alivisatos, *Science* **310**, 462–465 (2005).
6. W. C. W. Chan, S. Nie, *Science* **281**, 2016–2018 (1998).
7. S. Coe, W.-K. Woo, M. Bawendi, V. Bulović, *Nature* **420**, 800–803 (2002).
8. V. L. Colvin, M. C. Schlamp, A. P. Alivisatos, *Nature* **370**, 354–357 (1994).
9. S. A. McDonald *et al.*, *Nat. Mater.* **4**, 138–142 (2005).
10. C. Burda, T. C. Green, S. Link, M. A. El-Sayed, *J. Phys. Chem. B* **103**, 1783–1788 (1999).
11. I. Robel, M. Kuno, P. V. Kamat, *J. Am. Chem. Soc.* **129**, 4136–4137 (2007).
12. K. E. Knowles, M. Malicki, E. A. Weiss, *J. Am. Chem. Soc.* **134**, 12470–12473 (2012).
13. R. Reisfeld, M. Gaft, T. Saridarov, G. Panczer, M. Zelner, *Mater. Lett.* **45**, 154–156 (2000).
14. M. Wojdak *et al.*, *Phys. Rev. B* **69**, 233315 (2004).
15. Z. Han, F. Qiu, R. Eisenberg, P. L. Holland, T. D. Krauss, *Science* **338**, 1321–1324 (2012).
16. K. Wu, Q. Li, Y. Du, Z. Chen, T. Lian, *Chem. Sci.* **6**, 1049–1054 (2015).
17. H. B. Yang *et al.*, *ACS Nano* **8**, 10403–10413 (2014).
18. E. Khon *et al.*, *Nano Lett.* **13**, 2016–2023 (2013).
19. M. Tabachnyk *et al.*, *Nat. Mater.* **13**, 1033–1038 (2014).
20. N. J. Thompson *et al.*, *Nat. Mater.* **13**, 1039–1043 (2014).
21. G. D. Scholes, *Adv. Funct. Mater.* **18**, 1157–1172 (2008).
22. A. L. Efros *et al.*, *Phys. Rev. B* **54**, 4843–4856 (1996).
23. M. Mengfei *et al.*, *Nat. Photon.* 10.1038/nphoton.2015.226 (2015).
24. S. A. Crooker, T. Barrick, J. A. Hollingsworth, V. I. Klimov, *Appl. Phys. Lett.* **82**, 2793 (2003).
25. S. Hirayama, *J. Chem. Soc., Faraday Trans. I* **78**, 2411 (1982).
26. Y. Niko, Y. Hiroshige, S. Kawauchi, G. Konishi, *Tetrahedron* **68**, 6177–6185 (2012).
27. W. W. Yu, L. Qu, W. Guo, X. Peng, *Chem. Mater.* **15**, 2854–2860 (2003).
28. D. R. Baker, P. V. Kamat, *Langmuir* **26**, 11272–11276 (2010).
29. M. Montalti, A. Credi, L. Prodi, T. Gandolfi, *Handbook of Photochemistry* (CRC Press, Boca Raton, FL, ed. 3, 2006).
30. H. Zhu, Y. Yang, T. Lian, *Acc. Chem. Res.* **46**, 1270–1279 (2013).
31. J. M. Masnovi, E. A. Seddon, J. K. Kochi, *Can. J. Chem.* **62**, 2552–2559 (1984).
32. V. N. Soloviev, A. Eichhöfer, D. Fenske, U. Banin, *J. Am. Chem. Soc.* **123**, 2354–2364 (2001).
33. R. Bakalova, H. Ohba, Z. Zhelev, M. Ishikawa, Y. Baba, *Nat. Biotechnol.* **22**, 1360–1361 (2004).
34. E. I. Zenkevich *et al.*, *J. Phys. Chem. C* **115**, 21535–21545 (2011).
35. A. C. S. Samia, X. Chen, C. Burda, *J. Am. Chem. Soc.* **125**, 15736–15737 (2003).
36. T. N. Singh-Rachford, F. N. Castellano, *Inorg. Chem.* **48**, 2541–2548 (2009).
37. Z. Huang *et al.*, *Nano Lett.* **15**, 5552–5557 (2015).
38. Z. Huang *et al.*, *Chem. Mater.* **27**, 7503–7507 (2015).

ACKNOWLEDGMENTS

This work was supported by the Air Force Office of Scientific Research (grant FA9550-13-1-0106) and the Ultrafast Initiative of the U. S. Department of Energy, Office of Science, Office of Basic Energy Sciences, through Argonne National Laboratory under contract no. DE-AC02-06CH11357. M.Z. was supported by NSF (grant CHE-1465052).

SUPPLEMENTARY MATERIALS

www.sciencemag.org/content/351/6271/369/suppl/DC1
Materials and Methods
Figs. S1 to S15
Table S1
References (*39*–*41*)

14 October 2015; accepted 9 December 2015
10.1126/science.aad6378

GEOCHEMISTRY

Archean upper crust transition from mafic to felsic marks the onset of plate tectonics

Ming Tang,[1]* Kang Chen,[2,1] Roberta L. Rudnick[1]†

The Archean Eon witnessed the production of early continental crust, the emergence of life, and fundamental changes to the atmosphere. The nature of the first continental crust, which was the interface between the surface and deep Earth, has been obscured by the weathering, erosion, and tectonism that followed its formation. We used Ni/Co and Cr/Zn ratios in Archean terrigenous sedimentary rocks and Archean igneous/metaigneous rocks to track the bulk MgO composition of the Archean upper continental crust. This crust evolved from a highly mafic bulk composition before 3.0 billion years ago to a felsic bulk composition by 2.5 billion years ago. This compositional change was attended by a fivefold increase in the mass of the upper continental crust due to addition of granitic rocks, suggesting the onset of global plate tectonics at ~3.0 billion years ago.

Magnesium content (and its ratio to other elements) is commonly used as an index of igneous differentiation and melting conditions, which are responsible for much of the compositional variation seen in silicate rocks. Thus, MgO content serves as a first-order measure of silicate rock differentiation. Estimating the average MgO content in the upper continental crust, and from that the bulk composition of this crust is, however, challenging. There are two basic approaches to determine the composition of the upper continental crust (*1*–*3*): (i) weighted averages of surface rocks and (ii) average compositions of terrigneous sediments such as shales (*1*, *2*) and glacial diamictites (*4*) that naturally sample large areas of the upper continental crust. The surface rock method is compromised by sampling bias, which becomes increasingly critical with age, because erosion removes the upper continental crust with time, and ultramafic and mafic (magnesium- and iron-rich) rocks may be eroded faster than felsic (silica- and aluminum-rich) rocks (*1*). The terrigenous sediment method cannot provide robust average concentrations of soluble elements such as Mg, which are preferentially dissolved and transported to the oceans during chemical weathering (*5*).

We compiled geochemical data for Archean shales (including pelites and graywackes), glacial diamictites (*4*), and igneous rocks from 18 Archean cratons (*6*) to demonstrate that Ni/Co and Cr/Zn ratios provide relatively tight constraints on the MgO content in the Archean upper continental crust. We use the term "continental crust" here, although the nature of the crust that was emergent (i.e., exposed to weathering, and hence the generation of terrigenous sedimentary deposits) in the Archean may have been very different from the felsic crust that we know today (*7*).

First-row transition metal ratios Ni/Co and Cr/Zn show positive correlations with MgO content in igneous and metaigneous rocks from Archean cratons (Fig. 1) due to the differences in their partition coefficients between the crystallizing phases

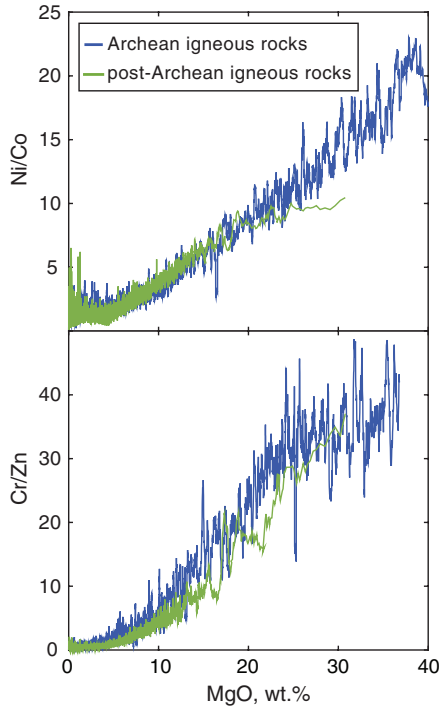

Fig. 1. Igneous Ni/Co-MgO and Cr/Zn-MgO differentiation trends for Archean and post-Archean rocks. We averaged every 20 samples to reduce scatter. Archean igneous trajectories are based on compiled igneous and metaigneous rocks from Archean cratons (*6*); post-Archean trajectories are plotted using compiled data from (*32*).

[1]Department of Geology, University of Maryland, College Park, MD 20742, USA. [2]State Key Laboratory of Geological Processes and Mineral Resources, School of Earth Sciences, China University of Geosciences, Wuhan 430074, China.
***Corresponding author. E-mail: tangmyes@gmail.com**
†Present address: Department of Earth Science, University of California, Santa Barbara, CA 93106, USA.

and melts. In particular, Ni and Cr are more compatible than Co and Zn in fractionating phases [such as olivine, spinel, and pyroxenes (*8*–*10*)], making Ni/Co and Cr/Zn ratios sensitive to the earliest stages of igneous differentiation.

Ni, Co, Cr, and Zn are generally insoluble during chemical weathering (*2*), and their ratios should thus reflect the provenance of fine-grained terrigenous sedimentary rocks. The Ni/Co and Cr/Zn ratios show secular trends in sedimentary records (Fig. 2). Archean sedimentary rocks are characterized by high Ni/Co and Cr/Zn ratios, whereas post-Archean sedimentary rocks have much lower and relatively constant Ni/Co and Cr/Zn ratios. The average Ni/Co and Cr/Zn ratios in the latter (*11*) are consistent with estimates of the present-day upper continental crust composition derived from average loess and from large-scale surface sampling (Fig. 2). Cr can be oxidized to soluble Cr^{6+} in contact with present-day atmosphere (*12*). However, the low concentrations of Cr in present-day seawater [~4.0×10^{-9} mol/kg (*13*)], which hosts large amounts of soluble elements from the continents (~4.7×10^{-1} mol/kg of Na and ~5.3×10^{-2} mol/kg of Mg), does not support the idea that there was significant Cr loss from the upper crust due to oxidative weathering. In the anoxic Archean, Cr is expected to have been even less mobile. Lithology-sensitive weathering rates may potentially bias the composition of terrigenous sediments, but currently we don't see evidence for this effect on Ni/Co and Cr/Zn ratios (*6*). We thus conclude that there is limited fractionation between Ni and Co, or Cr and Zn, due to the processes that occur during weathering, erosion, sedimentation, and diagenesis.

The Ni/Co and Cr/Zn ratios in fine-grained terrigenous sedimentary rocks decrease with time within the Archean Eon, approaching the values of the present-day upper continental crust at the end of the Archean (Fig. 3). The decreasing Ni/Co and Cr/Zn ratios with time reflect progressively more felsic (lower MgO) upper continental crust from the Mesoarchean [3.5 to 3.0 billion years ago (Ga)] to the Neoarchean (3.0 to 2.5 Ga). The Ni/Co- and Cr/Zn-age correlations established for samples from many continents suggest that these systematics reflect global crustal evolution rather than regional phenomena.

We conducted a Monte Carlo mixing simulation to determine the average MgO content of the Archean upper crust (*6*), which we assumed was composed of rocks represented in the compiled Archean craton rock data set (n = 5063 for samples with complete SiO_2, MgO, Ni, Co, Cr, and Zn data), in order to match the average Ni/Co and Cr/Zn ratios recorded by the Archean sediments. The mixing scenarios that pass the Ni/Co and Cr/Zn filters yield the average MgO content for the Archean upper continental crust. Using this approach, we tracked the evolution of the MgO content in the Archean upper continental crust (Fig. 4) based on binned locality average Ni/Co

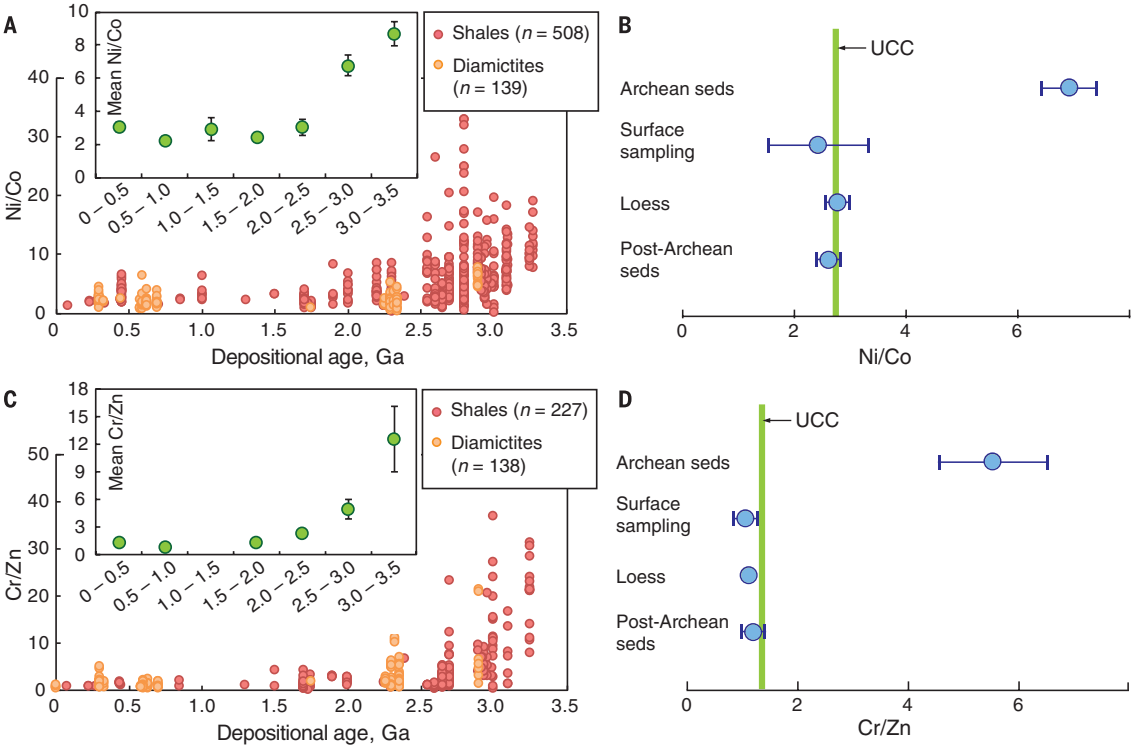

Fig. 2. Ni/Co and Cr/Zn ratios in terrigenous fine-grained sedimentary rocks (seds) through time [(A) and (C)] compared with the present-day upper continental crust [(B) and (D)]. Insets in (A) and (C) show age-binned Ni/Co and Cr/Zn ratios in terrigenous sediments (bin size = 0.5 Ga). Shale and diamictite data are provided in (*6*); loess data are from (*33*); and large-scale surface sampling data are from (*3*) and references therein. The green bars in (B) and (D) denote the reference values for present-day upper continental crust (UCC) (*3*). Error bars are 2 SE.

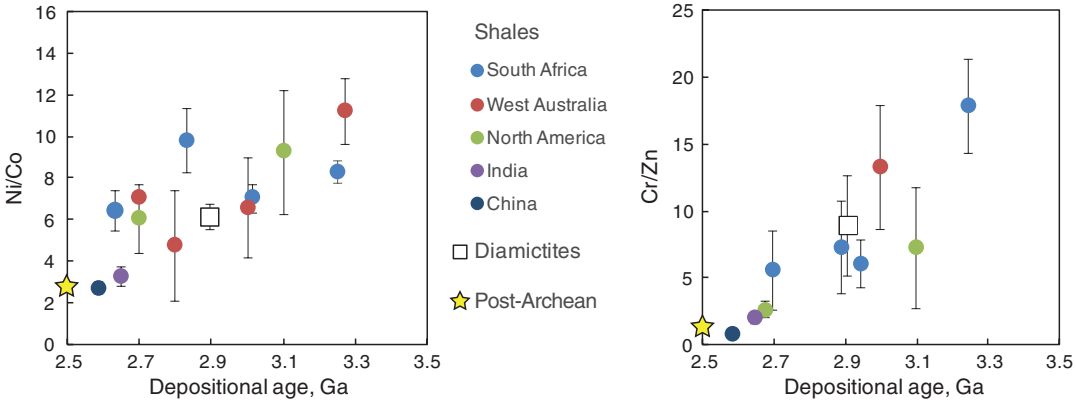

Fig. 3. Average Ni/Co and Cr/Zn ratios versus depositional ages in Archean fine-grained terrigneous sedimentary rocks from different localities. Data for individual samples were grouped by their localities (reflected by different colors) within 0.2-Ga bins. Error bars are 2 SE.

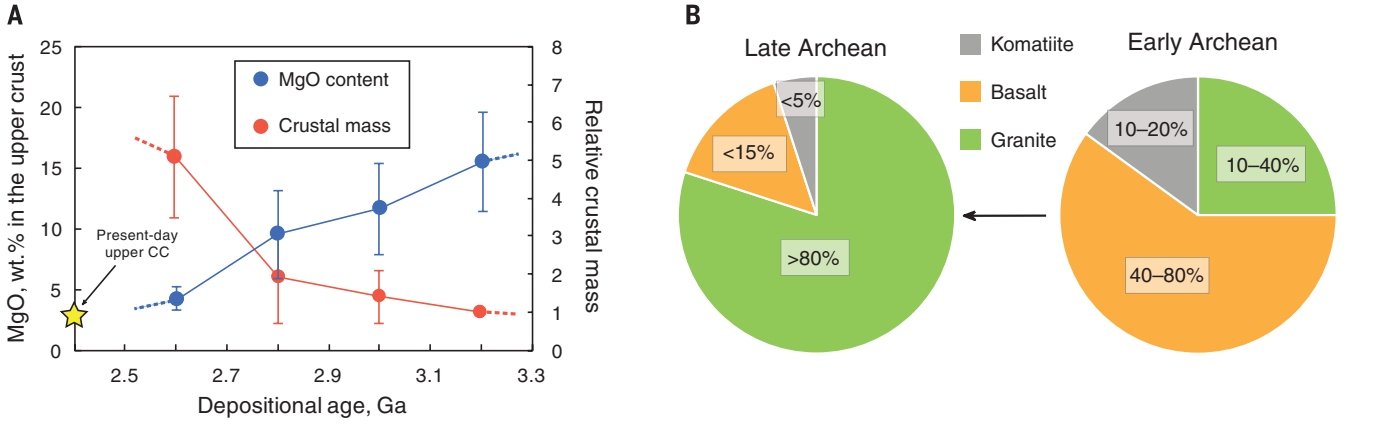

Fig. 4. Evolution of MgO content, relative mass (A), and the proportions of major rock types (B) of the upper continental crust in the Archean Eon. (A) MgO content was calculated based on the locality average Ni/Co and Cr/Zn ratios within each 0.2-Ga time interval, so that larger numbers of samples for particular localities do not have an undue influence on the outcome. Because the depositional ages of sedimentary rocks represent the minimum formation ages of the crust being sampled, both the MgO and upper crustal growth curves could shift toward older ages. Upper crustal masses are relative to that of the Mesoarchean upper continental crust. Error bars are 2 SD. (B) We calculated the proportions of TTGs, basalts, and komatiites, assuming that TTGs, basalts, and komatiites have average MgO contents of 1.4 wt % (*17*), 11 wt % (from compiled Archean craton samples with SiO_2 of 45 to 54%), and 30 wt % (*34*), respectively.

and Cr/Zn (Fig. 3). We found that the MgO content in the upper continental crust decreases from >11 weight % (wt %) in the Mesoarchean to ~4 wt %, at the end of the Archean, which is close to the present-day level of 2 to 3 wt % (*3*). The mafic upper continental crust in the early Archean was gradually replaced by a felsic upper continental crust in the Neoarchean and reached an average composition much like that of today around the Archean-Proterozoic boundary. The consistently low Ni/Co and Cr/Zn ratios in post-Archean sediments (Fig. 2) suggest a nearly constant composition for the upper continental crust since 2.5 Ga.

Although it has a high MgO content, the Archean upper continental crust may contain up to 40% tonalite-trondhjemite-granodiorites (TTGs) (Fig. 4). The budgets of incompatible elements in the sediments are controlled by the TTG components (yielding high La/Sm ratios), whereas transition metals (Ni, Co, Cr, and Zn) are controlled by mafic components.

Through most of the Archean, the upper continental crust had a mafic bulk composition (Fig. 4). This mafic composition, however, is not reflected in the mineralogy of Archean clastic sediments, which typically contain felsic minerals (e.g., detrital quartz, muscovite, and feldspar) (*14*). This disconnect between geochemical and mineralogical observations, as well as the low MgO contents in most Archean terrigenous sedimentary rocks (*15*), probably reflects preferential dissolution of mafic components (minerals and glasses) during chemical weathering (*6*). Minerals such as olivine weather congruently, releasing Mg, which is then transported to the ocean, where it may be sequestered into altered seafloor basalts through reverse weathering (*16*). Mafic to ultramafic volcanic glasses weather in a similar manner. In contrast to MgO, Ni, Co, Cr, and Zn may be incorporated into clay minerals or incorporated as metal-rich accessory phases after their release from the primary igneous phases.

We constructed a growth curve for the Archean upper continental crust based on MgO mass conservation. We assumed dilution of the upper continental crust MgO by addition of TTGs with an average of 1.4 wt % MgO (*17*). To make an upper continental crust with MgO of 4 wt % at the end of Archean requires the addition of a TTG mass that is four times that of the mafic upper continental crust older than 3.0 Ga (Fig. 4). Any addition of mafic igneous rocks to the upper continental crust would require even more felsic magma to balance the MgO content. Together, these observations suggest at least a fivefold mass increase of the upper crust in the Archean, with much of the felsic rocks being delivered in the Neoarchean. This inferred massive crustal growth in the Neoarchean is in line with certain crustal growth models (*2*, *18*) and corresponds to the peaks at ~2.7 Ga seen in both zircon U-Pb age (*18*, *19*) and mantle xenolith Re depletion age (*20*) spectra. Because our calculations are based on insoluble elements, the results are insensitive to weathering processes.

Such dramatic changes in the composition and mass of the upper continental crust suggest a profound and fundamental change in the processes that formed the Archean crust (Fig. 4). The rise of voluminous felsic magmatism that produced the TTGs, and the processes that formed the Archean TTGs, might have driven the evolution of the Archean crust. TTGs may be generated from both nonsubduction (the melting of mafic rocks in the lower crust) (*21*–*24*) and subduction (the melting of subducted plates) (*17*, *25*, *26*) origins. Melting and recycling of lower crustal mafic granulites might have persisted throughout the Archean Eon because of the high mantle temperature at that time (*27*). However, lower crust is generally depleted in water, which is important in the generation of granitic melts, including TTGs (*28*). It is thus doubtful that lower crustal melting, in the absence of subduction processes, would be efficient in producing such large amounts of TTGs that increased the mass of the Archean upper continental crust by a factor of 5. Assuming that Earth experienced a period of stagnant lid or drip tectonics before the onset of plate tectonics (*29*), the subaerial crust, which probably evolved from oceanic plateaus, had a total area of a fraction of the present-day continental crust and a composition dominated by basalt mixed with komatiites and minor TTGs generated by lower crustal melting. Approaching 3.0 Ga, the onset of global plate tectonics would have provided a continuous supply of water to the mafic source (such as subducted oceanic crust) that resulted in the rise of voluminous TTGs and other felsic magmas (*25*). Modern-style continental crust started to emerge, attended by extensive subduction in the Neoarchean. Substantially earlier global-scale plate tectonics (>3.5 Ga) are unlikely, considering the rapid mafic-felsic transition within the last 0.5 billion years of the Archean Eon. This timing is consistent with the constraints from diamonds from the subcontinental mantle (*30*), secular changes in Hf and O isotopes in zircon (*31*), and Rb-Sr systematics in magmatic records (*7*).

REFERENCES AND NOTES

1. K. C. Condie, *Chem. Geol.* **104**, 1–37 (1993).
2. S. R. Taylor, S. M. McLennan, *The Continental Crust* (Wiley, 1985).
3. R. L. Rudnick, S. Gao, 4.1 - Composition of the continental crust, in *Treatise on Geochemistry (Second Edition)*, H. D. Holland, K. K. Turekian, Eds. (Elsevier, Oxford, 2014), pp. 1–51.
4. R. M. Gaschnig *et al.*, *Earth Planet. Sci. Lett.* **408**, 87–99 (2014).
5. H. D. Holland, *The Chemical Evolution of the Atmosphere and Oceans* (Princeton Univ. Press, 1984).
6. Materials and methods are available as supplementary materials on *Science* Online.
7. B. Dhuime, A. Wuestefeld, C. J. Hawkesworth, *Nat. Geosci.* **8**, 552–555 (2015).
8. W. Leeman, K. Scheidegger, *Earth Planet. Sci. Lett.* **35**, 247–257 (1977).
9. I. Horn, S. F. Foley, S. E. Jackson, G. A. Jenner, *Chem. Geol.* **117**, 193–218 (1994).
10. H. Bougault, R. Hekinian, *Earth Planet. Sci. Lett.* **24**, 249–261 (1974).

11. In calculating the post-Archean average, we excluded data for Paleoproterozoic (2.5 to 2.0 Ga) sedimentary rocks, which might oversample the Archean upper crust and thus show slightly higher Ni/Co and Cr/Zn ratios.
12. R. Frei, C. Gaucher, S. W. Poulton, D. E. Canfield, *Nature* **461**, 250–253 (2009).
13. www.mbari.org/chemsensor/pteo.htm
14. S. M. McLennan, S. R. Taylor, A. Kröner, *Precambrian Res.* **22**, 93–124 (1983).
15. R. Feng, R. Kerrich, *Geochim. Cosmochim. Acta* **54**, 1061–1081 (1990).
16. P. Michalopoulos, R. C. Aller, *Science* **270**, 614–617 (1995).
17. H. Martin, J.-F. Moyen, *Geology* **30**, 319–322 (2002).
18. K. C. Condie, R. C. Aster, *Precambrian Res.* **180**, 227–236 (2010).
19. K. C. Condie, *Earth Planet. Sci. Lett.* **163**, 97–108 (1998).
20. D. G. Pearson, S. W. Parman, G. M. Nowell, *Nature* **449**, 202–205 (2007).
21. F. Albarède, *Tectonophysics* **296**, 1–14 (1998).
22. R. L. Rudnick, *Nature* **378**, 571–578 (1995).
23. R. H. Smithies, *Earth Planet. Sci. Lett.* **182**, 115–125 (2000).
24. J. H. Bédard, *Geochim. Cosmochim. Acta* **70**, 1188–1214 (2006).
25. S. Foley, M. Tiepolo, R. Vannucci, *Nature* **417**, 837–840 (2002).
26. R. P. Rapp, N. Shimizu, M. D. Norman, *Nature* **425**, 605–609 (2003).
27. T. E. Johnson, M. Brown, B. J. P. Kaus, J. A. VanTongeren, *Nat. Geosci.* **7**, 47–52 (2014).
28. N. T. Arndt, *Geochem. Perspect.* **2**, 405–533 (2013).
29. T. Gerya, *Gondwana Res.* **25**, 442–463 (2014).
30. S. B. Shirey, S. H. Richardson, *Science* **333**, 434–436 (2011).
31. B. Dhuime, C. J. Hawkesworth, P. A. Cawood, C. D. Storey, *Science* **335**, 1334–1336 (2012).
32. C. B. Keller, B. Schoene, M. Barboni, K. M. Samperton, J. M. Husson, *Nature* **523**, 301–307 (2015).
33. M. Tang, R. L. Rudnick, W. F. McDonough, R. M. Gaschnig, Y. Huang, *Geology* **43**, 703–706 (2015).
34. C. Herzberg *et al.*, *Geochem. Geophys. Geosyst.* **8**, Q02006 (2007).

ACKNOWLEDGMENTS

This project was supported by NSF grant EAR 0948549 and a Wylie Fellowship to M.T. We appreciate discussions with C. Hawkesworth, S. McLennan, K. Condie, N. Arndt, I. Puchtel, R. Gaschnig, D. Lowe, A. Hessler, and J. Hurowitz. We also thank three anonymous reviewers for their constructive comments. Geochemical data for the sedimentary rocks and Archean craton rocks (http://georoc.mpch-mainz.gwdg.de/georoc/) used in this work are available in the supplementary materials.

SUPPLEMENTARY MATERIALS

www.sciencemag.org/content/351/6271/372/suppl/DC1
Materials and Methods
Supplementary Text
Figs. S1 to S3
Databases S1 and S2
References (*35*–*38*)

29 September 2015; accepted 10 December 2015
10.1126/science.aad5513

COMPARATIVE BEHAVIOR

Oxytocin-dependent consolation behavior in rodents

J. P. Burkett,[1,2,3]* E. Andari,[1,2,3] Z. V. Johnson,[1,2,3] D. C. Curry,[2,3] F. B. M. de Waal,[2,3,4] L. J. Young[1,2,3,5]*

Consolation behavior toward distressed others is common in humans and great apes, yet our ability to explore the biological mechanisms underlying this behavior is limited by its apparent absence in laboratory animals. Here, we provide empirical evidence that a rodent species, the highly social and monogamous prairie vole (*Microtus ochrogaster*), greatly increases partner-directed grooming toward familiar conspecifics (but not strangers) that have experienced an unobserved stressor, providing social buffering. Prairie voles also match the fear response, anxiety-related behaviors, and corticosterone increase of the stressed cagemate, suggesting an empathy mechanism. Exposure to the stressed cagemate increases activity in the anterior cingulate cortex, and oxytocin receptor antagonist infused into this region abolishes the partner-directed response, showing conserved neural mechanisms between prairie vole and human.

Consolation, which entails comforting contact directed at a distressed party, is a common empathetic response in humans that emerges in the second year of life (*1*). Until now, consolation behavior has only been documented in a few nonhuman species and only in the context of naturally occurring aggressive conflicts, as first described in great apes (*2*, *3*) and subsequently in canids (*4*, *5*), corvids (*6*, *7*), and elephants (*8*). These observations have, so far, been taken to mean that consolation behavior may require advanced cognitive capacities (*9*). Nonetheless, rodents also manifest some of the empathy-related capacities (*10*–*16*) thought to underlie consolation in humans and chimpanzees (*1*, *17*). If consolation behavior were to be observed outside of species with advanced cognition, this would suggest that it rests on much older, more widespread, and less cognitive capacities and may be variably expressed because of species-specific evolutionary context. Moreover, observing consolation behavior in a laboratory rodent under reproducible conditions would allow for empirical research on causal biological mechanisms relevant to human mental health.

Rodents in the genus Microtus display diverse mating strategies and social structures. The prairie vole (*Microtus ochrogaster*) is a socially monogamous, biparental rodent species in which both males and females may participate in philopatric cooperative breeding in the parental nest (*18*). These social traits frequently coevolve with other cooperative or altruistic behaviors that increase direct or indirect fitness, including social buffering among colony members (*19*). In contrast, closely related meadow voles (*M. pennsylvanicus*) are promiscuous breeders with no formal social structure that show comparatively abbreviated, uniparental care of pups (*20*). We hypothesized that the prairie vole, but not the meadow vole, would show consolation behavior under reproducible laboratory conditions. Additionally, we hypothesized that as suggested for humans and great apes, consolation behavior in the prairie vole would be based on an empathy mechanism. Last, we hypothesized that consolation behavior would be mediated by conserved neurobiological and neurochemical mechanisms consistent with those implicated in empathy in humans.

Consolation behavior has been defined as an increase in affiliative contact in response to and directed toward a distressed individual, such as a victim of aggression, by an uninvolved bystander, which produces a calming effect (*2*). This definition emphasizes victims of aggression due to observational constraints in naturalistic studies. In humans, the definition includes individuals experiencing stress from other sources (*1*), a strategy used in elephants (*8*) and suggested for primates (*9*). On the basis of this research, we first developed a set of laboratory conditions under which unstressed male and female prairie voles ("observers") would respond spontaneously and selectively to stressed conspecifics ("demonstrators") with a prosocial, other-directed behavior (the "consolation test") (Fig. 1A). In this protocol, an observer and a demonstrator housed together are separated from each other, and the demonstrator either sits alone in a home cage compartment or is exposed to a stressor consisting of five tones paired with light foot-shocks (0.8 mA, 0.5 s) distributed over the course of 24 min (Pavlovian fear conditioning). The demonstrator is then reunited with the naïve observer, and the natural response is recorded and measured. Under these experimental conditions, licking and grooming directed by observers toward demonstrators (or "allogrooming") was significantly longer in duration (time-treatment interaction, $F_{1,11} = 6.7$, $P < 0.025$) and shorter in latency ($t_{11} = 3.9$, $P < 0.003$) after a separation during which the demonstrator was stressed (Fig. 1B and fig. S1). Prairie vole observers did not increase allogrooming toward demonstrators after a control separation, demonstrating the selectivity of the response. Both male and female observers

[1]Silvio O. Conte Center for Oxytocin and Social Cognition, Emory University, Atlanta, GA, USA. [2]Center for Translational Social Neuroscience, Emory University, Atlanta, GA, USA. [3]Yerkes National Primate Research Center, Emory University, Atlanta, GA, USA. [4]Utrecht University, Utrecht, Netherlands. [5]Department of Psychiatry, School of Medicine, Emory University, Atlanta, GA, USA.
*Corresponding author. E-mail: jpburke@emory.edu (J.P.B.); lyoun03@emory.edu (L.J.Y.)

showed this behavioral response, differing only in baseline allogrooming (sex-time interaction, $F_{1,73}$ = 6.4, P < 0.015) (fig. S2). Meta-analysis across 13 experiments shows that observers initiate allogrooming within the first minute and continue for at least the first 10 min of reunion time (Fig. 1C, figs. S3 and S4, and table S1). Additionally, stressed demonstrators that rested alone in the home cage after the stressor subsequently showed increased anxiety-like behavior relative to unstressed controls, whereas those that interacted with the observer for the same period of time showed completely normalized anxiety behavior (interaction effect, $F_{2,63}$ = 3.2, P < 0.05) (Fig. 1D). This suggests that the observer provided social buffering to the demonstrator, which is consistent with other studies showing stress reduction in rodents (*21*, *22*) and primates (*3*, *23*). In contrast, meadow vole observers showed no differences in allogrooming based on the stress state of the demonstrator (fig. S5). The combination of a selective increase in directed affiliation with a social buffering effect supports the designation of the prairie vole's natural response as a consolation behavior.

The observation that prairie voles detect the stress state of conspecifics and form a directed prosocial response raises the question of whether the behavior is empathy-based. The empathy hypothesis was tested by assaying for some of its purported characteristics in human and other mammalian species, including emotional contagion, state matching, familiarity bias, and self-other differentiation (*24*–*26*). In accordance, prairie vole observers showed behavioral responses consistent with emotional contagion by mimicking the anxiety- and fear-related behaviors of stressed demonstrators (Fig. 2). Observers interacting with a stressed demonstrator after separation matched the increase in self-grooming shown by the demonstrator (main effect of time, $F_{1,23}$ = 12.7, P < 0.002) (Fig. 2A). Additionally, when observing a fear-conditioned demonstrator freezing during presentations of the conditioned stimulus (tones), the unconditioned observers showed an increase in freezing (main effect of time, $F_{1,22}$ = 22.2, P < 0.0002) (Fig. 2B) concurrently with the demonstrator's freezing (Fig. 2C). Observers separated from stressed demonstrators across a clear, perforated barrier had significantly elevated plasma corticosterone afterward (main effect of barrier, $F_{2,27}$ = 4.8, P < 0.017) (Fig. 3A), which strongly correlated with that of the demonstrator (stressor, R^2 = 0.82, P < 0.001; separation, R^2 < 0.01, P > 0.98; difference between correlations, Fisher's transformation, Z = 2.8, P < 0.006) (Fig. 3B), representing a clear example of physiological state–matching similar to that attributed to empathy in humans (*27*). Observers in full contact with demonstrators without a barrier showed no increase, suggesting that active performance of consolation behavior may ameliorate the observer's physiological stress response. Consolation behavior was significantly biased toward familiar individuals: Although baseline allogrooming did not differ between groups containing mates, siblings, cagemates, and strangers, observers directed consolation behavior only toward familiar stressed demonstrators and not toward stressed strangers (time-relation interaction, $F_{2,73}$ = 13.6, P < 0.0001; main effect of relation, $F_{2,73}$ = 26.6, P < 0.0001; cagemates, $t(8)$ = −6.1, P < 0.0003) (Fig. 3C and figs. S6 and S7). Last, although observers and stressed demonstrators both showed signs of anxiety and stress during reunion, observers increased allogrooming toward demonstrators, whereas demonstrators themselves did not alter their allogrooming (time-subject interaction, $F_{1,70}$ = 35.6, P < 0.0001) (Fig. 3D). This differential response dependent on the source of the individual's stress (vicarious or personal) is an example of self-other differentiation, which shows that the allogrooming response is not a general stress-coping behavior.

The combination of behavioral and physiological state matching in the observer shows that the observer is not neutral to the stress state of the demonstrator, as might be predicted if the allogrooming response were purely information-gathering behavior. Empathy-related responses and behaviors are biased toward familiar individuals in many species, including humans (*10*, *11*, *17*, *28*); the allogrooming response in prairie voles is also selective for familiar conspecifics (including unrelated long-term cagemates), representing a true social behavior rather than reproductive or kinship-related. Additionally, the lack of response toward strangers shows that observers are not simply reacting to aversive

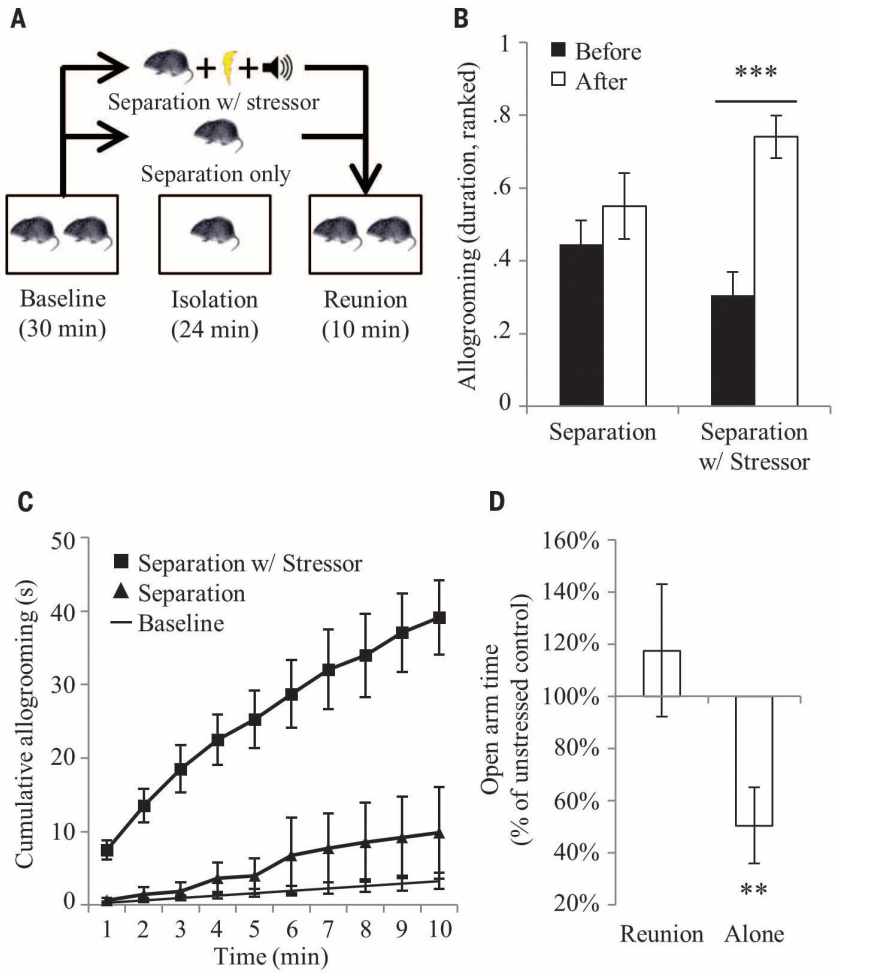

Fig. 1. The consolation test. (**A**) The consolation test protocol. (**B**) Observer-demonstrator pairs (n = 12 pairs) underwent both control separations without a stressor, and separations in which the demonstrator was stressed. Duration of allogrooming was nonparametric in these experiments and was transformed to ranks, and the ranks normalized to a 0–1 scale. Bars represent the mean ± SEM of the ranked duration of allogrooming directed by the observer toward the demonstrator. (**C**) A meta-analysis of results from 13 experiments shows the precise expected duration of observer-demonstrator allogrooming over the course of 10 min. Points represent cumulative seconds with 95% confidence intervals. (**D**) After resting alone in the home cage for 5 min, stressed demonstrators (n = 10 voles) showed a significant decrease in open-arm time on the elevated plus maze test relative to unstressed controls (n = 11 voles). Stressed (n = 11 voles) and unstressed (n = 11 voles) demonstrators reunited with the observer for 5 min showed no differences in open-arm time. Bars represent the mean ± SEM of the percent change in open-arm time between stressed and unstressed demonstrators. **P < 0.005, ***P < 0.0005.

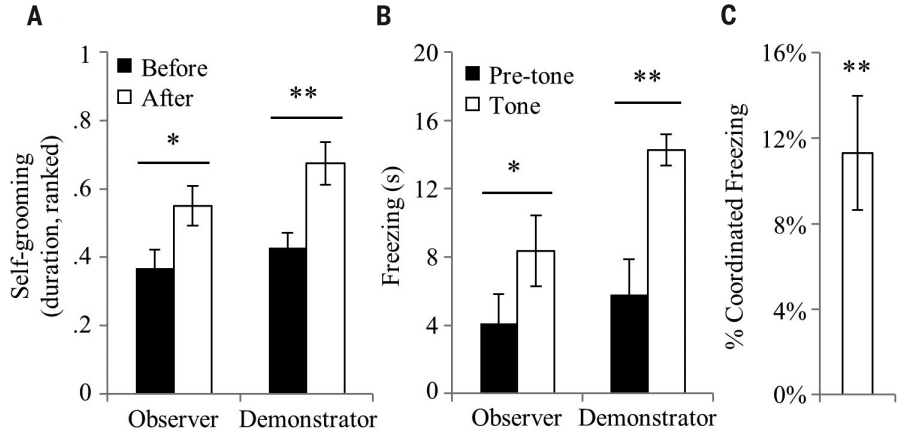

Fig. 2. Emotional contagion. Prairie vole observers exposed to a stressed demonstrator show anxiety- and fear-related responses that match the demonstrator's responses. (**A**) Anxiety-related behavior was measured in observers and demonstrators (n = 24 pairs) interacting after reunion. Bars represent the mean ± SEM of the ranked duration of self-grooming performed by the observer and demonstrator. (**B**) Freezing was measured while fear-conditioned demonstrators and unconditioned observers (n = 12 pairs) were exposed together to a 30-s conditioned stimulus (CS). Bars represent the mean ± SEM of freezing before and after the CS. (**C**) Coordinated freezing during the CS between observer and demonstrator pairs (n = 12 pairs), calculated as the within-pair difference between the observed percent of simultaneous freezing and the simultaneous freezing expected by chance. *P < 0.05, **P < 0.005.

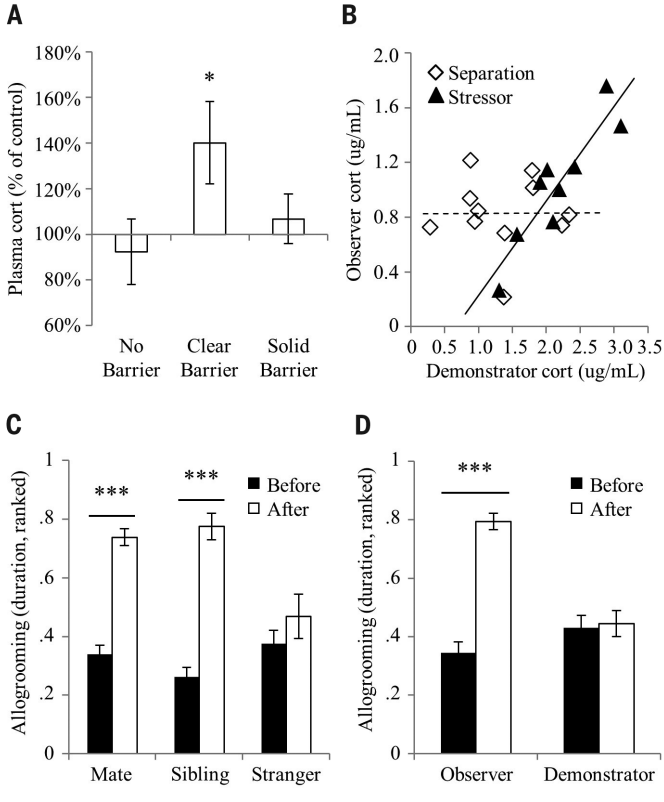

Fig. 3. State matching, familiarity bias, and self-other differentiation. (**A**) Observer-demonstrator pairs underwent either control separations or separations with stressor and subsequently were either reunited in the home cage with no barrier (separated, n = 11 pairs; stressed, n = 12 pairs), reunited across a clear perforated barrier (separated, n = 11 pairs; stressed, n = 11 pairs), or in independent sections of the home cage separated by a solid opaque barrier (separated, n = 7 pairs; stressed, n = 9 pairs). Bars represent the mean ± SEM percent change in plasma corticosterone concentration in observers between the control separations and separations with stressor in each cage configuration. (**B**) Correlations between the plasma corticosterone concentrations of observers and demonstrators that interacted across a clear perforated barrier. The dashed and solid lines represent regression lines for the separation (n = 11 pairs) and stressor (n = 9 pairs) conditions, respectively. (**C**) Prairie vole mated pairs (n = 37 pairs), same-sex sibling pairs (n = 22 pairs), and same-sex stranger pairs (n = 20 pairs) underwent separations in which one cagemate was stressed. Bars represent the mean ± SEM of the ranked duration of allogrooming directed by the observer toward the demonstrator. (**D**) Observer-demonstrator pairs (n = 37 pairs) underwent separations during which the demonstrator was stressed. Bars represent the mean ± SEM of the ranked duration of allogrooming by either the observer or the demonstrator. *P < 0.05, **P < 0.005, ***P < 0.0005.

cues. Whereas some empathy-related studies used training or conditioning (*15*, *16*, *29*, *30*), the consolation test in the present experiments was administered only once to each set of subjects and therefore captured unconditioned responses. The focus on unconditioned responses means that the consolation test does not assume or necessarily require any particular cognitive capacities, including conscious knowledge or perspective taking—which, in a multilayered view of empathy, may be included but are not required (*24*–*26*). Several empathy-related paradigms require priming the observer with direct exposure to the stressor (*12*–*15*); in contrast, observers in the present paradigm neither experienced nor witnessed the stressor, and therefore self-referential anticipation of a threat can be ruled out as an explanation. Last, a novel experience alone was not sufficient to elicit a consolation response in absence of a stressor (time-treatment interaction, $F_{1,16}$ = 7.1, P = 0.017) (fig. S8). This confluence of evidence and exclusion of alternative explanations supports the interpretation that an empathy mechanism underlies the increase in affiliative behavior in prairie voles in response to a stressed conspecific.

In humans, the oxytocin receptor (OTR) has been linked to empathy, emotion recognition, and socioemotional engagement (*31*–*33*). Observers that received an injection of an oxytocin antagonist (OTA) into the cerebral ventricle before the consolation test did not change their baseline allogrooming but showed no consolation response (time-treatment interaction, $F_{1,27}$ = 5.0, P < 0.04) (Fig. 4A), demonstrating that OTR activation in the brain is necessary for consolation behavior. The prairie vole anterior cingulate cortex (ACC), adjacent prelimbic cortex (PLC), and nucleus accumbens shell (NACS) all express high densities of OTR (Fig. 4B); in humans, the ACC and homologous medial prefrontal cortex have been linked to empathy (*34*), and the NACS is typically linked to social and nonsocial reward (*35*). Using immunohistochemistry targeting the immediate early gene protein FOS, we determined that the ACC, but not PLC or NACS, is differentially active in observers interacting with stressed demonstrators as compared with unstressed demonstrators (treatment-region interaction, $F_{2,34}$ = 6.7, P < 0.004; post-hoc t test, P < 0.02 uncorrected) (Fig. 4, C and D, and fig. S9). This result was validated in observers exposed to stressed demonstrators across a clear perforated barrier (t test, P < 0.04) (fig. S10), suggesting that the difference in activity was due to exposure to the stressed demonstrator rather than caused by the observer's behavior. Following these results, we hypothesized that oxytocin may act region-specifically on OTR in the ACC to enable consolation behavior. An injection of OTA directly into ACC abolished the consolation response in observers (time-treatment interaction, $F_{1,13}$ = 7.4, P < 0.02) (Fig. 4E and fig. S11A), whereas injections into adjacent PLC had no effect (Fig. 4F and fig. S11B); this shows that OTR signaling within the ACC modulates consolation, possibly by disrupting physiological, emotional,

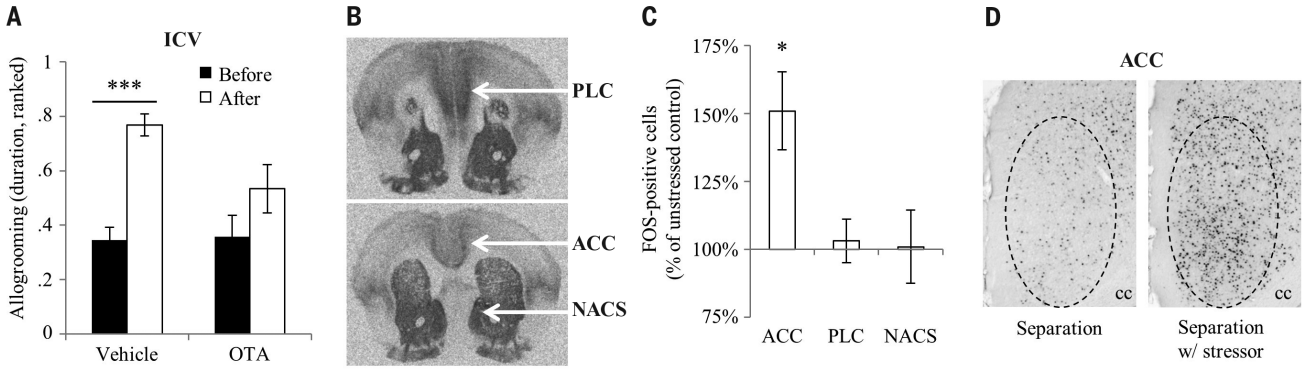

Fig. 4. Neural mechanisms of consolation behavior. (**A**) Observers received an intracerebroventricular (ICV) injection of OTA (n = 16 voles) or vehicle (n = 12 voles) before the consolation test. Bars represent mean ± SEM. (**B**) Receptor autoradiographs show the presence of OTR in prairie vole PLC, ACC, and NACS. (**C**) Observers were administered a consolation test with control separations (n = 10 voles) or separations with stressor (n = 9 voles). Bars represent mean ± SEM. (**D**) Images show FOS immunoreactivity in the right ACC of observers representing the mean from each treatment group. Dashed circles show the quantified area. cc, corpus callosum. (**E**) Observers received a bilateral injection of OTA (n = 8 voles) or vehicle (n = 7 voles) directly into the ACC before the consolation test. Bars represent mean ± SEM. (**F**) Observers received a bilateral injection of OTA (n = 8 voles) or vehicle (n = 9 voles) directly into the PLC before the consolation test. Bars represent mean ± SEM. *P < 0.05, **P < 0.005, ***P < 0.0005.

and/or behavioral responses. This evidence demonstrates that the ACC is one node where activity increases during interaction with a stressed conspecific, and where OTR activation is necessary for the expression of consolation behavior. These neural substrates suggest conserved biological mechanisms for consolation behavior between prairie vole and human.

The presence of consolation behavior in prairie voles demonstrates that this behavior does not require advanced cognitive capacities, and the conserved neurobiology of consolation between prairie voles and humans suggests a deep homology of the underlying neural substrates. The ancestral biological mechanisms supporting maternal care in mammals have likely served as the basis from which many complex social behaviors evolved, including empathy (*24*, *36*) and pair bonding (*37*), both of which involve the reorienting of parental behaviors toward adult conspecifics. Nonetheless, the confirmed absence of consolation in the closely related meadow vole and in most macaques (*9*, *38*) shows that consolation behavior emerges only under particular social and evolutionary conditions. Understanding the neurobiology of oxytocin-dependent consolation behavior in prairie voles may help us to understand the diverse deficits in detecting and responding to the emotions of others that are present in many psychiatric conditions, including autism, schizophrenia, and psychopathy.

REFERENCES AND NOTES

1. C. Zahn-Waxler, M. Radke-Yarrow, E. Wagner, M. Chapman, *Dev. Psychol.* **28**, 126–136 (1992).
2. F. B. M. de Waal, A. van Roosmalen, *Behav. Ecol. Sociobiol.* **5**, 55–66 (1979).
3. Z. Clay, F. B. M. de Waal, *PLOS ONE* **8**, e55206 (2013).
4. E. Palagi, G. Cordoni, *Anim. Behav.* **78**, 979–986 (2009).
5. A. K. A. Cools, A. J. M. van Hout, M. H. J. Nelissen, *Ethology* **114**, 53–63 (2008).
6. O. N. Fraser, T. Bugnyar, *PLOS ONE* **5**, e10605 (2010).
7. A. M. Seed, N. S. Clayton, N. J. Emery, *Curr. Biol.* **17**, 152–158 (2007).
8. J. M. Plotnik, F. B. M. de Waal, *PeerJ* **2**, e278 (2014).
9. F. B. M. de Waal, F. Aureli, in *Reaching into Thought: The Minds of the Great Apes*, A. E. Russon, K. A. Bard, S. T. Parker, Eds. (Cambridge Univ. Press, 1996).
10. D. J. Langford *et al.*, *Science* **312**, 1967–1970 (2006).
11. D. Jeon *et al.*, *Nat. Neurosci.* **13**, 482–488 (2010).
12. E. J. Kim, E. S. Kim, E. Covey, J. J. Kim, *PLOS ONE* **5**, e15077 (2010).
13. Q. Chen, J. B. Panksepp, G. P. Lahvis, *PLOS ONE* **4**, e4387 (2009).
14. J. Sanders, M. Mayford, D. Jeste, *PLOS ONE* **8**, e74609 (2013).
15. R. M. Church, *J. Comp. Physiol. Psychol.* **52**, 132–134 (1959).
16. G. E. Rice, P. Gainer, *J. Comp. Physiol. Psychol.* **55**, 123–125 (1962).
17. T. Romero, M. A. Castellanos, F. B. de Waal, *Proc. Natl. Acad. Sci. U.S.A.* **107**, 12110–12115 (2010).
18. L. L. Getz, B. Mcguire, T. Pizzuto, J. E. Hofmann, B. Frase, *J. Mammal.* **74**, 44–58 (1993).
19. S. Nunes, in *Rodent Societies: An Ecological & Evolutionary Perspective*, J. O. Wolff, P. W. Sherman, Eds. (Univ. of Chicago Press, 2007), chap. 13.
20. L. L. Getz, *J. Mammal.* **53**, 310–317 (1972).
21. T. Kikusui, J. T. Winslow, Y. Mori, *Philos. Trans. R. Soc. London B Biol. Sci.* **361**, 2215–2228 (2006).
22. A. S. Smith, Z. Wang, *Biol. Psychiatry* **76**, 281–288 (2014).
23. O. N. Fraser, D. Stahl, F. Aureli, *Proc. Natl. Acad. Sci. U.S.A.* **105**, 8557–8562 (2008).
24. S. D. Preston, F. B. M. de Waal, *Behav. Brain Sci.* **25**, 1–20, discussion 20–71 (2002).
25. F. B. de Waal, *Annu. Rev. Psychol.* **59**, 279–300 (2008).
26. C. D. Batson, in *The Social Neuroscience of Empathy*, J. Decety, W. Ickes, Eds. (MIT Press, 2009).
27. T. W. Buchanan, S. L. Bagley, R. B. Stansfield, S. D. Preston, *Soc. Neurosci.* **7**, 191–201 (2012).
28. E. Palagi, I. Norscia, E. Demuru, *PeerJ* **2**, e519 (2014).
29. S. Watanabe, K. Ono, *Behav. Processes* **13**, 269–277 (1986).
30. I. Ben-Ami Bartal, J. Decety, P. Mason, *Science* **334**, 1427–1430 (2011).
31. G. Domes, M. Heinrichs, A. Michel, C. Berger, S. C. Herpertz, *Biol. Psychiatry* **61**, 731–733 (2007).
32. E. Andari *et al.*, *Proc. Natl. Acad. Sci. U.S.A.* **107**, 4389–4394 (2010).
33. R. Hurlemann *et al.*, *J. Neurosci.* **30**, 4999–5007 (2010).
34. C. Lamm, J. Decety, T. Singer, *NeuroImage* **54**, 2492–2502 (2011).
35. K. C. Berridge, M. L. Kringelbach, *Neuron* **86**, 646–664 (2015).
36. S. D. Preston, *Psychol. Bull.* **139**, 1305–1341 (2013).
37. M. Numan, L. J. Young, *Horm. Behav.* 10.1016/j.yhbeh.2015.05.015 (2015).
38. G. Schino, S. Geminiani, L. Rosati, F. Aureli, *J. Comp. Psychol.* **118**, 340–346 (2004).

ACKNOWLEDGMENTS

This research was supported by grants from the National Institutes of Health (1P50MH100023 and R01MH096983) to L.J.Y. and by predoctoral fellowships from the NIH (NIGMS T32GM08605-10, F31 MH102911-01) and Emory University (Emory Neuroscience Initiative Scholars Program in Interdisciplinary Neuroscience Research) to J.P.B. Additional support was provided by a grant from the NIH (OD P51OD011132) to Yerkes National Primate Research Center. We gratefully acknowledge colony management by L. Mathews, cage design and assembly by G. Feldpausch, and assistance from F. Haddad, L. Hearn, L. S. Jones, K. Kittelberger, R. C. Pearcy, M. Reyes, and M. Carr-Reynolds.

SUPPLEMENTARY MATERIALS

www.sciencemag.org/content/351/6271/375/suppl/DC1
Materials and Methods
Figs. S1 to S12
Table S1
References (*39*–*47*)

30 April 2015; accepted 18 December 2015
10.1126/science.aac4785

NEURODEVELOPMENT

Oligodendrocyte precursors migrate along vasculature in the developing nervous system

Hui-Hsin Tsai,[1]* Jianqin Niu,[1]* Roeben Munji,[2] Dimitrios Davalos,[3] Junlei Chang,[4] Haijing Zhang,[4,5,6,7] An-Chi Tien,[1] Calvin J. Kuo,[4] Jonah R. Chan,[8] Richard Daneman,[2] Stephen P. J. Fancy[1,8,9,10]†

Oligodendrocytes myelinate axons in the central nervous system and develop from oligodendrocyte precursor cells (OPCs) that must first migrate extensively during brain and spinal cord development. We show that OPCs require the vasculature as a physical substrate for migration. We observed that OPCs of the embryonic mouse brain and spinal cord, as well as the human cortex, emerge from progenitor domains and associate with the abluminal endothelial surface of nearby blood vessels. Migrating OPCs crawl along and jump between vessels. OPC migration in vivo was disrupted in mice with defective vascular architecture but was normal in mice lacking pericytes. Thus, physical interactions with the vascular endothelium are required for OPC migration. We identify Wnt-Cxcr4 (chemokine receptor 4) signaling in regulation of OPC-endothelial interactions and propose that this signaling coordinates OPC migration with differentiation.

Oligodendrocytes, the myelinating cells of the central nervous system (CNS), support rapid saltatory nerve conduction and maintain axon integrity through metabolic coupling (*1*, *2*). Oligodendrocyte precursor cells (OPCs) arise from the ventricular zone in the embryonic brain and spinal cord, in domains defined through pattern formation (*3*, *4*). From these domains, OPCs migrate widely through the CNS to achieve uniform distribution (fig. S1).

The CNS is built by cells migrating away from their places of origin to construct mature neural tissue. Neuroblasts disperse in radial and tangential patterns (*5*) following substrates such as radial glial cells (*5*, *6*), corticofugal fibers (*7*), or Bergmann glia (*8*). Postnatal neuronal migration is more limited. In the rostral migratory stream, neuroblasts crawl over one another (*9*) and along blood vessels to get from the subventricular zone to the olfactory bulb (*10*–*12*). Astrocytes seem to migrate only radially during development, following radial glia without secondary tangential migration. Thus, astrocytes occupy restricted spatial domains in adulthood related to their embryonic site of origin (*13*).

[1]Department of Pediatrics, University of California at San Francisco (UCSF), San Francisco, CA 94158, USA. [2]Departments of Pharmacology and Neuroscience, University of California at San Diego (UCSD), San Diego, CA 92093, USA. [3]Department of Neurosciences, Lerner Research Institute, Cleveland Clinic Foundation, Cleveland, OH 44195, USA. [4]Division of Hematology, Department of Medicine, Stanford University, Stanford, CA 94305, USA. [5]Department of Urology, Cleveland Clinic Foundation, Cleveland, OH 44195, USA. [6]Howard Hughes Medical Institute (HHMI), Chevy Chase, MD 20815, USA. [7]Duke University School of Medicine, Durham, NC 27710, USA. [8]Department of Neurology, UCSF, San Francisco, CA 94158, USA. [9]Division of Neonatology, UCSF, San Francisco, CA 94158, USA. [10]Newborn Brain Research Institute, UCSF, San Francisco, CA 94158, USA.
*These authors contributed equally to this work. †Corresponding author. E-mail: stephen.fancy@ucsf.edu

Oligodendrocyte precursor cells, which migrate more extensively than neurons and other glia (*4*), must also recognize their path and migrate through often-compact developing tissue before interactions with their targets halt their migration. OPCs also maintain this capacity in response to demyelination in the adult CNS (*14*). OPC motility is regulated by cell-intrinsic mechanisms (*15*, *16*), polarity (*17*), and extracellular cues (*18*–*20*). Various substrates have been proposed as putative candidates for OPC migration (*21*). Here we show that OPCs migrate along the vasculature through the developing CNS and that Wnt signaling regulates these OPC-endothelial interactions.

In the developing mouse forebrain, the first OPCs originate from ventral regions of the medial ganglionic eminence and anterior entopeduncular area at embryonic day 12 (E12) (Fig. 1A) (*4*). The vascular network is established before OPC emergence (*22*). At E7.5 to E8.5, a perineural vascular plexus surrounds the ventral neural tube. Angiogenic endothelial sprouts invade the neuroepithelium from the pial surface to periventricular areas by E11.5, with the blood-brain barrier likely established at this time (*22*, *23*), generating a periventricular vascular plexus (*24*).

We first assessed the migration of OPCs in the developing mouse brain (see supplementary materials and methods). Migratory OPCs, defined by the expression of platelet-derived growth factor receptor α (PDGFRα), appear at E12 and stream away from the medial ganglionic eminence, in association with this vascular scaffold (Fig. 1B and fig. S2). Many of these migratory OPCs are elongated along blood vessels (Fig. 1C), with their cell bodies directly on the abluminal endothelial surface and a single, long leading process along the vessel (Fig. 1D and *A in fig. S1D). Indeed, 58% (±4.4%) of OPCs have their cell bodies directly on a vessel wall (Fig. 1F), and of the remainder, 67% (±8.9%) display at least one observable process (which can be more than 30 μm in length) that engages a vessel (* in Fig. 1, E and F). By E14, OPCs migrating dorsally reach the subpallial-to-pallial boundary (Fig. 1A and fig. S1B), continuing to show an intimate association with the vasculature (Fig. 1G), elongated along vessels (Fig. 1H), and often extending one or more processes between vessels (* in Fig. 1I and *B and *C in fig. S1D). The number of OPCs in the mouse cortex increases (*4*) by a factor of ~3 between E16 and E18. Olig2$^+$ cells migrating from deep to superficial cortical layers palisade along the vasculature that penetrates the cortex at E18 (Fig. 1J and fig. S1C).

A similar association of OPCs with vasculature is seen during development of the human cortex. The first Olig2-expressing cells to arrive in the human outer cortex at gestational week 14 appose penetrating vessels (Fig. 1K); association of Olig2$^+$ and PDGFRα$^+$ OPCs with blood vessels remains evident at gestational weeks 18 and 24 (Fig. 1, L and M). Migrating human OPCs, expressing PDGFRα, are morphologically similar to those of mice in that they extend single leading processes in the direction of movement along and toward vessels (Fig. 1N).

To live-image OPC migration in acute slices of the developing brain, we labeled vessels of *Olig2–green fluorescent protein (GFP)* reporter mice by intracardiac infusion of rhodamine-lectin. We selected brain slices to observe regions with actively migrating OPCs (*4*), including E16 and E18 cortex. OPCs demonstrate two behaviors during migration on vessels: crawling and jumping. Crawling is characterized by the cell body maintaining contact with the abluminal endothelial surface (Fig. 2A, fig. S3, and movies S1 and S2). Jumping is characterized by the OPC extending a leading process from one vessel toward another, followed by translocation of the cell body to make contact with the new vessel (Fig. 2B and movie S3). Jumping is more rapid than crawling, presumably entailing fewer physical contacts with the endothelial surface. The association of migrating OPCs with the vasculature is not limited to the embryonic brain; it is also found in the spinal cord (Fig. 2, C to H) and at later postnatal times when OPCs are required to migrate (fig. S4).

To study the requirement for OPC migration along a vascular scaffold, we used both conventional and conditional transgenic knockout mice to disrupt vascular development. In mice, the orphan G protein–coupled receptor 124 (GPR124), which is expressed by endothelium and pericytes within the CNS, is essential for developmental vascular sprouting (*25*) (Fig. 3A). At E11, mice lacking GPR124 exhibit CNS vascular patterning defects and reduced vascularization (*25*), as well as glomeruloid vascular abnormalities (Fig. 3J) characterized by highly irregular, multilayered endothelial aggregates with peripheral PDGFRβ$^+$ pericyte investment and lack of ventricularly directed endothelial filopodia (*25*).

We hypothesized that OPC dispersal would be abnormal in E14 *GPR124*$^{-/-}$ embryos. In these mice, Isl1/2-expressing motor neurons, which also derive from the motor neuron precursor (pMN) domain of the spinal cord, migrate in normal

numbers to the ventral gray matter (Fig. 3C). Additionally, Glast$^+$ radial glial fibers appear normal (fig. S5A), and brain lipid binding protein (BLBP)–expressing astrocytes, which leave the ventricular zone at the same time as OPCs from domains adjacent to the pMN, migrate normally in spinal cord (Fig. 3D). However, OPCs abnormally accumulated in the pMN and failed to egress normally from the spinal cord ventricular zone (Fig. 3E). Seventy percent fewer OPCs dispersed into the surrounding gray matter (fig. S7A) ($*P = 7.3 \times 10^{-5}$). Rates of OPC cell death were unchanged (fig. S5B), which suggests that the problem is in migration. Because GPR124 is expressed by both endothelium and pericytes, we used *Cdh5-cre:Gpr124(fl/fl)* mice (Cdh5cre is vascular endothelium–specific VE-Cadherin-cre) to target loss of function to the vascular endothelium (Fig. 3F and fig. S6). We observed the same OPC migration deficit, ruling out a cell-intrinsic effect of Gpr124 loss in OPCs and showing that *GPR124* function in the endothelium is required to regulate OPC migration. Vascular development is also deficient in the brains of E14 GPR124$^{-/-}$ mice, with associated severe OPC migration deficits. OPCs expressing PDGFRα and Olig2 show reductions in migration (Fig. 3, G and H, and fig. S7B), reaching only as far as the limits of the ventral vascular plexus (Fig. 3H), and accumulate in clumps around glomeruloid malformations (Fig. 3K and fig. S7D). In *PDGFR*β-null mice, which lack all pericytes (*26*), OPC migration was maintained (fig. S8). Thus, OPCs require an endothelial vascular scaffold, but not pericytes, as a physical substrate for migration throughout the developing CNS (Fig. 3I).

Cessation of OPC migration on vasculature and detachment from the endothelium might be coupled to the onset of OPC differentiation, which suggests that negative regulators of OPC terminal differentiation might mediate an interaction between OPCs and the endothelium. The Wnt pathway inhibits OPC differentiation (*27*–*29*), leading us to question its role in OPC migration and interaction with the endothelium. We made use of *Olig2-cre:Apc(fl/fl)* mice (*28*) because they show constitutively active Wnt signaling in OPCs due to the conditional loss of the obligate Wnt repressor *adenomatous polyposis coli* (*APC*). In addition to delays in OPC differentiation in these mice (fig. S9) (*28*) with resulting hypomyelination, we observed aberrant clusters of OPCs associated with vasculature throughout the brain and spinal cord (Fig. 4, A to D, and fig. S10A) at early postnatal times. OPC aggregation around vessels and absence of increased proliferation (fig. S10B) suggest that Wnt activation in OPCs drives their attraction to the vascular scaffold and that high Wnt tone in OPCs in *Olig2-cre:Apc(fl/fl)* mice leads to an inability to dissociate from the vasculature and disperse normally into CNS parenchyma (fig. S11). A loss of Wnt tone in OPCs, in cortical slice cultures treated with the small-molecule Wnt inhibitor XAV939 (*29*), results in a 76% ($P = 1.55 \times 10^{-5}$) reduction in OPC recruitment to the microvasculature at postnatal day 1 (P1) and

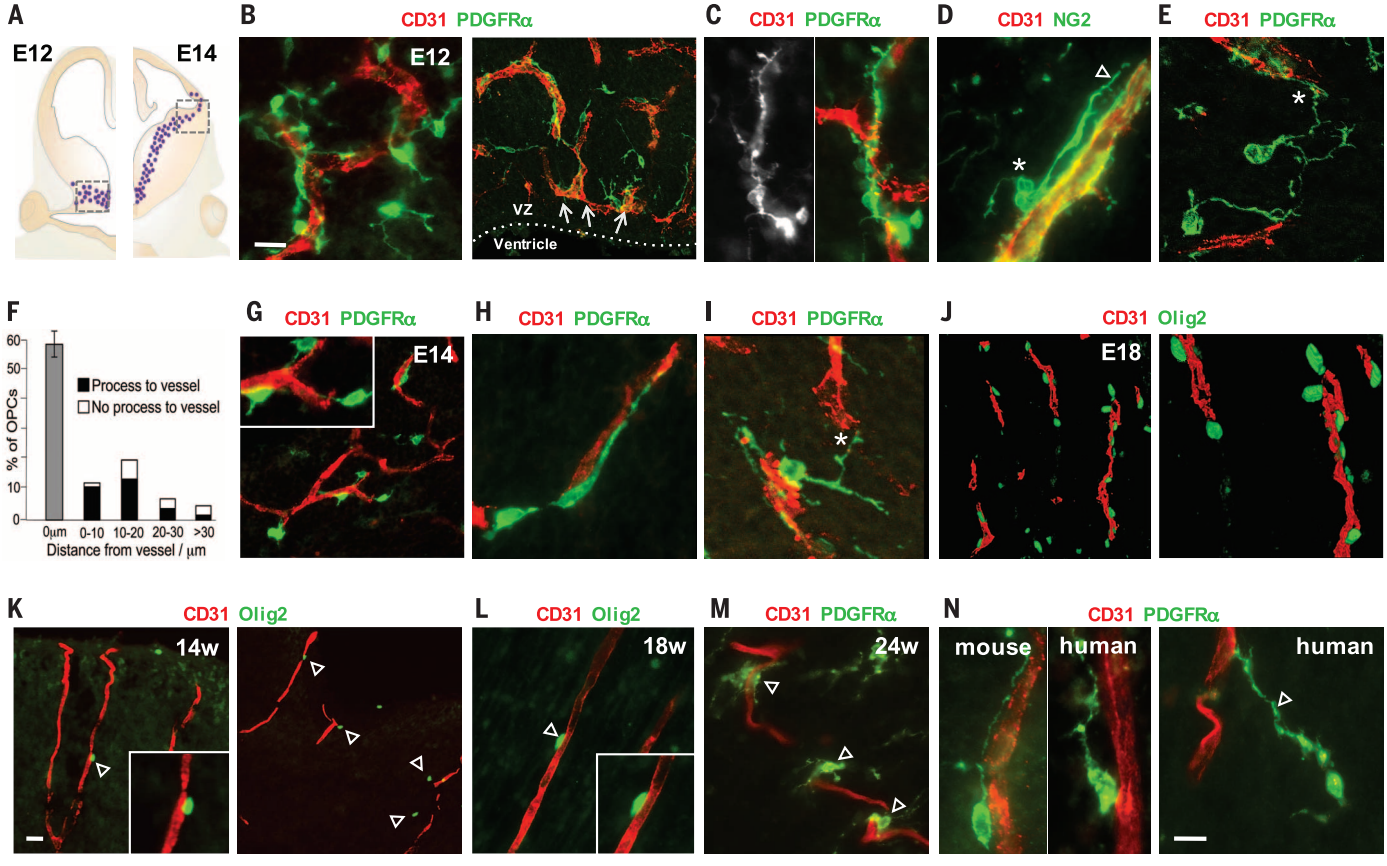

Fig. 1. Association of migratory OPCs with vessels in the developing mouse and human brain. (**A**) OPCs (dots) first appear from the ventral medial ganglionic eminence of the mouse brain at E12 (left) and migrate away from the ventricular zone to reach the subpallial-to-pallial boundary at E14 (right). (**B** to **E**) Images taken from the boxed area on the left side of (A). (B) PDGFRα$^+$ migratory OPCs at E12 associate tightly with CD31$^+$ vasculature and show elongated morphology along vessels (C), often with cell bodies on the endothelial surface [* in (D)], extending a leading process along [arrowhead in (D)] or toward [* in (E)] a vessel. VZ, ventricular zone. (**F**) Quantification of OPC association with vessels at E12 (1056 cells measured, $n = 4$ animals). Error bar indicates SD. (**G** to **I**) Images taken from the boxed area on the right side of (A). Migratory OPCs at the subpallial-to-pallial boundary at E14 maintain tight association with the vasculature (G), with process extension along (H) and between [* in (I)] vessels. Inset in (G) shows zoomed-in view. (**J**) Migrating Olig2$^+$ OPCs in the E18 cortex palisade along cortical penetrating vessels. (**K** to **N**) (K) The first OPCs (Olig2$^+$ and PDGFRα$^+$) to arrive in the developing human outer cortex closely associate with vessels at gestational weeks 14 (14w) (K), 18 (L), and 24 (M) and show similar morphological association with vessels as in mice [left, (N)], with leading processes that can be as long as 65 μm [arrowhead, right (N)]. Scale bars: 10 μm [(B) and (N)]; 20 μm (K).

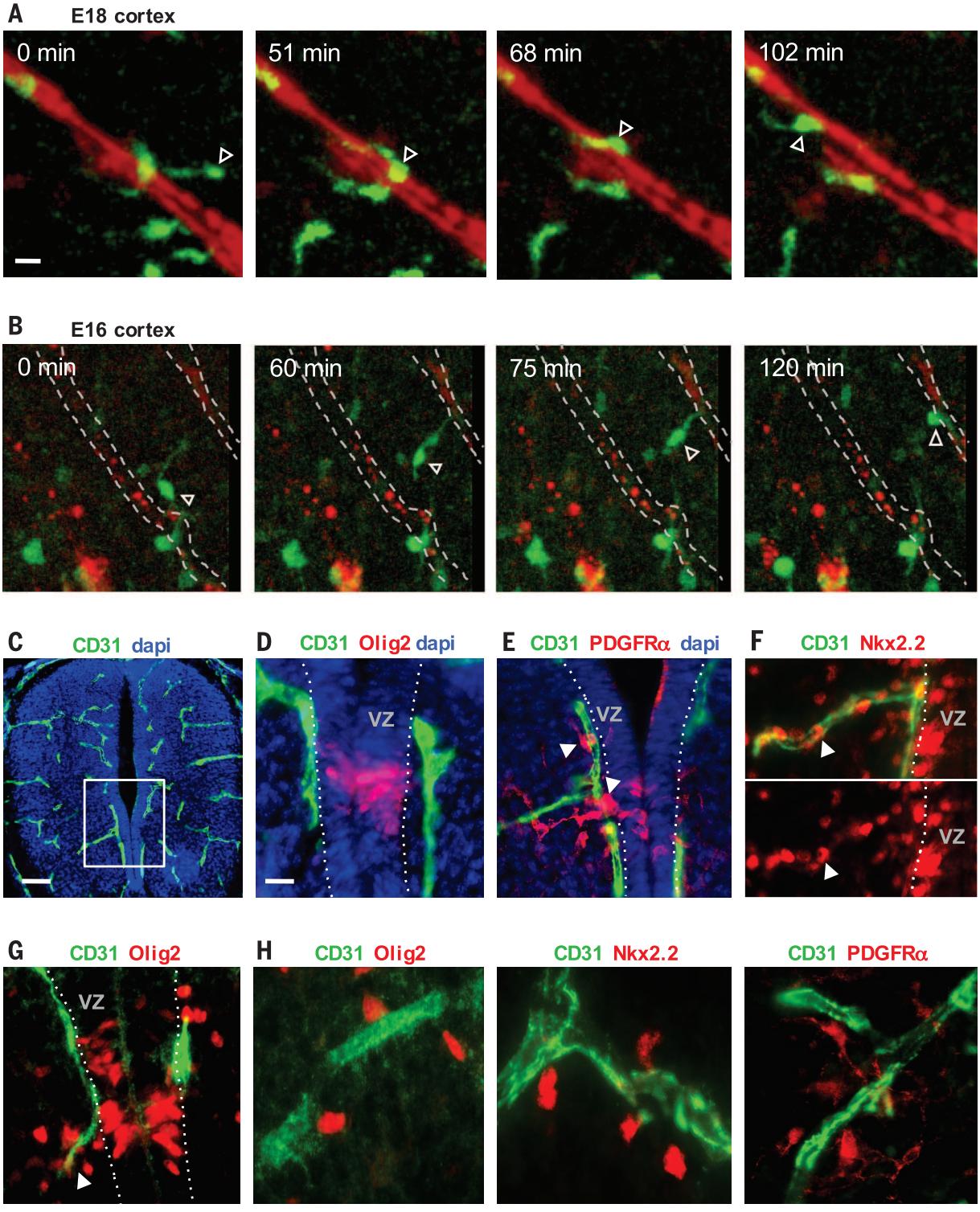

Fig. 2. OPC crawling and jumping directed motility on vessels. (**A** and **B**) Time-lapse imaging in slice cultures of the embryonic *Olig2-GFP* mouse cortex showing GFP expression (green) and vessels (red). (A) A GFP-expressing OPC (arrowhead) crawls along a penetrating vessel in the E18 cortex (movie S1). (B) An OPC in the E16 cortex (arrowhead) (movie S3) demonstrates jumping motility between vessels, extending a process to a parallel cortical penetrating vessel, before movement of the cell body onto the new vessel. (**C** and **D**) Olig2-expressing OPCs define the pMN domain of the spinal cord ventricular zone at E12. (D) shows a zoomed-in view of the boxed area in (C). dapi, 4′,6-diamidino-2-phenylindole. (**E** and **F**) The first PDGFRα- and Nkx2.2-expressing OPCs (arrowheads) emerge from the pMN immediately onto and along the adjacent $CD31^+$ vasculature. (**G** and **H**) (G) OPCs tend to leave the pMN at E14 along a vessel that branches at the pMN (arrowhead), and these cells remain associated with vessels as they continue to disperse throughout the ventral spinal cord (H). Scale bars: 10 μm [(A) and (D)]; 40 μm (C).

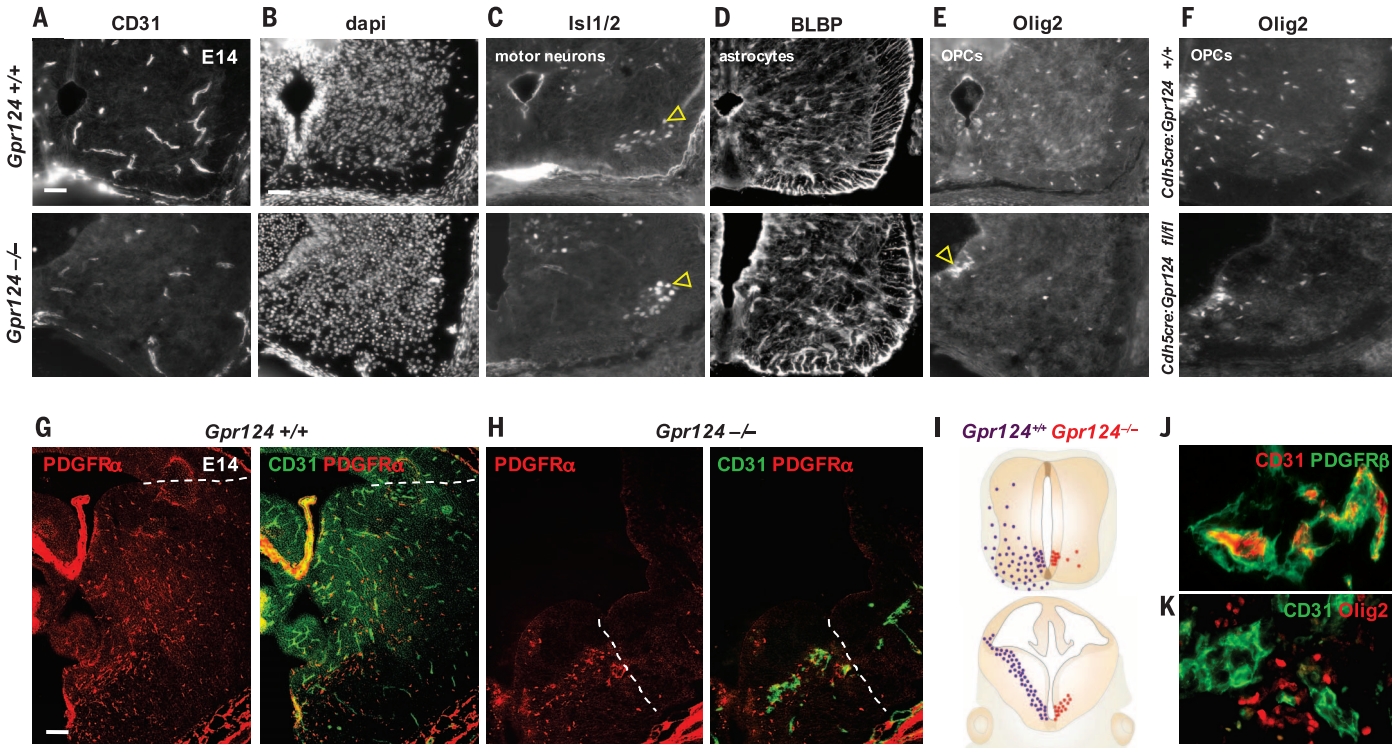

Fig. 3. OPCs require a vascular scaffold for migration. (**A** and **B**) (A) Gpr124$^{-/-}$ embryos exhibit CNS vascular patterning defects at E14, leaving the ventral spinal cord [dapi in (B)] with reduced vascularization compared with controls. (**C**) Islet1/2^{+} motor neurons migrate in normal numbers at E14, from the pMN to ventrolateral gray matter (arrowheads) in Gpr124$^{-/-}$ cords. (**D**) BLBP-expressing astrocytes also migrate normally from ventricular zone domains adjacent to the pMN into the surrounding gray matter in Gpr124$^{-/-}$. (**E** and **F**) (E) OPC (Olig2^{+}) emigration from the ventricular zone is severely disrupted in Gpr124$^{-/-}$ [(E) and (I)] and Cdh5cre/Gpr124-floxed (F) spinal cord with accumulation of OPCs in the pMN [arrowhead in (E)]. (**G**) By E14, OPCs (PDGFRα^{+}) in wild-type (WT) Gpr124$^{+/+}$ brains migrate as far as the subpallial-to-pallial boundary (dotted line). (**H** and **I**) (H) Vascular development (CD31^{+} vessels) is highly truncated in the brains of E14 Gpr124$^{-/-}$ mice, with associated severe OPC migration deficits (I). OPCs migrate only as far as the limits of the ventral vascular plexus [dotted line in (H)]. (**J** and **K**) (J) Absence of Gpr124 leads to vascular abnormalities (glomeruloid malformations) in which OPCs (Olig2^{+}) accumulate in clumps in the E14 Gpr124$^{-/-}$ brain (K). Scale bars: 30 μm [(A) and (B)]; 60 μm (G).

a 71% (P = 0.0004) reduction in their migration to the outer cortex (fig. S12). OPCs themselves are a source of the ligands Wnt7a and Wnt7b during their embryonic migration in the brain and spinal cord (Fig. 4E and fig. S13). These ligands act cell-autonomously to activate the Wnt pathway in OPCs at later postnatal times (*30*), suggesting them as candidates for the source of Wnt mediating the interaction with the endothelium during earlier OPC migration.

To identify how Wnt pathway activation in OPCs promotes their attraction to the endothelium, we analyzed mRNA transcripts up-regulated in mouse Wnt-activated OPCs [from Olig2cre/DA-Cat mice (*27*, *29*), in which Olig2-cre allows conditional expression of floxed dominant-active β-catenin]. One of the most highly up-regulated factors in Wnt-activated OPCs was the chemokine receptor Cxcr4, which is a direct Wnt target in other systems (*31*) and binds the ligand Sdf1 (Cxcl12), which is expressed by the endothelium throughout OPC developmental migration (Fig. 4H and fig. S14A). Cxcr4 has been implicated in OPC migration (*32*, *33*), but not in connection with the Wnt pathway or the vasculature. We detected up-regulation of *Cxcr4* mRNA in the clustered Wnt-activated OPCs associated with vessels in the brain and spinal cord of *Olig2-cre:Apc(fl/fl)* mice (Fig. 4, F and G). Furthermore, treatment of these mice in vivo with the Cxcr4/Sdf1 antagonist AMD3100 (*10*) between developmental ages P3 and P10 leads to a reversal of vessel-associated OPC clustering [which is not due to direct AMD3100 effects on OPC differentiation (figs. S15 and S16)] throughout the CNS (Fig. 4, I and J, and fig. S10A, spinal cord; Fig. 4K and fig. S10C, ex vivo corpus callosum), demonstrating a Wnt-activated, Cxcr4-dependent mechanism driving attraction of OPCs to the vascular scaffold. *Cxcr4* is expressed by OPCs during embryonic developmental migration (fig. S14B) but is down-regulated along with Wnt pathway down-regulation in differentiating mature oligodendrocytes (fig. S14, C and D). Furthermore, the loss of *Cxcr4* function leads to a diminished migratory ability of OPCs in the developing CNS (fig. S17). Wnt activation in OPCs therefore mediates their attraction to the vasculature during migration and also blocks their differentiation (*27*), coupling the timing of these two events, with Wnt down-regulation required for appropriate endothelial dissociation and subsequent differentiation (fig. S18).

Until now, the means by which OPCs negotiate their way through dense CNS tissue and distribute throughout the developing CNS have been unclear. We show that OPCs require a vascular scaffold as a physical substrate for migration. A similar association of OPCs with vasculature in the developing human cortex suggests common modes of migration across mammalian species. We demonstrate a physical interaction that brings migrating OPCs into intimate contact with the endothelium. Wnt pathway activation of Cxcr4 in OPCs mediates their attraction to the endothelium, most likely via the endothelial-expressed Sdf1 ligand (although an alternative cannot be completely excluded), and prevents these cells from differentiating while associated with the vasculature during migration. OPCs are a source of Wnt7a and Wnt7b, and considering that endothelial-expressed Gpr124 is a Wnt7-specific coactivator of canonical Wnt signaling (*34*, *35*), it will be interesting to consider the effects of OPCs on the developing vasculature during their migration.

The mechanisms directing OPC migration during development are likely to be similar, if not identical, to those of the injured or diseased nervous system. OPC migration into demyelinated

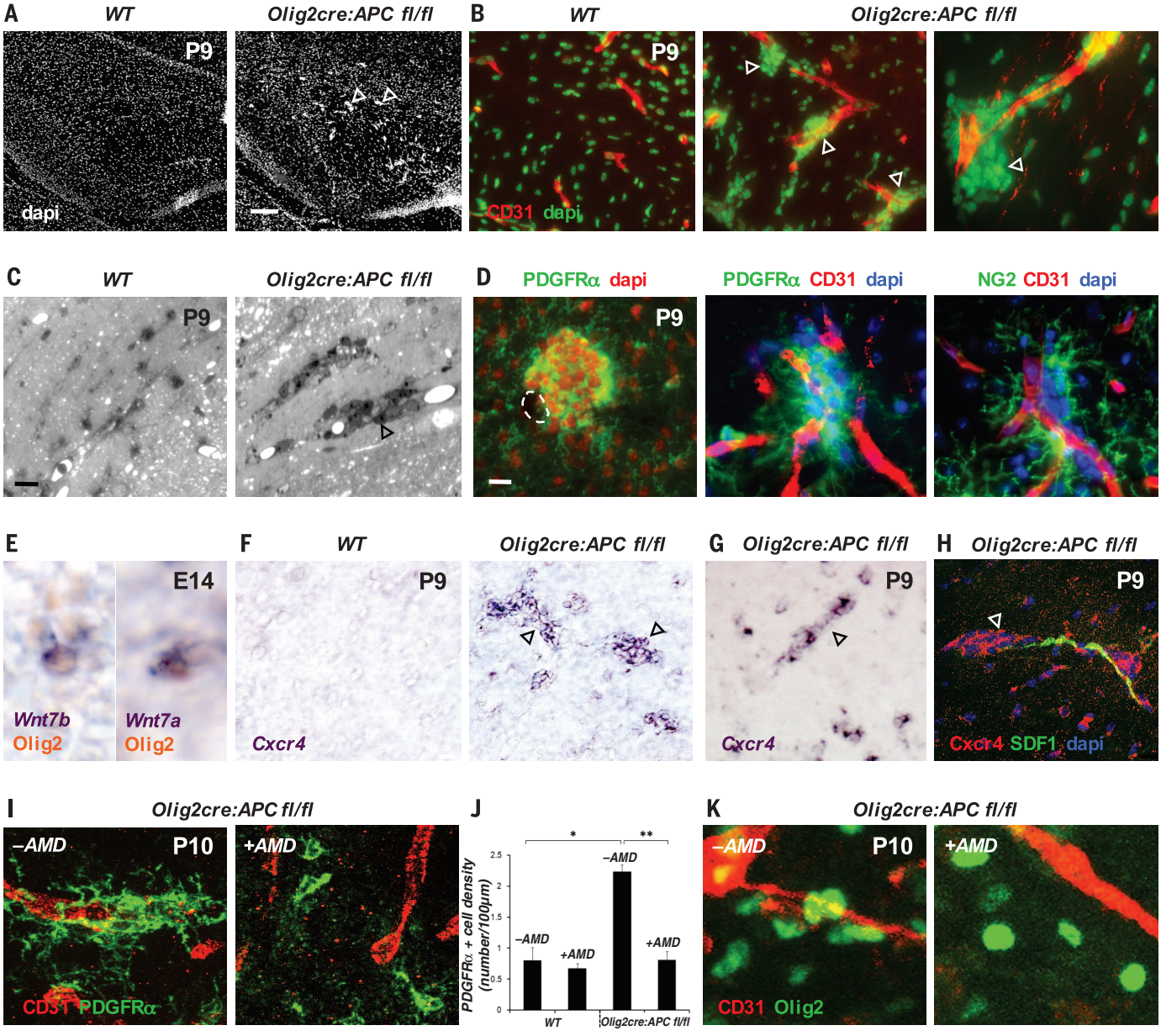

Fig. 4. A Wnt-activated, Cxcr4-dependent mechanism drives OPC attraction to the vasculature. (**A** to **D**) (A) Aberrant accumulations of cells (arrowheads) appear in the P9 corpus callosum associated with the CD31^{+} vasculature (B) of *Olig2-cre:Apc$^{flox/flox}$* mice; can be seen in resin sections stained with Toluidine blue (C); and represent OPCs, as labeled by PDGFRα and NG2 staining (D). (**E**) OPCs produce Wnt7a and Wnt7b at E14 during embryonic migration. (**F** to **H**) (F) Wnt activation in P9 *Olig2-cre:Apc$^{flox/flox}$* corpus callosum (F) or spinal cord (G) leads to marked up-regulation (compared with wild type) of *Cxcr4* mRNA [(F) and (G)] and protein (H) in clustered OPCs (arrowheads) associated with SDF1-expressing endothelium (H). (**I**) Treatment of *Olig2-cre:Apc$^{flox/flox}$* spinal cord with the Cxcr4/SDF1 inhibitor AMD3100 (+AMD) leads to a reduction in clustered OPCs associated with the vasculature, as compared with controls (–AMD). (**J**) Number of PDGFRα^{+} OPCs on a vessel in P10 spinal cord in WT versus untreated or AMD3100-treated *Olig2-cre:Apc$^{flox/flox}$* mice, expressed as number of cells on each 100-μm CD31 vessel segment ($*P = 8.9 \times 10^{-5}$, $**P = 1.9 \times 10^{-4}$, Bonferroni test, $n = 4$ animals per group). (**K**) Treatment of P10 corpus callosum *Olig2-cre:Apc$^{flox/flox}$* slices ex vivo overnight with 10 μg/ml of AMD3100 (+AMD, right panel) leads to a reduction in vessel-associated OPC clustering, as compared with untreated controls (–AMD, left panel). Scale bars: 120 μm (A); 10 μm [(C) and (D)].

areas is critical in human diseases (*14*) such as multiple sclerosis and also in hypoxic injury of the newborn brain. It will be important to establish the contribution of this mode of migration for OPC distribution into areas of injury and to uncover how dysfunction may contribute to disease progression in these debilitating human conditions.

REFERENCES AND NOTES

1. U. Fünfschilling *et al.*, *Nature* **485**, 517–521 (2012).
2. Y. Lee *et al.*, *Nature* **487**, 443–448 (2012).
3. Q. R. Lu *et al.*, *Cell* **109**, 75–86 (2002).
4. N. Kessaris *et al.*, *Nat. Neurosci.* **9**, 173–179 (2006).
5. R. L. Sidman, P. Rakic, *Brain Res.* **62**, 1–35 (1973).
6. B. Nadarajah, J. E. Brunstrom, J. Grutzendler, R. O. Wong, A. L. Pearlman, *Nat. Neurosci.* **4**, 143–150 (2001).
7. N. A. O'Rourke, M. E. Dailey, S. J. Smith, S. K. McConnell, *Science* **258**, 299–302 (1992).
8. H. Komuro, P. Rakic, *J. Neurosci.* **15**, 1110–1120 (1995).
9. C. Lois, A. Alvarez-Buylla, *Science* **264**, 1145–1148 (1994).
10. E. Kokovay *et al.*, *Cell Stem Cell* **7**, 163–173 (2010).
11. M. Snapyan *et al.*, *J. Neurosci.* **29**, 4172–4188 (2009).
12. S. A. Goldman, Z. Chen, *Nat. Neurosci.* **14**, 1382–1389 (2011).

13. H. H. Tsai *et al.*, *Science* **337**, 358–362 (2012).
14. R. J. M. Franklin, C. ffrench-Constant, *Nat. Rev. Neurosci.* **9**, 839–855 (2008).
15. M. Finzsch, C. C. Stolt, P. Lommes, M. Wegner, *Development* **135**, 637–646 (2008).
16. F. Binamé, D. Sakry, L. Dimou, V. Jolivel, J. Trotter, *J. Neurosci.* **33**, 10858–10874 (2013).
17. Y. Miyamoto, J. Yamauchi, A. Tanoue, *J. Neurosci.* **28**, 8326–8337 (2008).
18. H.-H. Tsai, M. Tessier-Lavigne, R. H. Miller, *Development* **130**, 2095–2105 (2003).
19. E. Garcion, A. Faissner, C. ffrench-Constant, *Development* **128**, 2485–2496 (2001).
20. H. H. Tsai *et al.*, *Cell* **110**, 373–383 (2002).
21. A. Baron-Van Evercooren *et al.*, *Glia* **16**, 147–164 (1996).
22. R. Daneman *et al.*, *Proc. Natl. Acad. Sci. U.S.A.* **106**, 641–646 (2009).
23. J. M. Stenman *et al.*, *Science* **322**, 1247–1250 (2008).
24. K. A. Hogan, C. A. Ambler, D. L. Chapman, V. L. Bautch, *Development* **131**, 1503–1513 (2004).
25. F. Kuhnert *et al.*, *Science* **330**, 985–989 (2010).
26. R. Daneman, L. Zhou, A. A. Kebede, B. A. Barres, *Nature* **468**, 562–566 (2010).
27. S. P. Fancy *et al.*, *Genes Dev.* **23**, 1571–1585 (2009).
28. S. P. Fancy *et al.*, *Nat. Neurosci.* **17**, 506–512 (2014).
29. S. P. Fancy *et al.*, *Nat. Neurosci.* **14**, 1009–1016 (2011).
30. T. J. Yuen *et al.*, *Cell* **158**, 383–396 (2014).
31. Y. Choe, S. J. Pleasure, *Dev. Neurosci.* **34**, 502–514 (2012).
32. G. Banisadr *et al.*, *Neurobiol. Dis.* **44**, 19–27 (2011).
33. M. Dziembowska *et al.*, *Glia* **50**, 258–269 (2005).
34. B. Vanhollebeke *et al.*, *eLife* **4**, e06489 (2015).
35. E. Posokhova *et al.*, *Cell Rep.* **10**, 123–130 (2015).

ACKNOWLEDGMENTS

We thank D. Rowitch (UCSF) for *Olig2-GFP* mice and comments on the manuscript. Procurements of human brain tissues from the UCSF Pediatric Neuropathology Research Laboratory have been supported by grants from the University of California (142657), the National Institute of Neurological Disorders and Stroke (1P01 NS083513), and HHMI. J.C. is supported by an American Heart Association Postdoctoral Fellowship (15POST23020039). This work was supported by grants from the NIH (1R01NS064517 to C.J.K.) and the National Multiple Sclerosis Society (RG 5216-A-1 to S.P.J.F.) and Race to Erase MS (to S.P.J.F.). The supplementary materials contain additional data.

SUPPLEMENTARY MATERIALS

www.sciencemag.org/content/351/6271/379/suppl/DC1
Materials and Methods
Figs. S1 to S18
References (*36*–*40*)
Movies S1 to S3

4 September 2015; accepted 1 December 2015
10.1126/science.aad3839

PLANT DEVELOPMENT

Cyclic programmed cell death stimulates hormone signaling and root development in *Arabidopsis*

Wei Xuan,[1,2,3] Leah R. Band,[4]* Robert P. Kumpf,[1,2]* Daniël Van Damme,[1,2] Boris Parizot,[1,2] Gieljan De Rop,[1,2] Davy Opdenacker,[1,2] Barbara K. Möller,[1,2] Noemi Skorzinski,[5] Maria F. Njo,[1,2] Bert De Rybel,[1,2,6] Dominique Audenaert,[1,2]† Moritz K. Nowack,[1,2] Steffen Vanneste,[1,2] Tom Beeckman[1,2]‡

The plant root cap, surrounding the very tip of the growing root, perceives and transmits environmental signals to the inner root tissues. In *Arabidopsis thaliana*, auxin released by the root cap contributes to the regular spacing of lateral organs along the primary root axis. Here, we show that the periodicity of lateral organ induction is driven by recurrent programmed cell death at the most distal edge of the root cap. We suggest that synchronous bursts of cell death in lateral root cap cells release pulses of auxin to surrounding root tissues, establishing the pattern for lateral root formation. The dynamics of root cap turnover may therefore coordinate primary root growth with root branching in order to optimize the uptake of water and nutrients from the soil.

The root cap is the outermost tissue covering the root tip and represents a major root-rhizosphere interaction site (*1*–*3*). It is commonly recognized as a protective tissue for the meristematic cells of the root apex and as a sensory organ that perceives environmental signals such as gravity, water, and nutrients to direct root growth (*4*–*6*). Although it persists during the life span of roots, it is subjected to a regeneration process in which new cell layers are continuously produced internally while superficial cell layers are regularly sloughed off. In *Arabidopsis*, the root cap consists of a central columella and peripheral lateral root cap cells (*7*). Programmed cell death (PCD) of lateral root cap cells occurs when they reach the onset of the elongation zone (*8*, *9*) (fig. S1A). This region is also designated as the oscillation zone because it displays massive oscillations in gene expression (*10*). These oscillations periodically define the prebranch sites, which may further develop as lateral roots (*10*). Root cap–specific conversion of the auxin precursor indole-3-butyric acid (IBA) into indole-3-acetic acid (IAA) creates a local auxin source that is essential for the oscillating transcriptional mechanism, which installs the regular spacing of lateral roots (*11*, *12*).

Analysis of the transcriptional auxin signaling output reporter *DR5rev:VENUS-N7* (*13*) by means of stereomicroscopy revealed a striped *DR5* pattern in the most distal lateral root cap cells, a pattern that could also be observed for the root cap–expressed early-stage PCD marker *pPASPA>>H2A-GFP* (GFP, green fluorescent protein) (Fig. 1, A and B, and fig. S1) (*8*). In vivo time-lapse imaging of vertically growing roots showed that the most distal stripe of *DR5* expression faded out every ~4 hours (Fig. 1C; fig. S2, A and B; and movie S1). When tracing back the site of origin of lateral root primordia (n = 96 primordia) (Fig. 1C), we found that all primordia were initiated at positions where a distal *DR5* stripe had vanished. Furthermore, the disappearance of the *DR5* signal from the lateral root cap preceded the *DR5:Luciferase* maximum in the oscillation zone (fig. S3) and occurred with a similar periodicity (fig. S2B). By rotating the roots by 135°, the orientation of root growth is corrected toward the gravity vector, and a bend is formed. During the reorientation, the period of *DR5* oscillations in the oscillation zone is transiently shortened, and lateral root formation is stimulated (*10*, *14*–*16*). Likewise, the period between successive losses of *DR5* stripes was also shortened from ~4 to ~2 hours (fig. S2, C and D, and movie S2). Altogether, these results show that the disappearance of the *DR5* signal from the lateral root cap, the *DR5* oscillations in the oscillation zone, and the formation of lateral root primordium are temporally and spatially interconnected.

The longitudinal extent of the lateral root cap is developmentally restricted by induction of PCD in the most distal lateral root cap cells (*8*), raising the possibility that the periodic disappearance of the *DR5* signal coincides with PCD in the lateral root cap. Consistently, *pPASPA3>>H2A-GFP* showed a striped pattern in the lateral root cap (Fig. 1B). Moreover, coexpression of the *DR5rev:VENUS-N7* reporter with *pPASPA3:NLS-tdTomato* revealed overlapping expression in the most distal lateral root cap cells (Fig. 2A and fig. S4A). Time-lapses showed that both signals disappeared synchronously (Fig. 2A and fig. S4B), with a period of ~4 hours (fig. S2B) and spatially correlating

[1]Department of Plant Systems Biology, Vlaams Instituut voor Biotechnologie (VIB), Technologiepark 927, 9052 Ghent, Belgium. [2]Department of Plant Biotechnology and Bioinformatics, Ghent University, Technologiepark 927, 9052 Ghent, Belgium. [3]State Key Laboratory of Crop Genetics and Germplasm Enhancement and MOA Key Laboratory of Plant Nutrition and Fertilization in Lower-Middle Reaches of the Yangtze River, Nanjing Agricultural University, Weigang No. 1, Nanjing 210095, PR China. [4]Centre for Plant Integrative Biology, University of Nottingham, Nottingham LE12 5RD, UK. [5]Max Planck Institute for Developmental Biology, Spemannstrasse 35, 72076 Tübingen, Germany. [6]Laboratory of Biochemistry, Wageningen University, Dreijenlaan 3, 6703HA Wageningen, Netherlands.
*These authors contributed equally to this work. †Present address: Compound Screening Facility, VIB, Technologiepark 927, 9052 Ghent, Belgium. ‡**Corresponding author. E-mail: tobee@psb.vib-ugent.be**

with sites of new lateral root primordia (movie S3). Moreover, a 135° gravistimulation also transiently decreased the periodicity of disappearance of *PASPA3* stripes to ~2 hours (fig. S2D and movie S4). Thus, PCD in the lateral root cap is predictive of lateral root formation.

In *Arabidopsis*, the accurate timing of PCD in the lateral root cap requires the transcription factor SOMBRERO (SMB) (*8*, *17*). *pSMB:NLS-GFP* stripes overlapped with *pPASPA3:NLS-tdTomato* stripes in the most distal lateral root cap and disappeared every ~4 hours (figs. S2B and S4C). The *smb-3* mutant exhibits delayed PCD of the lateral root cap cells (*8*, *17*) and as a result has an increased number of the lateral root cap cells that ectopically extend into the elongation zone (fig. S5, A and B) (*8*, *17*). In this mutant, the typical stripe-like pattern of *DR5* expression had disappeared (Fig. 2B), whereas the signal intensity was reduced and extended into the elongation zone (fig. S5, A and C). Moreover, we observed a more variable periodicity of *DR5:Luciferase* oscillations (fig. S5D), fewer prebranch sites, and lateral roots (fig. S5, E to H). Strong activation of SMB-GR [10 μM Dexamethasone (Dex)] triggers ectopic formation of tracheary element–like cells and growth arrest of all tissues (*17*). Over a 2-day treatment with ≤1 μM Dex, root growth was maintained (fig. S6A) while showing a pronounced and

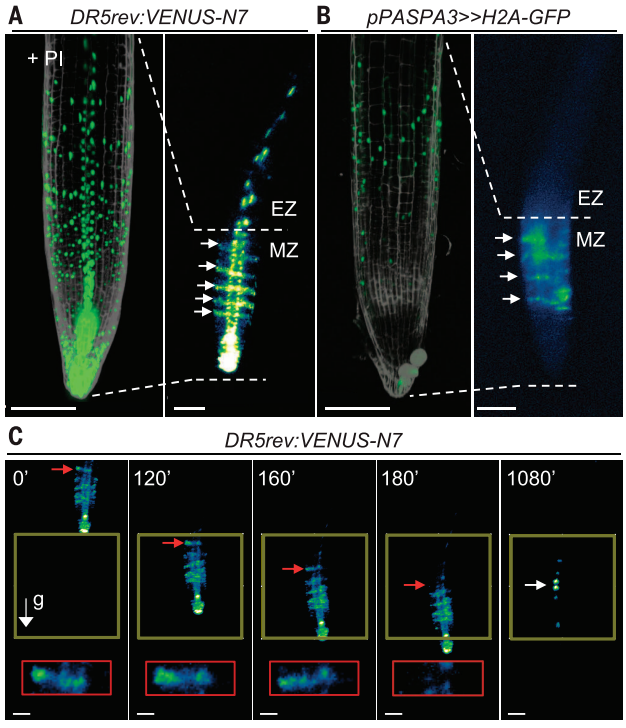

Fig. 1. Periodic disappearance of lateral root cap–*DR5* expression correlates with the sites of lateral root initiation. (**A** and **B**) Three-dimensional (3D) projection of confocal z-stacks [propidium iodide (PI) stained, left] and macroview stereo microscope images (right) of, respectively, (A) the auxin-responsive marker *DR5rev:VENUS-N7* expression and (B) the PCD marker *pPASPA3>>H2A-GFP* in seedling root tips. EZ, elongation zone; MZ, meristematic zone. (**C**) Time-lapse imaging of growing *DR5rev:VENUS-N7* roots over a growth period of 18 hours. Red arrows indicate the disappearance of a *DR5* stripe in the lateral root cap. White arrow indicates a lateral root initiation site at the site where the DR5 stripe disappeared previously. (Insets) The gradual reduction of *DR5* signal intensity in the most distal lateral root cap cells is highlighted by the red arrows during the first 3 hours. "g" and associated arrow indicate the gravitational vector. Scale bars, 100 μm.

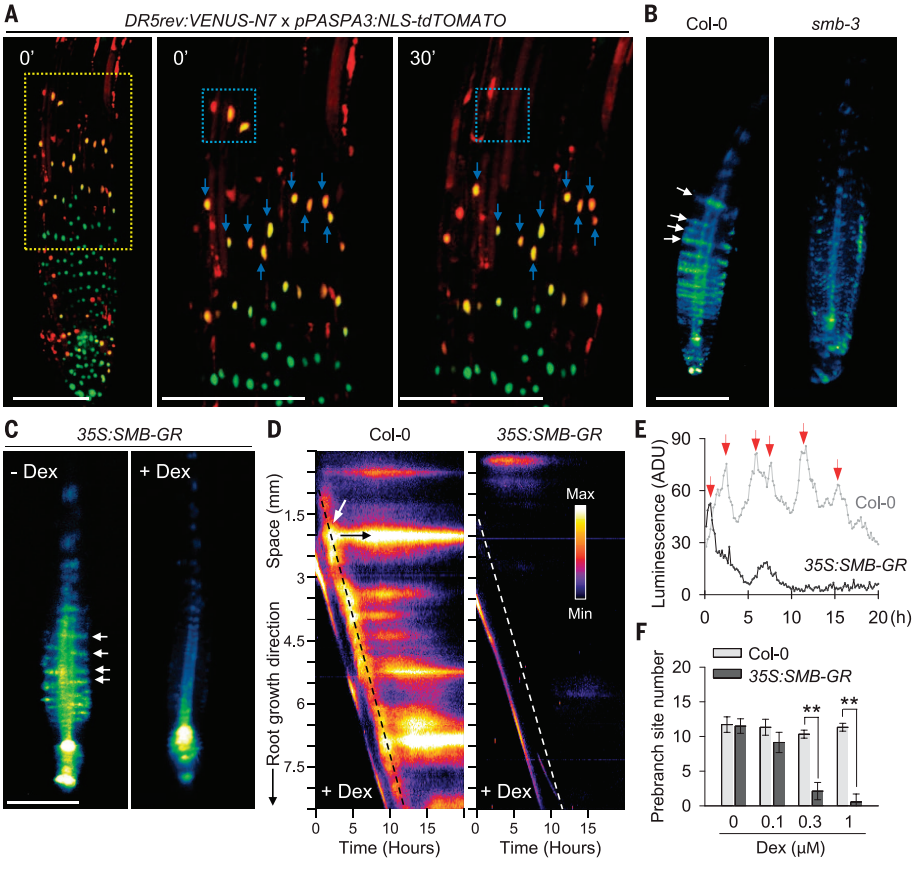

Fig. 2. Disappearance of *DR5* expression in the lateral root cap is triggered by PCD. (**A**) 3D projection of confocal z-stacks of a (green) *DR5rev:VENUS-N7*– and (red) *pPASPA3:NLS-tdTomato*–expressing transgenic seedling root tip imaged over time. Yellow indicates coexpression of both markers. (Middle and right) A close-up of the yellow boxed region at left over a 30-min time frame. Blue inset boxes indicate a set of nuclei expressing both markers that undergo PCD between the 0- and 30-min time points. Blue arrows indicate a set of lateral root cap nuclei for positional reference. (**B** and **C**) Macroview stereo microscopic view of *DR5rev:VENUS-N7* expression in root tips of (B) 3-day-old Col-0 and *smb-3* seedlings and (C) *35S:SMB-GR* seedlings treated for 24 hours with or without 1 μM Dex. White arrows indicate *DR5* stripes in the lateral root cap. (**D**) Kymograph representing *DR5:Luciferase* expression in Col-0 and *35S:SMB-GR* transgenic seedlings over 20 hours of treatment with 1 μM Dex. Dashed lines highlight the position of the oscillation zone. White arrow indicates onset of *DR5* maximum; black arrow indicates prebranch site revealed by persistent *DR5* signal. (**E**) Quantification of *DR5:Luciferase* luminescence over time measured along the dashed lines shown in (D). Red arrows indicate oscillation peaks. (**F**) Quantification of prebranch site number in 5-day-old *35S:SMB-GR* seedlings treated with Dex since day 3 after germination (n > 10 seedlings). The prebranch sites from the newly grown primary root after transfer were counted. **P < 0.01 indicates significant difference by Student's t test (n > 30 seedlings). Data are means ± SD. Scale bars, 200 μm.

specific PCD in the lateral root cap cells (fig. S6B). Additionally, these roots lacked *DR5* stripes (Fig. 2C) and *DR5:Luciferase* oscillations (Fig. 2, D and E, and movie S5), and the numbers of prebranch sites and lateral roots were reduced, respectively, by 79.4 and 87.5% at 0.3 μM Dex (Fig. 2F and fig. S6, A and C). When plants were transferred back to control medium, the newly formed root segment reestablished normal growth with the production of a normal lateral root cap and lateral roots (fig. S6, D to F). In contrast, the part of the root that was formed during Dex treatment remained devoid of lateral roots (fig. S6, D and E). These results indicate that the controlled and recurrent PCD of the lateral root cap cells is the driving factor for gene expression oscillations in the oscillation zone and subsequent lateral root induction.

Oscillations are modulated by a local auxin source in the root cap, derived from the auxin precursor IBA (*11*, *12*). Moreover, genetic ablation of the lateral root cap cells repressed the capacity to produce extra lateral roots in response to exogenous IBA application in Dex-treated *35S:SMB-GR* (fig. S6G). Therefore, we asked whether the auxin response that we observed in the root cap itself could be required for lateral root patterning. We conditionally repressed the auxin response in the lateral root cap cells through activation of a stabilized allele of the auxin response repressor IAA17/AXR3 (*pSMB:axr3-1-GR*) (*5*, *18*). Dex treatment resulted in agravitropic root growth (fig. S7A) and loss of *DR5* expression in the lateral root cap cells (fig. S7, B and C), but this did not alter the PCD process (fig. S7D) and did not affect the lateral root number (fig. S7E). Constitutive transactivation of *UAS:axr3-1* in the lateral root cap only slightly reduced lateral root formation, whereas transactivation of *UAS:axr3-1* in xylem pole pericycle cells blocked lateral root formation (fig. S7F) (*19*). Therefore, a transcriptional auxin response in the lateral root cap itself is not a decisive factor for lateral root patterning.

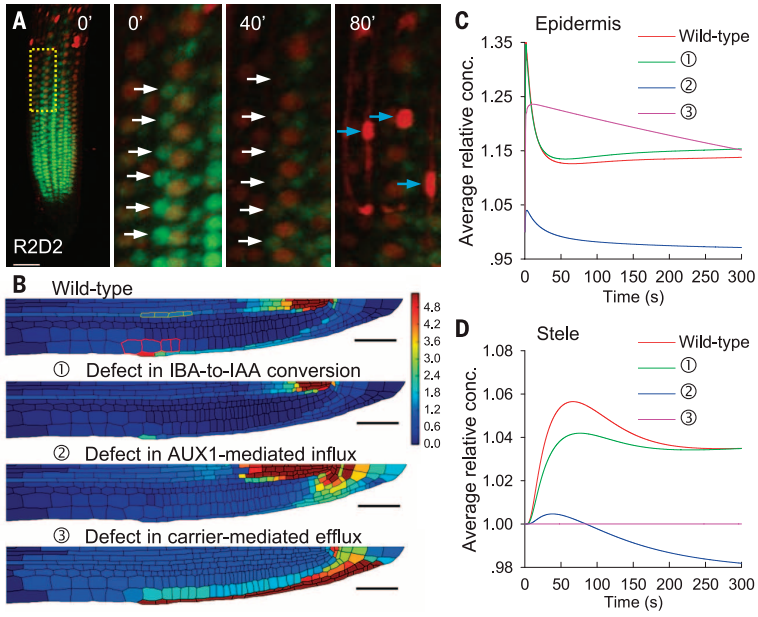

Fig. 3. Predicted auxin distributions and dynamics in the root tip. (**A**) 3D projection of confocal z-stacks of a R2D2 root tip, costained with PI, imaged over time. (Middle and right) A close-up of the yellow boxed region at left over an 80-min time frame. White arrows indicate the disappearance of yellow fluorescent protein (YFP) signals in epidermal cells, and blue arrows indicate the appearance of PI-stained nuclei in lateral root cap cells, as a late-stage PCD marker, at positions where R2D2 signals in the epidermis changed at earlier time points (movie S6). (**B**) Predicted steady-state distribution of auxin within a 3D axisymmetric multicellular geometry, for wild type, and in the situations with defects in IBA-to-IAA conversion, AUX1-mediated influx, and polar carrier-mediated efflux, respectively. Auxin concentrations are color-coded according to the rainbow scale to the right. (**C** and **D**) Predicted auxin dynamics in the (C) epidermal cells and (D) stele cells underlying the most distal LRC cells after PCD. Results show the auxin concentrations relative to that at time (t) = 0, taken as an average of the four epidermal cells (marked in red) or stele cells (marked in yellow) highlighted in (B). Scale bars, 50 μm.

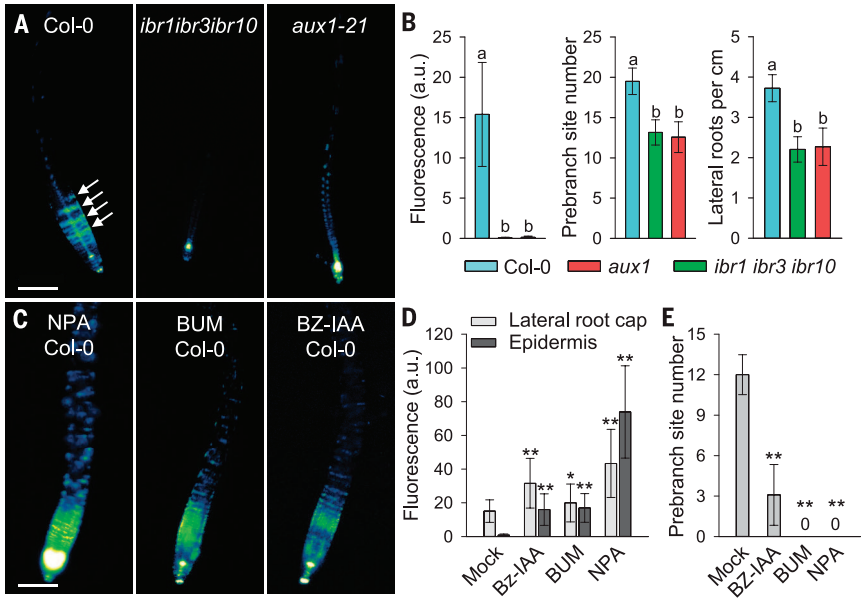

Fig. 4. Auxin flux carriers facilitate auxin transport from the lateral root cap into the oscillation zone. (**A**) *DR5rev:VENUS-N7* expression in 3-day-old Col-0, *ibr1ibr3ibr10* and *aux1* mutants in control conditions, in macroview stereomicroscope images. White arrows indicate the nuclear *DR5* signal in lateral root cap cells. (**B**) Quantification of *DR5rev:VENUS-N7* signal in lateral root cap, prebranch site number per root, and lateral root density in Col-0, *ibr1ibr3ibr10*, and *aux1* seedlings (P < 0.05 by one-way analysis of variance and Tukey's test as post hoc analysis, n > 10 seedlings). (**C** and **D**) *DR5rev:VENUS-N7* expression and quantification in 3-day-old Col-0 germinated on 10 μM NPA, 0.3 μM BUM, and 3 μM BZ-IAA expanded *DR5* expression in WT compared with Col-0 in (A). (**E**) Quantification of prebranch site number in 5-day-old *DR5:Luciferase* seedlings treated for 2 days with 10 μM NPA, 0.3 μM BUM, and 3 μM BZ-IAA. The prebranch sites formed in the newly grown primary root after transfer were measured. *P < 0.05 and **P < 0.01 compared with Mock-treatment Col-0 in (A) by Student's t test (n > 30 seedlings). Data are means ± SD. Scale bars, 200 μm.

Alternatively, auxin transport from the root cap to the root proper could be the connecting element for the oscillatory behavior in gene expression in the elongation zone. Consistently, time-lapse analyses of the semiquantitative auxin input reporter R2D2 (*20*) revealed a marked increase of auxin levels in epidermal cells, before loss of cellular integrity of adjacent lateral root cap cells (Fig. 3A and movie S6). This suggests that auxin released from lateral root cap cells during a late stage of PCD is efficiently taken up by the abutting epidermal cells. To understand how this could result in auxin signaling in stele cells of the oscillation zone, we adopted an in silico auxin-transport model (*21*) to simulate the auxin dynamics in the root apex (further details are available in the supplementary materials). Simulating the PCD of distal lateral root cap cells, under the assumption that PCD leads to a release of auxin into the surrounding apoplast, generated a transient auxin peak in stele cells in the elongation zone (Fig. 3, B to D; fig. S8; and movie S7), which is consistent with the oscillating activation of the *DR5:Luciferase*. When defects in either auxin uptake or IBA conversion are prescribed, the model fails to predict such a transient increase in stele auxin levels after lateral root cap cell turnover (Fig. 3, B to D; fig. S8; and movie S7). Our model suggests that the shootward auxin flux to the oscillation zone requires lateral root cap–expressed AUX1 (fig. S9, A and B), whereas auxin production was predicted to create high auxin levels in the lateral root cap before PCD.

Consistent with these simulations, we observed a reduced *DR5* signal in the lateral root cap that was correlated with less prebranch sites and lateral roots in *ibr1ibr3ibr10* and *aux1* mutants (Fig. 4, A and B). Moreover, PCD in the most distal lateral root cap cells was closely associated with increased auxin in the underlying epidermal cells (Fig. 3A and movie S6). We further tested the contribution of auxin transport within the lateral root cap by means of tissue-specific complementation of the *aux1* mutant. In agreement with model predictions (fig. S9, C to E), transactivation of AUX1 in the root cap rescued the defect in lateral root formation and agravitropic growth of *aux1* mutants (fig. S9, F and G). Thus, auxin transported within the (lateral) root cap allows the root cap to communicate with the elongation zone for establishing sites for lateral roots to develop. This process ensures that IBA-derived auxin can be transported toward the oscillation zone.

The auxin-transport topologies in our model also include carrier-mediated efflux and apoplastic diffusion. In the presence of influx carriers and auxin production, simulations lacking carrier-mediated efflux failed to generate an auxin transient in the elongation zone but generated an auxin accumulation in the lateral root cap (Fig. 3, B to D; fig. S8; and movie S7). In the model, diffusion rates were positively correlated with the strength of the auxin peak in the stele. However, apoplastic diffusion could not compensate for a lack in auxin efflux in our simulations (fig. S10). In an attempt to identify the components of this auxin transport machinery, we analyzed *pin2* and *pin2 abcb1 abcb19* mutants. Although these mutants are severely defective in shootward auxin transport and gravitropism, similar to *aux1* (*22*), they did not show defects in lateral root formation, nor did they have a reduced sensitivity to IBA (fig. S11, A to D), raising the possiblity that this reflux model requires the global features of the PIN and ABCB localization for directing auxin into the oscillation zone (*23*, *24*). We could find further evidence by using three chemically unrelated auxin transport inhibitors—1-*N*-naphtylphtalamic acid (NPA), 2-[4-(diethylamino)-2-hydroxybenzoyl]benzoic acid (BUM), and benzyloxy-IAA (BZ-IAA)—that target mainly ABCB-type transporters (NPA and BUM) (*22*, *25*) or generally interfere with AUX1-, PIN-, and ABCB-based auxin transport (BZ-IAA) (*26*). Consistent with our simulations, treatments with any of these inhibitors preserved the occurrence of PCD in the lateral root cap (fig. S11E) but resulted in ectopic *DR5* activity in the lateral root cap and epidermis (Fig. 4, C and D; fig. S11, F and G; and movie S8), as well as impaired *DR5:Luciferase* oscillations (movie S9) and lateral root formation (Fig. 4E and fig. S11, H and I), corroborating the auxin reflux model (*27*). Although we could not completely resolve the molecular mechanism for auxin efflux at present, our data underscore the necessity of auxin transport in the coordination of PCD in the most distal lateral root cap cells with oscillatory gene expression in the oscillation zone for lateral root spacing (fig. S12).

During the exploration of the soil, root tips sense, through the root cap, the nutrient and water status of the soil they are traversing, as well as obstacles they may encounter (*6*, *28*). Transduction of that information may serve to control the periodicity of programmed cell death, thus altering the frequency of lateral root development. In this way, root systems may adjust development according to the quality of the soils they are passing through.

REFERENCES AND NOTES

1. U. Baetz, E. Martinoia, *Trends Plant Sci.* **19**, 90–98 (2014).
2. A. Driouich, M. L. Follet-Gueye, M. Vicré-Gibouin, M. Hawes, *Curr. Opin. Plant Biol.* **16**, 489–495 (2013).
3. B. Plancot *et al*., *Plant Physiol.* **163**, 1584–1597 (2013).
4. L. R. Band *et al*., *Proc. Natl. Acad. Sci. U.S.A.* **109**, 4668–4673 (2012).
5. R. Swarup *et al*., *Nat. Cell Biol.* **7**, 1057–1065 (2005).
6. S. Svistoonoff *et al*., *Nat. Genet.* **39**, 792–796 (2007).
7. L. Dolan *et al*., *Development* **119**, 71–84 (1993).
8. M. Fendrych *et al*., *Curr. Biol.* **24**, 931–940 (2014).
9. R. P. Kumpf, M. K. Nowack, *J. Exp. Bot.* **66**, 5651–5662 (2015).
10. M. A. Moreno-Risueno *et al*., *Science* **329**, 1306–1311 (2010).
11. B. De Rybel *et al*., *Nat. Chem. Biol.* **8**, 798–805 (2012).
12. W. Xuan *et al*., *Curr. Biol.* **25**, 1381–1388 (2015).
13. M. G. Heisler *et al*., *Curr. Biol.* **15**, 1899–1911 (2005).
14. M. Lucas, C. Godin, C. Jay-Allemand, L. Laplaze, *J. Exp. Bot.* **59**, 55–66 (2008).
15. F. A. Ditengou *et al*., *Proc. Natl. Acad. Sci. U.S.A.* **105**, 18818–18823 (2008).
16. J. M. Van Norman, W. Xuan, T. Beeckman, P. N. Benfey, *Development* **140**, 4301–4310 (2013).
17. T. Bennett *et al*., *Plant Cell* **22**, 640–654 (2010).
18. D. Rouse, P. Mackay, P. Stirnberg, M. Estelle, O. Leyser, *Science* **279**, 1371–1373 (1998).
19. I. De Smet *et al*., *Development* **134**, 681–690 (2007).
20. C. Y. Liao *et al*., *Nat. Methods* **12**, 207–210 (2015).
21. L. R. Band *et al*., *Plant Cell* **26**, 862–875 (2014).
22. S. Henrichs *et al*., *EMBO J.* **31**, 2965–2980 (2012).
23. V. A. Grieneisen, J. Xu, A. F. Marée, P. Hogeweg, B. Scheres, *Nature* **449**, 1008–1013 (2007).
24. M. Laskowski *et al*., *PLOS Biol.* **6**, e307 (2008).
25. J. Y. Kim *et al*., *J. Biol. Chem.* **285**, 23309–23317 (2010).
26. E. Tsuda *et al*., *J. Biol. Chem.* **286**, 2354–2364 (2011).
27. I. Blilou *et al*., *Nature* **433**, 39–44 (2005).
28. Y. Bao *et al*., *Proc. Natl. Acad. Sci. U.S.A.* **111**, 9319–9324 (2014).

ACKNOWLEDGMENTS

This work was funded by grants from the Interuniversity Attraction Poles Programme (IAP VI/33 and IUAP P7/29 "MARS") initiated by the Belgian Science Policy Office, the Research Foundation-Flanders, and Ghent University Special Research Fund to T.B. and from the Netherlands Organization for Scientific Research (NWO VIDI 864.13.001) to B.D.R. W.X. is supported by a grant from the Chinese Scholarship Council (CSC) with cofunding from Ghent University Special Research Fund, and a grant sponsored by 111 Project (B12009) and Innovative Research Team Development Plan of the Ministry of Education of China (IRT1256), and Priority Academic Program Development in Jiangsu Higher Education Institutions. L.R.B. is supported by a Leverhulme Trust Early Career Fellowship and a Biotechnology and Biological Sciences Research Council New Investigator grant. B.K.M. and R.P.K. are the recipients of Omics@vib Marie Curie COFUND fellowship, and S.V. is a Postdoctoral Fellow of the Research Foundation-Flanders. We thank M. Bennett (University of ?tlsb=-.03w?>Nottingham, UK), B. Scheres (Wageningen University, the Netherlands), P. N. Benfey (Duke University, USA), J. Friml (Institute of Science and Technology, Austria), L. C. Strader (Washington University, St. Louis, Missouri, USA), M. Geisler (University of Fribourg, Fribourg, Switzerland), and N. Geldner (University of Lausanne, Switzerland) for the kind gifts of materials. We thank M. Van Durme for the help in cloning. The authors declare that they have no conflicts of interest. The supplementary materials contain additional data. W.X. and D.V.D. set up the in vivo root imaging system. W.X., R.P.K., G.D.R., and D.O. performed imaging and analysis. L.R.B. developed the mathematical modeling. W.X., B.D.R., and D.A. collected and analyzed the auxin transport mutants. B.P. and M.F.N. assisted in data analysis and art work. N.S. and M.K.N. provided material for the study. W.X., S.V., and T.B. directed and wrote the manuscript. L.R.B. and B.K.M. helped with the writing. All authors discussed the results and contributed in the finalization of the manuscript.

SUPPLEMENTARY MATERIALS

www.sciencemag.org/content/351/6271/384/suppl/DC1
Materials and Methods
Supplementary Text
Figs. S1 to S12
Table S1
References (*29*–*51*)
Movies S1 to S9

24 August 2015; accepted 11 December 2015
10.1126/science.aad2776

POLLINATOR DIVERSITY

Mutually beneficial pollinator diversity and crop yield outcomes in small and large farms

Lucas A. Garibaldi,[1]* Luísa G. Carvalheiro,[2] Bernard E. Vaissière,[3] Barbara Gemmill-Herren,[4] Juliana Hipólito,[5] Breno M. Freitas,[6] Hien T. Ngo,[7] Nadine Azzu,[4] Agustín Sáez,[8] Jens Åström,[9] Jiandong An,[10] Betina Blochtein,[11] Damayanti Buchori,[12] Fermín J. Chamorro García,[13] Fabiana Oliveira da Silva,[14] Kedar Devkota,[15] Márcia de Fátima Ribeiro,[16] Leandro Freitas,[17] Maria C. Gaglianone,[18] Maria Goss,[19] Mohammad Irshad,[20] Muo Kasina,[21] Alípio J.S. Pacheco Filho,[6] Lucia H. Piedade Kiill,[16] Peter Kwapong,[22] Guiomar Nates Parra,[13] Carmen Pires,[23] Viviane Pires,[24] Ranbeer S. Rawal,[25] Akhmad Rizali,[26] Antonio M. Saraiva,[27] Ruan Veldtman,[28,29] Blandina F. Viana,[5] Sidia Witter,[30] Hong Zhang[10]

Ecological intensification, or the improvement of crop yield through enhancement of biodiversity, may be a sustainable pathway toward greater food supplies. Such sustainable increases may be especially important for the 2 billion people reliant on small farms, many of which are undernourished, yet we know little about the efficacy of this approach. Using a coordinated protocol across regions and crops, we quantify to what degree enhancing pollinator density and richness can improve yields on 344 fields from 33 pollinator-dependent crop systems in small and large farms from Africa, Asia, and Latin America. For fields less than 2 hectares, we found that yield gaps could be closed by a median of 24% through higher flower-visitor density. For larger fields, such benefits only occurred at high flower-visitor richness. Worldwide, our study demonstrates that ecological intensification can create synchronous biodiversity and yield outcomes.

More than 2 billion people are reliant on smallholder agriculture (farms with less than 2 ha) in developing nations, representing 83% of the global agricultural population (*1*, *2*). In such countries, human population is growing faster than in developed nations, while many of the rural inhabitants are poor, undernourished, and live in conditions where the environment is either degraded or being degraded (*2*–*4*). As a result, improving the livelihoods of smallholders through higher and more stable crop yields, while minimizing negative environmental impacts, is essential for achieving global food security and poverty reduction (*3*, *5*). Ecosystem services enhanced through biodiversity (such as nutrient cycling, biotic pollination, or pest control) can replace, complement, or interact synergistically with external inputs (such as fertilizers, introduction of pollinator colonies, and pesticides) and should create mutually beneficial environmental and food-supply scenarios (*6*, *7*). Despite advocacy for such "ecological" intensification (*6*–*8*), its effectiveness in small versus large holdings is largely unknown. Moreover, smallholding crop systems in developing countries have been largely neglected in ecosystem-services research (*2*, *4*).

Yield gaps, defined here as the difference in crop yield between high- and low-yielding farms of a given crop system (Fig. 1), are pervasive for small holdings in many developing countries (*7*–*9*). This definition of yield gaps is particularly relevant for smallholders, as the attainable yields in field trials and research centers usually result from applying different technologies (e.g., nutrients provided as manure in crop-livestock smallholding systems versus synthetic fertilizers used in large monocultures in research centers) (*3*, *7*). Such empirical estimates of attainable yields are more conservative than modeled potential yields (*10*), but they are likely achievable with current technology (*9*). Indeed, the marginal returns from additional inputs can make modeled potential yields nonprofitable for farmers (*9*). Yield gaps can be partially closed through the provision of optimal amounts and quality of resources, such as water, nutrients, and pollen (*9*, *11*). Although fruit or seed set of many crops relies on wild pollinators (*12*), management for improved pollination services is uncommon in these systems (*13*), likely contributing to yield gaps globally (*11*). Indeed, pollination has been neglected even in studies analyzing the continental or global drivers of yield gaps (*5*, *7*, *9*, *10*). Pollinator deficits may be more relevant than before, as (i) other resources (e.g., nutrients) are increasingly provided (e.g., fertilizers) to crops (*6*, *8*); (ii) cultivated area of pollinator-dependent crops is expanding more rapidly than the area of pollinator-independent crops (*11*); (iii) cultivated area of pollinator-dependent crops is also expanding more rapidly than the stock of managed honey bee colonies (*14*); and (iv) populations of wild pollinators are increasingly threatened (*15*, *16*). Furthermore, pollinator-dependent crops provide essential micronutrients to humans in those regions of the world where micronutrient deficiencies are common (*4*). To date, it is uncertain to what degree local populations of pollinators need to be enhanced ("flower-visitor density gap"), and how much of the yield gaps (kg ha^{-1}) can be closed by such management (Fig. 1).

[1]Instituto de Investigaciones en Recursos Naturales, Agroecología y Desarrollo Rural (IRNAD), Sede Andina, Universidad Nacional de Río Negro (UNRN) and Consejo Nacional de Investigaciones Científicas y Técnicas (CONICET), Mitre 630, CP 8400, San Carlos de Bariloche, Río Negro, Argentina. [2]Departamento de Ecologia, Universidade de Brasília, Campus Universitário Darcy Ribeiro, Brasília - DF, 70910-900, Brazil; Centre for Ecology, Evolution and Environmental Changes (CE3C), Faculdade de Ciências da Universidade de Lisboa 1749-016 Lisboa, Portugal & Naturalis Biodiversity Center, postbus 9517, 2300, RA, Leiden, Netherlands. [3]Institut national de la recherche agronomique, UR406 Abeilles et Environnement, 228 route de l'Aérodrome, CS40509, F84914, Avignon Cedex 9, France. [4]Food and Agriculture Organization of the United Nations, Viale delle Terme di Caracalla 00153, Rome, Italy. [5]Departamento de Zoologia, Universidade Federal da Bahia, Instituto de Biologia, Rua Barão de Geremoabo, S/N, Campus de Ondina, CEP 40170110, Salvador, BA, Brazil. [6]Departamento de Zootecnia–Centro de Ciências Agrárias, Universidade Federal do Ceará, Campus Universitário do Pici, CEP 60021970, Fortaleza, CE, Brazil. [7]IPBES Secretariat, Intergovernmental Platform on Biodiversity and Ecosystem Services (IPBES), UN Campus, Platz der Vereinten Nationen 1, D-53113, Bonn, Germany. [8]Laboratorio Ecotono, Universidad Nacional del Comahue-CONICET, Instituto de Investigaciones en Biodiversidad y Medioambiente, Quintral 1250, CP 8400, San Carlos de Bariloche, Río Negro, Argentina. [9]Norwegian Institute for Nature Research, Post Office Box 5685 Sluppen, NO-7485, Trondheim, Norway. [10]Key Laboratory for Insect-Pollinator Biology of the Ministry of Agriculture, Institute of Apicultural Research, Chinese Academy of Agricultural Sciences, 100093, Beijing, China. [11]Pontifícia Universidade Católica do Rio Grande do Sul (PUCRS), Av. Ipiranga, 6681, CEP 90619900, Porto Alegre, RS, Brazil. [12]Department of Plant Protection, Faculty of Agriculture, Bogor Agricultural University. Jln. Kamper, Darmaga, Bogor 16680, West Java, Indonesia. [13]Laboratorio investigaciones en Abejas (LABUN), Departamento de Biología, Universidad Nacional de Colombia, Sede Bogotá, CP11001, Bogotá, Colombia. [14]Departamento de Educação em Ciências Agrárias e da Terra, Universidade Federal de Sergipe, Campus do Sertão, Rodovia Engenheiro Jorge Neto. Silos KM 0, CEP 49680000, Nossa Senhora da Gloria, SE, Brazil. [15]Institute of Agriculture and Animal Science, Rampur, Chitwan, Nepal. [16]Embrapa Semiárido, BR 428, Km 152, C.P. 23, zona rural, CEP 56302970, Petrolina, PE, Brazil. [17]Jardim Botânico do Rio de Janeiro (JBRJ), Rua Pacheco Leão 915, CEP 22460030, Rio de Janeiro, RJ, Brazil. [18]Laboratório de Ciências Ambientais, Universidade Estadual do Norte Fluminense Darcy Ribeiro, CEP 28013620, Campos dos Goytacazes, RJ, Brazil. [19]University of Zimbabwe, Faculty of Agriculture, Crop Science Department, Post Office Box MP167, Mt Pleasant, Harare, Zimbabwe. [20]Conservation and Management of Pollinators for Sustainable Agriculture through Ecosystem Approach project, Honey Bee Research Institute, National Agricultural Research Centre, Park Road, Post Office Box 44000, Islamabad, Pakistan. [21]Kenya Agricultural and Livestock Research Organisation-Sericulture, Post Office Box 7816 code 01000 Thika, Kenya. [22]College of Agriculture and Natural Sciences, School of Biological Sciences, University of Cape Coast, Cape Coast, Ghana. [23]Embrapa Recursos Genéticos e Biotecnologia, Parque Estação Biológica, W5 Norte (final), CEP 70770917, Brasília, DF, Brazil. [24]Instituto do Meio Ambiente e Recursos Hídricos (INEMA)–UR Extremo Sul, Rua Viena, no. 425, Bairro Dinnah Borges, CEP 45820970, Eunápolis, BA, Brazil. [25]G.B. Pant Institute of Himalayan Environment and Development, Kosi-Katarmal, Almora–263 643, Uttarakhand. India. [26]Department of Plant Pest Diseases, Faculty of Agriculture, University of Brawijaya. Jl. Veteran, Malang 65145, East Java, Indonesia. [27]Universidade de São Paulo, Escola Politécnica, Av. Prof. Luciano Gualberto Travessa 3, n.158, CEP 05508010, São Paulo, SP, Brazil. [28]South African National Biodiversity Institute, Kirstenbosch Research Centre, Private Bag X7, Claremont, 7735, South Africa. [29]Conservation Ecology and Entomology, Stellenbosch University, Private Bag X1, 7602, Matieland, South Africa. [30]Centro de Pesquisa Emílio Schenk, Fundação Estadual de Pesquisa Agropecuária (Fepagro Vale do Taquari), 1° Distrito, Fonte Grande, Caixa Postal 12, CEP 95860000, Taquari, RS, Brazil.
*Corresponding author. E-mail: lgaribaldi@unrn.edu.ar

We recorded flower-visitor density, flower-visitor richness, and crop yield in 344 fields of 33 crop systems across small and large holdings in Africa, Asia, and Latin America (figs. S1 and S2). To avoid the limitations of different methodologies, and considering the global nature of our focus, we performed coordinated experiments (*17*) over a 5-year period (2010–2014)—a collaborative approach that encompassed large geographic ranges involving a standardized protocol. This sampling protocol (*18*) used fields with contrasting flower-visitor density and richness not confounded with management variables other than the ones that were employed to influence flower-visitor assemblages (table S1). Therefore, crop systems are defined as a crop species in a particular year and region subject to similar management, except for flower-visitor density and richness (table S1). Following this protocol (*18*), flower-visitor density was measured by scan sampling a fixed number of open floral units (hereafter "flowers") in each of four subplots in each field, on at least four dates during the main flowering period (*19*). Flower-visitor species richness was measured by netting all visitors of crop flowers along six 25-m-long and 2-m-wide transects for herbaceous crops (or six pairs of adjacent trees for orchard crops). Crop yield was measured by harvesting all the fruits or seeds of 5 to 10 entire plants (kg plant^{-1}) and then multiplying those values by plant density (plants ha^{-1}), or by harvesting 1 to 5 m^2, according to the crop (*18*). Crop yield ($\log_{10}$ kg ha^{-1}) was analyzed through (hierarchical) mixed-effects models with fields nested within crop systems. Fixed effects were flower-visitor density (number of visitors in

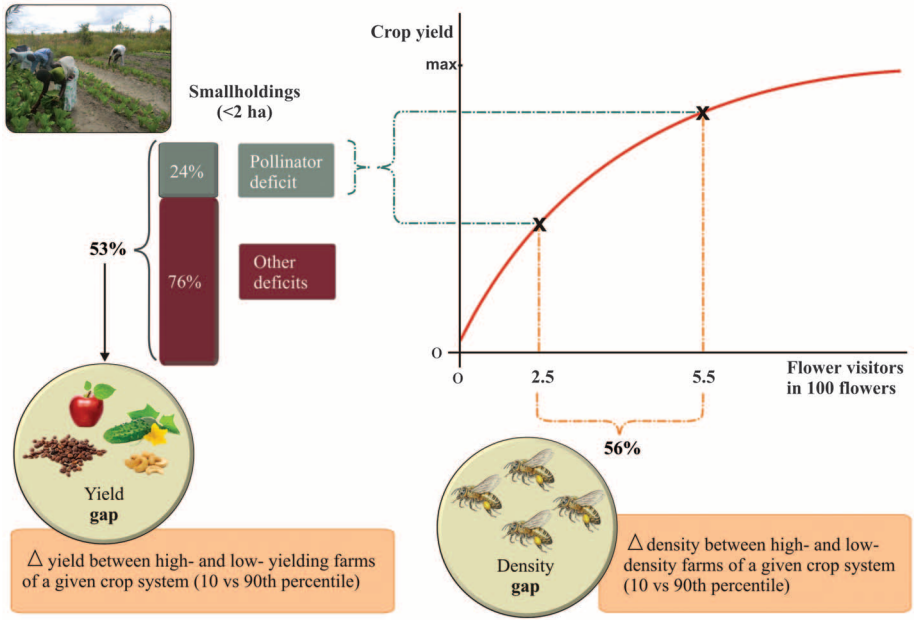

Fig. 1. Pollinator deficit is defined here as the amount of yield gap that can be accounted by closing flower-visitor density gap. Worldwide, for <2-ha fields, our study shows that yield gaps could be closed by a median of 24% (mean = 31%) through higher flower-visitor density (table S2). For larger fields, such a level of yield benefits only occurred if they sustained high flower-visitor richness (Fig. 2). Although the relation between crop yield and flower-visitor density is expected to be positive but asymptotic (*11*), our study supports a linear relation, demonstrating that the highest levels of flower-visitor density observed around the world are still at nonsaturating values.

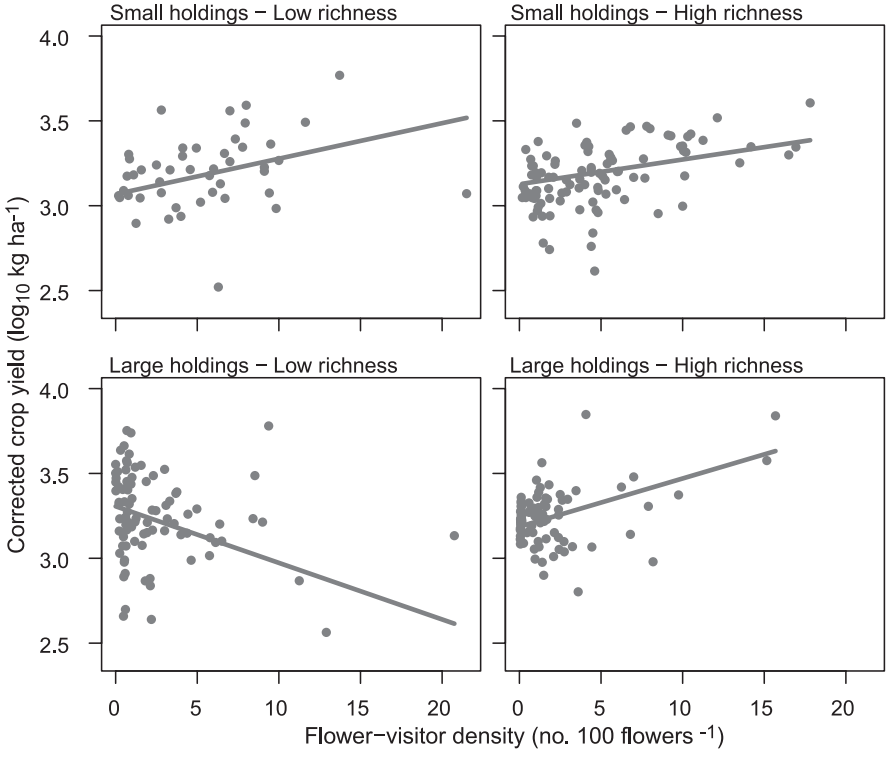

Fig. 2. Worldwide, the benefits of flower-visitor density to crop yield are greater for smaller than larger holdings, and when flower-visitor richness is higher. Moreover, high richness can compensate this negative influence of field size. Each point is a field within a crop system; lines are the fixed-effect predictions from the best hierarchical model without covariables. Small (<2 ha) versus large holdings, and low (<3 species) versus high richness, are categories only for graphical purposes, while the model considers field size and species richness as quantitative variables. By using the same protocol, we could express density as number of visitors in 100 crop flowers, avoiding standardizations to integrate results from different crop systems. Because yield (kg ha^{-1}) is harvested in different magnitudes for different crop species (e.g., coffee versus tomatoes), we present the crop yield after subtracting the random intercept for each crop system.

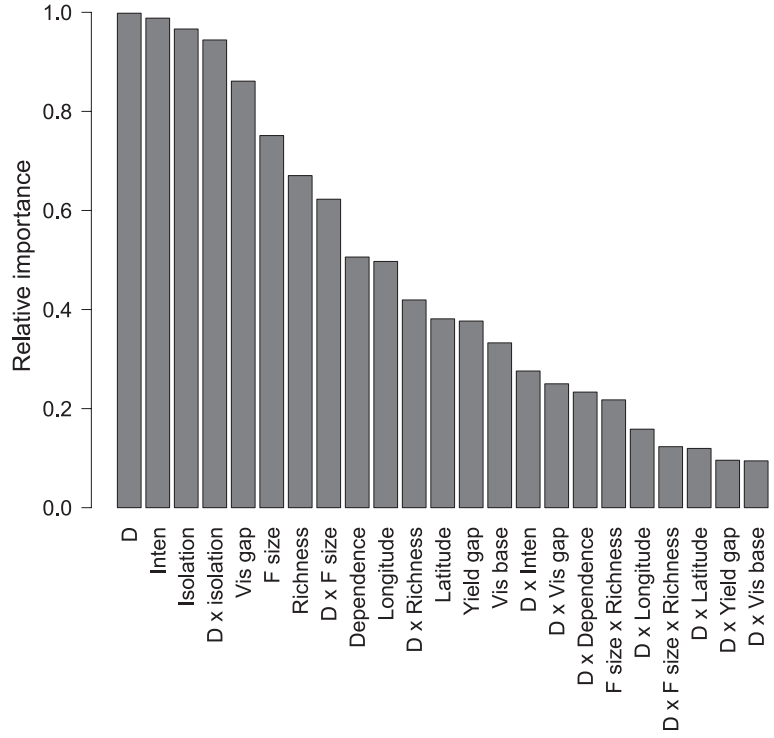

Fig. 3. Flower-visitor density (D) was the most important predictor of crop yield for pollinator-dependent crops globally. The relative importance is the sum of the Akaike information criterion weights of the models with each predictor. Inten, level of conventional intensification; Isolation, distance to seminatural or natural areas; Vis gap, magnitude of flower-visitor gap; F size, field size; Richness, flower-visitor richness; Dependence, crop pollinator dependence; Vis base, baseline level of flower-visitor density.

100 crop flowers), flower-visitor richness (number of species per field in 30 min of net sampling), field size (log_{10} ha), and their interactions (*19*). Random effects were intercepts and slopes for each crop system for the relation between crop yield and flower-visitor density and richness. Although our focus was on developing countries, research partners from Norway followed the same protocol in three crop systems, and their data were included in the analyses for comprehensiveness.

Globally, yield gaps were large and common across fields in each crop system (Fig. 1 and table S2). Crop yield in low-yielding fields (10th percentile) was, on average, only 47% of the value in high-yielding fields (90th percentile; see table S2 for kg ha^{-1}). Differences in flower-visitor density (i.e., flower-visitor density gaps) were similarly large (Fig. 1 and table S2). The fields with low flower-visitor density (10th percentile: 2.5 flower visitors in 100 flowers on average across crop systems) had only 44% of the individuals of the fields with high values (90th percentile: 5.5 flower visitors in 100 flowers on average across crop systems). These results indicate that even for crops of a given variety planted within a particular region and year, and managed similarly, there are large opportunities to increase flower-visitor densities and yields to the values of the best farms (90th percentile).

The effects of flower-visitor density on crop yield were largely influenced by field size (which ranged from 0.1 to 327.2 ha in our study) and flower-visitor richness (which ranged from 0 to 11 species in our study), as reflected by a three-way interaction (Fig. 2 and table S3). For smallholdings worldwide, crop yield increased linearly with flower-visitor density, suggesting that inadequate pollination quantity and/or quality is partly responsible for yield gaps (*11*, *20*). These benefits were irrespective of flower-visitor richness. In contrast, for larger holdings, the benefits of flower-visitor density on crop yield were greater in fields with higher flower-visitor richness (Fig. 2 and table S3). Therefore, greater flower-visitor richness could compensate the negative influence that field size had on the relationship (slope) between crop yield and flower-visitor density. For example, in fields with only one flower-visitor species, the increase in crop yield per unit of flower-visitor density was 106% higher for fields of 2 ha than for those of 20 ha. However, this difference was reduced to only 16% when four flower-visitor species were present. Globally, our results suggest that the effectiveness of ecological intensification (represented here by flower-visitor density) differs between small and large holdings, being greater for small holdings and when species richness is enhanced.

To test if these results could be explained by environmental and management aspects that covary with flower-visitor density, flower-visitor richness, or field size (table S1), we added to the previous mixed-effects model the following fixed effects: level of conventional intensification (a quantitative index based on the presence of monocultures, synthetic fertilizers, herbicides, pesticides, and fungicides) (*19*); isolation from seminatural or natural habitats (log_{10} km); crop pollinator dependence (%); latitude (decimal degrees); longitude (decimal degrees); baseline level of flower-visitor density (10th percentile: number per 100 flowers); magnitude of yield gap (%); magnitude of flower-visitor gap (%); and the two-way interactions between each of these covariables and flower-visitor density (*19*). The best-fitting model (i.e., lower corrected Akaike's information criterion, AICc) (*19*) was then derived from evaluation of all possible combinations of predictors and covariables, including a model without predictors. The influences of flower-visitor density, flower-visitor richness, field size, and their interactions were still included as predictors of crop yield in the best model, in addition to the intensification level, isolation from natural habitats, and flower-visitor gap (table S3). Importantly, fixed-effect values (and standard errors) for these predictors were of similar magnitude in the models with and without covariables (table S3), reflecting their independent contribution from the covariables in predicting crop yield [see also VIF (variance inflation factor) values in table S3]. The sum of the AICc weights of all the models for each predictor and covariable was used as an estimate of its relative importance (*19*). Notably, among all the variables we tested, flower-visitor density was the most important predictor of crop yield (Fig. 3). As expected (*21*), the level of conventional intensification was an important predictor of crop yield (Fig. 3), showing a positive relation (table S3). Crop yield decreased with isolation from natural habitats, and more so when flower-visitor density was lower (table S3). Worldwide, our data show that effects of flower-visitor density, flower-visitor richness, and field size are highly relevant in the context of, and not confounded by, other environmental and management variables affecting crop yield.

Our best-fitting model (table S3) allows the estimation of the degree to which yield gaps (kg ha^{-1}) can be closed by enhancing local populations of flower visitors for a given field size and several other key management and environmental covariables (note the high coefficient of determination, R^2, of 0.97 in table S3). In fields of less than 2 ha, the enhancement of flower-visitor density in fields with the lowest values (10th percentile) to those of the best fields (90th percentile) should close yield gaps by a median of 24% (Fig. 1 and table S2). The remaining 76% of the yield gap may be partially closed by technologies oriented to the optimal provision and efficient use of other resources (e.g., radiation, nutrients, water), including sowing date, plant density, genetic material, conservation agriculture, and integrated pest management, among many others (*5*–*7*, *9*, *10*). In contrast, for larger fields, such level of yield benefits from enhancement of flower-visitor density occurs only if these fields have high flower-visitor richness (Fig. 2 and table S2). In our study, the influences of field size were not confounded by several important environmental and management variables affecting crop yield (table S3). Lower benefits from flower-visitor density in larger fields may reflect the fact that they are only

pollinated by flower visitors with large foraging ranges, which are usually generalist species, such as honey bees (*12*). In accordance with this hypothesis, we found greater dominance of *Apis* spp. in larger holdings regardless of species richness (fig. S3), and that flower-visitor density effects were enhanced when richness increased in large fields (Fig. 2). Such synergistic influences among pollinator species on crop yield (kg ha^{-1}) are likely due to different nonexclusive mechanisms (*22*), including pollination niche complementarity (*23*, *24*), interspecific interactions (*25*, *26*), or raising the chances of providing effective pollinator species (i.e., sampling effects of biodiversity) (*27*, *28*).

Pollinator deficits have been neglected from previous global or continental yield gap analyses (*5*, *7*, *9*, *10*). However, here we found that they are responsible to a large degree for yield gaps of pollinator-dependent crops in small holdings (Fig. 1 and table S2), even after considering several environmental and management predictors of crop yield (Fig. 3). Indeed, flower-visitor density was the most important predictor of crop yield. Closing flower-visitor density gaps is a realistic objective, as our figures are based on the densities observed in real-world farms (i.e., the difference between the 90th and 10th percentiles). Unfortunately, recent studies suggest that flower-visitor assemblages in agroecosystems are increasingly threatened because of declining floral abundance and diversity, as well as increasing exposure to pesticides and parasites (*15*, *16*). Such trends can be reversed by a combination of practices, the effectiveness of which is context dependent, including sowing flower strips and planting hedgerows, providing nesting resources, more targeted use of pesticides, and/or restoration of seminatural and natural areas adjacent to crops (table S1) (*13*, *29*).

Enhancing smallholder livelihoods through greater crop yields while reducing negative environmental impacts from agriculture is one of the greatest challenges for humanity (*3*, *5*). Moreover, from a food-security point of view, pollinator-dependent crops provide essential micronutrients to human health where needed (*4*). Our data indicate that the effectiveness of ecological intensification through pollination services was greater for small, rather than large, holdings. Using pollination services as a case study, we demonstrated that ecological intensification can create mutually beneficial scenarios between biodiversity and crop yields worldwide.

REFERENCES AND NOTES

1. S. K. Lowder, J. Skoet, S. Singh, "What do we really know about the number and distribution of farms and family farms worldwide?" Background paper for the State of Food and Agriculture 2014 (Food and Agriculture Organization of the United Nations, Rome, 2014).
2. P. R. Steward *et al.*, *Agric. Food Security* **3**, 5 (2014).
3. M. Herrero *et al.*, *Science* **327**, 822–825 (2010).
4. R. Chaplin-Kramer *et al.*, *Proc. R. Soc. B Biol. Sci.* **281**, 20141799 (2014).
5. H. C. J. Godfray *et al.*, *Science* **327**, 812–818 (2010).
6. R. Bommarco, D. Kleijn, S. G. Potts, *Trends Ecol. Evol.* **28**, 230–238 (2013).
7. P. Tittonell, K. E. Giller, *Field Crops Res.* **143**, 76–90 (2013).
8. J. A. Foley *et al.*, *Nature* **478**, 337–342 (2011).
9. N. D. Mueller *et al.*, *Nature* **490**, 254–257 (2012).
10. D. B. Lobell, K. G. Cassman, C. B. Field, *Annu. Rev. Environ. Resour.* **34**, 179–204 (2009).
11. L. A. Garibaldi, M. A. Aizen, A. M. Klein, S. A. Cunningham, L. D. Harder, *Proc. Natl. Acad. Sci. U.S.A.* **108**, 5909–5914 (2011).
12. L. A. Garibaldi *et al.*, *Science* **339**, 1608–1611 (2013).
13. L. A. Garibaldi *et al.*, *Front. Ecol. Environ.* **12**, 439–447 (2014).
14. M. A. Aizen, L. D. Harder, *Curr. Biol.* **19**, 915–918 (2009).
15. D. Goulson, E. Nicholls, C. Botías, E. L. Rotheray, *Science* **347**, 1255957 (2015).
16. M. Rundlöf *et al.*, *Nature* **521**, 77–80 (2015).
17. L. H. Fraser *et al.*, *Front. Ecol. Environ.* **11**, 147–155 (2013).
18. B. E. Vaissière, B. M. Freitas, B. Gemmill-Herren, Protocol to detect and assess pollination deficits in crops: a handbook for its use (Food and Agriculture Organization of the United Nations, Rome, 2011).
19. See supplementary materials on *Science* Online.
20. M. A. Aizen, L. D. Harder, *Ecology* **88**, 271–281 (2007).
21. V. Seufert, N. Ramankutty, J. A. Foley, *Nature* **485**, 229–232 (2012).
22. T. Tscharntke, A. M. Klein, A. Kruess, I. Steffan-Dewenter, C. Thies, *Ecol. Lett.* **8**, 857–874 (2005).
23. P. Hoehn, T. Tscharntke, J. M. Tylianakis, I. Steffan-Dewenter, *Proc. R. Soc. B Biol. Sci.* **275**, 2283–2291 (2008).
24. J. Fründ, C. F. Dormann, A. Holzschuh, T. Tscharntke, *Ecology* **94**, 2042–2054 (2013).
25. L. G. Carvalheiro *et al.*, *Ecol. Lett.* **14**, 251–259 (2011).
26. C. Brittain, N. Williams, C. Kremen, A. M. Klein, *Proc. Biol. Sci.* **280**, 20122767 (2013).
27. B. J. Cardinale *et al.*, *Nature* **443**, 989–992 (2006).
28. M. Schleuning, J. Fründ, D. García, *Ecography* **38**, 380–392 (2015).
29. D. Kleijn *et al.*, *Nat. Commun.* **6**, 7414 (2015).

ACKNOWLEDGMENTS

Funding was provided by the Global Environment Fund, United Nations Environment Program, United Nations Food and Agriculture Organization (GEF/UNEP/FAO) Global Pollination Project, with additional support to the Food and Agriculture Organization of the United Nations from the Norwegian Environment Agency for a project on "Building Capacity in the Science-Policy Interface of Pollination Services," and from the International Fund for Agricultural Development for the development of the sampling protocol (*18*). Other funding: Conselho Nacional de Desenvolvimento Científico e Tecnológico Brazil, CONICET Argentina (PIP 114-201101-00201), Norwegian Environment Agency (2012/16642), The Research Council of Norway (225019), and Universidad Nacional de Río Negro Argentina (PI 40-B-259, PI 40-B-399). The data used in the analyses are available in the supplementary materials. L.A.G., L.G.C., and J.H. compiled data; L.A.G. and L.G.C. analyzed data; L.A.G. wrote the first version of the manuscript; the authors named between L.A.G. and J.Ås. discussed and revised earlier versions of the manuscript. The authors named between J.An and H.Z. are listed alphabetically, as they contributed equally, gathering field data, providing corrections to subsequent manuscript drafts, and discussing ideas. G. Andersson, B. Geslin, and P. Steward provided insightful comments on previous versions of this paper.

SUPPLEMENTARY MATERIALS

www.sciencemag.org/content/351/6271/388/suppl/DC1
Materials and Methods
Figs. S1 to S3
Tables S1 to S3
References (*30*–*44*)
Database S1

22 June 2015; accepted 15 December 2015
10.1126/science.aac7287

SMALL RNAS

Biogenesis and function of tRNA fragments during sperm maturation and fertilization in mammals

Upasna Sharma,[1]* Colin C. Conine,[1]* Jeremy M. Shea,[1] Ana Boskovic,[1] Alan G. Derr,[2,3] Xin Y. Bing,[1] Clemence Belleannee,[4] Alper Kucukural,[2,3] Ryan W. Serra,[1] Fengyun Sun,[1] Lina Song,[1] Benjamin R. Carone,[1] Emiliano P. Ricci,[5]† Xin Z. Li,[1,5]‡ Lucas Fauquier,[1] Melissa J. Moore,[1,5,6] Robert Sullivan,[4] Craig C. Mello,[2,5,6] Manuel Garber,[2,3] Oliver J. Rando[1]§

Several recent studies link parental environments to phenotypes in subsequent generations. In this work, we investigate the mechanism by which paternal diet affects offspring metabolism. Protein restriction in mice affects small RNA (sRNA) levels in mature sperm, with decreased let-7 levels and increased amounts of 5′ fragments of glycine transfer RNAs (tRNAs). In testicular sperm, tRNA fragments are scarce but increase in abundance as sperm mature in the epididymis. Epididymosomes (vesicles that fuse with sperm during epididymal transit) carry RNA payloads matching those of mature sperm and can deliver RNAs to immature sperm in vitro. Functionally, tRNA-glycine-GCC fragments repress genes associated with the endogenous retroelement MERVL, in both embryonic stem cells and embryos. Our results shed light on sRNA biogenesis and its dietary regulation during posttesticular sperm maturation, and they also link tRNA fragments to regulation of endogenous retroelements active in the preimplantation embryo.

Accumulating evidence indicates that parental environments can affect the health of offspring. For example, paternal nutrition influences offspring metabolism in mammals (*1*). Our prior published work showed that male mice consuming a low-protein diet fathered offspring exhibiting altered hepatic cholesterol biosynthesis, relative to the offspring of control males (*2*). The mechanisms by which paternal conditions reprogram offspring phenotype remain elusive, as males can influence offspring via the sperm epigenome, microbiome

transfer, seminal fluid signaling, or indirectly through maternal judgment of mate quality (*3*, *4*). Therefore, we first tested whether metabolic gene expression was altered in offspring generated via in vitro fertilization (IVF) using sperm obtained from animals consuming a control or low-protein diet (19 or 10% protein, respectively) (see supplementary materials and methods). Despite the potential for IVF and embryo culture to obscure paternal effects on offspring metabolism, we found that, compared with control IVF offspring, IVF-derived offspring of males consuming a low-protein diet exhibited significant hepatic up-regulation of the gene encoding the cholesterol biosynthesis enzyme squalene epoxidase (*2*) (fig. S1). This finding demonstrates that paternal diet can affect offspring metabolism via information located in sperm.

Because small RNAs (sRNAs) are central to a broad range of epigenetic phenomena (*5*), we isolated cauda sperm from males consuming a control or low-protein diet and purified small [<40 nucleotide (nt)] RNAs for analysis by deep sequencing. The resultant sequencing libraries reveal markedly abundant (~80% of sRNAs) ~28- to 34-nt tRNA fragments (tRFs), which are predominantly derived from the 5′ ends of tRNAs (Fig. 1, A to D, and tables S1 and S2) (*6*). 5′ tRFs are also abundant in cauda sperm from the bull *Bos taurus* (table S3), which suggests that tRNA cleavage in gametes is conserved among mammals, and perhaps more broadly (*7*). Given the low RNA content of sperm relative to oocytes, we focused our analyses on highly abundant sRNAs in sperm. The low-protein diet affected levels of multiple sRNAs, including highly abundant tRNA fragments, across eight pairs of sperm samples (Fig. 1, E and F). Most notably, 5′ fragments of tRNA-Gly-CCC, -TCC, and -GCC exhibited a ~two- to threefold increase in low-protein sperm, and tRF-Lys-CTT and tRF-His-GTG were similarly up-regulated. In addition to tRFs, other RNA species differ in abundance between sperm samples, with several let-7 species being down-regulated in low-protein sperm.

[1]Department of Biochemistry and Molecular Pharmacology, University of Massachusetts Medical School, Worcester, MA 01605, USA. [2]Program in Molecular Medicine, University of Massachusetts Medical School, Worcester, MA 01605, USA. [3]Program in Bioinformatics and Integrative Biology, University of Massachusetts Medical School, Worcester, MA 01605, USA. [4]Department of Obstetrics, Gynecology and Reproduction, Université Laval, Centre Hospitalier Universitaire de Québec Research Center, Quebec City, Quebec G1V 4G2, Canada. [5]RNAi Therapeutics Institute, University of Massachusetts Medical School, Worcester, MA 01605, USA. [6]Howard Hughes Medical Institute, University of Massachusetts Medical School, Worcester, MA 01605, USA. *These authors contributed equally to this work. †Present address: INSERM U1111, Centre International de Recherche en Infectiologie, Ecole Normale Supérieure de Lyon, Université de Lyon, 69364 Lyon, France. ‡Present address: Center for RNA Biology: From Genome to Therapeutics, University of Rochester, Rochester, NY 14642, USA. §Corresponding author. E-mail: oliver.rando@umassmed.edu

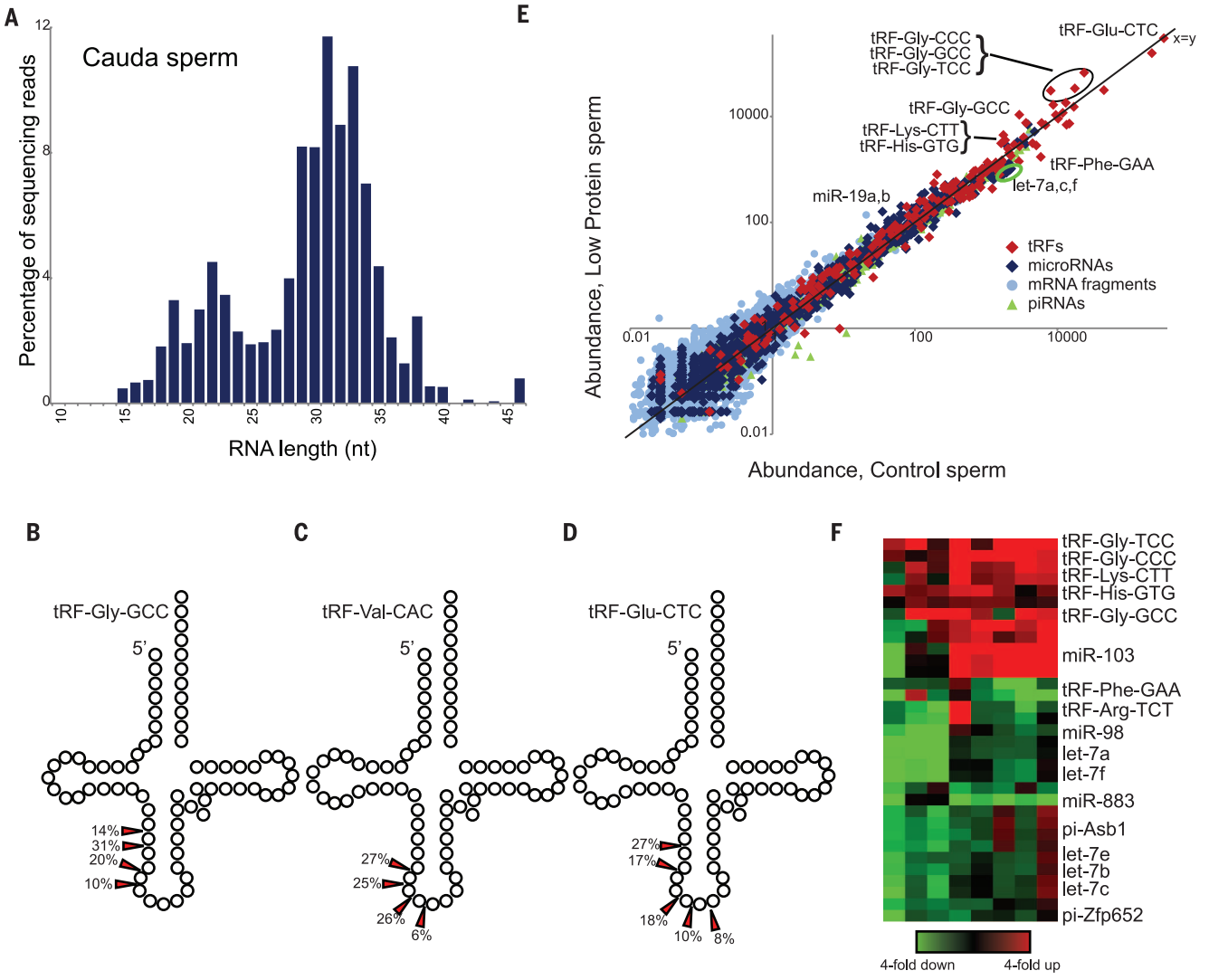

Fig. 1. Dietary effects on sRNAs in sperm. (**A**) Size distribution of sequencing reads for cauda sperm sRNAs. (**B** to **D**) 5′ fragments of tRNA are shown schematically, with arrowheads indicating dominant 3′ ends. (**E**) Dietary effects on sperm sRNA content. The scatter plot shows RNA abundance (in parts per million) for sperm isolated from control animals (*x* axis, $\log_{10}$) versus low-protein sperm (*y* axis), with various RNA classes indicated. Multiple points for tRFs result from sequence differences between genes encoding a given tRNA isoacceptor. (**F**) Heat map showing RNAs responding to diet across eight paired sperm samples.

We next assayed levels of intact tRNAs in the testis, finding no correlation between dietary effects on testicular tRNA levels and tRF changes in cauda sperm (fig. S2). This finding provides evidence against the hypothesis that tRFs in mature sperm result simply from random degradation of tRNAs used during spermatogenesis. Moreover, deep sequencing and Northern blot analyses (Fig. 2, A and C; fig. S3; and tables S1 and S2) revealed very low levels of tRNA fragments in the testes or in various purified testicular spermatocyte/spermatid populations, raising the question of when sperm gain tRFs during maturation. After exiting the testis, sperm continue to mature for several days in the epididymis, and we noted robust tRNA cleavage throughout this tissue (Fig. 2, B and D, and fig. S4). Not only do overall tRF levels increase distally in the male reproductive system, but the spectrum of specific tRFs also differs between the testis, proximal caput epididymis, and distal cauda epididymis (Fig. 2D and table S2).

Because our data suggest that sRNAs in mature sperm could have originated at multiple locations throughout the reproductive tract, we assessed the effect of paternal diet on sRNAs in the testis (n = 9 pairs), caput epididymis (n = 6), and cauda epididymis (n = 5) (fig. S5). Two prominent dietary effects on the cauda sperm RNA repertoire—increased abundance of glycine tRFs and decreased abundance of let-7—were recapitulated in the testis and epididymis but not in the liver, muscle, or blood (table S1). Thus, tissues throughout the male reproductive tract, including mature sperm, exhibit consistent changes in glycine tRFs and let-7 in response to the low-protein diet, suggesting that similar diet-responsive pathways are present throughout the tract and providing technical replication of the fundamental epigenomic changes wrought by the low-protein diet.

Our finding of robust tRNA cleavage in the epididymis but not the testis raises the possibility that the abundant tRFs in the cauda sperm might be trafficked to sperm from the epididymal epithelium, rather than arising during testicular spermatogenesis. During transit through the epididymis, sperm fuse with small extracellular vesicles known as epididymosomes (*8*–*11*). To test the hypothesis that epididymosomes deliver sRNAs (*12*, *13*) to sperm, we purified epididymosomes (fig. S6) and characterized their sRNA payload by deep sequencing. Epididymosomes carry high levels (~87% of reads) of 5′ tRFs such as tRF-Glu-CTC and tRF-Gly-GCC, and sRNAs found in purified epididymosomes closely mirror (correlation coefficient r = 0.96) those in cauda sperm (Fig. 2E and fig. S6). Epididymosomal RNAs were resistant to ribonuclease treatment and were found in epididymosomes from spermless *Tdrd1*$^{-/-}$ mice,

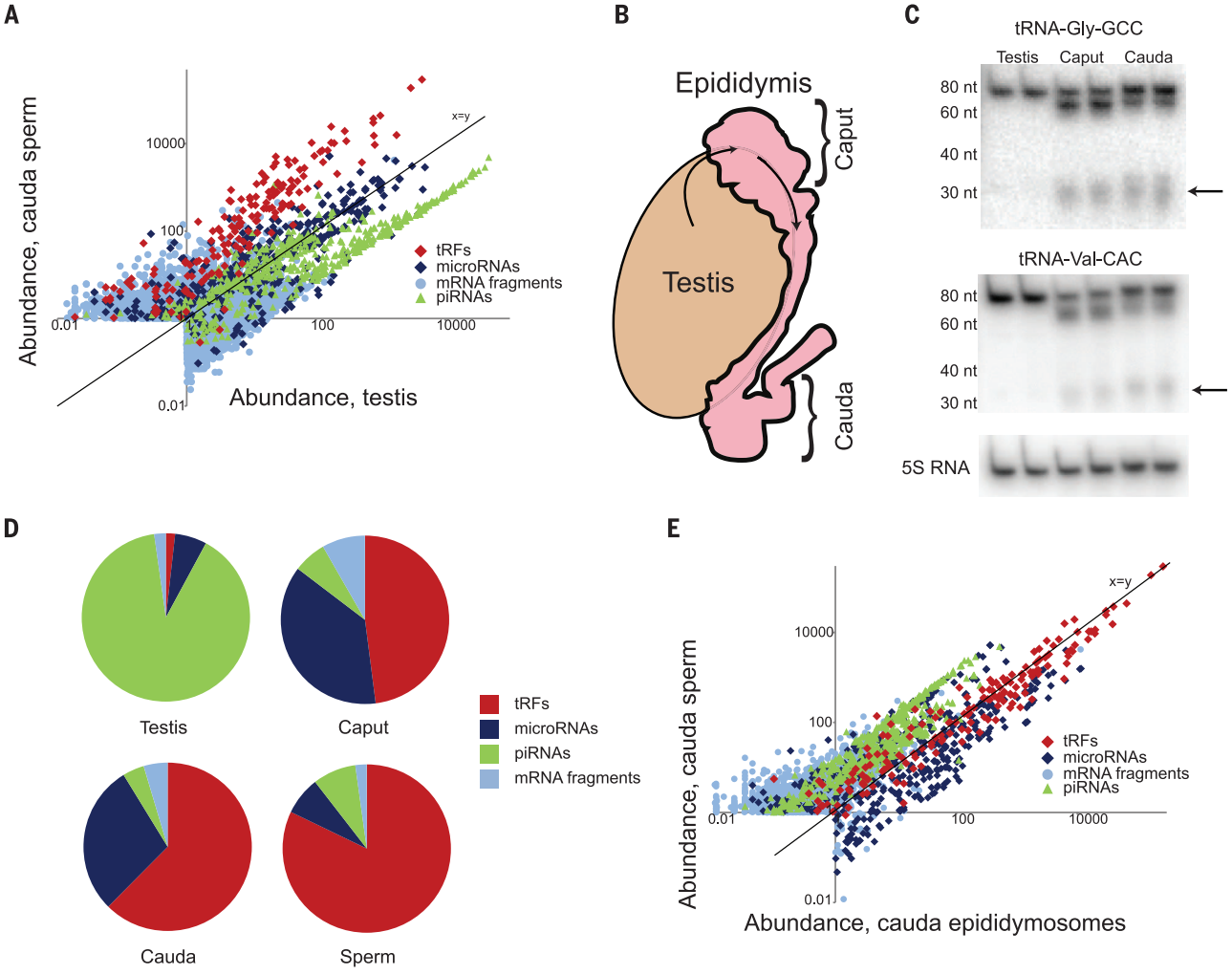

Fig. 2. Cleavage of tRNA occurs predominantly in the epididymis. (**A**) Sperm RNA payload diverges dramatically from testicular RNA. The scatter plot shows sRNAs in the testis versus sperm, as in Fig. 1E. (**B**) Schematic of the epididymis. Sperm exiting the testis enter the proximal (caput) epididymis, then proceed distally to the corpus and cauda epididymis, and exit via the vas deferens. (**C**) tRFs are primarily generated in the epididymis. Northern blots are shown for 5′ ends of tRNA-Gly-GCC or tRNA-Val-CAC on RNA extracted from the testis, caput epididymis, and cauda epididymis. Arrows indicate ~30- to 34-nt 5′ tRFs. 5S RNA served as a loading control. (**D**) Pie charts showing the percentage of sRNAs mapping to the indicated features. (**E**) Scatter plot of sRNA abundance for sperm versus epididymosomes. Sperm-enriched RNAs include piRNAs and fragments of mRNAs involved in spermatogenesis (e.g., *Prm1*) and represent RNAs synthesized during testicular spermatogenesis.

ensuring that vesicles purified from the epididymis are not generated from maturing sperm (fig. S6G).

To further test the hypothesis that epididymosomes are responsible for shaping the RNA payload of sperm, we characterized sRNAs in sperm isolated from the proximal caput epididymis, finding that the RNA payload of caput sperm differs substantially from that of distal cauda sperm (Fig. 3 and fig. S7) (*14*). Proximal-distal biases for specific tRFs along the epididymis were reflected in maturing sperm, showing a dramatic ~10-fold enrichment of tRF-Val-CAC, for example, in cauda relative to caput samples. To directly test whether epididymosomes can deliver their RNAs to caput sperm, we purified caput sperm and incubated them with cauda epididymosomes, then pelleted and washed the resulting reconstituted sperm. Epididymosomal fusion with caput sperm was sufficient to deliver tRF-Val-CAC and other cauda-enriched tRFs to caput sperm in both mouse and bull (Fig. 3, C and D) (*15*). Taken together, these results are most consistent with a mechanism of RNA biogenesis in mammalian sperm in which tRFs generated in the epididymis are trafficked to sperm in epididymosomes. However, our results do not rule out the alternative hypothesis that intact tRNAs in immature sperm (fig. S7F) are cleaved as sperm mature in the epididymis.

We next turned to potential functions of diet-regulated tRFs, using an embryonic stem (ES) cell system amenable to mechanistic analysis. We used antisense locked nucleic acid (LNA)–containing oligonucleotides to interfere with the function of specific tRFs and assayed mRNA abundance as a readout of tRF inhibition. Most antisense oligos had no effect on mRNA abundance (table S4), suggesting that the targeted tRFs are not functional in ES cells or exert regulatory effects that are not assayed by mRNA abundance (*16*). In contrast, interfering with tRF-Gly-GCC resulted in dramatic up-regulation of ~70 genes (Fig. 4, A to C). These genes were unaffected by antisense oligos against other tRNA-Gly isoacceptors or against the middle or 3′ end of tRNA-Gly-GCC (Fig. 4B). The genes derepressed upon tRF-Gly-GCC inhibition are highly expressed in preimplantation embryos and are regulated by the long terminal repeat (LTR) of the endogenous retroelement MERVL (*17*) (Fig. 4D). Regulation of MERVL LTR-driven transcription by tRF-Gly-GCC could be recapitulated in LTR reporter cell lines and is not secondary to translational effects of tRF-Gly-GCC inhibition (figs. S8 and S9 and table S5). Microinjection of antisense oligos targeting tRF-Gly-GCC into zygotes also resulted in derepression of MERVL targets later in development (Fig. 4, E and F, and table S6), indicating that tRF-Gly-GCC also regulates MERVL in a more physiological context.

Given the robust connection between a diet-regulated sRNA and a highly specific set of target genes, we asked whether tRF-Gly-GCC targets are affected in preimplantation embryos generated using sperm from animals consuming a control or low-protein diet. RNA sequencing (RNA-seq) (*18*, *19*) of individual mouse embryos cultured to various stages of development robustly clustered embryos by developmental stage (Fig. 5, A and B; fig. S10; and table S7), with the first two principal components of the data set representing oocyte-derived transcripts and the products of embryonic genome activation.

Because single-embryo RNA-seq data are not suitable for identification of modest changes in individual mRNAs, we searched for consistent changes in larger gene sets: the subset of MERVL targets that respond to tRF-Gly-GCC inhibition (Fig. 4) and the remaining MERVL targets (*17*). At the two-cell stage, both tRF-Gly-GCC targets and the remaining MERVL targets were down-regulated in low-protein embryos relative to controls (Fig. 5C), consistent with the hypothesis that tRF-Gly-GCC in sperm affects expression of MERVL targets in early embryos. We carried out several independent tests of this hypothesis. First, we injected <40-nt RNA populations purified from control and low-protein sperm into control zygotes and discovered that low-protein RNAs could inhibit tRF-Gly-GCC targets in two-cell embryos (Fig. 5D and fig. S11A), indicating that paternal diet can affect preimplantation gene regulation via RNAs in sperm. Second, further defining the relevant RNA from low-protein sperm, microinjection of a synthetic tRF-Gly-GCC oligo resulted in repression of MERVL target genes in two-cell embryos (Fig. 5E and fig. S11B). In addition, because tRFs in sperm are gained during epididymal

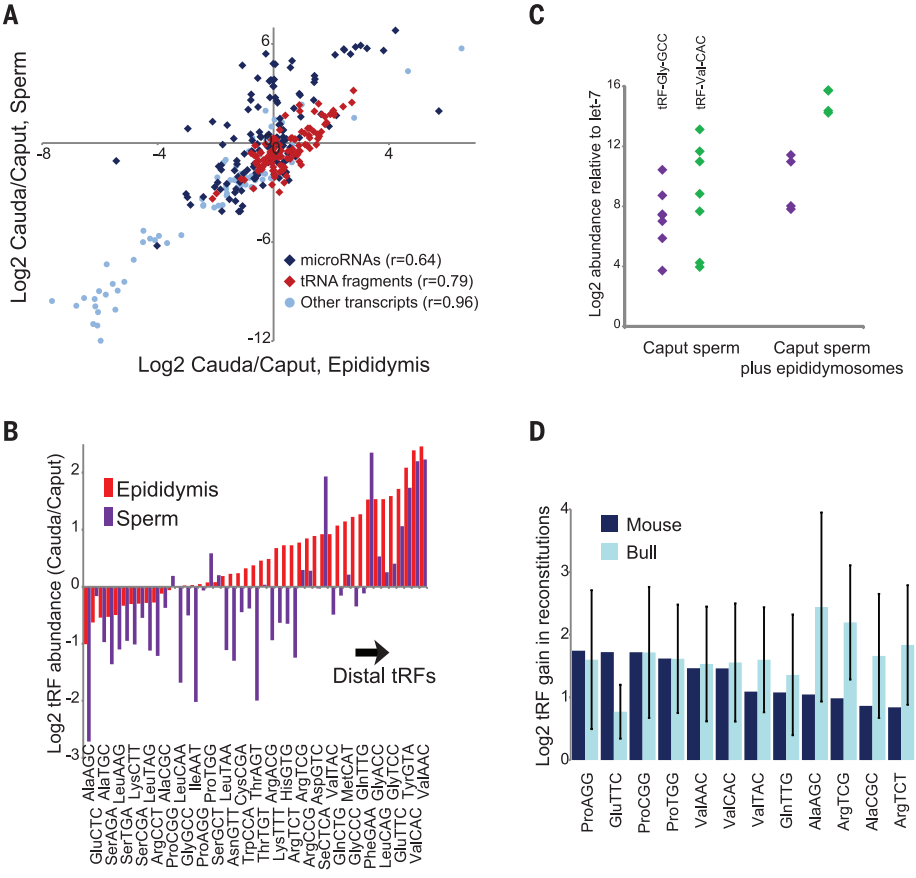

Fig. 3. Changes in sperm tRF payload during epididymal transit. (**A**) Proximal-distal biases observed for RNAs in the epididymis are recapitulated in sperm samples. (**B**) Proximal-distal biases for tRFs, aggregated by anticodon, in the epididymis and sperm. (**C**) TaqMan assay of the indicated tRFs in caput sperm and reconstituted sperm, showing gain of tRFs relative to let-7 (*t* test, P = 0.05 for Gly-GCC and 0.004 for Val-CAC). (**D**) Deep sequencing of reconstituted sperm. tRFs are aggregated by codon and normalized to levels of tRF-Glu-CTC. Caput versus cauda differences were broadly recapitulated in reconstitutions, with tRFs such as tRF-Val-CAC being delivered to caput sperm via fusion with the cauda epididymosomes.

transit (fig. S3), we used testicular spermatozoa or cauda sperm to generate embryos via intracytoplasmic sperm injection (ICSI). Consistent with the higher levels of tRF-Gly-GCC in cauda sperm, embryos generated using cauda sperm expressed MERVL targets at lower levels than embryos generated using testicular sperm (Fig. 5F and fig. S12). Together, these findings all support the hypothesis that tRF-Gly-GCC in sperm is capable of delaying or repressing MERVL target expression in two-cell embryos.

Finally, we note that tRF-Gly-GCC is one of several abundant RNAs regulated by a low-protein diet, and MERVL-driven genes are not the only diet-responsive genes in preimplantation embryos. Ribosomal protein genes were down-regulated in low-protein embryos, and correspondingly, low-protein embryos developed slower than controls (fig. S13) (*20*). Whether altered preimplantation growth kinetics or regulation of MERVL targets could be responsible for the eventual metabolic consequences in offspring remains to be determined. However, as the MERVL program is linked to totipotency (*17*), we speculate that tRF-Gly-GCC repression of MERVL-regulated genes could affect placental size or function, causing downstream effects on metabolism secondary to altered placentation (*1*).

Taken together, our data identify a role for paternal diet in regulating the sperm epigenome in mammals. We show that (i) paternal diet can influence offspring phenotype via information in sperm; (ii) diet alters the level of sRNAs, including tRNA fragments, throughout the male reproductive tract and in mature sperm; and (iii) tRNA fragments can regulate expression of transcripts driven by endogenous retroelements. Our data also illuminate temporal dynamics of sRNA biogenesis during posttesticular sperm maturation and suggest that epididymosomes traffic RNAs from somatic cells of the epididymis to maturing gametes.

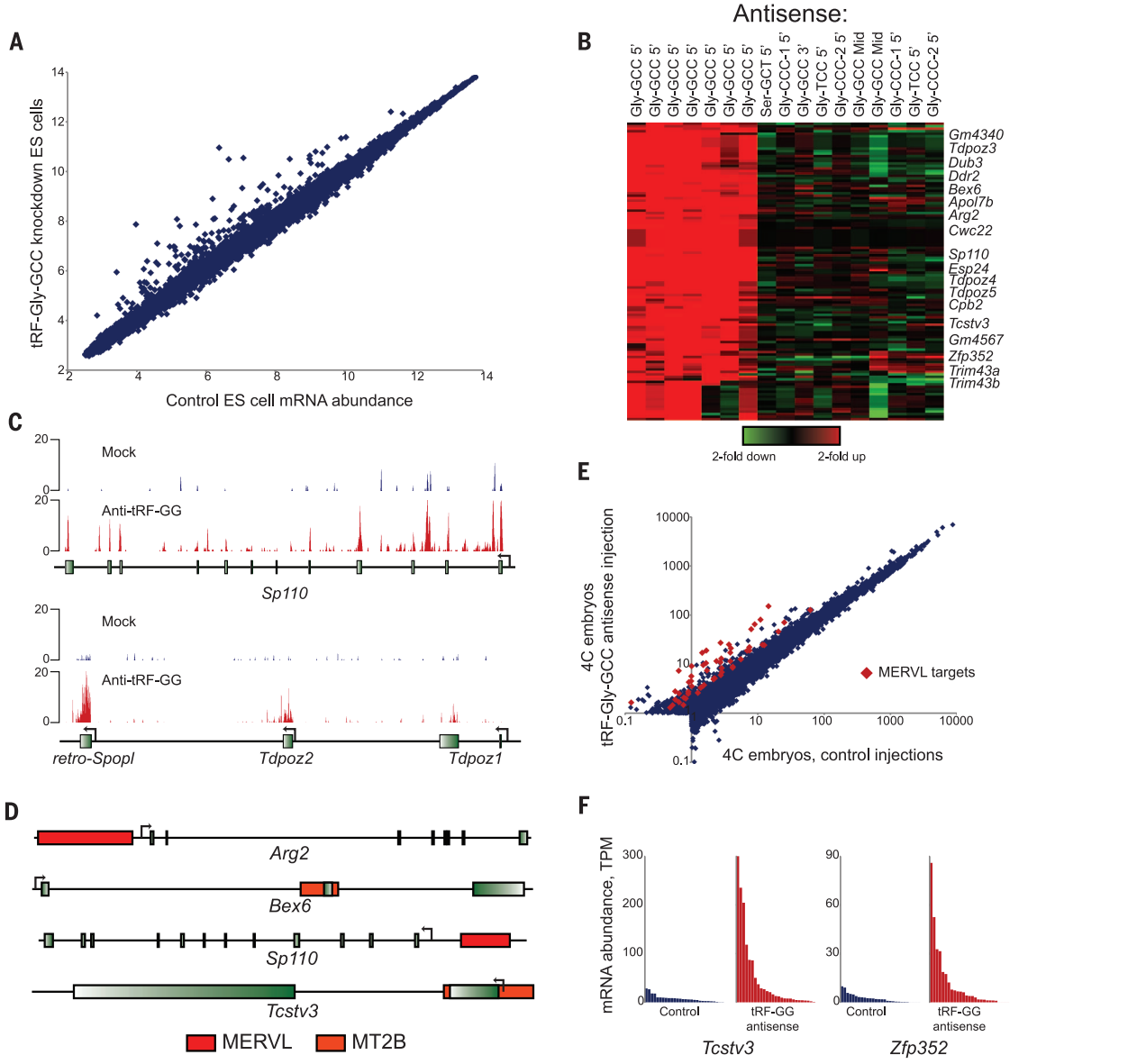

Fig. 4. Regulation of MERVL-driven transcripts by tRF-Gly-GCC. (**A**) Scatter plot shows mRNA abundance in ES cells transfected with green fluorescent protein (GFP) small interfering RNA (siRNA), as compared with LNA antisense oligonucleotides to the 5′ end of tRF-Gly-GCC. (**B**) Effect of tRF-Gly-GCC inhibition on MERVL-regulated genes is isoacceptor-specific. Affymetrix data for ES cells transfected with LNA antisense oligos, relative to matched GFP controls, showing genes changing twofold in two or more samples. (**C**) RNA-seq data for ESCs transfected with GFP siRNA or anti-tRF-Gly-GCC. (**D**) Genomic context of tRF-Gly-GCC target genes, showing nearby MERVL LTRs. (**E**) Inhibition of tRF-Gly-GCC affects MERVL targets in embryos. Averaged single-embryo RNA-seq data for control (n = 28) or tRF-inhibited (n = 27) four-cell-stage (4C) embryos. Among twofold up-regulated genes, known MERVL targets (*17*) are indicated. (**F**) Single-embryo data for two MERVL targets. TPM, transcripts per million.

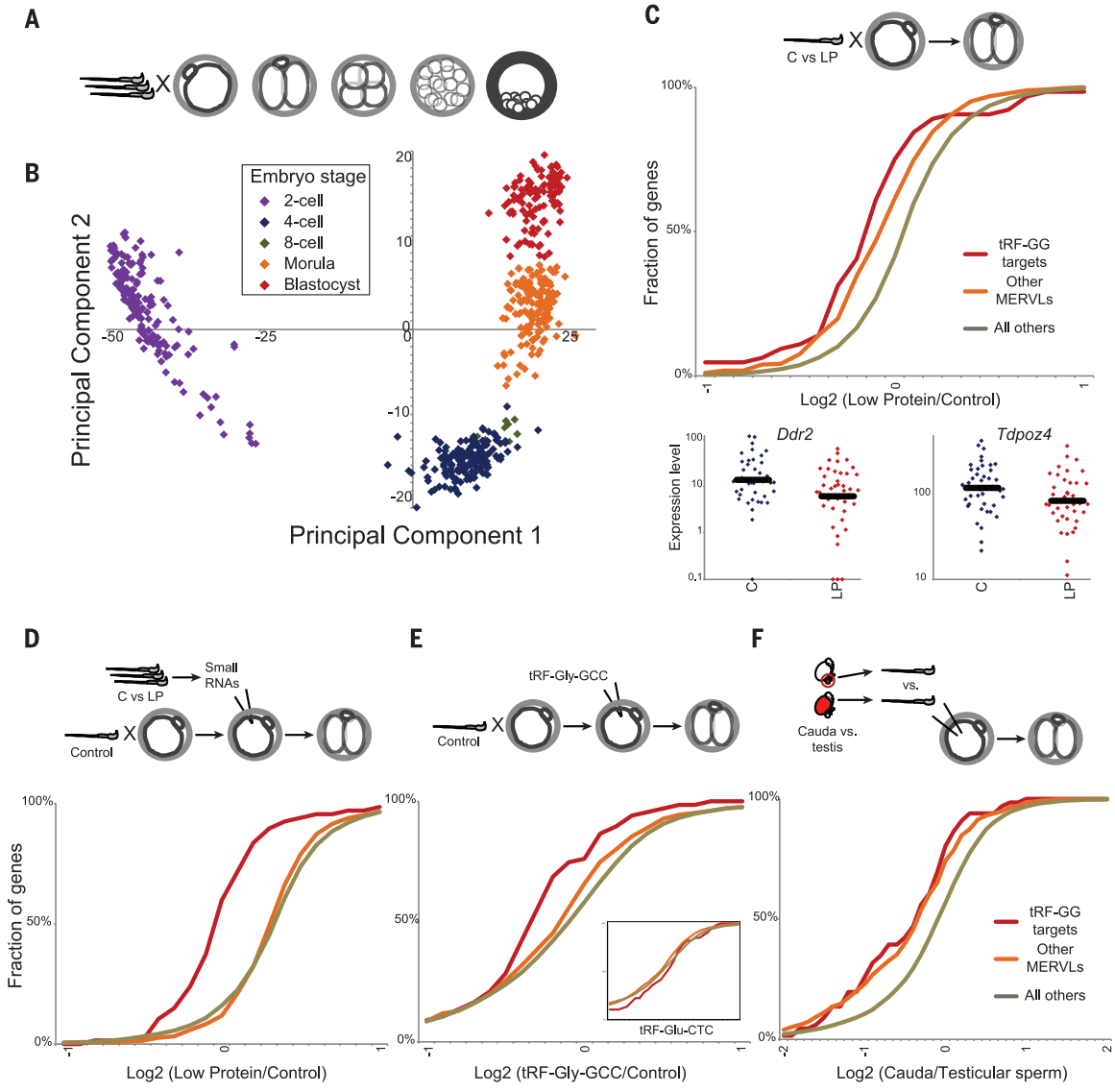

Fig. 5. Paternal dietary effects on preimplantation development. (**A**) Embryos generated by IVF were cultured for varying times and then subjected to single-embryo RNA-seq. (**B**) Single-embryo data for preimplantation embryos represented via principal components analysis: The first two principal components explain 74% of the data set variance. (**C**) Abundance of mRNA in two-cell embryos generated via IVF using control versus low-protein sperm (n = 41 C and 39 LP embryos). Cumulative distribution plots for tRF-Gly-GCC targets ($P = 4.5 \times 10^{-7}$, Kolmogorov-Smirnov test), other MERVL targets (*17*) ($P = 2.5 \times 10^{-13}$), and all remaining genes, showing the percentage of genes with the average $\log_2$(LP/C) indicated on the x axis. Low-protein embryos exhibit a significant shift to lower expression of MERVL targets. Bottom panels show individual embryo data for two targets. (**D**) Small RNAs isolated from control or low-protein cauda sperm were microinjected into control zygotes. RNA-seq (n = 42 C and 46 LP embryos) reveals down-regulation of tRF-Gly-GCC targets ($P = 4.8 \times 10^{-14}$) driven by low-protein RNAs. (**E**) Effects of synthetic tRF-Gly-GCC on two-cell gene regulation, showing significant (P = 0.0001) down-regulation of target genes in embryos injected with tRF-Gly-GCC (n = 26) versus GFP controls (n = 11). The inset shows effects of tRF-Glu-CTC (n = 6). (**F**) Effects of epididymal passage on embryonic gene regulation. Intact sperm isolated from the rete testis (n = 12) or cauda epididymis (n = 9) were injected into control oocytes, and mRNA abundance was analyzed as described above.

REFERENCES AND NOTES

1. O. J. Rando, R. A. Simmons, *Cell* **161**, 93–105 (2015).
2. B. R. Carone *et al.*, *Cell* **143**, 1084–1096 (2010).
3. L. Daxinger, E. Whitelaw, *Nat. Rev. Genet.* **13**, 153–162 (2012).
4. O. J. Rando, *Cell* **151**, 702–708 (2012).
5. E. Heard, R. A. Martienssen, *Cell* **157**, 95–109 (2014).
6. H. Peng *et al.*, *Cell Res.* **22**, 1609–1612 (2012).
7. M. T. Couvillion, R. Sachidanandam, K. Collins, *Genes Dev.* **24**, 2742–2747 (2010).
8. J. L. Dacheux, F. Dacheux, *Reproduction* **147**, R27–R42 (2014).
9. R. Sullivan, G. Frenette, J. Girouard, *Asian J. Androl.* **9**, 483–491 (2007).
10. R. Sullivan, F. Saez, *Reproduction* **146**, R21–R35 (2013).
11. D. Krapf *et al.*, *Dev. Biol.* **369**, 43–53 (2012).
12. H. Valadi *et al.*, *Nat. Cell Biol.* **9**, 654–659 (2007).
13. N. Regev-Rudzki *et al.*, *Cell* **153**, 1120–1133 (2013).
14. B. Nixon *et al.*, *Biol. Reprod.* **93**, 91 (2015).
15. J. N. Caballero, G. Frenette, C. Belleannée, R. Sullivan, *PLOS ONE* **8**, e65364 (2013).
16. A. Sobala, G. Hutvagner, *WIREs RNA* **2**, 853–862 (2011).
17. T. S. Macfarlan *et al.*, *Nature* **487**, 57–63 (2012).
18. D. Ramsköld *et al.*, *Nat. Biotechnol.* **30**, 777–782 (2012).
19. A. K. Shalek *et al.*, *Nature* **498**, 236–240 (2013).
20. M. Mitchell, H. W. Bakos, M. Lane, *Fertil. Steril.* **95**, 1349–1353 (2011).

ACKNOWLEDGMENTS

We thank H. Florman, P. Visconti, R. Sadeh, and N. Friedman for reading the manuscript; P. Visconti and M. Jungnickel for training in caput sperm purification; K. Sutton for training in ICSI; A. Shalek and A. Regev for training in single-cell RNA-seq; T. Fazzio, S. Hainer, and B. Chen for assistance with ES studies; and J. Lawrence and K. Creamer for help with microscopy. This research was supported by NIH grants R01HD080224 and DP1ES025458 and March of Dimes grant FY13-1268. C.C.C. was supported by a Helen Hay Whitney Postdoctoral Fellowship, and A.B. was supported by a Human Frontiers Science Program Fellowship. Data can be accessed at Gene Expression Omnibus with accession numbers GSE74537, GSE75613, and GSE75622.

SUPPLEMENTARY MATERIALS

www.sciencemag.org/content/351/6271/391/suppl/DC1
Materials and Methods
Figs. S1 to S13
Tables S1 to S8
References (*21*–*35*)

19 October 2015; accepted 10 December 2015
Published online 31 December 2015
10.1126/science.aad6780

SMALL RNAS

Sperm tsRNAs contribute to intergenerational inheritance of an acquired metabolic disorder

Qi Chen,[1,3]*† Menghong Yan,[2]† Zhonghong Cao,[1,5]† Xin Li,[1]† Yunfang Zhang,[1,5]† Junchao Shi,[1,5]† Gui-hai Feng,[1] Hongying Peng,[1,4] Xudong Zhang,[1,5] Ying Zhang,[1] Jingjing Qian,[1,5] Enkui Duan,[1]* Qiwei Zhai,[2]* Qi Zhou[1]*

Increasing evidence indicates that metabolic disorders in offspring can result from the father's diet, but the mechanism remains unclear. In a paternal mouse model given a high-fat diet (HFD), we showed that a subset of sperm transfer RNA–derived small RNAs (tsRNAs), mainly from 5′ transfer RNA halves and ranging in size from 30 to 34 nucleotides, exhibited changes in expression profiles and RNA modifications. Injection of sperm tsRNA fractions from HFD males into normal zygotes generated metabolic disorders in the F_1 offspring and altered gene expression of metabolic pathways in early embryos and islets of F_1 offspring, which was unrelated to DNA methylation at CpG-enriched regions. Hence, sperm tsRNAs represent a paternal epigenetic factor that may mediate intergenerational inheritance of diet-induced metabolic disorders.

Increasing lines of evidence from worms to mammals suggest that parental environmental exposure can affect the germ line and influence future generations through epigenetic mechanisms (*1*, *2*). Specifically, diet-induced metabolic changes in mammals are transmitted from father to offspring (*3*, *4*), suggesting sperm-mediated epigenetic inheritance (*5*). DNA methylation is affected (*6*, *7*), yet a causal relationship in transgenerational inheritance has not been established. Small noncoding RNAs (sncRNAs) regulate DNA methylation, histone modifications, and mRNA transcription (*8*) and can induce non-Mendelian transgenerational inheritance in mammals (*9*–*13*). Altered sperm microRNA (miRNA) profiles have been observed after paternal exposure to dietary changes or trauma (*14*, *15*); however, because mammalian sperm harbors a diversity of sncRNAs (*16*), the specific population of RNAs that mediate intergenerational epigenetic memory remains unknown (*17*, *18*). Here we report that a subset of sperm tRNA–derived small RNAs (tsRNAs), mainly from 5′ tRNA halves and about 30 to 34 nucleotides (nt) in size (*19*), showed alterations in expression profiles and RNA modifications after paternal exposure to a high-fat diet and transmitted certain metabolic disorders from father to offspring.

To establish a model of intergenerational transmission of paternal diet–induced metabolic disorder (*4*, *7*, *14*), we continuously fed F_0 male mice with a high-fat diet (HFD, 60% fat) or a normal diet (ND, 10% fat) for 6 months beginning at 5 weeks of age. As expected, males fed a HFD became obese, glucose intolerant, and insulin resistant, whereas males in the ND group did not (fig. S1). The sperm heads of ND and HFD mice were injected into normal mouse oocytes, and the embryos were transferred into surrogate mothers. Male offspring resulting from the HFD- and ND-group sperm were fed a ND and exhibited no obvious differences in body weight over 16 weeks (fig. S2A). However, offspring produced by the HFD-group sperm exhibited the onset of impaired glucose tolerance and insulin resistance as early as 7 weeks of age (fig. S2, B and C), which became more severe at 15 weeks, as revealed by a glucose tolerance test (GTT) and an insulin tolerance test (ITT) (fig. S2, D and F). Although embryo manipulation procedures may induce epigenetic alterations, our parallel sperm-head injection experiments have eliminated the potential influence of male-female contact and semen factors during natural mating (*20*), suggesting that the sperm itself contains sufficient information

[1]State Key Laboratory of Stem Cell and Reproductive Biology, Institute of Zoology, Chinese Academy of Sciences, Beijing 100101, China. [2]Key Laboratory of Nutrition and Metabolism, Chinese Academy of Sciences Center for Excellence in Molecular Cell Science, Institute for Nutritional Sciences, Shanghai Institutes for Biological Sciences, Chinese Academy of Sciences, Shanghai 200031, China. [3]Department of Physiology and Cell Biology, School of Medicine, University of Nevada, Reno, NV 89512 USA. [4]Beijing Royal Integrative Medicine Hospital, Beijing University of Chinese Medicine, Beijing, China. [5]University of Chinese Academy of Sciences, Beijing 100049, China.
***Corresponding author. E-mail: cqi@medicine.nevada.edu (Q.C.); duane@ioz.ac.cn (E.D.); qwzhai@sibs.ac.cn (Q.Zha.); qzhou@ioz.ac.cn (Q.Zho.)** †These authors contributed equally to this work.

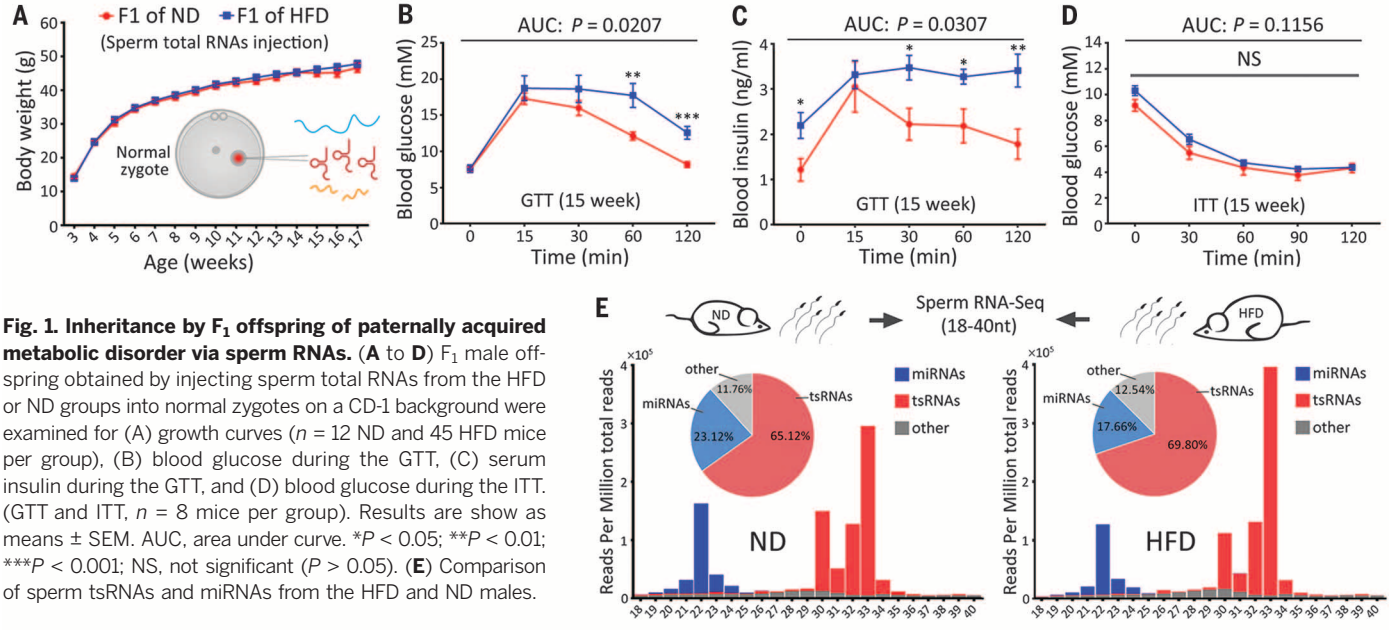

Fig. 1. Inheritance by F_1 offspring of paternally acquired metabolic disorder via sperm RNAs. (**A** to **D**) F_1 male offspring obtained by injecting sperm total RNAs from the HFD or ND groups into normal zygotes on a CD-1 background were examined for (A) growth curves (n = 12 ND and 45 HFD mice per group), (B) blood glucose during the GTT, (C) serum insulin during the GTT, and (D) blood glucose during the ITT. (GTT and ITT, n = 8 mice per group). Results are show as means ± SEM. AUC, area under curve. *P < 0.05; **P < 0.01; ***P < 0.001; NS, not significant (P > 0.05). (**E**) Comparison of sperm tsRNAs and miRNAs from the HFD and ND males.

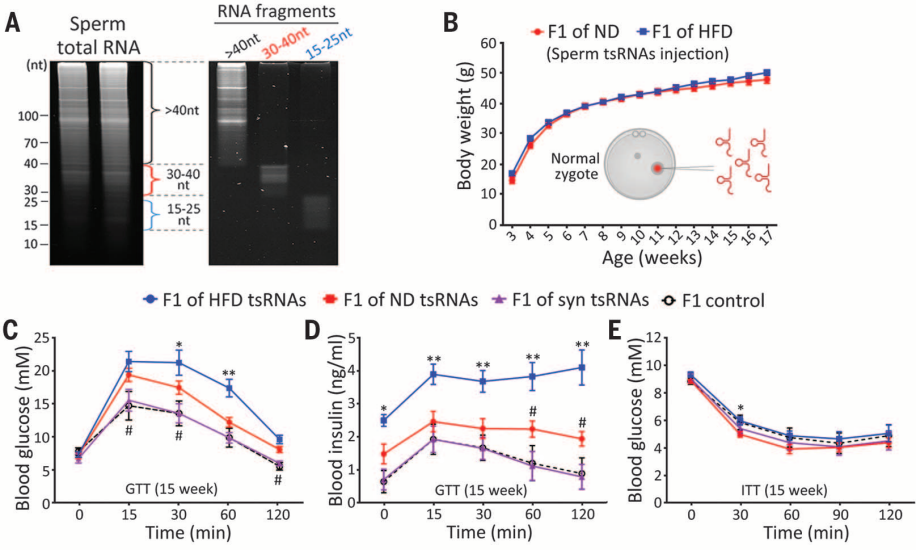

Fig. 2. Sperm tsRNAs conferred paternally acquired metabolic disorder to F_1 offspring. (**A**) PAGE image of sperm total RNAs and isolated RNA fragments. (**B**) Growth curves for F_1 male offspring generated by injecting sperm tsRNAs (30- to 40-nt RNAs) from the HFD or ND group (n = 12 ND and 32 HFD mice per group). (**C** to **E**) F_1 male offspring generated by injecting HFD-group sperm tsRNAs, ND-group sperm tsRNAs, or synthetic (syn) tsRNAs into CD-1 zygotes were examined, relative to F_1 control mice, for (C) blood glucose during the GTT, (D) serum insulin during the GTT, and (E) blood glucose during the ITT (GTT and ITT, n = 8 to 14 mice per group). Results are show as means ± SEM. $^{*}P < 0.05$; $^{**}P < 0.01$ (HFD versus ND tsRNAs); $^{\#}P < 0.05$ (ND versus syn tsRNAs).

to transmit an acquired metabolic disorder to offspring.

To assess whether sperm RNAs can induce intergenerational phenotypes (*15*), we purified total RNAs from the sperm of both HFD and ND mice and injected them into normal zygotes (RNA injection was normalized to about the amount of 10 sperm). Again, although the male offspring from both groups exhibited similar body-weight growth (Fig. 1A), the offspring from the HFD group developed impaired glucose tolerance, showing significantly higher blood glucose and serum insulin levels during the GTT than offspring from the ND group at both 7 and 15 weeks of age (Fig. 1, B and C, and fig. S3). However, the insulin sensitivity of the HFD group's offspring, as determined by the ITT test, was comparable to that of the ND group's offspring (Fig. 1D and fig S3), which differs from the results produced by sperm-head injection (fig. S2, D and F). These data demonstrate that total RNAs from the sperm of HFD males contain the information to induce glucose intolerance, but not insulin resistance, in the F_1 offspring, suggesting the involvement of other layers of regulations such as DNA methylation and histone modifications (*7*, *21*).

To identify the subpopulation of sperm RNAs that mediates paternally acquired metabolic disorder, we examined the sperm sncRNA profiles of the HFD and ND F_0 males by small RNA–seq. (18 to 40 nt) (fig. S4). Analysis of the sequencing data reinforced our recent discovery (*19*) that, in addition to the well-known miRNA population, mature mouse sperm carry tsRNAs (Fig. 1E). Comparative analysis of sperm small RNAs from HFD and ND mice showed that a larger proportion of tsRNAs (11.53%) exhibited significant differences compared with miRNAs (3.23%) (fig. S5 and tables S1 and S2), suggesting that the population of sperm tsRNAs is more sensitive to HFD exposure.

To further investigate whether sperm tsRNAs or other sperm RNA fragments are able to induce intergenerational transmission of acquired traits, we ran sperm RNAs on a 15% PAGE (polyacrylamide gel electrophoresis) gel and separately collected RNA fragments at sizes of 30 to 40 nt (predominantly tsRNAs), 15 to 25 nt (predominantly miRNAs), and >40 nt from both HFD and ND males; this was followed by RNA extraction and confirmation by polymerase chain reaction and RNA-seq (Fig. 2A and figs. S6 and S7). The three types of RNA fragments were injected separately into normal zygotes, with the same concentration as that of the injected sperm total RNAs.

We found that injecting 15- to 25-nt RNAs at this concentration resulted in embryo lethality, whereas injecting 30- to 40-nt or >40-nt RNAs did not (table S3). The embryonic lethal effect in the former case was probably due to the knockdown effects of miRNAs on multiple mRNAs, which would interfere with normal embryonic development. Injection of a 20× dilution of the 15- to 25-nt RNAs did not cause embryo lethality, nor did it cause metabolic disorder in F_1 offspring (fig. S8, A and B). Injection of >40-nt RNAs also did not cause a metabolic phenotype in F_1 offspring (fig. S8, C and D). However, injection of 30- to 40-nt RNAs from HFD and ND groups led to phenotypes that mimicked those in the F_1 offspring that were produced by injecting sperm total RNAs: There was no significant difference in body-weight growth between HFD and ND offspring (Fig. 2B), but male offspring of the HFD group developed glucose intolerance (evident in the GTT; Fig. 2, C and D, and figs. S9 and S10) compared with those of of ND group, though with mild or no insulin resistance evident in the ITT (Fig. 2E and figs. S9 and S10). These results demonstrate that sperm 30- to 40-nt RNAs (predominantly tsRNAs) are necessary to reproduce the effect of sperm total RNAs in inducing acquired metabolic disorder in offspring.

We next synthesized a combination of the most highly expressed tsRNAs in the sperm

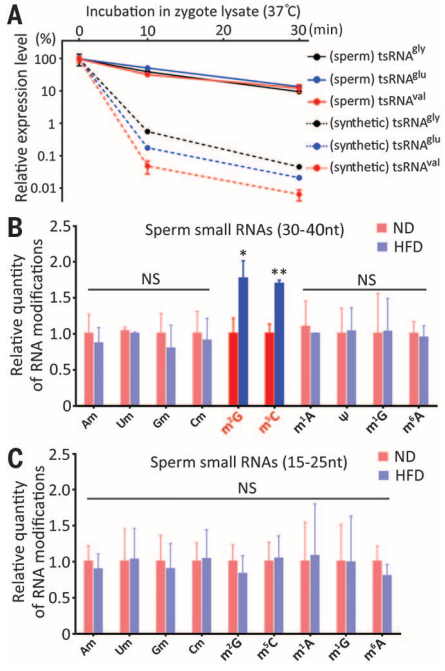

Fig. 3. HFD alters RNA modifications in the sperm tsRNA fraction. (**A**) Comparison of RNA stability between sperm tsRNAs and chemically synthesized tsRNAs without RNA modifications (gly, glycine; glu, glutamic acid, val, valine). (**B** and **C**) HFD-group sperm shows significantly increased m^{5}C and m^{2}G in (B) the tsRNA fraction (30- to 40-nt) but not in (C) the miRNA fraction (15- to 25-nt) of RNAs, as compared with ND-group sperm (n = 3 independent samples per group). Results are show as means ± SEM.

(accounting for ~70% of sperm tsRNAs; table S4) to investigate whether they could resemble the function of endogenous sperm tsRNAs. However, injecting synthetic tsRNAs into normal zygotes with the same protocol that was

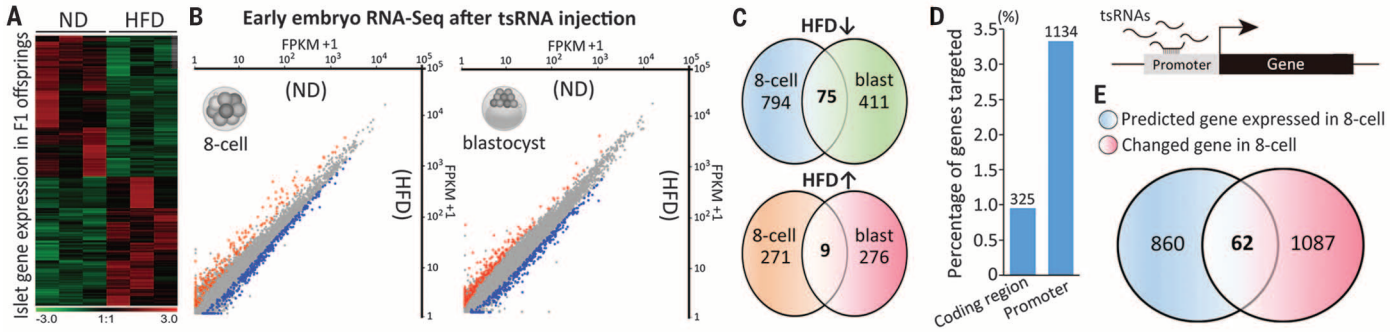

Fig. 4. tsRNAs from HFD-group sperm dysregulated gene expression in early embryos and islets of F_1 offspring. (**A**) Heat map of differentially expressed genes in islets of F_1 offspring. (**B**) Scatterplot analysis for differential gene expression in eight-cell embryos and blastocysts after injecting ND- or HFD-group sperm tsRNAs (FPKM, fragments per kilobase of transcript per million mapped reads). (**C**) Venn diagrams showing number of genes with significant changes at the eight-cell and blastocyst stages (upward- and downward-pointing arrows indicate up- and down-regulation, respectively). (**D**) Sperm tsRNA sequences preferentially match to gene promoter regions rather than to mRNA coding regions. (**E**) Venn diagrams of tsRNA-matched genes that are expressed in eight-cell embryos (blue) and significantly changed genes (red) in eight-cell embryos after injecting sperm tsRNAs.

used for sperm tsRNAs did not induce metabolic disorder in the offspring (Fig. 2, C to E). One explanation for this result could be that the chemically synthesized tsRNAs are not as stable as physiologically derived sperm tsRNAs (*22*). The synthetic tsRNAs showed faster degradation rates in zygote lysates than did the sperm-derived tsRNAs (Fig. 3A). In contrast to the unmodified synthetic tsRNAs, sperm tsRNAs might harbor various RNA modifications (inherited from their tRNA precursors) that influence RNA stability.

To systematically analyze the RNA modification profiles of HFD and ND sperm tsRNAs, we applied our recently developed high-throughput quantitative approach, which is based on liquid chromatography–tandem mass spectrometry (fig. S11) (*23*) and which simultaneously identifies and quantifies multiple types of RNA modifications (table S5) in one RNA sample. With this approach, we stably detected and quantified 10 types of RNA modifications in 30- to 40-nt sperm RNAs (predominantly tsRNAs) and found that two RNA modifications, 5-methylcytidine (m^5C) and N^2-methylguanosine (m^2G), were significantly up-regulated in HFD-group sperm compared with ND-group sperm (Fig. 3B), whereas no significant differences in 15- to 25-nt sperm RNAs (predominantly miRNAs) were found using the same protocol (Fig. 3C). Although the function of m^2G on RNAs in mammals remains unknown, the presence of mammalian m^5C has been reported to contribute to tRNA stability (*24*) and to be related to RNA-mediated transgenerational epigenetic inheritance (*25*). Thus, the elevated levels of m^5C and m^2G modifications in the tsRNAs of HFD-group sperm provide another clue in explaining the function of tsRNAs in mediating paternally acquired traits, pointing to a new direction for future investigations.

To uncover the potential causes of glucose intolerance in F_1 offspring produced by injecting HFD-group sperm tsRNAs, we isolated the F_1 offspring islet and performed RNA-seq and RRBS (reduced representation bisulfite sequencing) analyses for a genome-wide comparison of both transcriptome and DNA methylation. RNA-seq analysis revealed that differentially expressed genes are dominantly enriched in metabolic pathways (including ketone, carbohydrate, and monosaccharide metabolisms) for down- but not up-regulated genes in the HFD group's offspring, as indicated by gene ontology analysis (Fig. 4A and tables S6 and S7). These changed transcription profiles in the F_1 islet could explain the observed metabolic disorder in F_1 offspring. On the other hand, genome-wide RRBS analysis revealed differentially methylated regions (DMRs) between the ND and HFD offspring in 28 genes (table S8). There were no overlaps between the DMR-associated genes and those showing transcriptional changes, suggesting that differential DNA methylation is not directly responsible for the changed transcriptional activity of the F_1 islet.

To test the alternate possibility that injecting sperm tsRNAs into the zygote might cause a transcriptional cascade change in the early embryo that ultimately guides altered gene expression in the islet of F_1 offspring, we collected eight-cell embryos and blastocysts after injection of ND- or HFD-group sperm tsRNAs for comparative RNA-seq analysis (Fig. 4B). Both eight-cell embryos and blastocysts showed that more genes were down-regulated (869 and 486, respectively, with 75 overlaps) than up-regulated (280 and 285, respectively, with nine overlaps) in the group injected with HFD sperm tsRNAs, compared with the group injected with ND sperm tsRNAs. (Fig. 4C and table S9). Embryonic genes showing down- but not up-regulation in the HFD group were enriched in metabolic regulation pathways, in addition to other essential cellular processes (e.g., protein transport and localization) (tables S10 and S11). These early-embryo transcriptional changes might cause profound downstream effects that result in reprogramed gene expression in the islet of F_1 offspring, hence leading to metabolic disorder.

To explore how the injection of tsRNAs could potentially affect embryonic gene expression, we analyzed sequence matches throughout the genome and found that sperm tsRNAs (differentially expressed between ND and HFD males) preferentially match to gene promoter regions (–2 kb from the transcription start site) rather than coding regions (Fig. 4D and table S12). Among the 1134 genes with a tsRNA-matching promoter, 922 of them are expressed in the eight-cell embryos, and 62 of them showed differential expression in the eight-cell embryos (Fig. 4E). Biological pathway analysis showed that these deregulated genes have regulatory potential for diverse cellular and molecular events, including apoptosis, autophagy, oxidative stress, glucose input, and others (fig. S12). The genes *Maea, Ccnc,* and *Deptor* have been reported to be involved in pancreatic β-cell function or to be associated with diabetic conditions (*26*–*28*). This correlation-based evidence suggests that sperm tsRNAs might affect metabolic gene expression through embryo to adulthood via a transcriptional cascade effect and that the deregulation of this process can affect F_1 offspring phenotypes (fig. S13).

REFERENCES AND NOTES

1. L. Daxinger, E. Whitelaw, *Nat. Rev. Genet.* **13**, 153–162 (2012).
2. O. Rechavi *et al.*, *Cell* **158**, 277–287 (2014).
3. B. R. Carone *et al.*, *Cell* **143**, 1084–1096 (2010).
4. S. F. Ng *et al.*, *Nature* **467**, 963–966 (2010).
5. O. J. Rando, *Cell* **151**, 702–708 (2012).
6. E. J. Radford *et al.*, *Science* **345**, 1255903 (2014).
7. Y. Wei *et al.*, *Proc. Natl. Acad. Sci. U.S.A.* **111**, 1873–1878 (2014).
8. D. Holoch, D. Moazed, *Nat. Rev. Genet.* **16**, 71–84 (2015).
9. V. Grandjean *et al.*, *Development* **136**, 3647–3655 (2009).
10. K. D. Wagner *et al.*, *Dev. Cell* **14**, 962–969 (2008).
11. M. Rassoulzadegan *et al.*, *Nature* **441**, 469–474 (2006).
12. S. Yuan, D. Oliver, A. Schuster, H. Zheng, W. Yan, *Sci. Rep.* **5**, 9266 (2015).
13. A. B. Rodgers, C. P. Morgan, N. A. Leu, T. L. Bale, *Proc. Natl. Acad. Sci. U.S.A.* **122**, 13699–13704 (2015).
14. T. Fullston *et al.*, *FASEB J.* **27**, 4226–4243 (2013).
15. K. Gapp *et al.*, *Nat. Neurosci.* **17**, 667–669 (2014).
16. M. Jodar, S. Selvaraju, E. Sendler, M. P. Diamond, S. A. Krawetz, *Hum. Reprod. Update* **19**, 604–624 (2013).
17. W. Yan, *Mol. Cell. Endocrinol.* **398**, 24–30 (2014).
18. R. Liebers, M. Rassoulzadegan, F. Lyko, *PLOS Genet.* **10**, e1004296 (2014).
19. H. Peng *et al.*, *Cell Res.* **22**, 1609–1612 (2012).

20. M. Lane, R. L. Robker, S. A. Robertson, *Science* **345**, 756–760 (2014).
21. K. Siklenka *et al.*, *Science* **350**, aab2006 (2015).
22. Y. Zhang *et al.*, *J. Mol. Cell Biol.* **6**, 172–174 (2014).
23. M. Yan *et al.*, *Anal. Chem.* **85**, 12173–12181 (2013).
24. F. Tuorto *et al.*, *Nat. Struct. Mol. Biol.* **19**, 900–905 (2012).
25. J. Kiani *et al.*, *PLOS Genet.* **9**, e1003498 (2013).
26. Y. S. Cho *et al.*, *Nat. Genet.* **44**, 67–72 (2012).
27. M. Jiménez-Palomares *et al.*, *Am. J. Physiol. Endocrinol. Metab.* **308**, E450–E459 (2015).
28. C. C. Dibble, L. C. Cantley, *Trends Cell Biol.* **25**, 545–555 (2015).

ACKNOWLEDGMENTS

Raw data are archived in the Gene Expression Omnibus under accession number GSE75544. This research was supported by the National Basic Research Program of China (grants 2012CBA01300 to Q.Zho., 2015CB943000 to Q.C., and 2014CB542300 to Q.Zha.), the Strategic Priority Research Program of the Chinese Academy of Sciences (grant XDA01000000 to Q.Zho. and E.D), and the National Natural Science Foundation of China (grants 81490742 to E.D., 31200879 to Q.C., 31300960 to H.P., 31300957 to Y.Z., 81472181 to M.Y., and 31470768 and 81321062 to Q.Zha.).

SUPPLEMENTARY MATERIALS

www.sciencemag.org/content/351/6271/397/suppl/DC1
Materials and Methods
Figs. S1 to S13
Tables S1 to S12
References (*29*–*38*)

4 November 2015; accepted 11 December 2015
Published online 31 December 2015
10.1126/science.aad7977

GENE EDITING

Postnatal genome editing partially restores dystrophin expression in a mouse model of muscular dystrophy

Chengzu Long,[1,2,3]* Leonela Amoasii,[1,2,3]* Alex A. Mireault,[1,2,3] John R. McAnally,[1,2,3] Hui Li,[1,2,3] Efrain Sanchez-Ortiz,[1,2,3] Samadrita Bhattacharyya,[1,2,3] John M. Shelton,[4] Rhonda Bassel-Duby,[1,2,3] Eric N. Olson[1,2,3]†

CRISPR/Cas9-mediated genome editing holds clinical potential for treating genetic diseases, such as Duchenne muscular dystrophy (DMD), which is caused by mutations in the dystrophin gene. To correct DMD by skipping mutant dystrophin exons in postnatal muscle tissue in vivo, we used adeno-associated virus–9 (AAV9) to deliver gene-editing components to postnatal *mdx* mice, a model of DMD. Different modes of AAV9 delivery were systematically tested, including intraperitoneal at postnatal day 1 (P1), intramuscular at P12, and retro-orbital at P18. Each of these methods restored dystrophin protein expression in cardiac and skeletal muscle to varying degrees, and expression increased from 3 to 12 weeks after injection. Postnatal gene editing also enhanced skeletal muscle function, as measured by grip strength tests 4 weeks after injection. This method provides a potential means of correcting mutations responsible for DMD and other monogenic disorders after birth.

Duchenne muscular dystrophy (DMD) is a fatal muscle disease affecting 1 in 3500 to 5000 boys. Cardiomyopathy and heart failure are common, incurable, and lethal consequences of DMD. The disease is caused by mutations in the gene encoding dystrophin, a large intracellular protein that links the dystroglycan complex at the cell surface with the underlying cytoskeleton, thereby maintaining integrity of muscle cell membranes during contraction (*1*, *2*). In the absence of dystrophin, muscles degenerate, causing weakness and myopathy (*3*). Many therapeutic approaches for DMD have failed, at least in part because of the size of the dystrophin protein and the necessity for lifelong restoration of dystrophin expression in the myriad skeletal muscles of the body as well as the heart.

The CRISPR (clustered regularly interspaced short palindromic repeats)/Cas9 (CRISPR-associated protein 9) system allows precise modification of the genome and represents a potential means of correcting disease-causing mutations (*4*, *5*). In the presence of single guide RNAs (sgRNAs), Cas9 is directed to specific sites in the genome adjacent to a protospacer adjacent motif (PAM), causing a double-strand break (DSB). When provided with an additional DNA template, a precise genomic modification is generated by homology-directed repair (HDR), whereas in the absence of an exogenous template, variable indel mutations are created at the target site via nonhomologous end joining (NHEJ) (*6*). Previously, we used CRISPR/Cas9 to correct a single nonsense mutation in *Dmd* by HDR in the germ line of *mdx* mice, which allowed the restoration of dystrophin protein expression (*7*). However, germline genomic editing is not feasible in humans (*8*) and HDR does not occur in postmitotic adult tissues, such as heart and skeletal muscle (*9*), necessitating alternative strategies of gene correction in postnatal tissues. Here, we devised a method to correct *Dmd* mutations by CRISPR/Cas9-mediated NHEJ (termed "Myoediting") in postnatal muscle tissues after delivery of gene-editing components by means of adeno-associated virus–9 (AAV9), which displays high tropism for muscle (*10*, *11*).

The dystrophin protein contains several domains (fig. S1), including an actin-binding domain at the N terminus, a central rod domain with a series of spectrin-like and actin-binding repeats, and WW and cysteine-rich domains at the C terminus that mediate binding to dystroglycan, dystrobrevin, and syntrophin (*12*). The actin-binding and cysteine-rich domains are essential for function, but many regions of the protein are dispensable (*3*). It has been estimated that as many as 80% of DMD patients could benefit from exon-skipping strategies that bypass mutations in nonessential regions of the gene and partially restore dystrophin expression (*13*). This approach has been validated in vitro by CRISPR/Cas9-mediated correction of *Dmd* mutations in patients' induced pluripotent stem cells (*14*) and immortalized myoblasts (*15*). Similarly, adenovirus-mediated gene editing was shown to restore dystrophin expression in specific muscles of *mdx* mice after intramuscular injection (*16*), but adenoviral delivery is not therapeutically favorable (*17*).

Shown in Fig. 1A is the strategy whereby CRISPR/Cas9-mediated NHEJ can create internal genomic deletions to bypass the premature termination codon in exon 23 responsible for the dystrophic phenotype of *mdx* mice, potentially allowing reconstitution of the *Dmd* open reading frame. In principle, this approach could be applied to many mutations within the gene, including large deletions, duplications, and pseudoexons. An advantage of this approach is that it does not require precise correction of the disease-causing mutation. Instead, imprecise deletions that prevent splicing of mutant exons are sufficient to restore dystrophin protein expression.

To test whether Myoediting could be adapted to skip the *Dmd* mutation in exon 23 in *mdx* mice, we first evaluated a pool of sgRNAs that potentially target the 5′ and 3′ ends of exon 23 (supplementary materials, fig. S2, and table S1). We co-injected Cas9 mRNA with sgRNA-mdx (directed toward the mutant sequence in exon 23) and either sgRNA-R3 or sgRNA-L8 (targeting the 3′ and 5′ end of exon 23, respectively) into *mdx* zygotes without a HDR template (fig. S3A). Strikingly, ~80% of progeny mice lacked exon 23 (termed *mdx*-ΔEx23) (fig. S3, B and C, and table S2), representing an increase in the efficiency of *mdx* editing relative to HDR (*7*). Genomic polymerase chain reaction (PCR) products from the target sites of exon 23 and reverse transcription PCR (RT-PCR) products of *mdx*-ΔEx23 mice were cloned and sequenced, confirming the skipping of exon 23 (fig. S3, D to F). As a result of skipping exon 23, the open reading frame of *Dmd* was restored, allowing dystrophin protein expression

[1]Department of Molecular Biology, University of Texas Southwestern Medical Center, Dallas, TX 75390, USA. [2]Hamon Center for Regenerative Science and Medicine, University of Texas Southwestern Medical Center, Dallas, TX 75390, USA. [3]Sen. Paul D. Wellstone Muscular Dystrophy Cooperative Research Center, University of Texas Southwestern Medical Center, Dallas, TX 75390, USA. [4]Department of Internal Medicine, University of Texas Southwestern Medical Center, Dallas, TX 75390, USA.
*These authors contributed equally to this work. **†Corresponding author. E-mail: eric.olson@utsouthwestern.edu**

(fig. S4A). In *mdx*-ΔEx23 mice, serum creatine kinase levels (a measure of muscle membrane permeability) and grip-strength tests both showed restoration of muscle function (fig. S4, B and C). Control *mdx* mice without treatment (–) and *mdx* mice with Myoediting (+) were tested for potential off-target effects of Myoediting with sgRNA-R3 (fig. S5). Ten potential genome-wide off-target sites (OT-01 to OT-10) were predicted by the CRISPR design tool (http://crispr.mit.edu; see supplementary materials and table S4) (*7*). Only the target site *Dmd* R3 of Myoedited *mdx* mice showed cleavage bands in the T7 endonuclease I (T7E1) assay, and no off-target effects were detected in the top 10 potential off-target sites (fig. S5).

To apply Myoediting to postnatal muscle tissues, we used AAV9, which displays tropism to cardiac and skeletal muscle (*10*, *11*), to deliver Cas9 and sgRNAs to muscles of mice. AAV-guide RNAs were generated by cloning sgRNA-mdx and sgRNA-R3 into AAV-sgRNA vector containing a human U6 promoter and green fluorescent protein (GFP) (Fig. 1B). We generated AAV-Cas9 using a unique AAV-Cas9 vector (miniCMV-Cas9-short-PolyA) (*18*, *19*), which uses a "mini"-CMV promoter/enhancer sequence to drive expression of the humanized *Streptococcus pyogenes* Cas9 (SpCas9). Different modes of AAV9 delivery and variations in timing of expression were systematically compared to identify the optimal method for *Dmd* Myoediting in postnatal *mdx* mice: (i) intramuscular (IM) at P12, (ii) retro-orbital (RO) at P18, and (iii) intraperitoneal (IP) at P1 (see supplementary materials) shown in Fig. 1C.

After IM injection of P12 mice with AAVs, muscle tissues were analyzed by immunostaining

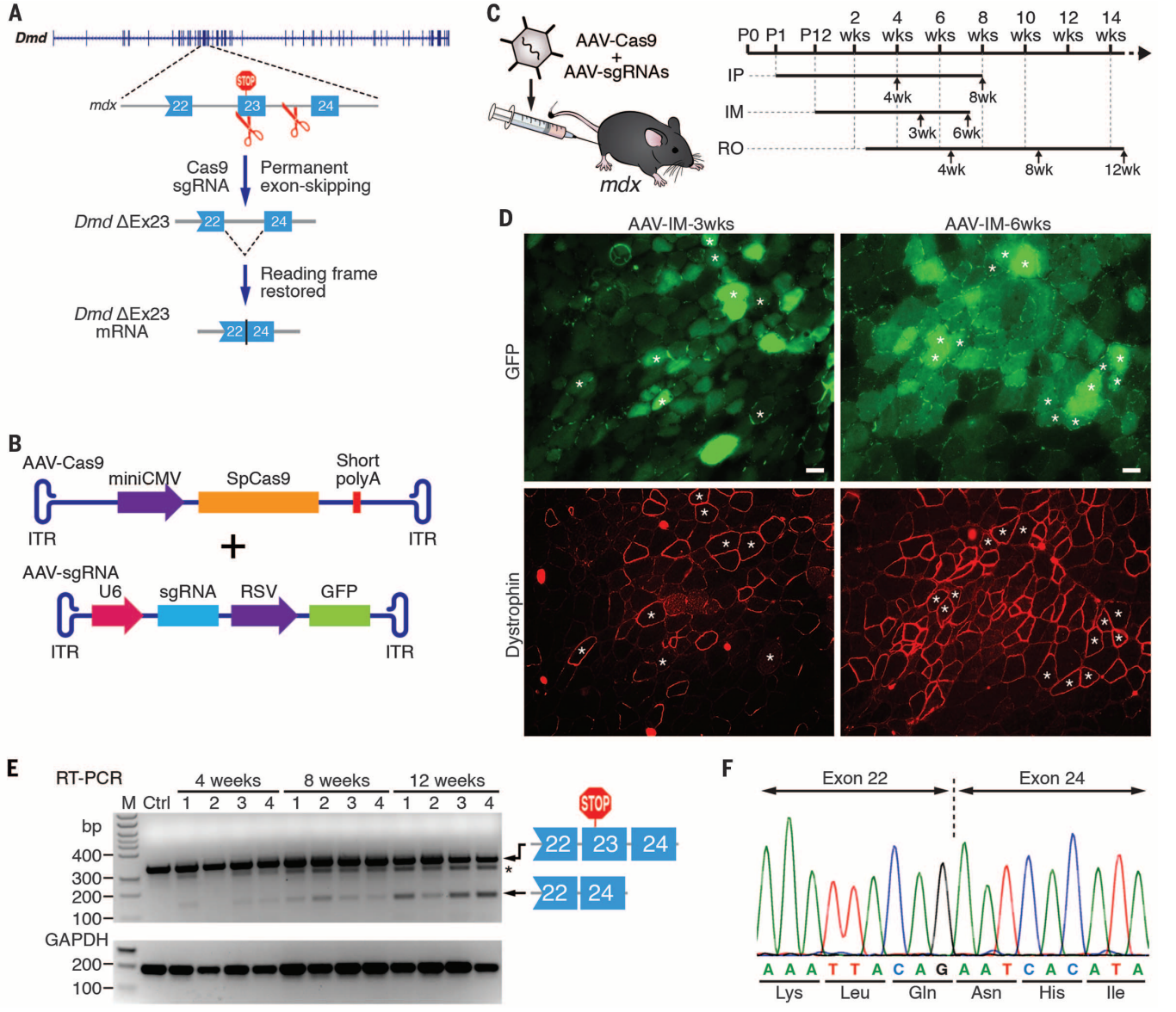

Fig. 1. Permanent exon skipping in postnatal *mdx* mice by AAV-mediated Myoediting. (**A**) Strategy for bypassing exon 23 of the *mdx* locus by NHEJ. (**B**) AAV vectors for expression of Cas9 (AAV-Cas9, upper), guide RNAs, and GFP (AAV-sgRNA, lower). ITR, inverted terminal repeat; RSV, Rous sarcoma virus promoter; U6, human U6 promoter. (**C**) Different modes of AAV9 delivery. Black arrows indicate time points for tissue collection after injection. (**D**) Rescue of dystrophin expression in *mdx* mouse by IM injection of Myoediting components. GFP and dystrophin immunostaining from serial sections of *mdx* mouse TA muscle are shown 3 and 6 weeks after AAV-IM injection of AAV-Cas9 sgRNAs at P12 (three male *mdx* mice in each group). Asterisks indicate serial section myofiber alignment. Scale bar, 40 μm. (**E**) RT-PCR of RNA from Myoedited *mdx* mice indicates deletion of exon 23 (termed ΔEx23, lower band) and shows increase in intensity of ΔEx23 bands from 4 to 12 weeks after AAV-RO injection (four male *mdx* mice in each group). Asterisk indicates the RT-PCR products with small deletions; M denotes size marker lane; bp indicates the length of the marker bands. (**F**) Sequence of the RT-PCR products of ΔEx23 band confirmed that exon 22 spliced directly to exon 24, excluding exon 23.

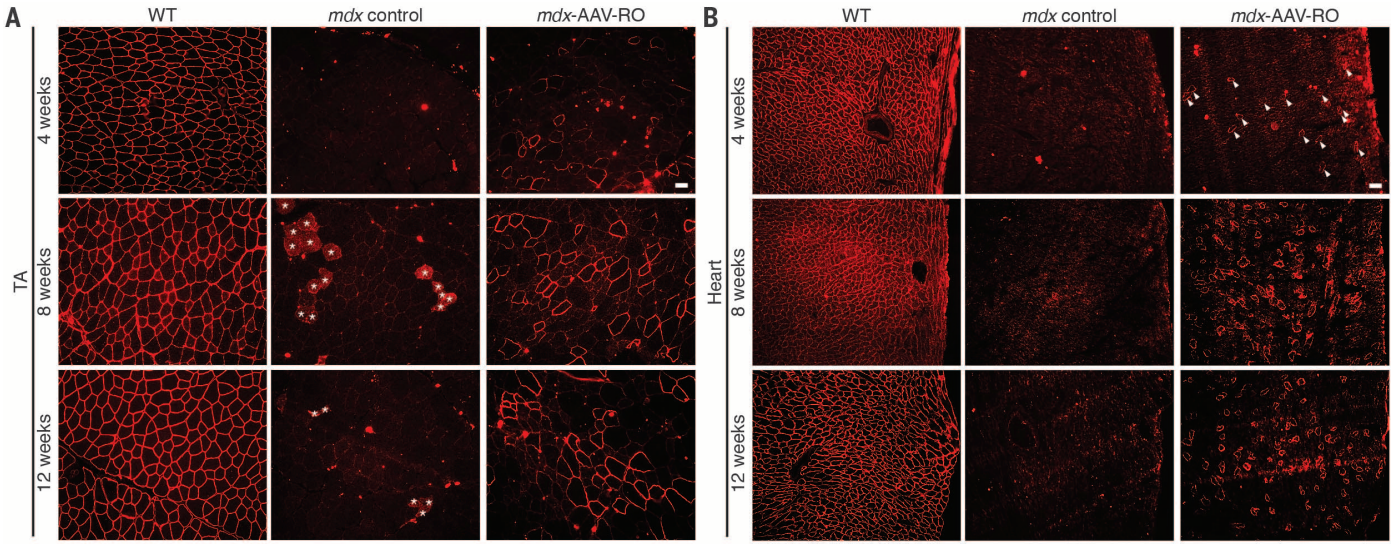

Fig. 2. Rescue of dystrophin expression in postnatal *mdx* mice by retro-orbital injection of AAV-Cas9 sgRNAs. (**A**) Dystrophin immunostaining of TA muscle is shown for wild-type (WT), *mdx*, and AAV-RO–treated *mdx* mice at 4, 8, and 12 weeks after injection (AAV-RO at P18, four male *mdx* mice in each group). TA muscle of unedited *mdx* control mice exhibits myonecrosis, indicated by cytoplasm-filling autofluorescence (highlighted with white asterisks). (**B**) Dystrophin immunostaining of the heart is illustrated for WT, *mdx*, and AAV-RO–treated *mdx* mice at 4, 8, and 12 weeks after injection (AAV-RO at P18, four male *mdx* mice in each group). Arrowheads indicate dystrophin-positive cardiomyocytes 4 weeks after AAV-RO injection into *mdx* mouse heart. Scale bar, 40 μm.

for dystrophin expression 3 weeks later (Fig. 1D and fig. S6A). Native GFP identified AAV-mediated gene expression in myofibers. Skeletal muscle from the IM-AAV–injected mice showed a mosaic pattern of dystrophin-positive fibers (Fig. 1D). The percentage of dystrophin-positive myofibers was calculated as a fraction of total estimated fibers. In the *mdx* mouse shown in Fig. 1D, 7.7 ± 3.1% of myofibers in the tibialis anterior (TA) muscle expressed dystrophin 3 weeks after IM-AAV injection (all errors reported are SD). Rescue increased to an estimated 25.5 ± 2.9% of myofibers by 6 weeks after IM-AAV injection (three male *mdx* mice per group) (fig. S6A). Hematoxylin and eosin (H&E) staining of muscle showed that histopathologic hallmarks of muscular dystrophy, such as necrotic myofibers, were diminished in TA muscle at 6 weeks after AAV delivery. Inflammatory cell invasion and centralized myofiber nuclei were minimal, in marked contrast to uninjected control *mdx* TA (fig. S6B).

RO injection of AAV into the venous sinus of the mouse represents an alternative to tail vein injection for the systemic administration via blood circulation in young mice. Muscle tissues from mice after RO-AAV injection at P18 were examined by RT-PCR (Fig. 1E). RT-PCR of RNA from Myoedited *mdx* mice showed that deletion of exon 23 (ΔEx23) allowed splicing from exon 22 to 24 (lower band) and the intensity of ΔEx23 bands was increased from 4 to 12 weeks after RO-AAV injection. Sequencing of RT-PCR products of the ΔEx23 band confirmed that exon 22 spliced to exon 24 (Fig. 1F). Muscle tissues were analyzed by immunohistochemistry (Fig. 2) and H&E staining (fig. S7). At 4 weeks after RO-AAV injection in *mdx* mice, 2.5 ± 1.1% of myofibers were dystrophin-positive, whereas 1.1 ± 0.3% of cardiomyocytes were dystrophin-positive. Progressive improvement with age was also observed from 4 to 8 and 12 weeks after RO-AAV injection. Rescue increased to an estimated 6.1 ± 3.2% of myofibers in TA muscle, and 5.0 ± 2.1% of cardiomyocytes, by 8 weeks after RO-AAV injection. At 12 weeks after injection, 4.6 ± 3.2% of myofibers were dystrophin-positive in TA muscle and 9.6 ± 3.9% of cardiomyocytes were dystrophin-positive. Western blot analysis confirmed the restoration of dystrophin expression in both heart and skeletal muscle (fig. S8).

After IP injection of AAV editing components (fig. S9), dystrophin expression was rescued in 1.4 ± 1.2% of TA myofibers and 1.1 ± 1.1% of cardiomyocytes in treated *mdx* mice after 4 weeks. Higher percent correction was observed in *mdx*-injected mice at 8 weeks after IP-AAV injection with 1.8 ± 1.2% of dystrophin-positive myofibers and 3.2 ± 2.4% dystrophin-positive cardiomyocytes. Grip strength testing (see supplementary materials) showed a significant increase in strength of *mdx* mice at 4 weeks after IP-AAV injection relative to uninjected *mdx* controls (Fig. 3).

Semiquantitative immunohistochemistry was performed to quantify dystrophin expression levels, normalized to laminin, in wild-type (WT) and AAV-injected *mdx* mice (see supplementary materials). Integrated density measurements of sarcolemmal staining in TA myofibers showed dystrophin protein levels that were 23.7 ± 11.6% of WT after AAV-IP injection, 27.7 ± 6.6% of WT after AAV-RO injection, and 53.2 ± 18.5% of WT after AAV-IM injection (figs. S10 and S12A). Integrated density of dystrophin in cardiomyocytes showed dystrophin protein levels that were 52.4 ± 14.3% of WT after AAV-IP injection, 71.1 ± 21.0% of WT after AAV-RO injection, and 69.7 ± 19.8% of WT after AAV-IM injection (figs. S11 and S12B).

IM, RO, and IP injection all provide transducing potential in organs and muscle groups remote from the injection site, presumably through intravasculature circulation of AAV. Dystrophin expression in *mdx* mice was restored in vascular smooth muscle cells by all three modes of AAV delivery, but most effectively by RO (fig. S13A). In contrast, no mode of AAV delivery was able to cross the blood-brain barrier to restore dystrophin expression in hippocampal CA1/CA2 regions of *mdx* mice (fig. S13, B and C). AAV transduction across the blood-brain barrier and subsequent restoration

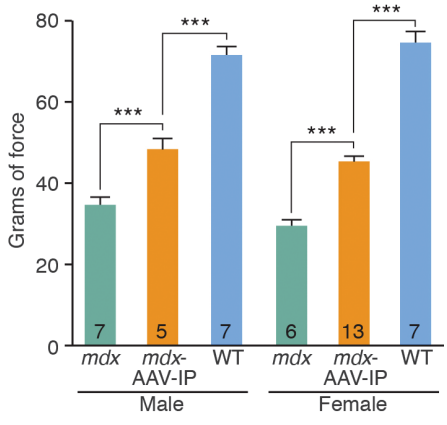

Fig. 3. Forelimb grip strength of *mdx*, *mdx*-AAV-IP, and wild-type mice 4 weeks after injection. *mdx*, *mdx*-AAV-IP, and WT mice were subjected to grip strength testing to measure muscle performance (grams of force), and the *mdx*-AAV-IP mice showed enhanced muscle performance relative to *mdx* mice at 4 weeks of age (*mdx* male control, 34.7 ± 1.8%; *mdx*-AAV-IP male mice, 48.4 ± 2.5%; WT male, 71.8 ± 1.9%; *mdx* female control, 29.7 ± 1.4%; *mdx*-AAV-IP female mice, 45.5 ± 1.4%; WT female, 75 ± 2.4%). Numbers of mice in each group are labeled in the bar, six trials for each mouse. Data are means ± SEM. Significant differences between conditions are indicated (***$P < 0.0005$).

of brain dystrophin expression will likely require other methods (*20*–*23*). We also harvested sperm from AAV-injected male *mdx* mice and tested gene editing by T7E1 assay. No cleavage bands were detected (fig. S13D); however, more sensitive methods such as deep sequencing might be required to evaluate the risk of unexpected germline editing. Additionally, AAV vectors with tissue-specific promoters should enhance the safety of systemic gene editing.

Our results show that AAV-mediated Myoediting can rescue the reading frame and expression of dystrophin in postnatal *mdx* mice. The efficiency of restoration of dystrophin-positive myofibers increases with time, likely reflecting persistent expression of gene-editing components. Exon skipping by NHEJ-mediated genomic editing allows for the permanent removal of the disease-causing mutation and was about 10 times as efficient as gene correction by HDR (*7*). Myoediting by NHEJ does not require precise genetic modification. Instead, any types of indels that disrupt either a splice donor or acceptor sequence in a mutant exon result in exon skipping. It is noteworthy that the consensus sequence for splice acceptors is NAG, corresponding to the PAM sequence for Cas9 from *S. pyogenes* (NGG or NAG), so any exon can potentially be skipped by this approach.

It has been estimated that even low-level expression of dystrophin (4 to 15%) can partially ameliorate cardiomyopathy (*24*) and protect against eccentric contraction-induced injury in skeletal muscle (*25*). The efficiency of restoration of dystrophin expression observed after delivery of Myoediting components to *mdx* mice by AAV is therefore within the range expected to provide therapeutic benefit.

Off-target effects are a safety concern in the eventual translation of gene-editing methods to humans. We did not observe off-target mutations at 10 potential off-target sites in the mouse genome nor any abnormalities in mice after AAV9 delivery of Myoediting components. However, off-target mutations may occur at sites beyond those predicted in silico; hence, a comprehensive and unbiased analysis, such as whole-genome sequencing, would be an essential component of future efforts to establish the safety of this approach (*26*–*28*). Given that Myoediting offers the potential for durable and progressive therapeutic response in postmitotic adult tissue, we propose that this methodology may warrant investigation as a way to restore muscle function in DMD patients, alone or in combination with other therapies (*3*, *29*).

REFERENCES AND NOTES

1. K. P. Campbell, S. D. Kahl, *Nature* **338**, 259–262 (1989).
2. J. M. Ervasti, K. Ohlendieck, S. D. Kahl, M. G. Gaver, K. P. Campbell, *Nature* **345**, 315–319 (1990).
3. R. J. Fairclough, M. J. Wood, K. E. Davies, *Nat. Rev. Genet.* **14**, 373–378 (2013).
4. M. Jinek *et al.*, *Science* **337**, 816–821 (2012).
5. J. A. Doudna, E. Charpentier, *Science* **346**, 1258096 (2014).
6. P. Mali, K. M. Esvelt, G. M. Church, *Nat. Methods* **10**, 957–963 (2013).
7. C. Long *et al.*, *Science* **345**, 1184–1188 (2014).
8. K. S. Bosley *et al.*, *Nat. Biotechnol.* **33**, 478–486 (2015).
9. P. D. Hsu, E. S. Lander, F. Zhang, *Cell* **157**, 1262–1278 (2014).
10. S. Zacchigna, L. Zentilin, M. Giacca, *Circ. Res.* **114**, 1827–1846 (2014).
11. C. Zincarelli, S. Soltys, G. Rengo, J. E. Rabinowitz, *Mol. Ther.* **16**, 1073–1080 (2008).
12. K. E. Davies, K. J. Nowak, *Nat. Rev. Mol. Cell Biol.* **7**, 762–773 (2006).
13. T. Yokota, W. Duddy, T. Partridge, *Acta Myol.* **26**, 179–184 (2007).
14. H. L. Li *et al.*, *Stem Cell Rev.* **4**, 143–154 (2015).
15. D. G. Ousterout *et al.*, *Nat. Commun.* **6**, 6244 (2015).
16. L. Xu *et al.*, *Mol. Ther.* 10.1038/mt.2015.192 (2015).
17. J. C. van Deutekom, G. J. van Ommen, *Nat. Rev. Genet.* **4**, 774–783 (2003).
18. E. Senís *et al.*, *Biotechnol. J.* **9**, 1402–1412 (2014).
19. F. Schmidt, D. Grimm, *Biotechnol. J.* **10**, 258–272 (2015).
20. H. Zhang *et al.*, *Mol. Ther.* **19**, 1440–1448 (2011).
21. C. N. Cearley, J. H. Wolfe, *J. Neurosci.* **27**, 9928–9940 (2007).
22. D. Weber-Adrian *et al.*, *Gene Ther.* **22**, 568–577 (2015).
23. C. Bing *et al.*, *J. Ther. Ultrasound* **2**, 13 (2014).
24. M. van Putten *et al.*, *J. Mol. Cell. Cardiol.* **69**, 17–23 (2014).
25. C. Godfrey *et al.*, *Hum. Mol. Genet.* **24**, 4225–4237 (2015).
26. S. W. Cho *et al.*, *Genome Res.* **24**, 132–141 (2014).
27. S. Q. Tsai *et al.*, *Nat. Biotechnol.* **33**, 187–197 (2015).
28. X. Wang *et al.*, *Nat. Biotechnol.* **33**, 175–178 (2015).
29. K. J. Nowak, K. E. Davies, *EMBO Rep.* **5**, 872–876 (2004).

ACKNOWLEDGMENTS

We thank D. Grimm and F. Schmidt for AAV-hCas9 and the sgRNA Cloning Vector plasmids; C. Wang for AAV9 packaging; J. Schneider and P. Mammen for discussions; C. Rodriguez for technical help; Z. Wang for input; S. Rovinsky and E. Plautz (UT Southwestern Neuro-Models Facility) for grip strength testing; X. Li and R. Gordillo (UT Southwestern Mouse Metabolic Phenotyping Core Facility) for CK level measurement; and J. Cabrera for graphics. Supported by NIH grants HL-077439, HL-111665, HL-093039, DK-099653, U01-HL-100401, and U54 HD 087351; Fondation Leducq Networks of Excellence; and the Robert A. Welch Foundation (grant 1-0025, E.N.O.). The pSpCas9(BB)-2A-GFP (PX458) plasmid is available for purchase from Addgene under a material transfer agreement. The University of Texas Southwestern Medical Center and the authors (E.N.O., R.B.-D., J.M.S., C.L., J.R.M.) have filed a patent application (#14/823,563) related to the use of CRISPR/Cas9 technology to treat muscle disease.

SUPPLEMENTARY MATERIALS

www.sciencemag.org/content/351/6271/400/suppl/DC1
Materials and Methods
Figs. S1 to S13
Tables S1 to S4
References (*30*–*33*)

2 October 2015; accepted 4 December 2015
Published online 31 December 2015
10.1126/science.aad5725

GENE EDITING

In vivo genome editing improves muscle function in a mouse model of Duchenne muscular dystrophy

Christopher E. Nelson,[1,2] Chady H. Hakim,[3] David G. Ousterout,[1,2] Pratiksha I. Thakore,[1,2] Eirik A. Moreb,[1,2] Ruth M. Castellanos Rivera,[4] Sarina Madhavan,[1,2] Xiufang Pan,[3] F. Ann Ran,[5,6] Winston X. Yan,[5,7,8] Aravind Asokan,[4] Feng Zhang,[5,9,10,11] Dongsheng Duan,[3,12] Charles A. Gersbach[1,2,13]*

Duchenne muscular dystrophy (DMD) is a devastating disease affecting about 1 out of 5000 male births and caused by mutations in the dystrophin gene. Genome editing has the potential to restore expression of a modified dystrophin gene from the native locus to modulate disease progression. In this study, adeno-associated virus was used to deliver the clustered regularly interspaced short palindromic repeats (CRISPR)–Cas9 system to the *mdx* mouse model of DMD to remove the mutated exon 23 from the dystrophin gene. This includes local and systemic delivery to adult mice and systemic delivery to neonatal mice. Exon 23 deletion by CRISPR-Cas9 resulted in expression of the modified dystrophin gene, partial recovery of functional dystrophin protein in skeletal myofibers and cardiac muscle, improvement of muscle biochemistry, and significant enhancement of muscle force. This work establishes CRISPR-Cas9–based genome editing as a potential therapy to treat DMD.

Duchenne muscular dystrophy (DMD) is among the most prevalent fatal genetic diseases, occurring in 1 out of 5000 male births (*1*). It results in muscle degeneration, loss of mobility, and premature fatality. DMD mutations are often deletions of one or more exons in the dystrophin gene that disrupt the reading frame of the gene and lead to a complete loss of functional dystrophin expression (*2*). In contrast, Becker muscular dystrophy (BMD) is associated with much milder symptoms relative to DMD and is caused by internal, in-frame deletions of the dystrophin gene, resulting in expression of a truncated but partially functional dystrophin protein (*3*). Because of the genetic nature of the disease, gene therapy is a promising option to treat DMD. However, the very large size of the dystrophin cDNA presents a challenge to gene delivery. Consequently, some therapeutic strategies aim to generate a BMD-like dystrophin. These approaches include the development of mini/micro-dystrophin genes for delivery by adeno-associated virus (AAV) vectors (*4*–*7*) and oligonucleotide-mediated exon-skipping therapies designed to restore the reading frame of the transcript (*8*, *9*). For example, removal of exon 51 can address 13% of DMD patient mutations, and exon-skipping strategies could be extended to other regions of the gene to collectively treat 83% of DMD patients (*10*). In

contrast, genome editing technologies can be used to directly correct disease-causing genetic mutations (*11*) and may be a preferred approach for a single treatment to restore stable expression of a dystrophin protein that contains most of the normal structure and function and is also under physiologic control of the natural promoter. In particular, the clustered regularly interspaced short palindromic repeats (CRISPR)–Cas9 genome editing system, which uses the Cas9 nuclease to cleave DNA sequences targeted by a single guide RNA (gRNA) (*12*), has recently created new possibilities for gene therapy by making precise genome modifications possible in cultured cells (*13*–*16*) and in animal studies (*17*–*20*). Analogous to exon-skipping therapies, CRISPR-mediated removal of one or more exons from the genomic DNA could be applied to the treatment of 83% of DMD patients. Moreover, this approach can be readily extended to targeting multiple exons within mutational hotspots, such as the deletion of exons 45 to 55 that could address 62% of DMD patients with a single-gene editing strategy (*21*). We and others have applied these tools to correct dystrophin mutations in cultured human cells from DMD patients (*21*–*26*) and in *mdx* mouse embryos (*27*). A critical remaining challenge is to translate these proof-of-principle results into a clinically relevant approach for genome editing in muscle tissue in vivo (*28*). The use of genome editing for exon removal, rather than replacing missing exons to restore a full-length gene, may be desirable for several reasons. Editing by exon removal takes advantage of the relatively efficient nonhomologous end joining pathway that is active in all cell types, in contrast to targeted gene addition by the homology-directed repair pathway that is down-regulated in postmitotic cells such as skeletal myocytes and myofibers. This method also avoids the need to deliver a DNA repair template. Finally, gene editing to delete exons will be more applicable to large patient populations that include a variety of mutations, in contrast to patient-specific editing strategies that restore unique gene deletions.

The *mdx* mouse model of DMD has a nonsense mutation in exon 23, which prematurely terminates protein production (*29*). Removal of exon 23 from the transcript through oligonucleotide-mediated exon skipping restores functional dystrophin expression and improves muscle contractility (*30*, *31*). Here, we have developed an AAV-based strategy for the treatment of DMD in the *mdx* mouse by harnessing the unique multiplexing capacity of CRISPR-Cas9 to excise exon 23 from the dystrophin gene. We hypothesized that CRISPR-mediated removal of exon

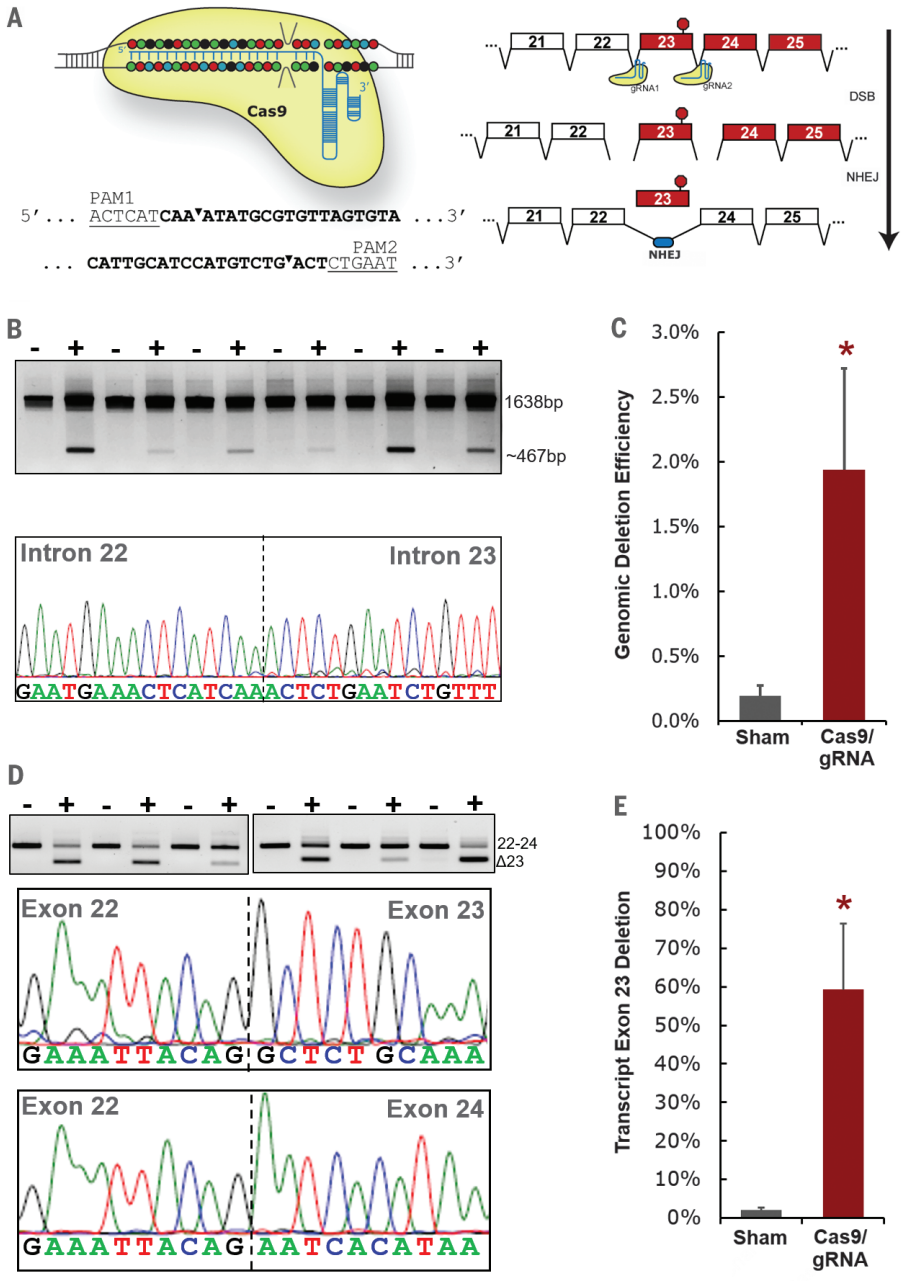

Fig. 1. CRISPR-Cas9–mediated genomic and transcript deletion of exon 23 through intramuscular AAV-CRISPR administration. (**A**) The Cas9 nuclease is targeted to introns 22 and 23 by two gRNAs. Simultaneous generation of double-stranded breaks (DSBs) by Cas9 leads to excision of the region surrounding the mutated exon 23. The distal ends are repaired through nonhomologous end joining (NHEJ). The reading frame of the dystrophin gene is recovered and protein expression is restored. (**B**) PCR across the genomic deletion region shows the smaller-deletion PCR product in treated muscles. Sequencing of the deletion band shows perfect ligation of Cas9 target sites (+, AAV-injected muscles; -, contralateral muscles). (**C**) ddPCR of genomic DNA shows 2% genome editing efficiency (n = 6 muscles, mean + SEM). (**D**) RT-PCR across exons 22 and 24 of dystrophin cDNA shows a smaller band that does not include exon 23 in treated muscles. Sanger sequencing confirmed exon 23 deletion. (**E**) ddPCR of intact dystrophin transcripts and Δ23 transcripts shows that 59% of transcripts do not have exon 23 (n = 6 muscles, mean + SEM). Asterisk, significantly different from the sham group (P < 0.05).

[1]Department of Biomedical Engineering, Duke University, Durham, NC, USA. [2]Center for Genomic and Computational Biology, Duke University, Durham, NC, USA. [3]Department of Molecular Microbiology and Immunology, University of Missouri, Columbia, MO, USA. [4]Gene Therapy Center, Departments of Genetics, Biochemistry and Biophysics, School of Medicine, University of North Carolina at Chapel Hill, Chapel Hill, NC, USA. [5]Broad Institute of MIT and Harvard, Cambridge, MA, USA. [6]Society of Fellows, Harvard University, Cambridge, MA, USA. [7]Graduate Program in Biophysics, Harvard Medical School, Boston, MA, USA. [8]Harvard–MIT Division of Health Sciences and Technology, Harvard Medical School, Boston, MA, USA. [9]McGovern Institute for Brain Research, Massachusetts Institute of Technology, Cambridge, MA, USA. [10]Department of Brain and Cognitive Sciences, Massachusetts Institute of Technology, Cambridge, MA, USA. [11]Department of Biological Engineering, Massachusetts Institute of Technology, Cambridge, MA, USA. [12]Department of Neurology, University of Missouri, Columbia, MO, USA. [13]Department of Orthopaedic Surgery, Duke University Medical Center, Durham, NC, USA.
***Corresponding author. E-mail: charles.gersbach@duke.edu**

23 from the genomic DNA would restore dystrophin expression and improve muscle function (Fig. 1A).

We used AAV serotype 8 (AAV8) as a vector for delivery and expression of the components of the CRISPR-Cas9 system to skeletal and cardiac muscle (*32*). Owing to the packaging size restrictions of AAV (~4.7 kb), we used the 3.2-kb *Staphylococcus aureus* Cas9 (SaCas9) cDNA that was recently

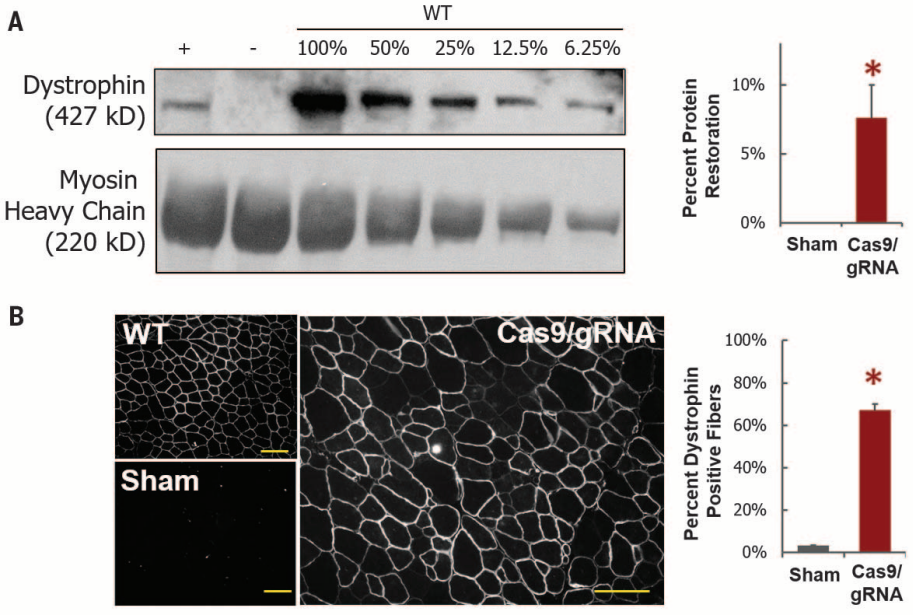

Fig. 2. In vivo genome editing restores dystrophin protein expression. (**A**) Western blot for dystrophin shows recovery of dystrophin expression (+, AAV-injected muscle; -, contralateral muscle). Comparison to protein from wild-type (WT) mice indicates restored dystrophin is ~8% of normal amounts (n = 6 muscles, mean + SEM). (**B**) Dystrophin immunofluorescence staining shows abundant (67%) dystrophin-positive fibers in Cas9-gRNA–treated groups (scale bar, 100 μm; n = 7 muscles, mean + SEM). Asterisk, significantly different from the sham group (P < 0.05).

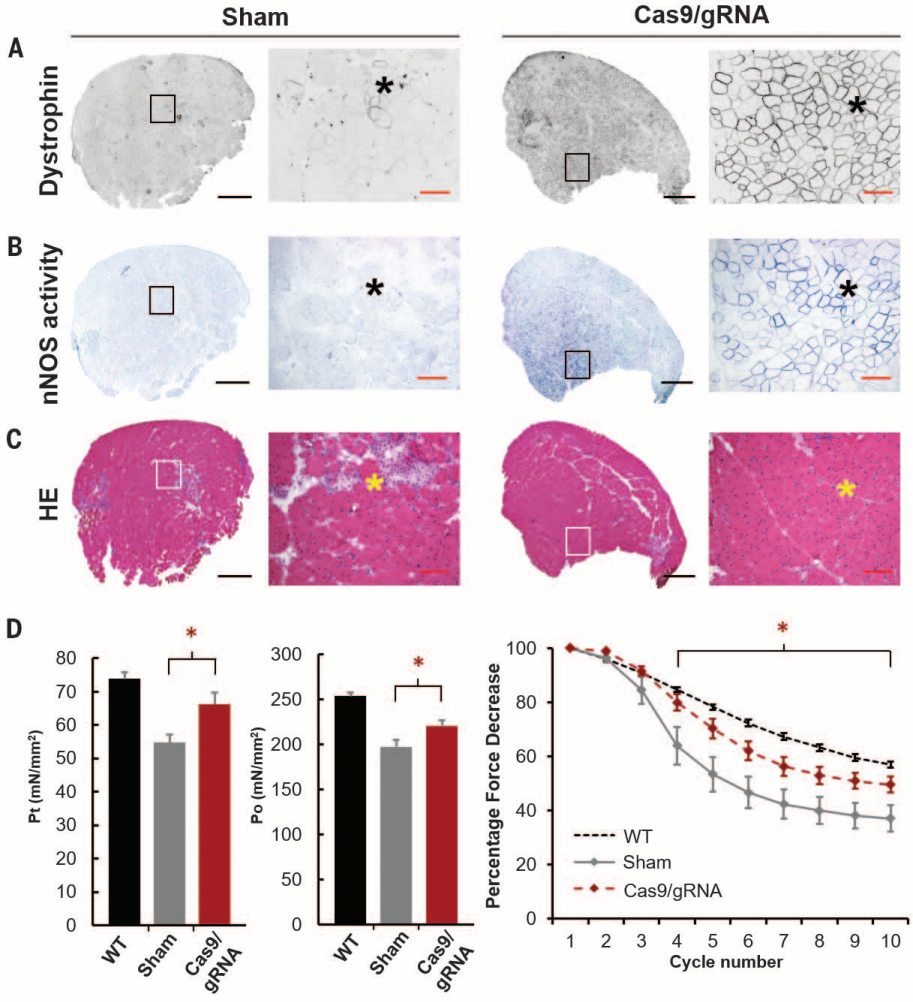

Fig. 3. CRISPR-Cas9 gene editing restores nNOS activity and improves muscle function. (**A**) Whole-muscle transverse sections show abundant dystrophin expression throughout the tibialis anterior muscle. (**B**) Staining of serial sections shows recruitment and activity of nNOS in a pattern similar to that of dystrophin expression. (**C**) H&E staining shows no obvious adverse response to the AAV-Cas9 treatment. Additionally, there is reduced area of necrotic fibers. Scale bars: 600 μm (full-view images); 100 μm (high-power images). For panels A to C, asterisk marks the same area in serial sections. (**D**) Significant improvement in specific twitch force (Pt) and tetanic force (Po), as measured by an in situ contractility assay in Cas9-gRNA–treated muscles. Treated muscles also showed significantly better resistance to damage caused by repeated cycles of eccentric contraction (n = 7 muscles, mean + SEM). Overall treatment effect by analysis of variance (P < 0.05). Asterisk, significantly different from the sham group (P < 0.05).

described for in vivo genome editing applications (*20*). A second AAV vector with two gRNA expression cassettes was also produced to express gRNAs targeted to introns 22 and 23. We expected that simultaneous DNA cleavage in both introns by Cas9-gRNA complexes would remove exon 23 from the genome and result in production of an internally truncated, but highly functional, dystrophin protein. A panel of gRNAs was designed by manual inspection for the SaCas9 protospacer adjacent motif (PAM) (5′-NNGRRT-3′) with close proximity to exon 23 and prioritized according to predicted specificity by minimizing potential off-target sites in the mouse genome. The best set of gRNAs was then selected on the basis of in vitro gene editing efficiency (fig. S1).

The Cas9 and gRNA AAV vectors were premixed in equal amounts and injected into the tibialis anterior muscle of *mdx* mice. Contralateral limbs received saline injection. At 8 weeks after injection, the muscles were harvested and analyzed for deletion of exon 23 from the genomic DNA and mRNA, and expression of dystrophin protein. End-point polymerase chain reaction (PCR) across the genomic locus revealed the expected ~1171–base pair (bp) deletion in all injected limbs (Fig. 1B). Droplet digital PCR (ddPCR) was used to quantify the percentage of modified alleles by separately amplifying the unmodified or deleted DNA templates. ddPCR showed that exon 23 was deleted in ~2% of all alleles from the whole-muscle lysate (Fig. 1C). Sanger sequencing of gel-extracted bands confirmed the deletion of exon 23 as predicted, without any additional insertions or deletions (indels) (Fig. 1B). Deep sequencing of these amplicons indicated a strong preference (~66%) for precise ligation of cut products (fig. S2). Regardless, the distribution of indels in the deletion should not affect transcript production, as the indels occur in the intronic region. Deep sequencing of gRNA target sites and the top 10 predicted off-target sites for each gRNA indicated ~3% indel formation at the target sites and low (~1%, gRNA1-OT8) or undetectable off-target gene editing at the predicted off-target sites (tables S2 and S3 and fig. S3).

Reverse transcriptase (RT)–PCR of mRNA extracted from muscle lysates showed a fraction of transcripts without exon 23 (Fig. 1D). Quantitative ddPCR of the cDNA also showed significant editing of the mRNA transcript, with exon 23 excluded in 59% of transcripts (Fig. 1E). The high frequency of mRNA modification is likely due to protection of the Δ23 transcripts from nonsense-mediated decay. This is supported by an increase in total dystrophin mRNA from 5% of wild-type mRNA levels in nontreated muscles to 12% in Cas9-gRNA–treated muscles (fig. S4).

Western blot of whole-muscle lysates showed substantial recovery of dystrophin protein to ~8% of wild-type levels (Fig. 2A). By immunostaining, ~67% of myofibers expressed dystrophin (Figs. 2B and 3A). Immunofluorescence staining also confirmed Cas9 expression in myonuclei (fig. S5). Collectively, the molecular analyses of genomic deletion, exon removal from the transcript, and abundant protein expression validated CRISPR-mediated restoration of a near–full-length dystrophin protein to amounts above the established benchmarks for functional recovery and therapeutic benefit. In particular, it is reported that as little as 4% of normal dystrophin expression level is sufficient to improve muscle function (*33*, *34*), and human natural history studies show that 30% protein expression may be sufficient for a completely asymptomatic phenotype (*35*). Therefore, we evaluated therapeutic benefit in CRISPR-treated *mdx* mice. We first examined sarcolemmal neuronal nitric oxide synthase (nNOS) localization. nNOS is absent in the sarcolemma of the *mdx* mouse and DMD patients, owing to the loss of the nNOS-binding site in spectrin repeats 16 and 17 in the dystrophin protein (*36*, *37*). The mislocalization of nNOS contributes to DMD pathogenesis (*36*, *37*). In CRISPR-treated muscles, nNOS activity was restored at the sarcolemma, closely mirroring dystrophin staining in serial sections (Fig. 3, A and B) and resembling that of wild-type muscle (fig. S6).

Dystrophin assembles a series of transmembrane and cytosolic proteins into the dystrophin-associated glycoprotein complex (DGC) to link the cytoskeleton and the extracellular matrix (*1*). In *mdx* mice and DMD patients, these proteins are mislocalized. Immunostaining of serial muscle sections showed recovery of DGC proteins in Cas9-gRNA–treated muscles, but not the contralateral controls (figs. S7 to S9). Histological examination showed improved overall morphology of CRISPR-Cas9–treated muscles (Fig. 3C and fig. S10). The number of infiltrating macrophages and neutrophils was substantially decreased in treated muscle, indicating a reduction of the inflammation typical of dystrophic muscle (fig. S11). Hematoxylin and eosin (H&E) staining of serial sections showed no obvious toxicity in response to the vector or transgene in this study (Fig. 3C). However, potential immune responses to the AAV capsid, Cas9, and dystrophin are important subjects for future studies (*7*, *38*–*40*).

Next, we assessed muscle function. The specific twitch (Pt) and tetanic (Po) force were significantly improved in Cas9-gRNA–treated muscle ($^*P < 0.05$, Fig. 3D). Treated muscles showed significantly improved resistance to eccentric contraction injury, maintaining 50% of the initial force relative to 37% in untreated muscle ($^*P < 0.05$ at marked cycles, Fig. 3D). Further, pathologic hypertrophy was mitigated in Cas9-gRNA–treated muscle (table S4). Collectively, these results show that CRISPR-Cas9–mediated dystrophin restoration improved muscle structure and function.

To assess the effects of dystrophin restoration early in life, we performed intraperitoneal injections of the AAV vector into postnatal day 2 (P2) neonatal mice. This led to recovered dystrophin expression in abdominal muscles, diaphragm, and heart at 7 weeks after injection (figs. S12 and S13). Notably, these muscles are responsible for cardiac and pulmonary health, which are severely weakened and responsible for the premature death of DMD patients. Finally, intravenous administration of AAV vectors in 6-week-old adult *mdx* showed substantial recovery of dystrophin in the cardiac muscle (Fig. 4). Efficient correction in cardiac tissues will be an important end-point to prevent premature death of DMD patients.

In this study, we have demonstrated the therapeutic benefit of AAV-mediated CRISPR-Cas9 genome editing in an adult mouse model of DMD. Our results include correction in a single muscle following local delivery and in the heart following intravenous delivery to neonatal and adult mice. As systemic delivery of AAV vectors to skeletal and cardiac tissue is well established, we expect

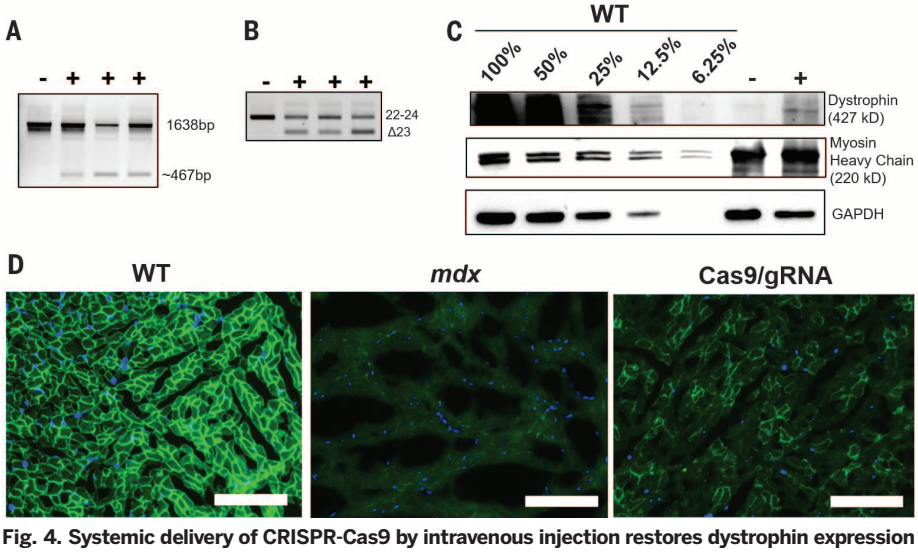

Fig. 4. Systemic delivery of CRISPR-Cas9 by intravenous injection restores dystrophin expression in adult *mdx* mouse cardiac muscle. (**A**) PCR across the deletion region in the genomic DNA from cardiac tissues shows the smaller-deletion PCR product in all treated mice. (**B**) RT-PCR across exons 22 and 24 of dystrophin cDNA from cardiac tissue shows a smaller band that does not include exon 23 in treated mice. (**C**) Western blot for dystrophin in protein lysates from cardiac tissue shows recovery of dystrophin expression (+, AAV-injected mice; -, saline injected controls). (**D**) Dystrophin immunofluorescence staining shows dystrophin recovery in cardiomyocytes. Scale bar, 100 μm.

this approach to confer body-wide therapeutic benefits. The accompanying articles from Wagers and colleagues (*41*) and Olson and colleagues (*42*) adopt a similar approach to CRISPR-Cas9–based correction of dystrophic mice using delivery with AAV9, demonstrating generality across muscle-tropic AAV serotypes. Moreover, the Wagers group's demonstration of efficient editing of Pax7-positive muscle satellite cells (*41*) suggests that gene correction may improve as the mature muscle fibers are populated with the progeny of these progenitor cells, as was observed in mosaic mice generated by CRISPR-Cas9 delivery to single-cell zygotes (*27*). Indeed, we have observed that dystrophin restoration by genome editing is maintained for at least 6 months after treatment (fig. S14).

Continued optimization of vector design will be important for potential clinical translation of this approach, including evaluation of various AAV capsids and tissue-specific promoters. Additionally, although dual-vector administration has been effective in body-wide correction of animal models of DMD (*43*), optimization to engineer a single-vector approach may increase efficacy and translatability. These three studies (*41*, *42*) establish a strategy for gene correction by a single-gene editing treatment that has the potential to achieve effects similar to those seen with weekly administration of exon-skipping therapies (*8*, *9*, *30*, *31*). More broadly, this work establishes CRISPR-Cas9–mediated genome editing as an effective tool for gene modification in skeletal and cardiac muscle and as a therapeutic approach to correct protein deficiencies in neuromuscular disorders and potentially many other diseases. The continued development of this technology to characterize and enhance the safety and efficacy of gene editing will help to realize its promise for treating genetic disease.

REFERENCES AND NOTES

1. R. J. Fairclough, M. J. Wood, K. E. Davies, *Nat. Rev. Genet.* **14**, 373–378 (2013).
2. E. P. Hoffman, R. H. Brown Jr., L. M. Kunkel, *Cell* **51**, 919–928 (1987).
3. S. B. England *et al.*, *Nature* **343**, 180–182 (1990).
4. B. Wang, J. Li, X. Xiao, *Proc. Natl. Acad. Sci. U.S.A.* **97**, 13714–13719 (2000).
5. S. Q. Harper *et al.*, *Nat. Med.* **8**, 253–261 (2002).
6. J. H. Shin *et al.*, *Mol. Ther.* **21**, 750–757 (2013).
7. J. R. Mendell *et al.*, *N. Engl. J. Med.* **363**, 1429–1437 (2010).
8. S. Cirak *et al.*, *Lancet* **378**, 595–605 (2011).
9. N. M. Goemans *et al.*, *N. Engl. J. Med.* **364**, 1513–1522 (2011).
10. A. Aartsma-Rus *et al.*, *Hum. Mutat.* **30**, 293–299 (2009).
11. D. B. Cox, R. J. Platt, F. Zhang, *Nat. Med.* **21**, 121–131 (2015).
12. M. Jinek *et al.*, *Science* **337**, 816–821 (2012).
13. P. Mali *et al.*, *Science* **339**, 823–826 (2013).
14. L. Cong *et al.*, *Science* **339**, 819–823 (2013).
15. S. W. Cho, S. Kim, J. M. Kim, J. S. Kim, *Nat. Biotechnol.* **31**, 230–232 (2013).
16. M. Jinek *et al.*, *eLife* **2**, e00471 (2013).
17. H. Yin *et al.*, *Nat. Biotechnol.* **32**, 551–553 (2014).
18. L. Swiech *et al.*, *Nat. Biotechnol.* **33**, 102–106 (2015).
19. R. J. Platt *et al.*, *Cell* **159**, 440–455 (2014).
20. F. A. Ran *et al.*, *Nature* **520**, 186–191 (2015).
21. D. G. Ousterout *et al.*, *Nat. Commun.* **6**, 6244 (2015).
22. D. G. Ousterout *et al.*, *Mol. Ther.* **21**, 1718–1726 (2013).
23. L. Popplewell *et al.*, *Hum. Gene Ther.* **24**, 692–701 (2013).
24. D. G. Ousterout *et al.*, *Mol. Ther.* **23**, 523–532 (2015).
25. H. L. Li *et al.*, *Stem Cell Rev.* **4**, 143–154 (2015).
26. P. Chapdelaine, C. Pichavant, J. Rousseau, F. Pâques, J. P. Tremblay, *Gene Ther.* **17**, 846–858 (2010).
27. C. Long *et al.*, *Science* **345**, 1184–1188 (2014).
28. L. Xu *et al.*, *Mol. Ther.* 10.1038/mt.2015.192 (2015).
29. P. Sicinski *et al.*, *Science* **244**, 1578–1580 (1989).
30. C. J. Mann *et al.*, *Proc. Natl. Acad. Sci. U.S.A.* **98**, 42–47 (2001).
31. A. Goyenvalle *et al.*, *Nat. Med.* **21**, 270–275 (2015).
32. Z. Wang *et al.*, *Nat. Biotechnol.* **23**, 321–328 (2005).
33. D. Li, Y. Yue, D. Duan, *PLOS ONE* **5**, e15286 (2010).
34. M. van Putten *et al.*, *FASEB J.* **27**, 2484–2495 (2013).
35. M. Neri *et al.*, *Neuromuscul. Disord.* **17**, 913–918 (2007).
36. Y. M. Kobayashi *et al.*, *Nature* **456**, 511–515 (2008).
37. Y. Lai *et al.*, *J. Clin. Invest.* **119**, 624–635 (2009).
38. S. Al-Zaidy, L. Rodino-Klapac, J. R. Mendell, *Pediatr. Neurol.* **51**, 607–618 (2014).
39. D. Wang *et al.*, *Hum. Gene Ther.* **26**, 432–442 (2015).
40. F. Mingozzi, K. A. High, *Blood* **122**, 23–36 (2013).
41. M. Tabebordbar *et al.*, *Science* **351**, 407–411 (2016).
42. C. Long *et al.*, *Science* **351**, 400–403 (2016).
43. Y. Lai *et al.*, *Nat. Biotechnol.* **23**, 1435–1439 (2005).

ACKNOWLEDGMENTS

We thank M. Gemberling, T. Reddy, W. Majoros, F. Guilak, K. Zhang and Y. Yue for technical assistance and X. Xiao and E. Smith for helpful discussion. This work was supported by the Muscular Dystrophy Association (MDA277360), a Duke-Coulter Translational Partnership Grant, a Hartwell Foundation Individual Biomedical Research Award, a March of Dimes Foundation Basil O'Connor Starter Scholar Award, and an NIH Director's New Innovator Award (DP2-OD008586) to C.A.G., as well as a Duke/UNC–Chapel Hill CTSA Consortium Collaborative Translational Research Award to C.A.G. and A.A. F.Z. is supported by an NIH Director's Pioneer Award (DP1-MH100706); NIH grant R01DK097768; a Waterman Award from the NSF; the Keck, Damon Runyon, Searle Scholars, Merkin Family, Vallee, Simons, Paul G. Allen, and the New York Stem Cell Foundations; and by Bob Metcalfe. A.A. is supported by NIH grants R01HL089221 and P01HL112761. D.D. is supported by NIH grant R01NS90634 and the Hope for Javier Foundation. C.E.N. is supported by a Hartwell Foundation Postdoctoral Fellowship. P.I.T. was supported by an American Heart Association Predoctoral Fellowship. W.X.Y. is supported by T32GM007753 from the National Institute of General Medical Sciences and a Paul and Daisy Soros Fellowship. F.A.R. is a Junior Fellow at the Harvard Society of Fellows. The SaCas9 gene is openly available through Addgene via a Uniform Biological Material Transfer Agreement. C.A.G., D.G.O., and P.I.T. are inventors on a patent application filed by Duke University related to genome editing for Duchenne muscular dystrophy (WO 2014/197748). F.Z. and F.A.R. are inventors on patents filed by the Broad Institute related to SaCas9 materials (U.S. patents 8,865,406 and 8,906,616 and accepted EP 2898075, from International patent application WO 2014/093635). C.A.G. is a scientific advisor to Editas Medicine, a company engaged in development of therapeutic genome editing. F.Z. is a founder of Editas Medicine and scientific advisor for Editas Medicine and Horizon Discovery. D.D. is a member of the scientific advisory board for Solid GT, a subsidiary of Solid Biosciences.

SUPPLEMENTARY MATERIALS

www.sciencemag.org/content/351/6271/403/suppl/DC1
Materials and Methods
Figs. S1 to S22
Tables S1 to S4
References (*44*–*48*)

24 September 2015; accepted 7 December 2015
Published online 31 December 2015
10.1126/science.aad5143

GENE EDITING

In vivo gene editing in dystrophic mouse muscle and muscle stem cells

Mohammadsharif Tabebordbar,[1,2]* Kexian Zhu,[1,3]* Jason K. W. Cheng,[1] Wei Leong Chew,[2,4] Jeffrey J. Widrick,[5] Winston X. Yan,[6,7] Claire Maesner,[1] Elizabeth Y. Wu,[1]† Ru Xiao,[8] F. Ann Ran,[6,7] Le Cong,[6,7] Feng Zhang,[6,7] Luk H. Vandenberghe,[8] George M. Church,[4] Amy J. Wagers[1]‡

Frame-disrupting mutations in the *DMD* gene, encoding dystrophin, compromise myofiber integrity and drive muscle deterioration in Duchenne muscular dystrophy (DMD). Removing one or more exons from the mutated transcript can produce an in-frame mRNA and a truncated, but still functional, protein. In this study, we developed and tested a direct gene-editing approach to induce exon deletion and recover dystrophin expression in the *mdx* mouse model of DMD. Delivery by adeno-associated virus (AAV) of clustered regularly interspaced short palindromic repeats (CRISPR)–Cas9 endonucleases coupled with paired guide RNAs flanking the mutated *Dmd* exon23 resulted in excision of intervening DNA and restored the *Dmd* reading frame in myofibers, cardiomyocytes, and muscle stem cells after local or systemic delivery. AAV-*Dmd* CRISPR treatment partially recovered muscle functional deficiencies and generated a pool of endogenously corrected myogenic precursors in *mdx* mouse muscle.

Duchenne muscular dystrophy (DMD) is a progressive muscle degenerative disease caused by point mutations, deletions, or duplications in the *DMD* gene that cause genetic frame-shift or loss of protein expression (*1*). Efforts under development to reverse the pathological consequences of DYSTROPHIN deficiency in DMD aim to restore its biological function through viral-mediated delivery of genes encoding shortened forms of the protein, up-regulation of compensatory proteins, or interference with the splicing machinery to "skip" mutation-carrying or mutation-adjacent exons in the mRNA and produce a truncated, but still functional, protein [reviewed in (*2*)].

The potential efficacy of exon-skipping strategies is supported by the relatively mild disease course of Becker muscular dystrophy (BMD) patients with in-frame deletions in *DMD* (*3*, *4*), and by the capacity of antisense oligonucleotides (AONs), which mask splice donor or acceptor sequences surrounding mutated exons in *DMD*

mRNA, to restore biologically active DYSTROPHIN protein in mice (*5*, *6*) and humans (*7*, *8*). Yet limitations remain for the use of AONs, including variable efficiencies of tissue uptake, depending on antisense oligonucleotide (AON) chemistry, a requirement for repeated AON injection to maintain effective skipping, and the potential for AON-associated toxicities [(*9*, *10*) and supplementary text].

Here, we sought to address these limitations by developing a one-time, multisystemic approach based on the genome-editing capabilities of the clustered regularly interspaced short palindromic repeats (CRISPR)–Cas9 system. This system, originally coopted from *Streptococcus pyogenes* (Sp), couples a DNA double-strand endonuclease with short "guide" RNAs (gRNAs) that provide target specificity to any site in the genome that also contains an adjacent "NGG" protospacer-adjacent motif (PAM) (*11*–*14*), which enables targeted gene disruption, replacement, and modification.

To apply CRISPR/Cas9 for exon deletion in DMD, we first established a reporter system for CRISPR activity by "repurposing" the existing Ai9 mouse reporter allele, which encodes the fluorescent tdTomato protein downstream of a ubiquitous CAGGS promoter and "floxed" STOP cassette (*15*, *16*) (fig. S1A). Exposure to SpCas9, together with paired gRNAs targeting near the Ai9 loxP sites (hereafter, Ai9 gRNAs), resulted in excision of intervening DNA and expression of tdTomato (fig. S1, A, B, and E). We next designed and tested paired gRNAs (hereafter, *Dmd*23 gRNAs) (fig. S1C) that were directed 5′ and 3′ of mouse *Dmd* exon 23, which in *mdx* mice carries a nonsense mutation that destabilizes *Dmd* mRNA and disrupts DYSTROPHIN expression (*17*). Finally, we coupled the paired *Dmd*23 and Ai9 gRNAs using a two-plasmid system that links expression of the CRISPR activity reporter (tdTomato) to genome editing events at the *Dmd* locus (fig. S1D). In vitro transfection of primary satellite cells from *mdx* mice carrying the Ai9 allele (hereafter, *mdx;Ai9* mice) with SpCas9 + Ai9-*Dmd*23 coupled gRNAs induced gene editing at both the Ai9 locus, demonstrated by tdTomato expression (fig. S1E), and *Dmd* locus, detected by genomic polymerase chain reaction (PCR) (Fig. 1A) and confirmed by amplicon sequencing (fig. S1F). *Dmd* editing was not detected in *mdx;Ai9* cells receiving Ai9 gRNAs alone (Fig. 1A), although tdTomato expression was equivalently induced (fig. S1E).

In order to confirm that CRISPR-mediated *Dmd* editing results in irreversible genomic modification and production of exon-deleted mRNA and protein, primary satellite cells from *mdx;Ai9* mice were cotransfected with SpCas9 + Ai9 or Ai9-*Dmd*23 gRNAs, isolated by fluorescence-activated cell sorting (FACS) on the basis of tdTomato expression, expanded in vitro (*18*), and differentiated to myotubes. Reverse transcription–PCR (RT-PCR) (Fig. 1B) and amplicon sequencing (fig. S1G) from these myotubes detected exon 23–deleted *Dmd* mRNA in cells receiving Ai9-*Dmd*23–coupled gRNAs but not in cells receiving only Ai9 gRNAs. TaqMan analysis (*9*) further indicated that exon 23–deleted transcripts represented 24 to 47% of total *Dmd* mRNA in cells receiving Ai9-*Dmd*23–coupled gRNAs, whereas exon 23 deletion was undetectable with Ai9 gRNAs alone (fig. S1H). DYSTROPHIN protein expression was also restored in CRISPR-modified *mdx;Ai9* cells, as detected by Western blot of in vitro differentiated myotubes (Fig. 1C) and immunostaining of muscle sections from *mdx* mice transplanted with gene-edited *mdx;Ai9* satellite cells (Fig. 1D and fig. S1I). These data demonstrate that CRISPR/Cas9 can direct sequence-specific modification of disease alleles in primary muscle stem cells that retain muscle engraftment capacity.

We next adapted CRISPR for delivery by means of AAV, using the smaller Cas9 ortholog from *Staphylococcus aureus* (SaCas9), which can be packaged in AAV and programmed to target any locus in the genome containing an "NNGRR" PAM sequence (*19*). We generated Sa gRNAs targeting Ai9 and introduced several base modifications into the gRNA scaffold to enhance gene targeting by SaCas9 (fig. S2, A to C). Using this modified scaffold, we tested *Dmd*23 Sa gRNAs (fig. S2D) and produced AAVs encoding SaCas9 and Ai9 Sa gRNAs or *Dmd*23 Sa gRNAs in a dual (fig. S3A) or single (fig. S3B) vector system. Comparison of exon 23 excision efficiencies in transduced *mdx* myotubes demonstrated more efficient excision by dual AAV-CRISPR (fig. S3, C and D), as compared with single vector AAVs. Therefore, to test the potential for in vivo *Dmd* targeting by CRISPR/Cas9, we pseudotyped dual AAVs (AAV-SaCas9 + AAV-Ai9 gRNAs; hereafter, AAV-Ai9 CRISPR) to serotype 9, which exhibits robust transduction of mouse skeletal and cardiac muscle (*20*), and injected these AAVs into the tibialis anterior (TA) muscles of *mdx;Ai9* mice (7.5E+11 vg each). Four weeks later, muscles were harvested to assess genome-editing events. TdTomato fluorescence was detected in muscles injected with AAV-Ai9 CRISPR but not in muscles injected with vehicle alone (fig. S4A). Codelivery of AAV9-SaCas9 + AAV9-*Dmd*23 gRNAs (hereafter,

[1]Department of Stem Cell and Regenerative Biology, Harvard University, and Harvard Stem Cell Institute, Cambridge, MA 02138, USA. [2]Biological and Biomedical Sciences Program, Harvard Medical School, Boston, MA 02115, USA. [3]Department of Molecular and Cellular Biology, Harvard University, Cambridge, MA 02138, USA. [4]Department of Genetics, Harvard Medical School, Boston, MA 02115, USA. [5]Division of Genetics and Program in Genomics, Boston Children's Hospital, Harvard Medical School, Boston, MA 02115, USA. [6]Broad Institute of MIT and Harvard, Cambridge, MA 02142, USA. [7]McGovern Institute for Brain Research, Department of Brain and Cognitive Science, and Department of Biological Engineering, Massachusetts Institute of Technology, Cambridge, MA 02139, USA. [8]Grousbeck Gene Therapy Center, Schepens Eye Research Institute, and Massachusetts Eye and Ear Infirmary, 20 Staniford Street, Boston, MA 02114, USA.
*These authors contributed equally to this work. †Present address: RaNA Therapeutics, 200 Sidney Street, Suite 310, Cambridge, MA 02139, USA. **‡Corresponding author. E-mail: amy_wagers@harvard.edu**

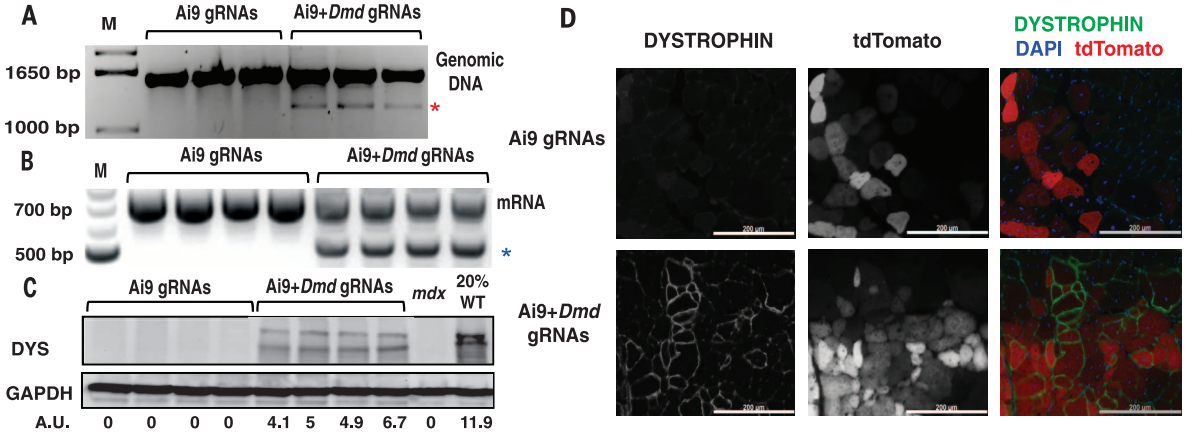

Fig. 1. DYSTROPHIN expression in CRISPR-modified dystrophic satellite cells. (**A**) Detection of exon 23 excision by genomic PCR in myotubes derived from satellite cells transfected with SpCas9 and Ai9 gRNAs (left lanes) or coupled Ai9-*Dmd*23 gRNAs (right lanes). Unedited genomic product, 1572 base pair (bp); gene-edited product (red asterisk), 1189 bp. M, molecular size marker. (**B**) RT-PCR detection of exon 23–deleted mRNA. Unedited RT-PCR product, 738 bp; exon 23–deleted product (blue asterisk), 525 bp. (**C**) Western blot detecting DYSTROPHIN in myotubes derived from gene-edited satellite cells. A.U., arbitrary unit, normalized to glyceraldehyde-3-phosphate dehydrogenase (GAPDH) (loading control). DYS, DYSTROPHIN; WT, wild type. (**D**) DYSTROPHIN immunofluorescence in *mdx* muscles transplanted with satellite cells transfected in vitro with SpCas9 + Ai9 gRNAs (top) or SpCas9 + Ai9-*Dmd*23–coupled gRNAs (bottom). For merge: green, DYSTROPHIN; red, tdTomato; blue, 4′,6′-diamidino-2-phenylindole (DAPI) (nuclei). Scale bar, 200 μm. See also fig. S1.

AAV-*Dmd* CRISPR) likewise yielded robust and specific modification of the *Dmd* locus in TA muscles in vivo. Genomic PCR (Fig. 2A) and Sanger sequencing (fig. S4B) demonstrated exon 23 excision in muscles injected with AAV-*Dmd* CRISPR but not AAV-Ai9 CRISPR. Next-generation sequencing indicated minimal activity at the predicted highest-ranking genomic off-target sites (fig. S12). RT-PCR (Fig. 2B) and sequencing (fig. S4C) further confirmed the presence of exon 23–deleted *Dmd* mRNA in muscles receiving AAV-*Dmd* CRISPR, with an average exon 23 excision rate of 39% ±1.8% (fig. S3E). In vivo CRISPR-mediated targeting of *Dmd* exon 23–restored DYSTROPHIN expression in skeletal muscle, as detected by Western blot (Fig. 2C), immunofluorescence (Fig. 2D), and capillary immunoassay (fig. S5A). Other pathological hallmarks of dystrophy were also restored in AAV-*Dmd* CRISPR–injected muscles, including sarcolemmal localization of the multimeric dystrophin-glycoprotein complex and neuronal nitric-oxide synthase (figs. S6 and S7). In contrast, DYSTROPHIN expression was undetectable by Western blot (Fig. 2C) and present only on rare revertant fibers in *mdx;Ai9* mice receiving control AAV-Ai9 CRISPR (Fig. 2D) (*21*). Finally, to evaluate the functional consequences of CRISPR-mediated induction of exon 23–deleted DYSTROPHIN, we subjected a subset of *mdx;Ai9* mice injected intramuscularly with AAV-*Dmd* CRISPR to in situ muscle force assessment. Muscles receiving AAV-*Dmd* CRISPR showed significantly increased specific force (Fig. 2E) and attenuated force drop after eccentric damage (Fig. 2F), as compared with contralateral, vehicle-injected muscles and also AAV-Ai9 CRISPR injected muscles. In contrast, differences in specific force (Fig. 2E) and force drop (Fig. 2F) for AAV-Ai9 CRISPR injected mice did not vary significantly between the virus-injected and vehicle-injected muscles.

We next evaluated the potential for multisystemic gene editing in vivo using AAV-CRISPR. Dual AAV-Ai9 CRISPR vectors (1.5E+12 vg each) were coinjected intraperitoneally into *mdx;Ai9* mice at postnatal day 3 (P3). Three weeks later, widespread tdTomato expression was detected in all cardiac and skeletal muscles analyzed (fig. S8A). Parallel injections of *mdx;Ai9* mice with AAV-*Dmd* CRISPR revealed exon 23–deleted transcripts in multiple skeletal muscles and cardiac muscle, with targeting levels varying from 3 to 18% in different muscle groups (Fig. 3A and fig. S3F). Exon 23 was not excised in animals receiving AAV-Ai9 CRISPR instead (Fig. 3A, and figs. S3F and S8B). Finally, Western blot (Fig. 3B and fig. S8C), immunofluorescence (Fig. 3C), and capillary immunoassay (fig. S5B) confirmed that DYSTROPHIN protein was largely absent in muscles of control *mdx;Ai9* mice receiving AAV-Ai9 CRISPR and was restored in mice receiving AAV-*Dmd* CRISPR. Similar systemic dissemination of AAV and excision of exon 23 in multiple organs were seen in two adult mice injected intravenously with AAV-*Dmd* CRISPR at 6 weeks of age (fig. S9).

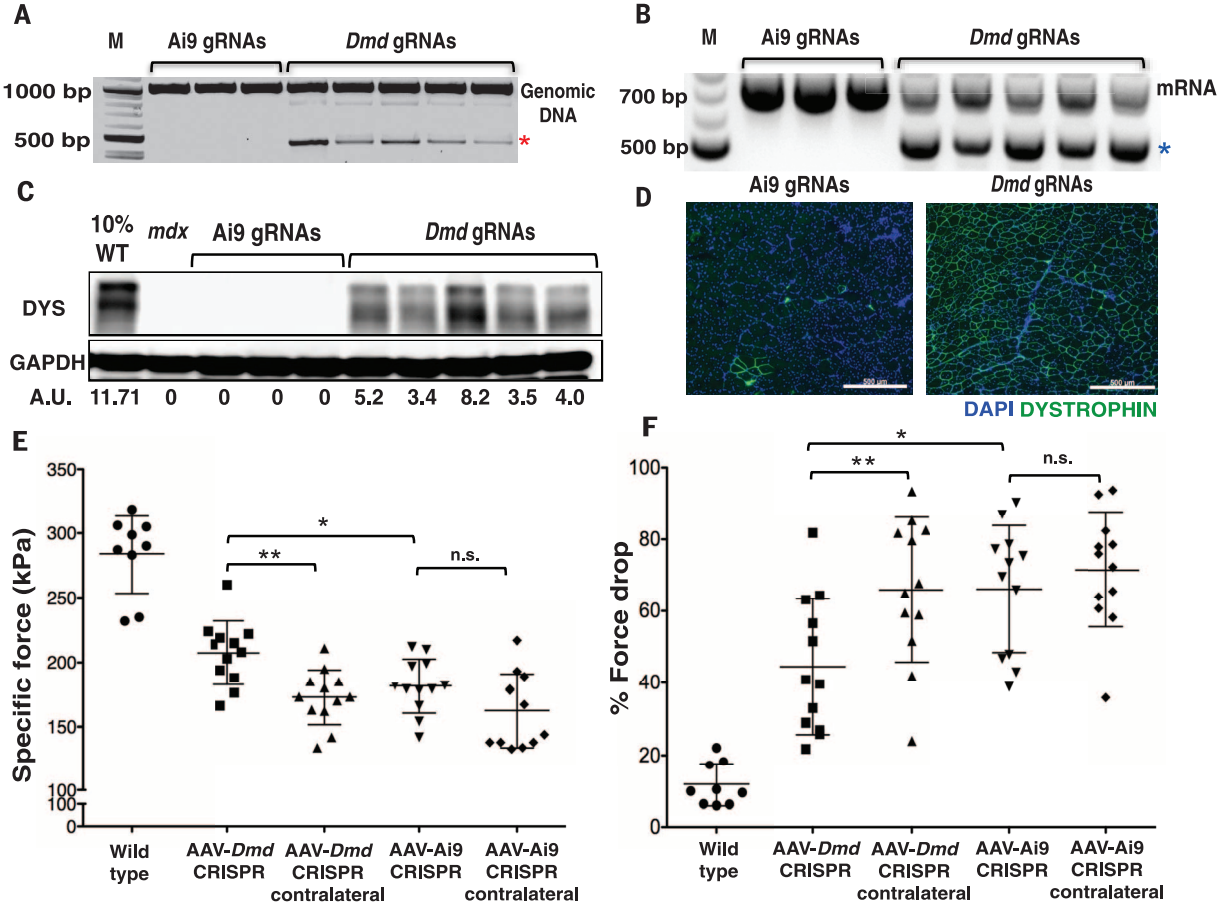

Fig. 2. AAV-CRISPR enables in vivo excision of *Dmd* exon 23 and restores DYSTROPHIN expression in adult dystrophic muscle. (**A** and **B**) Detection of exon 23 excision in TA muscles from *mdx;Ai9* mice injected intramuscularly with AAV-Ai9 CRISPR (left lanes) or AAV-*Dmd* CRISPR (right lanes) by genomic PCR (A). Unedited product, 1012 bp; exon-excised product, 470 bp; and RT-PCR (B). Asterisks mark gene-edited bands. M, molecular size marker. (**C**) Western blot detecting DYSTROPHIN in muscles injected with AAV-Ai9 CRISPR (left) or AAV-*Dmd* CRISPR (right), with relative signal intensity determined by densitometry at bottom. A.U., arbitrary unit, normalized to GAPDH. (**D**) Representative immunofluorescence images for DYSTROPHIN (green) and DAPI (blue) in *mdx;Ai9* muscles injected with AAV-Ai9 (left) or AAV-*Dmd* (right) CRISPR. Scale bar, 500 μm. (**E** and **F**) Muscle-specific force (E) and decrease in force after eccentric damage (F) for wild-type mice injected with vehicle (n = 9), *mdx;Ai9* mice injected with AAV-*Dmd* CRISPR in the right TA and vehicle in the left TA (n = 12), or *mdx;Ai9* mice injected with AAV-Ai9 CRISPR in the right TA and vehicle in the left TA (n = 12). *P < 0.05, **P < 0.01, n.s., not significant, one-way analysis of variance (ANOVA) with Newman-Keuls multiple comparisons test.

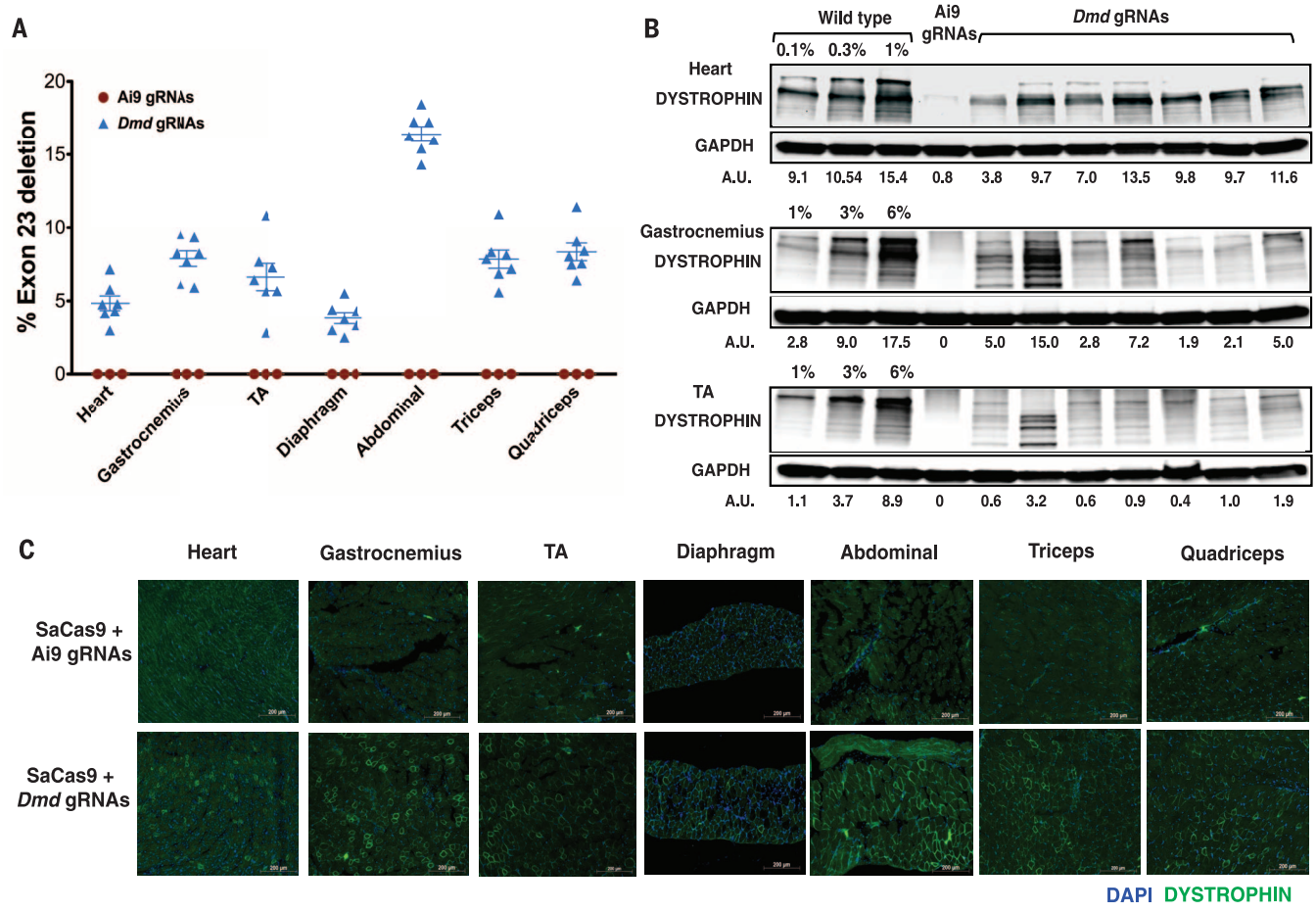

Fig. 3. Systemic dissemination of AAV-CRISPR targets *Dmd* exon 23 and restores DYSTROPHIN in dystrophic cardiac and skeletal muscles. (**A**) Exon 23–deleted transcripts in muscles quantified by TaqMan quantitative RT-PCR. Data plotted for individual mice [$n = 7$ receiving AAV-*Dmd* CRISPR (blue) and $n = 3$ receiving AAV-Ai9 CRISPR (red)] and overlaid with mean ± SEM. (**B**) Western blots detecting DYSTROPHIN in the indicated muscles of *mdx;Ai9* mice receiving systemic AAV-CRISPR. Right lanes correspond to muscles from seven different mice injected intraperitoneally with AAV-*Dmd* CRISPR. Relative signal intensity, determined by densitometry, presented as A.U., arbitrary unit normalized to GAPDH. (**C**) Representative immunofluorescence staining for DYSTROPHIN (green) in *mdx;Ai9* mice injected with AAV-Ai9 (top) or AAV-*Dmd* (bottom) CRISPR. Blue, DAPI (nuclei). Scale bar, 200 μm.

Dystrophic pathology and other muscle injuries activate muscle stem cells (also known as satellite cells), which leads to regenerative responses that add new nuclei to damaged fibers [(*2*) and supplementary text]. To evaluate AAV-CRISPR gene editing in satellite cells in vivo, we crossed *mdx;Ai9* mice with Pax7-ZsGreen animals, in which satellite cells are specifically marked by green fluorescence (*22*), and we injected these animals intramuscularly or systemically with AAV9 encoding Cre (hereafter, AAV-Cre) or Ai9-CRISPR components. Muscles were harvested 2 weeks later (Fig. 4A) and analyzed by FACS. TdTomato expression was apparent in Pax7-ZsGreen+ satellite cells after local or systemic delivery of AAV-Cre or AAV-Ai9 CRISPR (Fig. 4B and fig. S10, A to C), although excision rates were lower for AAV-Ai9 CRISPR than for AAV-Cre. In vitro differentiation of ZsGreen+ satellite cells from mice receiving intramuscular or systemic AAV-Cre or AAV-Ai9 CRISPR produced tdTomato+ myotubes, demonstrating preservation of myogenic potential in AAV-transduced and gene-edited satellite cells (Fig. 4C and fig. S10D). TdTomato+ gene–edited satellite cells also engrafted recipient *mdx* muscle and contributed to in vivo muscle regeneration after transplantation (fig. S10E).

We next analyzed *Dmd* editing in Pax7-ZsGreen+ satellite cells after intramuscular or systemic delivery of AAV-*Dmd* CRISPR or AAV-Ai9 CRISPR. Satellite cells were isolated by FACS, expanded, and differentiated in vitro (Fig. 4A). RT-PCR revealed a truncated *Dmd* transcript of the expected size and sequence for gene-edited *Dmd* in satellite cell–derived myotubes from many of the AAV-*Dmd* CRISPR-injected muscles but none of the AAV-Ai9 CRISPR-injected muscles (Fig. 4D and fig. S10, F, H, and I). Quantification of exon 23 excision revealed variable efficiencies (fig. S10, G and J), which likely reflected targeting of only a subset of endogenous satellite cells that may be variably represented among the isolated and cultured cells. Finally, genomic PCR and amplicon sequencing confirmed targeted excision at the *Dmd* locus in satellite cell–derived myotubes (fig. S10K), and capillary immunoassay analysis revealed restored DYSTROPHIN expression (fig. S10L). As expected, injection of AAV-*Dmd* CRISPR did not induce tdTomato expression in satellite cells or myofibers of *mdx;Ai9* mice (fig. S11).

In summary, this study provides proof-of-concept evidence supporting the efficacy of in vivo genome editing to correct disruptive mutations in DMD in a relevant dystrophic mouse model. We show that programmable CRISPR complexes can be delivered locally and systemically to terminally differentiated skeletal muscle fibers and cardiomyocytes, as well as muscle satellite cells, in neonatal and adult mice, where they mediate targeted gene modification, restore DYSTROPHIN expression, and partially recover functional deficiencies of dystrophic muscle. As prior studies in mice and humans indicate that DYSTROPHIN levels as low as 3 to 15% of wild type are sufficient to ameliorate pathologic symptoms in the heart and skeletal muscle (*23*–*26*) and that levels as low as 30% can suppress the dystrophic phenotype altogether (*27*), the restoration of DYSTROPHIN achieved here by one-time administration of AAV-*Dmd* CRISPR clearly encourages further evaluation and optimization of this system as a new candidate modality for the treatment of DMD (see supplementary text).

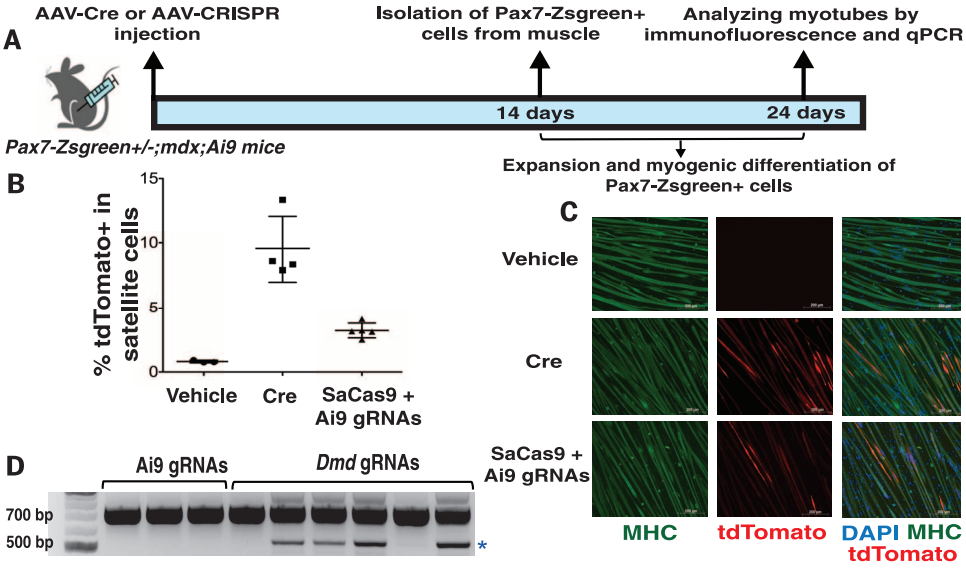

Fig. 4. Satellite cells in dystrophic muscles are transduced and targeted with systemically disseminated AAV-CRISPR. (**A**) Experimental design. (**B**) Percentage of ZsGreen+ satellite cells expressing tdTomato after intraperitoneal injection of *Pax7-ZsGreen*$^{+/-}$*;mdx;Ai9* mice. Individual data points overlaid with mean ± SD; vehicle (n = 3), AAV-Cre (n = 4), AAV-Ai9 CRISPR (n = 5). (**C**) Representative immunofluorescence of myotubes differentiated from FACS sorted satellite cells from mice injected intraperitoneally with vehicle, AAV-Cre, or AAV-Ai9 CRISPR. Green, myosin heavy chain (MHC); red, tdTomato; blue, DAPI (nuclei). Scale bar, 200 μm. (**D**) Exon 23–deleted *Dmd* mRNA in satellite cell–derived myotubes from mice previously injected intraperitoneally with AAV-*Dmd* CRISPR (right lanes), compared with control AAV-Ai9 CRISPR (left lanes).

REFERENCES AND NOTES

1. M. Koenig *et al.*, *Cell* **50**, 509–517 (1987).
2. M. Tabebordbar, E. T. Wang, A. J. Wagers, *Annu. Rev. Pathol.* **8**, 441–475 (2013).
3. A. Nakamura *et al.*, *J. Clin. Neurosci.* **15**, 757–763 (2008).
4. A. Taglia *et al.*, *Acta Myol.* **34**, 9–13 (2015).
5. Q. L. Lu *et al.*, *Nat. Med.* **9**, 1009–1014 (2003).
6. Y. Echigoya *et al.*, *Mol. Ther. Nucleic Acids* **4**, e225 (2015).
7. J. C. van Deutekom *et al.*, *N. Engl. J. Med.* **357**, 2677–2686 (2007).
8. M. Kinali *et al.*, *Lancet Neurol.* **8**, 918–928 (2009).
9. A. Goyenvalle *et al.*, *Nat. Med.* **21**, 270–275 (2015).
10. M. C. Vila *et al.*, *Skeletal Muscle* **5**, 44 (2015).
11. L. Cong *et al.*, *Science* **339**, 819–823 (2013).
12. P. Mali *et al.*, *Science* **339**, 823–826 (2013).
13. F. A. Ran *et al.*, *Nat. Protoc.* **8**, 2281–2308 (2013).
14. M. Jinek *et al.*, *Science* **337**, 816–821 (2012).
15. L. Madisen *et al.*, *Nat. Neurosci.* **13**, 133–140 (2010).
16. Materials and methods are available as supplementary materials on *Science* Online.
17. P. Sicinski *et al.*, *Science* **244**, 1578–1580 (1989).
18. C. Xu *et al.*, *Cell* **155**, 909–921 (2013).
19. F. A. Ran *et al.*, *Nature* **520**, 186–191 (2015).
20. C. Zincarelli, S. Soltys, G. Rengo, J. E. Rabinowitz, *Mol. Ther.* **16**, 1073–1080 (2008).
21. Q. L. Lu *et al.*, *J. Cell Biol.* **148**, 985–996 (2000).
22. D. Bosnakovski *et al.*, *Stem Cells* **26**, 3194–3204 (2008).
23. M. van Putten *et al.*, *J. Mol. Cell. Cardiol.* **69**, 17–23 (2014).
24. M. van Putten *et al.*, *FASEB J.* **27**, 2484–2495 (2013).
25. M. van Putten *et al.*, *PLOS ONE* **7**, e31937 (2012).
26. C. Long *et al.*, *Science* **345**, 1184–1188 (2014).
27. M. Neri *et al.*, *Neuromuscul. Disord.* **17**, 913–918 (2007).

ACKNOWLEDGMENTS

We thank the Harvard Department of Stem Cell and Regenerative Biology–Harvard Stem Cell Institute Flow Cytometry Core, the Schepens Eye Research Institute–Massachusetts Eye and Ear Institute Gene Transfer Vector Core, the Parker lab at Harvard and J. Goldstein for technical assistance. Work was funded in part by grants from Howard Hughes Medical Institute and NIH (1DP2OD004345, 5U01HL100402, and 5PN2EY018244) to A.J.W. M.T. is an Albert J. Ryan fellow. F.A.R. is a Junior Fellow at the Harvard Society of Fellows. W.X.Y. was supported by T2GM007753 from the National Institute of General Medical Sciences (NIGMS), NIH. F.Z. is a New York Stem Cell Foundation Robertson Investigator and is supported by National Institute of Mental Health, NIH (5DP1-MH100706) and National Institute of Diabetes and Digestive and Kidney Diseases, NIH (5R01DK097768-03); a Waterman Award from the NSF; the Keck, New York Stem Cell, Damon Runyon, Searle Scholars, Merkin, and Vallee Foundations; and B. Metcalfe. W.L.C. is supported by the National Science Scholarship from the Agency for Science, Technology, and Research (A*STAR), Singapore. G.M.C. is supported for this work by National Human Genome Research Institute (NIGMS), NIH, Centers of Excellence in Genomic Science, P50 HG005550. Content is solely the responsibility of the authors and does not necessarily represent the official views of NIGMS or NIH. M.T., A.J.W., W.L.C., and G.M.C. are inventors on a patent application (PCT/US15/63181) filed by Harvard University related to in vivo genetic modifications and gene editing in muscle. G.M.C. is an inventor on issued patents (US9023649 and US9074199) filed by Harvard University related to CRISPR. L.H.V. is an inventor on a patent application (US2007036760) filed by the University of Pennsylvania related to AAV capsid sequences. F.Z., L.C., F.A.R., and W.Y. are inventors on patents and patent applications (8,865,406; 8,906,616; and accepted EP 2898075, from international patent application WO 2014/093635) filed by the Broad Institute related to SaCas9-optimized components and systems. A.J.W. is an advisor for Fate Therapeutics. G.M.C and F.Z. are founders and scientific advisors of Editas Medicine, and F.Z. is a scientific advisor for Horizon Discovery. G.M.C. has equity in Caribou/Intellia, Egenesis, and Editas (for full disclosure list, see: http://arep.med.harvard.edu/gmc/tech.html). L.H.V. is cofounder, shareholder, member of the scientific advisory board, and consultant for GenSight Biologics, a consultant to Novartis and Eleven Bio, and has received honoraria and consulting fees from Regeneron Pharmaceuticals and Cowen, Jefferies, and Sectoral. AAV9 vector sequences are available through a material transfer agreement (MTA) from the University of Pennsylvania. SaCas9 plasmids are openly available through a Uniform Biological MTA from Addgene.

SUPPLEMENTARY MATERIALS

www.sciencemag.org/content/351/6271/407/suppl/DC1
Materials and Methods
Supplementary Text
Figs. S1 to S12
Tables S1 to S4
References (*28*–*54*)

23 September 2015; accepted 8 December 2015
Published online 31 December 2015
10.1126/science.aad5177

There's only one Stericup® filter.

Don't be fooled.

CAUTION:

- Sterile filters are posing as high-quality Stericup® filters, but are rather thinly disguised.
- These filters may exhibit clogging, loss of volume and unwanted binding of serum proteins and other additives.
- Victims report anxiety due to potential damage to cell health.

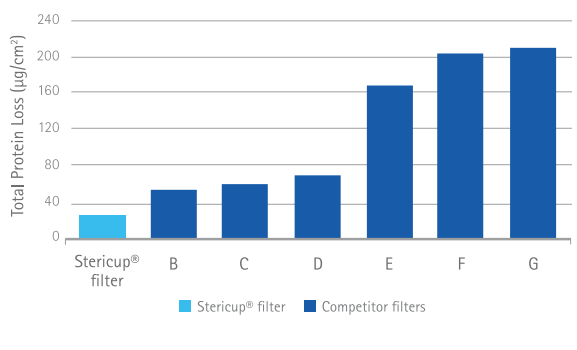

Protein Binding Performance

Don't be fooled – EMD Millipore's history of membrane technology and filter device engineering is unmatched.

View more data and place an order for the one and only true **Stericup® filter** at www.emdmillipore.com/oneStericup

EMD Millipore is a division of Merck KGaA, Darmstadt, Germany

EMD Millipore, the M logo and Stericup are registered trademarks of Merck KGaA, Darmstadt, Germany.
© 2015 EMD Millipore Corporation, Billerica, MA, USA. All rights reserved. BS GEN-15-11097 03/2015

Join AAAS. Get instant access to *Science*. Support all of the sciences.

When you subscribe to *Science*, you become part of the American Association for the Advancement of Science (AAAS), a nonprofit community of more than 100,000 members worldwide who believe in the power of science to make the world a better place. AAAS is hard at work promoting science in government, schools, and in the public commons around the globe.

AAAS's award-winning journal *Science* offers the top peer-reviewed research across multiple disciplines. With your subscription, you'll get:

- 51 weeks of home delivery of *Science*
- Instant online retrieval of every *Science* article ever published, dating back to 1880
- Full access to the *Science* mobile site and apps
- Career advice, webinars, blogs and fascinating features exclusively for AAAS members
- Members-only newsletters, and much more

With increasing public skepticism about science–and public funding for research more uncertain than ever–our work has never been more important. Join hands with us today!

Visit promo.aaas.org/joinaaas. Together, we can make a difference.

Science
AAAS

Table Top Centrifuges

Blue Line table top centrifuges can accommodate sample volumes from 18 × 0.2 ml up to 4 × 200 ml. They have a maximum speed of 18,000 rpm/maximum relative centrifugal force (RCF) of 30,065 x g. The MicroCen and the UniCen can be instantly recognized by their blue covers, and both series can be supplied as refrigerated versions. A range of rotors are available for all models. Customer safety is very important to Herolab, so all models come with a range of standard safety features. For example, the stainless steel chamber has an additional inner guard ring. The Automatic Positive Rotor Identification (APRI) system recognizes the rotor itself and checks for the speed setting. If the speed is selected too high for a particular rotor, the machine will automatically reduce the speed setting to the maximum speed possible for that rotor. If any imbalance is detected, an automatic cutoff will activate.

Herolab
For info: +44-(0)-1223-515440
www.herolab.de

Tube Racks

Hamilton introduces the RackWare HD138 and HD60 high-density Society for Biomolecular Screening (SBS)-footprint racks for microtube and cryovial storage. Designed for use with Hamilton's BiOS, Sample Access Manager (SAM), and Verso sample management and storage systems, the new RackWare increases the storage capacity in a given space by increasing the number of tubes that can be placed in an SBS-footprint rack. These new racks can also be used to maximize storage in manual freezers. RackWare HD138 supports most major 96-format labware and increases storage capacity in a comparable SBS footprint from 96 to 138 tubes. RackWare HD60 increases the storage from 48 to 60 larger cryovials. A common problem in today's labs is ever-growing sample collections coupled with less and less available space. Our new automation-friendly, high-density storage format can deliver space savings of more than 25%, combined with similar savings in both investment and operating costs per sample.

Hamilton Storage
For info: 800-310-5866
www.hamilton-storage.com

High-Voltage Power Supply

The high-voltage power supply series now features a 10,000-V configuration. The 10-kV model joins the already popular 1-, 2-, and 5-kV versions, all of which are used for many purposes in the laboratory. They power photomultiplier tubes, channel and electron multipliers, microchannel plates, and anything that benefits from a stable, adjustable high-voltage supply. Like existing models, the 10-kV Model 7645 is highly regulated and very stable. Voltage is set at the front panel by a precise 10-turn potentiometer. The easy to read 4.5-digit liquid crystal display (LCD) allows users to confidently set and deliver high-voltage levels with 0.001% peak-to-peak regulation. The instrument rear panel features a scaled analog input for remote control and a current monitor output. The new Model 7645 10-kV power supply operates sensitive photomultiplier tubes and related devices for critical photometric and spectroscopy applications.

McPherson
For info: 978-256-4512
www.mcphersoninc.com

Sample Cooling Block

The ChilliBlock is designed for precise, controlled cooling and heating of biological samples in microplates, vials, and Eppendorf tubes. ChilliBlocks can be used directly in conjunction with an ice bath to keep your samples cool and dry. For precise temperature-controlled experiments, ChilliBlocks should be used with our cooling/heating base unit. The ChilliBlock base unit attaches to most laboratory cooling/heating circulators, enabling precise, stable, and even temperature control of biological samples from –30°C to +160°C. Insulated to prevent ice formation at lower temperatures and ensure homogeneity, the ChilliBlock enables stable, consistent temperature control (+/–0.1°C) of biological samples, for a wide range of standard and custom container formats. Manufactured from clear, resistant, anodized aluminum, ChilliBlocks offer good chemical resistance and homogeneous sample temperatures. The ChilliBlock's low profile makes it fully compatible with robotic sample-handling systems.

Asynt
For info: +44-(0)-1638-781709
www.asynt.com

Horizontal Clean Benches

The new horizontal clean benches combine Class 100 (ISO 5) process protection with rugged, easy-to-clean polypropylene construction and microprocessor-based controls. Horizontal laminar flow clean benches from AirClean Systems are the ideal solution for Class 100 (ISO 5) applications where process protection is needed. Constructed from all-white, seamless polypropylene, these workstations are easy to clean and can be used for many applications, including electronic assembly, intravenous (IV) admixture preparation, tissue culture, optic repair, and media preparation. The horizontal clean benches are available in several sizes and can be placed on a benchtop or a cart/stand. Standard on all horizontal clean benches, the UVTect controller constantly monitors filter conditions and airflow. UVTect will alert the operator of insufficient airflow and needed filter changes. These workstations are made in the United States and are shipped fully assembled.

AirClean Systems
For info: 800-849-0472
www.aircleansystems.com

Electronically submit your new product description or product literature information! Go to www.sciencemag.org/products/newproducts.dtl for more information.

Newly offered instrumentation, apparatus, and laboratory materials of interest to researchers in all disciplines in academic, industrial, and governmental organizations are featured in this space. Emphasis is given to purpose, chief characteristics, and availability of products and materials. Endorsement by *Science* or AAAS of any products or materials mentioned is not implied. Additional information may be obtained from the manufacturer or supplier.

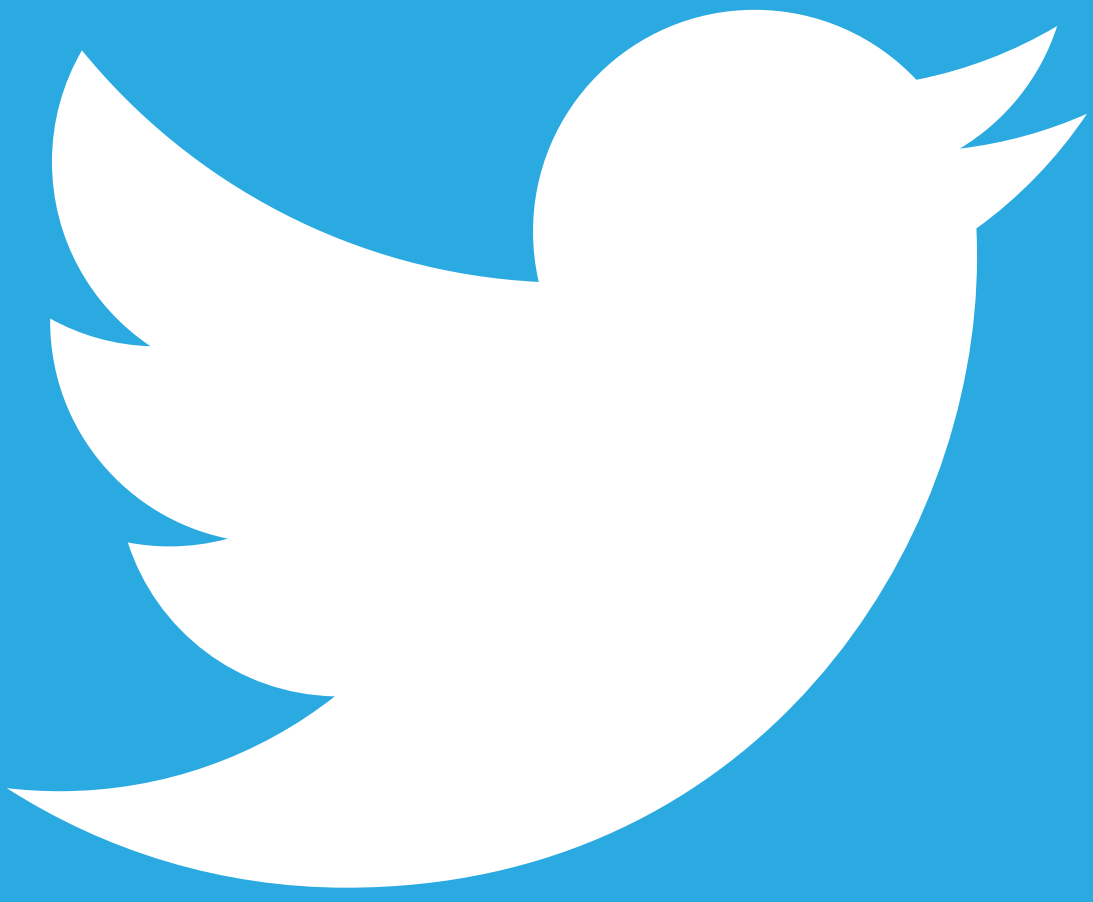

Join the Conversation!

Twitter is a great way to connect with AAAS members and staff about the issues that matter to you most. Be a part of the discussion while staying up-to-date on the latest news and information about your personal member benefits.

Follow us @AAASmember and join the conversation with #AAAS

AAAS MemberCentral

MemberCentral.aaas.org

want new technologies?

antibodies
apoptosis
biomarkers
cancer
cytometry
data
diseases
DNA
epigenetics
genomics
immunotherapies
medicine
microbiomics
microfluidics
microscopy
neuroscience
proteomics
sequencing
toxicology
transcriptomics

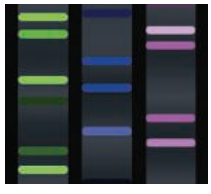

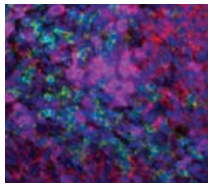

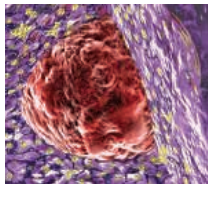

watch our webinars

Learn about the latest breakthroughs, new technologies, and ground-breaking research in a variety of fields. Our expert speakers explain their quality research to you and answer questions submitted by live viewers.

VIEW NOW!
webinar.sciencemag.org

Science
AAAS

Brought to you by the *Science*/AAAS Custom Publishing Office

@SciMagWebinars

Finding cures starts with research tools that actually work...

- Proteomic products and services
- Focused product portfolio
- Products tested for specificity and sensitivity
- Antibodies rigorously tested across a wide range of research applications
- Custom formulations
- GMP-grade recombinant rabbit monoclonal antibodies*
- Bulk orders and lot reservations

* Custom formulations of certain monoclonal antibodies can be produced by CST in compliance with FDA regulations governing ASRs. Such products would be classified as Analyte Specific Reagents. Analytical and performance characteristics are not established. All other products are for Research Use Only. Not For Use In Diagnostic Procedures.

Learn more at: www.cellsignal.com/drugdiscovery

GMP GOOD MANUFACTURING PRACTICES

bsi. ISO 9001 Quality Management

Cell Signaling TECHNOLOGY®

© 2015 Cell Signaling Technology, Inc. Cell Signaling Technology, and CST are trademarks of Cell Signaling Technology, Inc.

15PADINDUPHAR0001ENG_01

Science Careers Advertising

For full advertising details, go to ScienceCareers.org and click For Employers, or call one of our representatives.

Tracy Holmes
Worldwide Associate Director
Science Careers
Phone: +44 (0) 1223 326525

THE AMERICAS

E-mail: advertise@sciencecareers.org

Fax: +1 (202) 289 6742

Tina Burks
Phone: +1 (202) 326 6577

Nancy Toema
Phone: +1 (202) 326 6578

Online Job Posting Questions
Phone: +1 (202) 312 6375

EUROPE / INDIA / AUSTRALIA / NEW ZEALAND / REST OF WORLD

E-mail: ads@science-int.co.uk

Fax: +44 (0) 1223 326532

Sarah Lelarge
Phone: +44 (0) 1223 326527

Kelly Grace
Phone: +44 (0) 1223 326528

Online Job Posting Questions
Phone: +44 (0) 1223 326528

JAPAN

Katsuyoshi Fukamizu (Tokyo)
E-mail: kfukamizu@aaas.org
Phone: +81 3 3219 5777

Hiroyuki Mashiki (Kyoto)
E-mail: hmashiki@aaas.org
Phone: +81 75 823 1109

CHINA / KOREA / SINGAPORE / TAIWAN / THAILAND

Ruolei Wu
Phone: +86 186 0082 9345
E-mail: rwu@aaas.org

All ads submitted for publication must comply with applicable U.S. and non-U.S. laws. *Science* reserves the right to refuse any advertisement at its sole discretion for any reason, including without limitation for offensive language or inappropriate content, and all advertising is subject to publisher approval. *Science* encourages our readers to alert us to any ads that they feel may be discriminatory or offensive.

ScienceCareers
FROM THE JOURNAL SCIENCE AAAS

ScienceCareers.org

Assistant or Associate Professors
Pain and Inflammation

Center for Experimental Therapeutics and Reperfusion Injury
Department of Anesthesiology, Perioperative and Pain Medicine
Brigham and Women's Hospital
Harvard Medical School

We invite applications for tenure-track Assistant or Associate Professor positions; PhD. and/or M.D. will join pain and inflammation research mission of this department. Successful candidates will have maintained research in Translational pain/inflammation, receptors or metabolomics in inflammation-resolution research. Basic and Translational research and mentoring are integral to these positions.

Qualified individuals with post-doctoral training and/or faculty experience should submit a cover letter, and curriculum vitae online at website: **https://research.bwhanesthesia.org/research-groups/cetri/serhan-lab/position**.

The names of three references and application should be addressed to Prof. Charles N. Serhan and James P. Rathmell, M.D., Search Committee Co-Chairs.Deadline: February 27, 2016

Harvard Medical School is an Equal Opportunity/Affirmative Action Employer.

AAAS is here –
helping scientists achieve career sucess.

Every month, over 400,000 students and scientists visit ScienceCareers.org in search of the information, advice, and opportunities they need to take the next step in their careers.

A complete career resource, free to the public, *Science* Careers offers hundreds of career development articles, webinars and downloadable booklets filled with practical advice, a community forum providing answers to career questions, and thousands of job listings in academia, government, and industry. As a AAAS member, your dues help AAAS make this service available to the scientific community. If you're not a member, join us. Together we can make a difference.

To learn more, visit
aaas.org/plusyou/sciencecareers

AAAS + U = Δ

Advance your career with expert advice from *Science* Careers.

Download Free Career Advice Booklets!

ScienceCareers.org/booklets

Featured Topics:

- Networking
- Industry or Academia
- Job Searching
- Non-Bench Careers
- And More

ScienceCareers
FROM THE JOURNAL SCIENCE AAAS

| le savoir vivant |

UNIL | Université de Lausanne
Faculty of Biology and Medicine

THE FACULTY OF BIOLOGY AND MEDICINE OF THE UNIVERSITY OF LAUSANNE, SWITZERLAND AND THE UNIVERSITY MEDICAL CENTRE OF LAUSANNE (CHUV) INVITE APPLICATIONS FOR THE POSITION OF

FULL PROFESSOR OR ASSOCIATE PROFESSOR OF BACTERIOLOGY (METAGENOMICS AND/OR BACTERIAL GENOMICS)

Starting date: to be agreed

Your activities:

The successful candidate will lead the bacterial genomics and metagenomics unit, which is one of the 4 diagnostic unit of the institute of microbiology. He will provide undergraduate, postgraduate and further teaching in Bacteriology, with a specific focus in bacterial genomics, functional genomics and/or metagenomics. The successful candidate will also lead a high-level research program in bacteriology and will participate to the life of the Institute.

Would you like more informations about this position? Connect you with our QR Code

Your application:

The applications, in English, will include a motivation letter, the curriculum vitae, the list of publications with a copy of the five most significant ones, a brief statement of the research programme and teaching experience and a copy of diplomas. They should be sent by April 1st, 2016 as a single pdf file to www.unil.ch/iafbm/application.

The job description as well as a description of the Division are also available on the Web at the address www.unil.ch/emplois «Postes académiques». For further information, please contact Prof. Gilbert Greub (Gilbert.Greub@chuv.ch), Director and Head of Service.

Seeking to promote an equitable representation of women and men among their staff, the University and the University Medical Centre encourage applications from women.

Physiologist
Weill Cornell Medicine - Qatar (WCM-Q)

In a pioneering international initiative, Cornell University and Weill Cornell Medical College (WCMC) established Weill Cornell Medicine - Qatar (WCM-Q) through a unique partnership with the Qatar Foundation for Education, Science and Community Development. Operating in Doha, Qatar since 2002, WCM-Q seeks candidates for the position of

PHYSIOLOGIST

We are seeking a Physiologist, with a thorough understanding of organ systems physiology, who will teach human physiology and will contribute to team-taught courses for medical students, using an array of teaching methods, including problem based learning (PBL) and "flip classroom" and more, at various stages in the medical program. While proficiency in all areas of human physiology is required, preference will be given to candidates with teaching experience in organ based topics and metabolism. It is expected that the successful candidate will take on a leadership role in the continuing development of the pre-clinical curriculum.

Candidates should have a Ph.D. in Human Physiology or its accepted equivalent, a record of excellence in teaching and scholarship, and a minimum of five years of significant teaching experience, preferably of a North American or European medical school curriculum, although teaching experience in undergraduate courses will be considered. Preference will be given to applicants who demonstrate their strong leadership skills in developing and delivering a physiology curriculum in an integrated curriculum; who provide evidence of their successful involvement in the development and delivery of innovative approaches to teaching; and who demonstrate their strong record of excellence in and commitment to teaching in a team environment. Essential skills include a passion for student success, excellent communication and interpersonal skills, ability to work with colleagues and stakeholders, and ability to set and achieve goals.

WCM-Q and WCMC in New York share the same mission: to provide the finest education possible for medical students, conduct research at the cutting edge of knowledge, improve health care, both now and for future generations, and provide the highest quality of care to the community. Full details regarding the WCM-Q program and facilities, including affiliations with ACGME-I accredited clinical sites, can be accessed at **http://qatar-weill.cornell.edu**.

A comprehensive and highly competitive salary and foreign-service benefits package, including fully furnished housing and other supplementary benefits, is provided. The appointment will be on a non-tenure-track and is normally for three years in the first instance, renewable by mutual agreement.

Qualified applicants are invited to submit a thoughtful letter of application outlining their interest in the position and how their skills and experience match WCM-Q's requirements, along with a full curriculum vitae at **http://job.qatar-weill.cornell.edu**

Please note that due to the high volume of applications, only short-listed candidates will be contacted. The Search Committee will begin reviewing applications beginning January 2016 and will continue until the position is filled.

Weill Cornell Medicine-Qatar

Cornell University is an Affirmative Action/Equal Opportunity Educator and Employer (AA/EOE)

Science Careers online @sciencecareers.org

ScienceCareers online @sciencecareers.org

For recruitment in science, there's only one Science

Fantastic Recruiting Opportunity!

POSTDOC CAREERS | March 25, 2016

Be sure to promote your openings to the thousands of scientists who will be reading *Science* to find out about the latest postdoc opportunities.

Reserve ads by March 8 to guarantee space.

Produced by the *Science*/AAAS Custom Publishing Office.

SCIENCECAREERS.ORG

ScienceCareers
FROM THE JOURNAL SCIENCE AAAS

To book your ad: **advertise@sciencecareers.org**

The Americas
+202-326-6582

Japan
+81-3-3219-5777

Europe/RoW
+44(0)1223-326500

China/Korea/Singapore/Taiwan
+86-186-0082 9345

Government of India
Department of Biotechnology
Ministry of Science & Technology

RAMALINGASWAMI RE-ENTRY FELLOWSHIP : 2015-16

Applications are solicited from Indian nationals working in overseas research institutions for the "**Ramalingaswami Re-entry Fellowship**", a Re-entry scheme of the Department of Biotechnology (DBT), Ministry of Science & Technology, Government of India.

Aim of the Fellowship

The scheme is conceptualized with the aim of attracting highly skilled researchers (Indian nationals) working overseas in various cutting edge disciplines of biotechnology (agriculture, health sciences, bio-engineering, energy, environment, bioinformatics and other related areas), by providing them an attractive avenue to pursue their R&D in Indian institutions.

Who is eligible to apply ?

The applicant should possess a Ph.D., M.D., M. Tech, M.VSc. or equivalent degree with an outstanding track record as reflected in publications and other recognitions and with at least three years of post-doctoral research experience of which last two years should be from overseas laboratory.

Candidates (Indian nationals) working overseas are eligible to apply. Those who have already returned to India within one year of the closing date of this advertisement are also eligible. Researcher's upto 55 years of age as determined on closing date of application are eligible to apply.

Incentives of being a Ramalingaswami Fellow

1. This is a senior fellowship programme, and awardees are to be considered synonymous to the faculty/scientists at the level of Scientist-D. They are entitled to take up teaching/research assignments and supervising Doctoral/MS students.
2. The scheme provides a consolidated monthly remuneration of Rs. 85,000/- p.m In addition, a House Rent Allowance of Rs. 7,500/- p.m. is given to fellows. In case host institute provides accommodation to the fellow, no house rent allowance is admissible.
3. Fellows will receive a research/contingency grant of Rs. 10.00 lakhs for the 1st year, Rs. 7.50 lakhs for the 2nd year and Rs. 5.00 lakhs for the subsequent 3 yrs. for purchase of consumables, minor equipment, international and domestic travel, engaging manpower and other contingent expenditure to be incurred for the implementation of research proposal.
4. DBT encourages host institutions to provide medical benefits, transport allowance, leave travel allowance and other benefits as per their prevailing norms as applicable to their employees of the rank equivalent to Scientist D out of their own resources/ funds.
5. Fellows retain an option for drawing either the fellowship or salary if they are appointed at a suitable permanent scientific position. Fellows opting for salary can continue to avail the research /contingency grant with prior approval of DBT.
6. Ramalingaswami Re-entry Fellows could take up fellowship at any of the scientific institutes/ universities in the country. However, application should be duly forwarded by the competent authority of the host Institute.Fellows/Awardee can change his/her host institute only once during the tenure of the fellowship.
7. Awardees are eligible to apply for research grants to any of the funding agencies towards accomplishment of research proposal. However, the Co-PI has to be a permanent employee of the host institution.

Tenure of fellowship

Fellows can draw fellowship for a term of five years. Fellowship is further extendable for another term on a fresh appraisal of performance of the fellow.Those who are able to secure permanent positions will not be considered for 2nd term.

How to apply

Applications may be sent as per Proforma downloadable from DBT website (**www.dbtindia.nic.in**) and duly forwarded by the competent authority *to* **Dr. Meenakshi Munshi, Director, Department of Biotechnology, Block-2, 7th Floor, CGO Complex, Lodhi Road, New Delhi -110 003, both as hard copy as well as soft copy latest by 28 th February, 2016. soft copy to be mailed at Email : rlsfellowship.dbt@nic.in only a single file . The applications not forwarded by the host institution will not be considered.**

Download the
Science Careers jobs app from Science

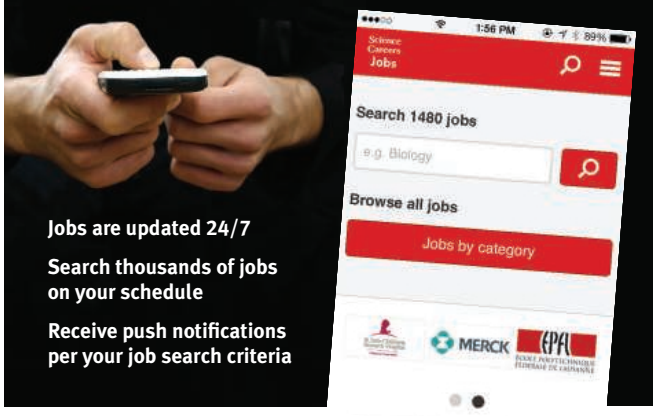

Jobs are updated 24/7

Search thousands of jobs on your schedule

Receive push notifications per your job search criteria

Get a job on the go.

Search worldwide for thousands of scientific jobs in academia, industry, and government. The application process is seamless, linking you directly to job postings from your customized push notifications.

Scan this code to download app or visit **apps.sciencemag.org** for information.

ScienceCareers | AAAS
FROM THE JOURNAL SCIENCE

ScienceCareers.org

UNC
SCHOOL OF MEDICINE

PHYSICIAN-SCIENTISTS –OPEN RANK (TENURE/TENURED TRACK)

The Department of Medicine at the University of North Carolina at Chapel Hill invites applications for Open Rank (tenure/tenured track) faculty in Medicine in the areas of Cardiology, Endocrinology, Gastroenterology and Hepatology, General Medicine, Geriatrics, Hematology/Oncology, Infectious Diseases, Nephrology and Hypertension, Pulmonary and Critical Care Medicine, and Rheumatology, Allergy and Immunology. Candidates must have an M.D. and be Board Certified in a medical subspecialty; a secondary Ph.D. is welcome. Successful applicants will possess an exceptional record of basic or translational research demonstrated by publications in leading peer-reviewed journals. Applicants at the Assistant Professor level will be expected to establish and maintain an extramurally funded research program. Those at the Associate Professor and above rank should have extramural funding and a national reputation in their field. Physician-Scientists will have clinical privileges in their Medicine subspecialty, as well as opportunity for joint appointment in a basic science department.

Candidates should apply online at **http://unc.peopleadmin.com/postings/87854** and include a cover letter, a curriculum vitae, a 2-3 page summary of past and future research goals, and contact information for 3 references.

The University of North Carolina at Chapel Hill is an Equal Opportunity Employer that welcomes all to apply, including protected veterans and individuals with disabilities.

WORKING LIFE

By **Jesse Shanahan**

Disability is not a disqualification

When I began my master's program in astronomy, I immediately encountered a substantial—and quite literal—obstacle to my pursuit of the cosmos: a flight of stairs. I have a physical disability, and stairs are a particular source of difficulty. Unfortunately, they lie in front of every entrance to the building where I take classes, teach labs, and conduct research. The four observatories I have visited for my research were all equally inaccessible, mostly because their age and historic significance exempt them from Americans with Disabilities Act requirements. So, besides coping with the stress and workload of graduate school, I must also struggle with architecture. Thankfully, I am mobile enough to make do by climbing slowly or using a cane, but it takes a toll.

The barriers don't end once I've reached the top of the stairs. I face hostility from other scientists, including the ire of professors who believe that my need for flexible deadlines or breaks during tests arises from laziness. This sentiment, rooted in a scientific culture that prioritizes a pathological devotion to work over mental and physical well-being, is best summed up by one of my professors, who commented on my disability: "It must be so nice to have an excuse not to do any work."

"The barriers don't end once I've reached the top."

Regrettably, my experiences are not unique; they are emblematic of the barriers disabled scientists contend with throughout their careers. Although science is by no means intrinsically inaccessible—nothing about the data we gather or the analyses we do inherently excludes people with disabilities—the prevailing attitudes in science create these barriers. Most science, technology, engineering, and math (STEM) programs insist that researchers sacrifice both their mental and physical health to succeed. Unnecessarily long hours, undue degrees of stress, and overwhelming pressure can cause even the healthiest person to develop anxiety and depression. For a person with a disability, coping with these pressures along with a permanent or chronic condition can be devastating.

The numbers tell the story: Only 9% to 10% of undergraduate STEM students in the United States have disabilities, compared with approximately 20% of Americans overall. Among those who obtain Ph.D.s, the number falls to just 1%. Of those who persist in STEM fields, many hide their disabilities out of concern for their careers, as several professors with disabilities shared with me after I spoke about inaccessibility at the Inclusive Astronomy conference this past June. One said she hid her disability because she expected it would affect her tenure evaluation. Another said she kept hers secret because she thought the progressive nature of her condition would make her unhireable.

Being visibly disabled, I do not have this option, and I worry about how it will affect my career. Any appearance of not being able to shoulder my graduate student duties will decrease my competitiveness when I apply for Ph.D. programs, postdoctoral fellowships, or faculty positions. If I seem to have a history of taking medical leaves because I need to prioritize my health, my value as a future faculty member or researcher may be diminished. And I fear the day when I may need a wheelchair, which would prevent me from accessing many of the necessary tools for my research.

Nonetheless, for now at least, I remain in astronomy, where my research drives me forward. First and foremost, though, the prospect of making astronomy more accessible helps me persevere. I hope to be a conspicuous example of a disabled astronomer so that future students with disabilities do not feel as isolated as I did. I have spoken about disability issues at several conferences and helped create the first American Astronomical Society (AAS) Working Group on Accessibility and Disability, and I recently began serving on the AAS Early Career Advisory Board. I already see positive changes as a result of this work. At the most recent AAS conference, we provided accessibility information about the convention center, and I met with journal publishers about creating accessible online publication formats. But a significant barrier still remains: the erroneous assumption that ableness is a prerequisite for scientific achievement. ■

Jesse Shanahan is a master's student in astronomy at Wesleyan University in Middletown, Connecticut. Send your story to SciCareerEditor@aaas.org.

ILLUSTRATION: ROBERT NEUBECKER

Published by AAAS